UNIVERSITE DE LIEGE

FACULTE DE MEDECINE VETERINAIRE

DEPARTEMENT DES SCIENCE FONCTIONELLES

LABORATOIRE D'IMMUNOPHYSIOLOGIE

Investigation spatio-temporelle et fonctionnelle de macrophages atypiques Ly6G^{+} recrutés suite à des lésions pulmonaires

Spatiotemporal and functional investigation of atypical Ly6G^{+} macrophages recruited after lung injury

Cecilia RUSCITTI

THESE PRESENTEE EN VUE DE L'OBTENTION DU GRADE DE

DOCTORAT EN SCIENCES VETERINAIRES

ANNEE ACADEMIQUE 2024-2025

Remerciements

Je souhaite exprimer mes plus sincères remerciements à toutes les personnes qui ont contribué, de près ou de loin, à l'élaboration et à l'aboutissement de cette thèse.

Je tiens à exprimer toute ma gratitude à mon promoteur, le professeur Thomas Marichal, pour sa confiance, son enthousiasme contagieux et sa disponibilité sans faille. Son accompagnement et ses précieux conseils, tant sur le plan scientifique que pratique, ont été essentiels tout au long de ce parcours. Dans les moments de doute et de difficulté, ses encouragements ont été une véritable bouée de sauvetage. J'ai eu la chance de pouvoir compter sur un leader comme lui, toujours présent pour partager autant les défis que les succès. Un remerciement spécial à ma co-promotrice, voisine de bench et de bureau Coraline Radermecker avec qui j'ai pu partager directement les hauts et les bas des projets. Elle m'a toujours soutenu, tant techniquement que émotivement, en prenant le temps de trouver des solutions aux défis continus de la recherche. Elle a été pour moi un point de repère et un modèle à suivre.

Je remercie également les membres de mon comité de thèse, Bénédicte Machiels et Julien Guiot, pour leurs suggestions et leurs échanges constructifs qui ont enrichi cette recherche. Leur contribution directe et leur expertise sur l'immunité pulmonaire, d'un côté, et la pneumologie clinique, de l'autre, ont permis des avancées majeures de ce projet. Je suis profondément reconnaissante de l'investissement et du temps qu'ils ont consacré à m'accompagner et à évaluer cette recherche.

Je souhaite exprimer ma gratitude à mes collègues de rêve, qui grâce à leurs mains gantées et surtout à leur présence quotidienne ont contribué à la réalisation de ce projet. Grace à eux le labo est devenu un lieu chaleureux et agréable, une deuxième maison.

Je tiens à remercier les collaborateurs et les plateformes techniques du GIGA. En particulier, je remercie la plateforme de d'imagerie et la plateforme de génomique pour avoir mis leur expertise et leur temps au service de ce projet. Je remercie également la plateforme de vecteur viraux pour leur gestion des laboratoires L3, sans lesquels le projet n'aurait pas pu être réalisé. Je remercie également le personnel de l'animalerie pour la gestion quotidienne des élevages.

Enfin, ma gratitude va à mes amis et à ma famille pour leur présence, leurs encouragements, et leur compréhension durant toutes ces années. Leur soutien m'a permis de garder le cap et d'achever, enfin, ce projet.

Table of contents

Abbreviations

AM: Alveolar Macrophages

ARDS: Acute Respiratory Distress Syndrome

Areg: Amphiregulin

Arg-1: Arginase-1

AT1 : Alveolar Type I epithelial cell

AT2: Alveolar Type II epithelial cell

BALF: Broncho-Alveolar Lavage Fluid

BM: Bone Marrow

CCL: C-C motif chemokine Ligand

cDC: conventional Dendritic Cell

cMoP: committed Monocyte Mrogenitor

CMP: Common Myeloid Progenitor

CSF-1: Colony Stimulating Factor 1

CSF-1R: Colony Stimulating Factor 1 Receptor

CSF-2: Colony Stimulating Factor 2

CSF-2R: Colony Stimulating Factor 2 Receptor

CXCL: C-X-C motif chemokine ligand

DATP: Damage-Associated Transient Progenitor

DC: Dendritic Cell

DT : Diphteria Toxin

ECM: Extracellular Matrix

EGF: Epidermal Growth Factor

EMPs: Erythro-Myeloid Precursor

FACS: Fluorescence-Activated Cell Sorting

FGF: Fibroblast Growth Factor

G-CSF: Granulocyte-Colony Stimulating Factor

GM-CSF: Granulocyte-Macrophage colony-stimulating factor

GMP: Granulocyte-Monocyte Progenitor

HA: Hemagglutinin

HDM: House Dust Mite

HSC: Hematopoietic Stem Cell

IAV: Influenza A virus

IGF-1: Insulin-like Growth Factor-1

IL-: Interleukin

IL-1ra: Interleukin-1 Receptor antagonist

ILC2: Innate Lymphoid Type 2 cell

IM: Interstitial Macrophages

iMo: inflammatory Monocytes

iNOS: inducible Nitric Oxide Synthase

IPF: Idiopathic Pulmonary Fibrosis

LPS: Lipopolysaccharide

$Ly6C^-$ Mo: patrolling $Ly6C^-$ Monocytes

$Ly6C^+$ Mo: classical $Ly6C^+$ Monocytes

M-CSF: Macrophage Colony Stimulating Factor

MDP: Monocyte and Dendritic cell Progenitor

MHC2: Major Histocompatibility Complex 2

MMP: Matrix MetalloProteases

Mo: Monocyte

MPS: Mononuclear Phagocyte System

NA: Neuraminidase

Neu: Neutrophils

NK: Natural killer

Opn: Osteopontin

p.i.: post-infection

Pdgfrα: Platelet-derived growth factor receptor alpha

PRR: Pattern Recognition Receptor

RELMα: Resistin-like molecules

scRNA-seq: single-cell RNA sequencing

SP: Surfactant Protein

TGF-β: Transforming Growth Factor β

TNF: Tumor Necrosis Factor

Treg: Regulatory T cells

VEGF: Vascular Endothelial Growth

RÉSUMÉ-SUMMARY

Résumé

En raison de leur structure et de leur rôle dans la respiration, les poumons sont continuellement exposés aux agents pathogènes présents dans l'air. Parmi ceux-ci, les virus respiratoires causent une mortalité importante et représentent un fardeau économique considérable. Les virus respiratoires courants entraînent généralement des infections légères et de courte durée, mais la pandémie de COVID-19 a révélé un taux élevé de persistance des pathologies respiratoires après des infections aiguës. Ces séquelles chroniques résultent de l'échec des mécanismes efficaces de réparation pulmonaire, entraînant fibrose, remodelage tissulaire anormal et bronchiolisation alvéolaire. Les cellules myéloïdes jouent un rôle central dans la réponse immunitaire lors des infections respiratoires et leurs fonctions pendant l'infection active sont bien caractérisées. Cependant, leurs fonctions pendant la phase de récupération restent peu comprises. Afin d'étudier les réponses immunitaires au cours de la réparation pulmonaire, un modèle murin cliniquement pertinent d'infection par le virus de la grippe A (utilisant la souche H1N1 PR8) a été employé. Des technologies de pointe, incluant le séquençage d'ARN unicellulaire, la transcriptomique spatiale, les tests métaboliques, la cytométrie en flux multiplexe et la microscopie, combinées à des modèles de chimères de moelle osseuse et des souris transgéniques, ont permis une analyse approfondie des populations de cellules myéloïdes durant les premières phases de réparation pulmonaire. Cette approche exhaustive a conduit à l'identification et à la caractérisation d'une population de macrophages dérivés de monocytes encore inconnue présente dans les poumons lors de la phase de récupération précoce. Ces macrophages, à courte durée de vie et exprimant Ly6G, sont recrutés après le pic de l'infection dans les alvéoles périlésionnelles en régénération, où ils montrent de fortes capacités d'efferocytose et sécrètent des molécules facilitant la résolution de l'inflammation. De plus, les macrophages Ly6G$^+$ jouent un rôle crucial dans la promotion de la régénération alvéolaire en interagissant avec les cellules épithéliales alvéolaires de type 2, progénitrices de l'épithélium alvéolaire et en soutenant leur rôle essentiel dans la réparation alvéolaire fonctionnelle. La présence de ce phénotype de macrophages a été observée dans d'autres modèles, incluant les lésions pulmonaires induites par la bléomycine et les dommages hépatiques aigus induits par le paracétamol, indiquant un rôle conservé à travers différents types et sites de lésions. Enfin, la pertinence potentielle de ces découvertes a été explorée en analysant les cellules de lavage bronchoalvéolaire chez des patients atteints de pneumonie, où des cellules semblables aux macrophages Ly6G$^+$ ont été identifiées. Nos résultats enrichissent la compréhension des mécanismes myéloïdes impliqués dans la régénération alvéolaire et suggèrent que la manipulation de ces macrophages pourrait constituer une stratégie pour améliorer la réparation pulmonaire après une lésion pulmonaire infectieuse aiguë.

Summary

The lungs, due to their structure and function, are constantly exposed to airborne pathogens, with respiratory viruses causing significant mortality and economic burden. Common respiratory viral pathogens typically cause mild, self-limiting infections, but the COVID-19 pandemic has underscored the high incidence of chronic sequelae following acute infections. Persistent respiratory symptoms arise from the failure of effective lung repair mechanisms, leading to fibrosis, abnormal tissue remodeling, and alveolar bronchiolization. Myeloid cells are central to the immune response during respiratory infections and their roles during active infection are well-characterized. Yet, their functions in the recovery phase remain poorly understood. To investigate immune responses during lung repair, a clinically relevant murine model of influenza A infection (using the H1N1 PR8 strain) was employed. Cutting-edge technologies including single-cell RNA sequencing, spatial transcriptomics, metabolic assays, multiplex flow cytometry, and microscopy, combined with bone marrow chimera models and transgenic mice enabled an in-depth analysis of the myeloid cell populations during the early stages of lung repair. This comprehensive approach led to the identification and characterization of as-yet unknown monocyte-derived macrophage population present in lung during the early recovery phase. These short-lived Ly6G-expressing macrophages were recruited after the peak of infection into perilesional regenerating alveoli where they exhibited high efferocytic capacities and secreted molecules facilitating the resolution of inflammation. Furthermore, Ly6G^{+} macrophages played a crucial role in promoting alveolar regeneration by interacting with alveolar type 2 epithelial cells, the progenitors of the alveolar epithelium, and by supporting their essential role in euplastic alveolar repair. The presence of this macrophage phenotype was observed in other models, including bleomycin-induced lung injury and acetaminophen-induced acute liver damage, indicating a conserved role across different types and sites of injury. Finally, the potential translational relevance of these findings was explored by analysing human bronchoalveolar lavage cells from pneumonia patient, in which Ly6G^{+} macrophage-like cells were identified. Our findings increase our understanding of the myeloid-mediated mechanisms involved in alveolar regeneration and suggested that manipulating these macrophages could serve as a strategy to enhance lung repair following acute infectious lung injury.

INTRODUCTION

1 Macrophages

1.1 Lung parenchyma: the respiratory community

Lungs are vital organs that are dedicated to respiration and located within the thoracic cavity. The respiratory system is composed of two main parts: the conducting airways, which facilitate air movement into and out of the lungs, and the respiratory parenchyma, where gas exchanges and blood oxygenation occur. Following the upper airways, which include the nose, nasopharynx, and larynx, the trachea branches into increasingly narrower bronchi and bronchioles. The respiratory parenchyma, accounting for approximately 90% of lung volume, starts with the respiratory bronchioles, which are absent in mice[1], and extends to the alveoli, the sac-like structures essential for gas exchanges. The alveolar architecture is optimized for respiration, featuring a large surface area and a 0.3 µm thin alveolo-capillary membrane, which facilitates rapid oxygen and carbon dioxide diffusion[2]. The alveolar-capillary barrier consists of two continuous cell layers: the epithelium facing the alveolar lumen and the endothelium facing the capillary lumen. Located between these layers and enveloping the bronchovascular tree is the interstitium, an extracellular matrix through which nerves and lymphatic vessels traverse the lungs.

Each part of the pulmonary tract is composed of a variety of specialized cells that perform specific functions. The airway surface is lined with secretory, goblet and ciliated cells, which serve to keep the inspired air moist and free from potentially harmful substances[3]. The alveoli are composed by a continuous mosaic of alveolar type I (AT1) and type II (AT2) epithelial cells. AT1 cells are responsible for gas exchanges and cover approximately 95% of the total alveolar surface with their thin, flat extensions. AT1 cells are interspersed with cuboidal AT2 cells, which produce surfactant, a liquid mixture that reduces surface tension at the air-liquid interface and prevents alveolar collapse at the end of expiration. Lipids constitute approximately 90% of the surfactant weight, with phosphatidylcholine being the predominant component responsible for its biomechanical properties. Additionally, the surfactant contains four associated proteins: surfactant protein A (SP-A), SP-B, SP-C, and SP-D. SP-A and SP-D are

members of the collectin family, which can interact with pathogens to inhibit their dissemination and modulate immune responses[4]. In contrast, SP-B and SP-C contribute to the formation and characteristics of the interfacial film[5].

However, this extensive barrier serves as an easy entry point for inhaled pathogens. A delicate balance is therefore essential to defend against external pathogens without causing long-lasting structural changes that could impair gas exchange efficiency. Two types of resident innate immune phagocytes contribute to this first line of defense: alveolar macrophages (AM) and interstitial macrophages (IM). Besides their sentinel role, AM and IM fulfil their roles of resident immune cells by actively contributing to tissue structural and functional integrity[6–9]. As discussed in following sections, significant differences in their localization, ontogeny, transcriptional profiles, phenotypes and functions necessitate their study as distinct populations.

AMs are the most prevalent macrophage population, primarily located in the alveolar lumen, with a smaller presence in the conducting small airways[10]. In contrast, IMs reside within the alveolar interstitium or around the bronchovascular bundles, in proximity to neurons, lymphatic vessels, or blood vessels[8,11,12]. Several studies utilizing single-cell RNA sequencing (scRNA-seq) and flow cytometry analyses have revealed additional heterogeneity within the IM population. The IM compartment contains at least two distinct subsets, distinguished by their expression of CD206[11,12]. $CD206^{+}$ IMs are predominantly localized in the interstitium surrounding the bronchi, in close contact with endothelial cells[11]. $CD206^{-}$ IMs, which express high levels of Major Histocompatibility Complex 2 (MHC2), are enriched in the alveolar interstitium and interact with nerves[8]. Transcriptional and protein markers of AM and IM in mice are summarized in Figure 1.

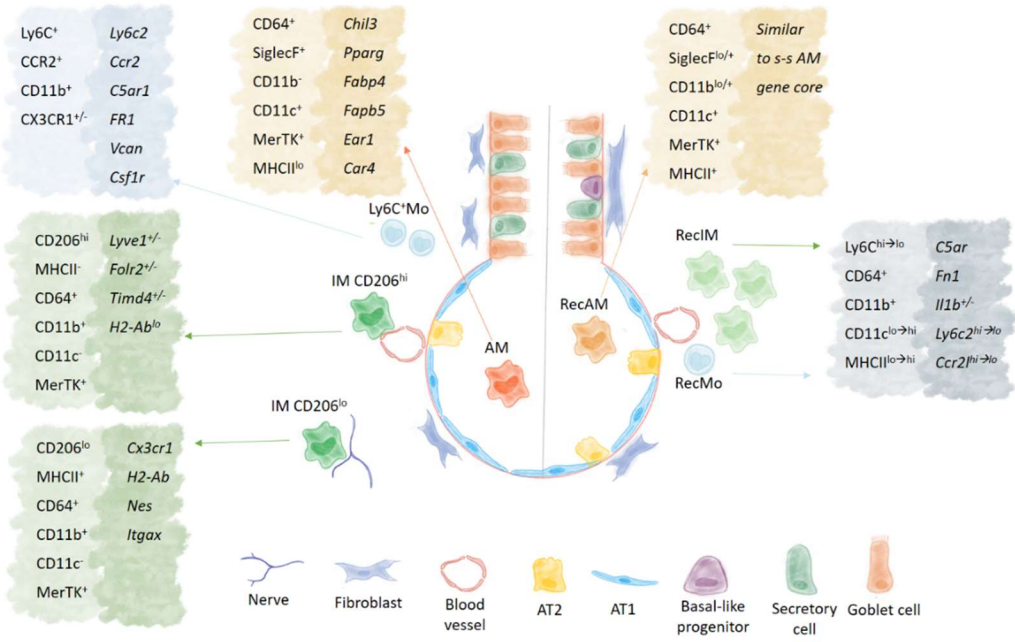

Figure 1 - The distinct subsets of lung macrophages and monocytes in the mouse lung, classified according to their protein and gene markers

Macrophages and monocytes are classified based on their expression of specific protein (left side) and gene (right side) markers within the lung, under steady-state and inflammatory conditions. Each subset occupies distinct regions within the lung environment and performs unique functions. Ly6C^{+} monocytes, also known as classical monocytes, are short-lived, bone marrow-derived cells. Unlike Ly6C^{lo} patrolling monocytes, which circulate along blood vessels, a portion of these cells are present in lung tissue. Their mobilization from the bone marrow is dependent on CCR2, and they express high levels of the Ly6C receptor, distinguishing them from patrolling Ly6C^{lo} monocytes. Similar to interstitial macrophages (IMs), but unlike resident alveolar macrophages (AMs), Ly6C^{+} monocytes express the integrin CD11b. Both AMs and IMs exhibit high expression of CD64 and MerTK, which are recognized as macrophage markers, but they are readily distinguished by the expression of SiglecF, which is uniquely found on AMs. Notably, eosinophils also express high levels of SiglecF; however, they are excluded from the AM population due to the absence of CD64. Several studies[11,12] have identified two major IM subsets, differentiated by their differential expression of CD206 and MHCII. CD206^{+}MHCII^{lo} IMs are preferentially located near blood vessels, while CD206^{lo}MHCII^{hi} IMs are mainly found around nerves. Consequently, the latter population is also referred to as nerve-associated macrophages (NAMs). During inflammatory conditions, the AM population is supplemented by monocyte-derived macrophages, which show varying levels of SiglecF and CD11b expression, called recruited AMs (RecAM). Similarly, the IM pool can also be supplemented by monocyte-derived cells, called recruited IMs (RecIMs), resulting in a continuum or gradient of marker expression, transitioning from monocyte-associated receptors to those found on fully differentiated IMs. Mo: Monocyte; IM: Interstitial Macrophage; AM: Alveolar Macrophage; RecAM: recruited Alveolar Macrophage; RecIM: recruited Interstial Macrophage; RecMO: Recruited Monocytes; s-s: steady state.

Inspired by *Aegerter, H., Lambrecht, B. N. & Jakubzick, C. V., Immunity 55, 1564–1580 (2022).*[9] and *Shi et al., Journal of Leukocyte Biology 110, 107–114 (2021)*[13]

1.2 Old but gold

Prior to the pioneering work of Charles Janeway[14], innate immunity was traditionally known as ancestral immunity[15]. In fact, since the emergence of the first eukaryotic cells, the need for a rapid host response to invading pathogens led to the evolution of defence mechanisms that could guarantee cellular integrity and survival. This ancestral immunity is believed to have arisen approximately one billion years ago, while the organization of adaptive immunity developed only around 450 million years ago in more complex organisms, such as primitive jawed fishes[16]. From unicellular amoebae to multicellular animals, one of the most conserved strategies for eliminating microorganisms, foreign substances, or dead cells is by engulfing these particulate matter, a process called phagocytosis[17,18]. Phagocytosis not only plays an indisputable role in host defence but is also crucial for organ development[19], the maintenance of healthy physiological states[20], and recovery from injury[21,22]. In multicellular organisms, the ability to perform phagocytosis is present in almost all cell types, but it is particularly effective in a specialized group of professional phagocytes[23], which are referred to as amoebocytes, hemocytes, or coelomocytes in invertebrates[24]. Despite the phylogenetic distance between hosts, phagocytes exhibit morphological and molecular characteristics similar to macrophages[25] (from the Greek "makros", large, and "phagein", to eat), which were first described by Elie Metchnikoff in 1882[26].

1.3 Morphology

Macrophages are generally large cells, with size variations dependent on the species and activation states[27], in human between 25 and 30 μm[28]. Main cellular and subcellular features are an irregular cell shape, oval- or kidney-shaped nucleus, cytoplasmic vesicles and a high cytoplasm-to-nucleus ratio[29] (Fig. 2). Both their shape and the intracellular vesicles are directly correlated with macrophage sentinel functions.

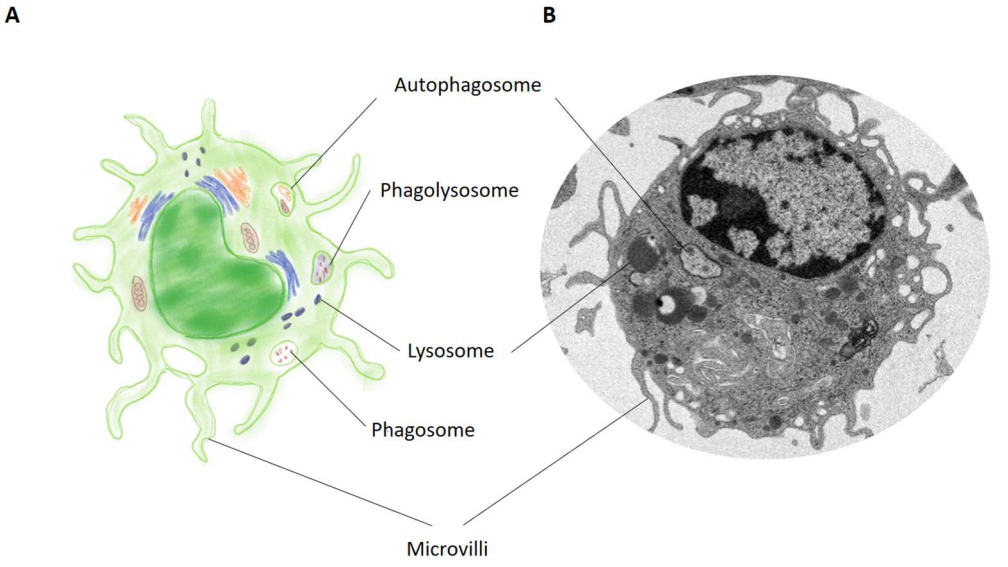

Figure 2 - Subcellular components of macrophages: focus on phagocytosis

A. Schematic illustration of a macrophage; B. Electron microscopy picture of a lung tissue macrophage.

As professional phagocytes, macrophages possess the capacity to rapidly recognize and target pathogens, such as bacteria, as well as apoptotic cells. The presence of microvilli, which are folds in the cytoplasmic membrane, enhance macrophage functionality by increasing the cell surface area, thereby improving particle binding. Additionally, these structures facilitate environmental sensing and cell migration. Target recognition occurs through surface receptors, after which the macrophage extends its membrane around the particle to form a phagocytic cup. This structure closes to engulf the target within a membrane-bound vesicle known as a phagosome. The phagosome subsequently fuses with lysosomes, organelles rich in catalytic enzymes, creating a phagolysosome, where the engulfed material is broken down into smaller molecules. The degraded material is either expelled from the macrophage or, in the case of pathogens, fragments can be presented on the cell surface via MHC molecules to initiate the adaptive immune response. Similarly, macrophages utilize a comparable mechanism to degrade and recycle their own cellular components. During autophagy, a portion of the cytoplasm is enveloped, forming a double-membrane vesicle called an autophagosome, which is then degraded by lysosomal enzymes.

B. Credit to Prof Marc Thiry, Cellular and tissular biology, University of Liege

Irregular shape - The cytoskeleton actin of macrophages reorganizes into pseudopodia, which are large protrusions that extend several microns from the cell body[30]. Even under homeostatic, unstimulated conditions, resident immune cells generate pseudopodia to actively patrol[31] or send long processes through the parenchyma to reach distant zones while remaining relatively sessile[32,33]. In addition, membrane protrusions may fold, fuse, trap, and sample large volumes of extracellular fluid through a process called micropinocytosis[34], or serve as the initial contact points for receptor-mediated phagocytosis of particulate targets[35]. Upon activation, particularly in concomitance with the expression of the class A scavenger receptor MARCO (macrophage receptor with collagenous structure)[36], cytoskeleton actin filaments organize into parallel bundles, forming thin, finger-like membrane protrusions known as microvilli (50-350 nm in diameter, less than 4 µm in length) or filopodia (100-400 nm in diameter, up to 40 µm in length) [37]. Filopodia, described as cellular tentacles, allow macrophages to overcome spatial constraints. By extending phagocytic filopods, macrophages can bind distant particles or pathogens[38]. Within seconds, filopodia retract and pull these particles towards the cell, facilitating their engulfment[39]. Moreover, membrane folds significantly increase the cell surface area and enhance the accuracy in sensing the spatial distribution of ligand gradients. The enrichment of chemokine receptors, such as CCR5, CCR2, and CXCR4[40], selectins[41], and integrins[42] on microvilli, enables precise localization of the environment, as well as improved adhesion and mobility through tissues, thereby enhancing the efficiency of chemotactic processes.

Cytoplasmic vesicles - There are several different vacuolar structures in the cytoplasm of macrophages, and each one has a specific purpose. Initially described by Christian de Duve[43], lysosomes are membrane-bound spherical organelles characterized by round or ovoid profiles. These organelles play a crucial role in protein degradation and the recycling of cellular waste[44]. The lysosomal membrane segregates the acidic environment of the lumen, which contains approximately 60 different soluble hydrolases, including peptidases, lipases, and nucleases. Lysosome fuse with other vesicles, the phagosomes, containing a wide range of extracellular and intracellular substrates and facilitate their digestion[45]. Endocytosis, a key cellular process for internalizing extracellular materials, includes mechanisms like

phagocytosis and macropinocytosis, which depend on the nature of the particles being internalized[46]. Phagocytosis, a receptor-initiated process, is specifically responsible for the uptake of larger particles such as apoptotic cells and microbial pathogens, typically those ≥ 0.5 µm in diameter. Macrophages, as professional phagocytes, are well-equipped with a range of receptors to recognize targets directly (non-opsonic recognition) or via host-derived proteins bound to targets (opsonic recognition). Non-opsonic receptors include: C-type lectins, such as Dectin-1[47] and Mincle (macrophage-inducible C-type lectin) [48], Lectin-like recognition molecules, such as CD33 and CD169[49] and scavenger receptors, such as CD206, MARCO, and CD68[50]. Opsonic receptors, on the other hand, bind to particles that have been labelled by soluble circulating molecules, which facilitate their recognition and uptake. Key opsonic receptors include: Fc receptors (FcR), binding the Fc portion of antibodies, includes CD64 which binds to IgG antibodies[51] and CD89 which binds to IgA antibodies[52]. Furthermore, macrophages are capable of recognizing dying cells and engulfing them through a phagocytic process known as efferocytosis. In both homeostasis and inflammatory conditions, apoptotic cells emit "find-me" and "eat-me" signals to recruit immune cells and induce their engulfment. Typically, apoptotic cells expose phosphatidylserine on the outer plasma membrane, which is recognized by the TIM family of receptors[53]. Macropinocytosis involves the non-selective uptake of solute macromolecules larger than 0.2 µm in diameter, allowing macrophages to early sense environmental changes and to trap and deliver to intracellular receptors[54] soluble ligands released by pathogens distant from the sites of infection[55]. This uptake of extracellular fluid results in large vacuoles called macropinosomes (>250 nm) [56]. While macropinocytosis is a constitutive ability of macrophages, it is enhanced in response to growth factors[55], chemokines such as CXCL12[57], or pathogen-derived molecules[58]. Constitutive macropinocytosis is related to surveillance and antigen presentation[59], whereas induced macropinocytosis is associated with the acquisition of extracellular nutrients that support cell growth and metabolism[60]. Autophagy is a cellular process in which intracellular components are captured, degraded, and recycled. This process can occur through several mechanisms: cytoplasmic materials may be directly engulfed by the invagination of the lysosomal membrane (microautophagy) [61], internalized through receptor-mediated

interactions (chaperone-mediated autophagy) [62], or sequestered within large vesicles known as **autophagosomes** (macroautophagy)[63]. Autophagosomes are particularly abundant in the cytoplasm of activated macrophages due to the regulation of autophagy by pattern recognition receptors (PRRs) that are activated by invading pathogens[64,65]. Autophagy plays a crucial role in the regulation of the activation of intracellular inflammatory pathways[66], the production of inflammatory cytokines[67], and the polarization of macrophages[68,69]. The breakdown products resulting from autophagy are recycled into new cellular components and energy to meet the cell's nutritional needs. Additionally, lysosomes can secrete their contents through exocytosis after fusing with the cellular membrane. This exocytosis is involved in the predigestion of pathogens[70] or apoptotic cells that are too large for phagocytosis[71] and in the remodelling of extracellular matrix[72]. Moreover, the fusion of lysosomal membranes with the plasma membrane is an efficient strategy to rapidly increase the membrane surface area, facilitating the engulfment of extracellular particles[73].

1.4 Origins

Despite sharing common characteristics, macrophages have developed tissue-specific functions to meet the unique needs of different tissues. It has been proposed that macrophage functional diversity is influenced by the nature and time of exposure to the tissue microenvironment[74,75] or by their origin[76,77].

In 1968, van Furth and colleagues first investigated macrophage ontogeny[78]. Through in vitro labeling studies, they proposed that bone marrow (BM) monocytes rapidly divide, migrate into the blood, and give rise to peritoneal macrophages[78]. The dependency of macrophage origin and renewal on monocytes was the main framework until the 90s, when several studies suggested that a substantial proportion of tissue myeloid cells actually originate from cells in the yolk sac[79] and were maintained by local proliferation rather than monocyte recruitment[80,81]. The last two decades took advantage of genetic fate-mapping strategies to better decipher macrophage origin in both homeostasis and inflammation[82,83]. Common tools used for macrophages ontology studies are resumed in Figure 3.

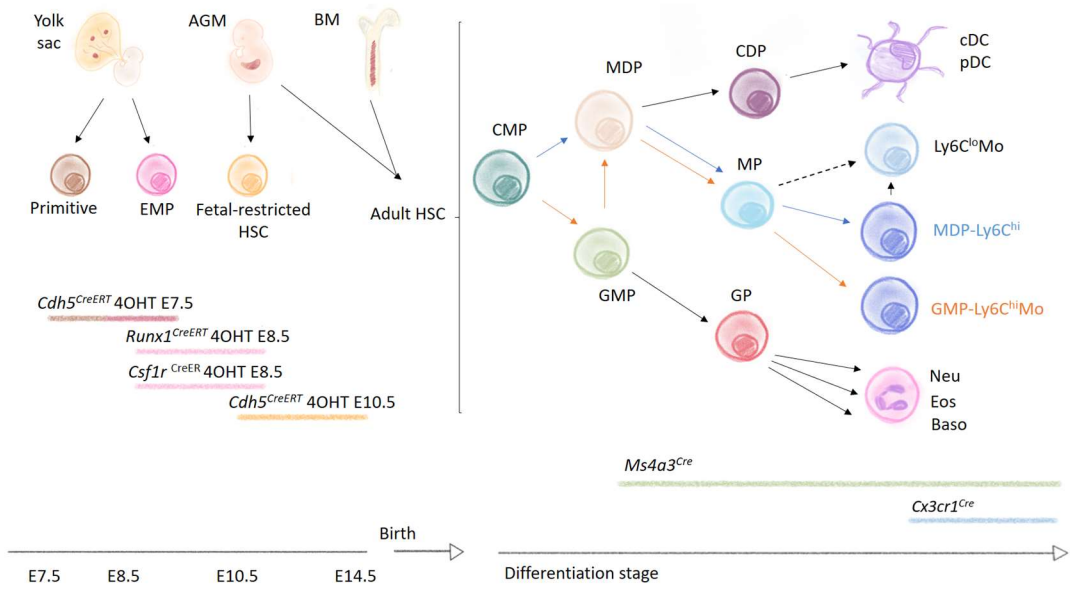

Figure 3 - Monocyte and macrophage ontogeny and the tools commonly used to fate-map embryonically-derived and bone marrow-derived macrophages

In developmental biology, genetically engineered animals are commonly employed to label and trace cells and their progeny. These fate-mapping tools facilitate the study of cellular origins and differentiation processes. This figure summarizes several fate-mapping tools used to define macrophage lineages. The ***Cdh5^{CreERT}*** model, where Cdh5 encodes VE-cadherin expressed in endothelial cells, is used to identify hematopoietic cells derived from endothelial cells. Administration of 4-hydroxytamoxifen (4OHT) at embryonic day (E) 7.5 or E10.5 labels erythromyeloid progenitors from the yolk sac and hematopoietic stem cells from the aorta-gonad-mesonephros region, respectively. While ***Cdh5^{CreERT}*** mice focus on tracing hemogenic endothelial origins, ***Runx1^{CreERT}*** labels cells undergoing hematopoietic differentiation, from hemogenic endothelial cells to hematopoietic progenitors. In ***Csf1r^{CreERT}*** mice, where cells expressing the colony-stimulating factor 1 receptor are tracked, tamoxifen administration at different developmental stages results in the labeling of erythromyeloid progenitors (E7.5–7.8) or monocytes derived from fetal liver hematopoietic stem cells (E10.5). Fate-mapping tools are also used to track monocytes and macrophages originating from adult myelopoiesis, helping to identify their specific precursors. ***Ms4a3^{tdTom}*** mice, which express the Tomato protein under the control of membrane-spanning 4-domains subfamily A member 3 (Ms4a3), a protein found in granulocyte-monocyte progenitors, enable the identification of granulocyte-monocyte progenitors and their progeny. Additionally, ***Cx3cr1^{cre}*** mice, often crossed with floxed reporter strains, permanently label CX3CR1-expressing cells and their progeny, allowing for the lineage tracing of monocytes and macrophages.

EMPs: erythromyeloid progenitors; AGM aorta-gonad-mesonephros; HSCs: hematopoietic stem cells; BM: bone marrow; CMPs: common myeloid progenitors; GMP: granulocyte-macrophage progenitors; MDP: monocyte-dendritic cell progenitor; GP: granulocytes progenitor; MP: monocyte progenitor;

CDP: commun dendritic cell progenitor; cDC: conventional dendritic cells; pDC: plasmacytoid dendritic cells; Mo: Monocyte; Neu: Neutrophil; Eos: Eosinophil; Baso: Basophil.

Inspired by *Ahlback et Gentek, Tissue-Resident Macrophages, Volume 2713, (2024)*

1.4.1 Embryonic origin

In adults, hematopoiesis is maintained by hematopoietic stem cells (HSCs), which begin to emerge during embryonic development at around day E10.5 in mice and at five weeks in human embryos[84,85]. Surprisingly, macrophages are already present in the brain[86] and skin[87] rudiments at this stage, suggesting that they can develop independently of HSCs. Prior to the emergence of HSCs, blood cells necessary for embryonic survival are produced by several transient waves of hematopoietic progenitors, each with distinct lineage potentials. In mice, the first wave, known as primitive hematopoiesis, begins as early as E7.0 from multi-lineage erythro-myeloid progenitors in the blood islands of the extraembryonic yolk sac, giving rise to primitive erythroblasts, megakaryocytes, and macrophages[88]. These primitive macrophages seed all fetal tissues, particularly the brain, where they develop into brain microglia, and the fetal liver, where they expand to form local macrophage populations. During the second wave, originating from the hemogenic endothelium of the yolk sac around E8.0 to E8.25, erythro-myeloid precursors (EMPs) migrate to the liver, giving rise to myeloid progenitors capable of generating fetal monocytes. These monocytes spread through the bloodstream to all tissues, differentiating into macrophages that retain the ability to self-renew throughout adulthood[76]. From the intraembryonic hemogenic endothelium at E8.5, a third wave of hematopoietic progenitors emerges, giving rise to fetal HSCs in the aorta, gonads, and mesonephros. These precursors also colonize the fetal liver and BM, establishing definitive hematopoiesis[89]. Thus, during organogenesis, tissues are seeded with macrophages originating from different embryonic progenitors, each characterized by distinct developmental pathways.

Yolk sac macrophages follow a rapid differentiation pathway, bypassing monocytic intermediates[90,91]. Unlike macrophages from definitive hematopoiesis, they develop independently of the transcription factor Myb, which is essential for the expansion and differentiation of all hematopoietic cell lineages[92], and instead rely on CSF1R (colony-

stimulating factor 1 receptor)[76,93]. These progenitors primarily give rise to local yolk sac macrophages and microglia. Late CSF1R^{lo} Myb^{+} progenitors pass through a CX3CR1-expressing intermediate population and represent the main precursors for most tissue-resident macrophages[94].

1.4.2 Monocyte development and heterogeneity

At birth, all organs are populated by fetal macrophages, which are gradually supplemented by HSC-derived monocytes to varying extents, particularly under conditions of tissue stress such as irradiation and inflammation[82]. Monocytes, an integral part of the mononuclear phagocyte system (MPS), constitute approximately 4% and 10% of blood nucleated cells in mice and humans, respectively[95]. At steady state, circulating monocytes enter the spleen, which serves as a secondary reservoir, allowing for their rapid mobilization from this marginal pool, in addition to the bone marrow, when needed[96]. In mice, monocytes are classified into Ly6C^{hi}CCR2^{+} classical monocytes and Ly6C^{low} CCR2^{-} patrolling monocytes[97]. Classical monocytes are major contributors to tissue-resident macrophage populations during both homeostasis and inflammation[82,98]. While Ly6C^{low} monocytes have been reported to differentiate into tissue-resident cells, their precursor function is less well established[99]. Despite the early assumption that monocytes serve merely as a transient reservoir for tissue-resident macrophages, they have emerged as an essential component of the MPS, acting as short-lived effector cells within tissues[100]. Monocytes arise from myeloid precursors in the BM. Bifurcating from lymphoid lineage, myeloid cells are derived from the common myeloid progenitor (CMP) that further develop in granulocyte-monocyte progenitors (GMP), the differentiation of which is dependent on *Cebpa* transcription factor[101]. GMPs give rise to both granulocytes and monocytes/macrophages and are identified by the specific expression of *Ms4a3*[98]. From CMPs, a specific restricted monocyte and dendritic cell progenitor (MDP) emerges. Using a reporter system for CX3CR1, the fractalkine chemokine receptor widely expressed by monocytes, dendritic cells (DCs) and macrophages, Fogg and colleagues isolated a BM population co-expressing CX3CR1 and CD117 (c-kit), the receptor for stem cell factor[102]. This subset, referred to as MDPs, exhibit a differentiation potential that is restricted to monocytes, macrophages, and DCs[102,103]. In both bone marrow and spleen, a committed

monocyte progenitor (cMoP) that gives rise solely to monocytes has been discovered and characterized[104]. The specification of classical monocytes is driven by the sequential expression of PU.1, IRF8, and Klf4[105]. Patrolling Ly6C^{low} monocyte subset is thought to derive from classical monocytes under the control of Nur77 (NR4A1) [106] and Notch signaling[107] and depends for their survival on endothelial cell niche[108]. Notably, of Ly6C^{low} monocytes actively patrol vascular endothelium where remove damaged cells and debris under homeostatic and inflammatory conditions. Blood vessels ensure the survival of these patrolling monocytes by enhancing the fractalkline (CX3CL1)-mediated uptaken of CSF-1 (colony stimulating factor 1) expressed on endothelial cells[108].

However, the classical developmental pathway CMP-> GMP-> MDP-> cMoP has been challenged by recent studies, suggesting that progenitors make lineage commitment decisions earlier than previously thought[109–111]. Yáñez and colleagues were the first to re-evaluate this assumption, demonstrating that GMPs and MDPs can independently produce monocytes, each exhibiting distinct gene expression signatures. Genes enriched in GMP-derived Ly6C^{hi} monocytes correlated with genes highly expressed by neutrophils, whereas genes enriched in MDP-derived Ly6C^{lo} monocytes were highly expressed among macrophages and dendritic cells [109]. Using double reporter mice for the transcription factors IRF8 and Gfi1, which specify monocyte and neutrophil fates, respectively, they determined that neutrophil-like transcription factor profiles drive GMP-derived monocyte differentiation and functional characteristics. Interestingly, GMPs produce Ly6C^{hi} monocytes with "neutrophil-like" characteristics, expressing genes typically related to neutrophil primary granules such as neutrophil elastase (*Elane*), proteinase 3 (*Prtn3*), cathepsin G (*Ctsg*), and chitinase-like protein 3 (*Chil3*) [110]. Morphologically, GMP-derived monocytes appeared larger and more granular, possessing larger amounts of myeloperoxidase compared to MDP-derived monocytes. Furthermore, GMP-derived monocytes respond to classical neutrophil chemoattractants and can produce extracellular traps[111]. In contrast, MDP-derived monocytes exhibit superior phagocytosis capabilities[111].

Recently, Trzebanski and colleagues provided surface markers to easily distinguish GMP-derived monocytes (CD177^{+}) from MDP-derived monocytes (CD319^{+}) in both bone marrow and blood[111]. Remarkably, under high mobilization demand during emergency myelopoiesis, GMP- and MDP-derived monocytes are differentially recruited depending on the type of pathogen. Lipopolysaccharide (LPS), which preferentially stimulates neutrophil and monocyte production, preferentially recruits GMP-derived monocytes, while unmethylated CpG DNA, which specifically induces monocyte and conventional dendritic cell (cDC) production, rather recruits MDP-derived monocytes[109]. Conversely, interferon-γ (IFN-γ) induces the expansion of MDP-derived monocytes, associated with the expression of MHC2 and CD11c[111]. Both GMP- and MDP-derived monocytes give rise to Ly6C^{low} monocytes, although they result in different phenotypes, and contribute to maintaining tissue-resident macrophages. Gut macrophages are equally replenished by GMP- and MDP-derived monocytes, whereas lung IM are predominantly derived from MDP-derived monocytes[111]. Interestingly, the transcriptome of GMP-derived IM overlaps with MHC2^{low} IMs and is associated with angiogenesis and wound healing pathways. Conversely, IMs originating from MDP are correlated with MHC2^{hi} IMs and are enriched in genes related to the immune response[111]. This dichotomy strongly suggest that cell ontogeny participates to macrophage identity and predispose to a specific function[111].

1.4.3 Monocyte Contribution to Resident Macrophage Populations

Monocyte contribution to the maintenance of resident macrophage populations varies across organs. Such monocyte-dependent replenishment is physiological, although the nature of cellular and exogenous signals controlling tissue resident macrophage capability of self-renewal and clonal expansion under homeostatic conditions remains unclear. Nevertheless, tissue and immune perturbations during inflammation have a long-term impact on local macrophage ontogeny.

In organs such as the intestine[112], dermis[113], heart[114], and pancreas[115], where the macrophage niche is relatively accessible (i.e., in communication with the blood stream), macrophages are primarily maintained by circulating precursor monocytes in adults. Conversely, microglia[77],

epidermal Langerhans cells[116] and lung AMs[117] populate more "closed" niches and show minimal monocyte need for replacement in adulthood. In the lungs, AMs develop from fetal monocytes in the early postnatal period without any contribution from primitive macrophages and maintain themselves throughout adulthood in the absence of inflammation or infection[117]. Signals from the alveolar niche are crucial for the commitment and maturation of AM. At birth, the increased oxygen concentration, sensed via the Von Hippel–Lindau protein, facilitates AM maturation, enhancing their phagocytic and self-renewal capacities[118]. Granulocyte-macrophage colony-stimulating factor (GM-CSF), also known as colony-stimulating factor 2 (CSF2) and mainly produced by alveolar AT2 cells, supports the proliferation and differentiation of fetal monocytes[117,119] by inducing the transcription factor peroxisome proliferator-activated receptor gamma (PPAR-γ) [120]. Alongside GM-CSF, autocrine transforming growth factor β (TGF-β) is also essential for AM maturation[121]. The ability of AMs to expand without losing cellular differentiation is regulated by the low expression of the b-ZIP transcription factors c-Maf and Maf-b[122]. The developmental origin of IMs has only been elucidated recently. Genetic fate mapping shows that the initial IM pool is constituted by yolk sac progenitors, which are then rapidly replaced by fetal liver macrophages and HSC-derived monocytes during the early postnatal period[123]. Lung IMs are then continuously replenished by CCR2-dependent Ly6C^{hi} monocytes in adults, which can proliferate in situ in a CSF-1-dependent manner before differentiating into IMs[124]. During this process, Maf-b, but not c-Maf, can restrict monocyte proliferation and facilitates IM development. Depletion of c-Maf does not affect IM differentiation but is specifically involved in the identity of the CD206^{+} IM subset[124].

In inflammatory conditions, macrophage expansion and repopulation depend on the nature and severity of the perturbation. Macrophage population reduction may result from cell depletion directly caused by the insult, such as in viral infections or ionizing radiation, or from the absence of niche signals following parenchymal destruction[125]. Depending on the extent of depletion, the AM pool may be restored by local proliferation or, if the injury is more severe, by recruitment of monocytes, giving rise to monocyte-derived AM (mo-AMs) [125,126].

IMs have been shown to expand from recruited CCR2-dependent or CCR2-independent monocytes following LPS or CpG stimulation, respectively[127].

The importance of cellular origin in determining macrophage function is a hot topic in the field. Distinct functions of fetal macrophages and BM-derived monocyte macrophages have been studied in cardiac[128] and liver[129] resident macrophages, where embryonic-derived macrophages assume a regulatory and pro-repair profile, while monocyte-derived macrophages are pro-inflammatory and lack reparative activities. In the lungs, the massive loss of AMs induces the infiltration of monocytes, which take about three weeks to differentiate into mo-AMs[130]. Similar to other tissue-resident macrophage populations, mo-AMs display pro-inflammatory features. These mo-AMs, exhibiting low levels of Siglec-F, express high levels of *Itgam* (CD11b), *H2-Ab1* (MHCII), *Cd14*, and *Fcgr2b* (CD32), along with elevated expression of pro-inflammatory chemokines (*Ccl2, Ccl4, Ccl7, Ccl9, Ccl17, and Cxcl16*), chemokine receptors (*Ccr2, Ccr5, Ccr7, and Cx3cr1*), cytokines (*Il1b, Spp1, Ebi3*, *Osm,* and IL-6) and a glycolytic profile[130,131]. The presence of mo-AMs is associated with increased fibrosis severity[132], increased morbidity during IAV infection[130], but better clearance of secondary pulmonary bacterial infections[131]. Conversely, mo-AMs can also acquire a tolerogenic profile, offering protection against allergic airway inflammation[126].

Macrophage ontogeny studies have traditionally relied on bone marrow chimeras, depletion of tissue macrophages through pharmacological or genetic ablation, and fate-mapping mouse models. Understand the translational possibilities of the founding related to animal studies is a far harder task. Nevertheless, advancements in single-cell technologies and the development of the Human Cell Atlas suggest the presence of a conserved precursor and tissue-specific macrophage phenotypes across species during the gestational period[133]. It is important to note, however, that the continuous exposure to pathogens throughout pregnancy and human life is not replicated in laboratory conditions. Since inflammatory events significantly influence macrophage renewal and function, studying macrophage ontogeny and ontogeny-related functions in humans remains difficult[134].

1.5 Functions

1.5.1 Macrophage roles in homeostasis – focus on lung macrophages

Macrophages are strategically located within body tissues, where they exert organ-specific homeostatic roles and contribute to host defense upon injury. Within tissues, macrophages assume highly specialized homeostatic roles. For instance, osteoclasts are responsible for bone degradation during normal remodeling[135], liver Kupffer cells can clear lipids[129] and damaged erythrocytes[136], gut macrophages can maintain tolerance to gut flora and food[137], and AMs catabolize alveolar surfactant[138]. Additionally, these cells function as transducers by collecting and integrating information from the microenvironment and conveying instructions to neighboring stromal cells, such as in the eyes[139] and joints[140]. At steady state, tissue-resident macrophages possess intrinsic anti-inflammatory functions that ensure baseline homeostasis and prevent constant inflammation. For example, colonic macrophages produce large amounts of interleukin-10 (IL-10) to suppress any inflammatory response to gut flora and their products[141], and macrophages in the marginal zone of the spleen suppress immune activation to reduce reactivity to apoptotic cells[142].

Moreover, macrophages are strategically distributed throughout the body to perform crucial immune surveillance functions. They help maintain healthy tissue by removing dead and dying cells or toxins. Through phagocytosis and cell surface receptors, they constantly monitor the surrounding environment for signs of tissue damage or invading organisms, ensuring the body's readiness to respond to potential threats[143].

Under homeostatic conditions, the primary role of AMs is to regulate pulmonary surfactant, a lipid-protein complex produced by the respiratory epithelium that lubricates the lungs and ensures mechanical compliance. Consequently, the transcriptional signature of AMs is dominated by genes associated with lipid metabolism in both mice and humans[120,144,145]. Beside the role in development, CSF2 signaling is essential for AM surfactant catabolism function[117]. Mice deficient in either CSF2 or CSF2R^{6}, as well as patients treated with neutralizing antibodies against CSF2, lack functional AMs, fail to properly remove surfactant,

and develop pulmonary alveolar proteinosis (PAP) [146]. Interestingly, in *SPC-GM* mice, in which the transgenic construction induces local overexpression of CSF2 by AT2 cells, both AM and AT2 cell proliferation is enhanced, causing AT2 cell hyperplasia and increased lung size[147]. Notably, PPAR-γ-deficient mice exhibit dysfunction in lipid clearance and metabolism, leading to spontaneous inflammation[148]. Surfactant proteins, particularly SP-A and SP-D, can directly modulate AM function. These proteins can opsonize pathogens and cell debris, facilitating their elimination[149]. In the absence of pathogens, SP-A and SP-D bind to signal-inhibitory regulatory protein-α (SIRP-α), inhibiting the production of inflammatory mediators[150]. This regulatory mechanism, along with the expression of CD200R[151], TGFβ[152] and IL-10 signals, and lipid metabolism, helps maintain immune tolerance to innocuous antigens and limit unwanted inflammatory responses[151]. CD200R expression by AMs is particularly significant in the airways, as its ligand, CD200, is expressed on the luminal side of respiratory epithelial cells, especially on AT2 cells. Absence of CD200 results in a two-fold increase in AM numbers, spontaneous upregulation of activation markers, and exacerbation of inflammatory responses[151]. The epithelium is also a source of IL-10[151], which suppresses the expression of pro-inflammatory cytokines[153]. Similarly, mice lacking activated TGFβ develop generalized lung inflammation and spontaneous pulmonary emphysema due to upregulation of MMP12 (matrix metalloproteases 12) [152]. Furthermore, apoptotic cell efferocytosis induces an anti-inflammatory state in AMs to prevent an excess of inflammatory responses[154]. Recognition of externalized) phosphatidylserine on apoptotic cells by the TAM receptor family inhibits cytokine receptor and toll like receptor (TLR) signaling[154]. Apoptotic cells also show increased expression of the CD200, transmitting inhibitory signals AMs[151]. This tolerogenic profile is counterbalanced by simultaneous activation of TLRs and their co-receptors by microbial particles, which enhance phagocytosis and the secretion of pro-inflammatory cytokines[155].

The role of IMs in homeostasis is less documented. However, compared to AMs, mouse IMs are more efficient at releasing immunoregulatory cytokines such as IL-1 and IL-6[7,156] and they are also the primary producers of IL-10 under steady-state conditions[7,127]. In non-homeostatic contexts, IMs have been suggested to modulate inflammation. When stimulated by LPS, CpG-DNA, or in models of house dust mite (HDM)-induced allergic asthma, IMs significantly expand

and increase their IL-10 production, contributing to maintaining immunosuppressive environment[7,127]. Moreover, IMs are capable of presenting soluble antigens and inducing regulatory T cells[157], participate in the organization of tertiary lymphoid tissue in allergen- and infection-driven inflammation models[158] . However, under inflammatory conditions, the resident IM population is supplemented by recruited monocyte-derived macrophages, which can adopt phenotypes similar to IMs, complicating the interpretation of the specific role of resident IMs[131,159]. IMs have been reported to engage in a crosstalk with neighboring structural cells, contributing to the integrity of nerves and blood vessels, respectively[7,127]. This interaction highlights the potential role of IMs in supporting tissue structure and function beyond their immunoregulatory capabilities.

Monocytes have been identified as contributors to the population of tissue-resident macrophages. During homeostasis, monocytes undergo an imprinting process that promotes differentiation signals conducive to a homeostatic macrophage phenotype. However, when differentiation occurs in altered, disease-associated environments, monocytes can give rise to dysfunctional macrophages, often characterized by a pro-inflammatory state. In patients with COVID-19, as well in infection animal model using other respiratory viruses[130,160], the loss of resident alveolar macrophages and the extensive infiltration of pro-inflammatory monocyte-derived macrophages are associated with poorer clinical outcomes[161]. Similarly, non-homeostatic monocyte-derived macrophages exhibit a pro-fibrotic genetic signature and have been implicated in the progression of lung fibrosis[132,162]. Therefore, both the origin and the differentiation environment influence macrophage behavior, leading to either homeostatic, tissue-preserving functions or non-homeostatic, disease-driving activities.

1.5.2 Macrophage polarization: A single frame of a complex movie

Macrophages play a pivotal role in responding to changes in their microenvironment. Their remarkable plasticity allows them to adapt and alter their identity and function in response to these signals. Furthermore, early danger signals in tissues can trigger monocyte recruitment and part of them can differentiate and engraft the resident macrophage pool[163]. In some cases, recruited monocytes give rise to short-lived macrophages whom persistence

in situ is limited at the time of inflammation and disappear during the resolution[83]. Together with the dynamic changes of signals from the initial trigger until the resolution of inflammation, all these factors result in the coexistence of a complex pool of macrophages with different origin and different activation states. Traditionally, macrophage activation was classified in a dualistic model of polarization resulting from tightly controlled *ex vivo* experiment. Following this framework, cultured macrophages are stimulated with cytokines artificially mimicking distinctive cytokines from polarized CD4 T cells. Hence, IFN-γ and tumor necrosis factor α (TNF-α) produced by Th1-polarized T cells induce M1 macrophages and IL-4 and IL-13 produced by Th2-polarized T cells induce M2 macrophages.

In such classification, M1 macrophages, also known as classically activated or pro-inflammatory macrophages, arise also from stimulation by microbial products such as lipopolysaccharides or other TLR ligands. This activation enhances their ability to eliminate microbes and present pathogenic antigens to T lymphocytes, thereby initiating adaptive immune responses. M1 macrophages express markers like CD80, CD86, and MHC-II, as well as inducible nitric oxide synthase (iNOS). They also secrete elevated levels of pro-inflammatory cytokines such as TNF-α, IL-1β, IL-6, IL-12, and IL-23[164]. During inflammation, IFN-γ is produced by innate immune cells like natural killer (NK) cells and adaptive Th1 cells. TNF-α is typically synthesized by antigen-presenting cells, and certain TLR ligands can induce TNF-α production in macrophages, which can act in an autocrine manner to promote the M1 phenotype[165].

In contrast, M2 macrophages, also referred to as alternatively activated or pro-resolving macrophages, are induced by IL-4 and/or IL-13 produced by Th2 lymphocytes, mast cells, basophils, and innate lymphoid cells (ILCs), as well as by IL-10[166]. M2 macrophages express high levels of CD206 and produce factors such as TGF-β, insulin-like growth factor-1 (IGF-1), matrix metalloproteases (MMPs), vascular endothelial growth factor A (VEGF-A), and arginase-1 (Arg-1). These molecules contribute to extracellular matrix deposition and tissue remodeling processes[166]. Serveral, in part overlapping, M2 subset have been identified (M2a,

M2b, M2c, M2d) distinguished by their inducers and surface markers. Markers commonly used for M1 and M2 classification are reported in Figure 4.

However, the applicability of such classification and activation states to the in vivo situation is highly questionable and could lead to misconceptions. In fact, characteristics of polarization results from tightly controlled in vitro experiments of myeloid cell stimulations, which do not reflect the spatiotemporally regulated bath of signals that macrophages receive from pathogens, structural and immune cells. Moreover, signals are themselves heterogeneous and time- and tissue- dependent. Hence, macrophage polarization should be viewed as a multidimensional approach integrating ontogeny and spatiotemporal factors[167].

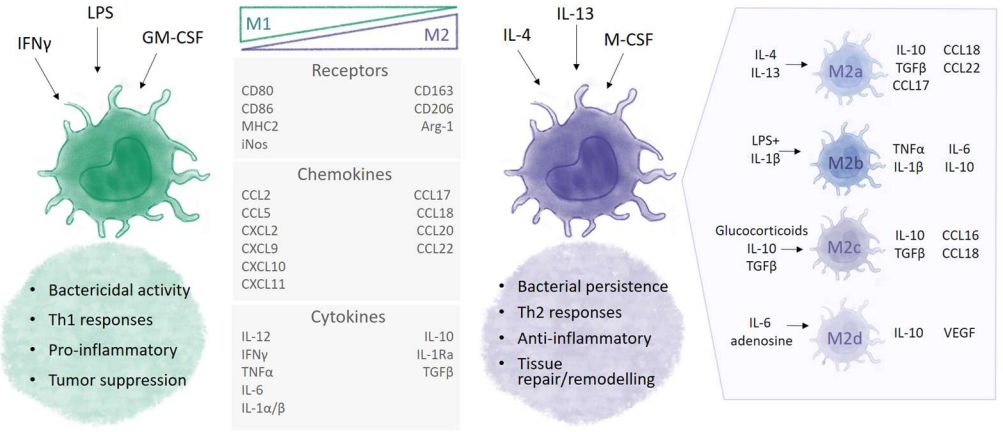

Figure 4 - Profiles and function of polarized macrophages

Macrophages are highly plastic immune cells that respond to various environmental stimuli, resulting in distinct activation or polarization states, mostly characterized by *ex vivo* experiments. These states are defined by their functional roles, surface receptor expression, cytokine secretion and transcriptomic (detailed elsewere[168]) profiles. The concept of macrophage polarization is classically used to predict macrophage behaviour and how these cells contribute to immune responses, tissue repair, and pathology. The two major phenotypes of macrophage polarization are M1 (classically activated) and M2 (alternatively activated) macrophages, each of which plays distinct roles in immunity and homeostasis. Additionally, M2 macrophages can further differentiate into several subtypes based on specific stimuli.
IFNγ: Interferon γ; LPS: Lipopolysaccharides; GM-CSF: Granulocyte-Macrophage Colony Stimulating Factor; IL-: Interleukin; M-CSF: Macrophage Colony Stimulating Factor; CCL: C-C motif chemokine ligand; CXCL: C-X-C motif chemokine ligand; TNF: Tumor Necrosis Factor; TFGβ: Transforming growth factor β; VEGF: Vascular Endothelial Growth Factor

Inspired by *Pérez et al., Antioxidants (Basel) 11, 1394 (2022)*[169] *and* Strizova *et al., Clin Sci (Lond)* **137**, 1067–1093 (2023)[170]

2 Influenza A virus

Influenza viruses are prevalent and highly contagious respiratory pathogens, leading to significant morbidity and mortality through seasonal cycles or occasional pandemics. Belonging to the Orthomyxoviridae family, influenza viruses are categorized into four types: A, B, C, and D, with types A-C infecting humans, while type D primarily infects cattle[171]. Type A influenza viruses (IAV) are particularly common and responsible for seasonal flu. Due to their relevance to human health and the ease of studying them in rodent models, IAVs serve as well-accepted model for investigating viral-triggered lung injury[172]. IAVs are enveloped RNA viruses with a segmented negative-sense genome, comprising eight viral segments that encode for twelve proteins. These viruses are further classified into subtypes based on the differential expression of glycoproteins, hemagglutinin (HA) and neuraminidase (NA). The HA protein contains the sialic-acid receptor binding site and acts as the major antigen, while NA prevents non-productive binding of HA of new virions to sialic acid-bearing receptors on viral glycoproteins and host cell membranes, thereby facilitating viral spread[173]. The high error rate of RNA polymerase and RNA segment reassortment during co-infections result in new genetic combinations, promoting the spread and circulation of the virus in new hosts. Currently, the subtypes of influenza A viruses that routinely circulate among humans include H1N1 and H3N2[174].

IAV virions are transmitted via droplet inhalation and bind to α-2,3 and α-2,6 sialylated glycans on the surface of host epithelial cells along the respiratory tract[175]. Following binding, the virus is internalized via the endosomal pathway, leading to fusion of the viral envelope with the endosome and release of viral RNA into the cytoplasm, which is then imported into the nucleus for replication. After assembly and budding, new virions are released into the extracellular space[176]. Viral infection induces apoptosis and necrosis of infected cells, which likely play a pro-viral role in IAV pathogenesis, but also contribute to immune activation and help in disease resolution[177].

2.1 Immune response to IAV infection

The immune system provides the first line of defense against IAV. Viral RNA is recognized by various pattern recognition receptors (PRRs) on host cells: Toll-like receptors TLR3 and TLR7 (TLR8 in humans); retinoic acid-inducible gene I (RIG-I); melanoma differentiation-associated protein 5 (MDA-5); and the NOD-like receptor family member NOD-, LRR-, and pyrin domain-containing 3 (NLRP3). TLR3 recognizes unidentified dsRNA present in phagocytosed dying virus-infected cells[178], while TLR7 recognizes ssRNA in endocytosed virions[179]. RIG-I, MDA-5[180], and NLRP3[181] detect viral presence within the cytosol of infected cells. Binding of viral RNA by intracellular PRRs in immune and non-immune cells activates transcription factors, including interferon regulatory factors 3 (IRF3) and 7 (IRF7), and nuclear factor kappa-light-chain-enhancer of activated B cells (NF-κB), leading to the expression of various interferons (IFNs) and cytokines (TNF, IL-6, IL-1β) [182]. Type I IFNs, such as IFN-α and IFN-β, along with type III IFNs (also known as IFN-λ), play a crucial role in the antiviral response. IFNs induce the expression of IFN-stimulated genes (ISGs), creating an antiviral state by interfering with different stages of the IAV life cycle[183].

Furthermore, infected epithelial cells produce chemotactic molecules such as RANTES, MIP-1α, MCP-1, MCP-3, and IP-10, which initiate the rapid recruitment of innate immune cells[184]. Upon reaching infection sites, **natural killer** cells recognize IAV-HA on the surface of infected cells through the cytotoxicity receptors NKp44 and NKp46, leading to the lysis of these cells[185]. NK cells can also bind to the Fc portion of antibodies attached to influenza-infected cells, mediating their destruction[186]. **Dendritic cells** process viral antigens, thus initiating the adaptive immune response. Infected DCs degrade viral proteins into peptides and present MHC1-associated epitopes on their cell membranes. Virus-specific $CD8^+$ T cells recognize these complexes and activate their cytotoxic activity. Simultaneously, viral proteins acquired through phagocytosis of virus particles or apoptotic epithelial cells are degraded in lysosomes and associated with MHC2 molecules for recognition by $CD4^+$ helper and $CD8^+$ T cells[187]. Additionally, DCs produce lymphotoxin (LT) β and chemokines (CXCL-12 and -13, and CCL-19

and -21), contributing to the maintenance of inducible bronchus-associated lymphoid tissue and ensuring efficient humoral immunity[188].

The role of **neutrophils** in influenza infection remains controversial. While their depletion leads to increased viral load and worsening clinical conditions[189,190], excessive recruitment has been linked to exacerbation of lung injury[191]. Neutrophils are among the first immune cells recruited to the lungs following infection, peaking around day 5 post-infection and gradually decreasing until day 10 post-infection, contributing to viral clearance[192]. Similar to macrophages, neutrophils can phagocytose infected cells[193], produce antiviral MMP-9[194], and secrete pro-inflammatory cytokines[195]. Furthermore, neutrophils recruit CD8+ T cells and can function as APCs to activate these cells[192].

The adaptive immune response represents the second line of defense against IAV infection. In the draining lymph nodes, virus-specific CD8+ **cytotoxic T cells**, activated by APCs and pro-inflammatory cytokines[196], reduce the expression of CCR7 and upregulate CXCR4 and CCR4 to facilitate their migration to the lungs[197]. In the lungs, T cell receptor engagement by virus-specific epitope-MHC I complexes triggers the release of perforin and granzymes, causing apoptosis and lysis of infected cells[198]. Perforin binds to target cells, inducing pore formation in the cell membrane and promoting granzyme diffusion and related apoptosis[199]. Additionally, granzymes can cleave viral and host proteins, thereby restricting viral protein synthesis[199]. $CD8^+$ T cells also produce pro-inflammatory cytokines like TNF-α, enhancing lytic activity[200]. Unlike other APCs, CCR2-dependent monocytes play a role in establishing a CD8+ T memory cell response through prolonged antigen presentation[201]. IAV-specific CD8+ T cells can persist for up to two years in murine models and are crucial for protection against heterologous influenza challenges[202].

The activation of **$CD4^+$ T cells** during IAV infection, depending on the pro-inflammatory cytokine milieu, leads to their differentiation into Th1 cells[203]. Th1 effector cells can produce antiviral cytokines such as TNF, IFN-γ, and IL-2[204], further contributing to inflammation and virus clearance by promoting CD8+ cytotoxic responses[205]. Moreover, co-stimulatory ligands like CD40L, expressed by CD4+ T cells, aid in B cell activation and antibody production[206].

B cells are essential for priming the defense against homologous or heterosubtypic influenza strains[207]. Antibodies against HA and NA correlate with protective immunity. HA-specific antibodies inhibit virus attachment and entry into host cells, thus neutralizing the infection[208]. Similarly, antibodies against NA inhibit its enzymatic activity, limit virus spread, and contribute to the clearance of virus-infected cells[209]. Neutralizing and non-neutralizing antibodies facilitate the elimination of viruses and virus-infected cells. Antibodies recognized by Fc receptors on phagocytic cells enhance viral particle engulfment or antibody-dependent cell-mediated cytotoxicity[209]. IgG antibodies are the dominant class in this process and can directly inhibit influenza pathogenesis, whereas IgA antibodies are crucial for inhibiting IAV transmission[210].

2.2 The Journey of Monocytes and Macrophages upon Influenza A Virus Infection

This chapter is inspired by a recent review article published in Current Opinion in Virology, Mucosal Immunology issue[211], in which we highlight the dynamics and functions of lung-resident macrophages, recruited monocytes and monocyte-derived cells in viral clearance, inflammation and the consequences of IAV-induced macrophage alterations on long-term lung immunity. Their role in lung repair is described in the respective section below.

2.2.1 IAV-triggered perturbations and functions of resident homeostatic AMs

AMs are strategically located in the alveolar lumen to be the first responders to IAV and investigations about resident AMs in IAV infections consistently pointed towards beneficial, protective roles, as reviewed in detail elsewhere [212,213]. Human and mouse AMs are permissive to IAV and AMs can uptake viruses by direct infection, or by phagocytosis of infected apoptotic cells[193]. Viral replication in AMs is limited by their production of type I interferons [214,215], which can also orchestrate recruitment of other immune cells [216]. Of note, AM infection rate is highly variable, with higher infectivity by highly pathogenic strains and rather unproductive infections by moderate viral strains, which is thought to contribute to

limit viral spread [217–220]. Human AMs are less permissive and responsive to IAVs than monocyte-derived macrophages [217], which also produce larger amounts of TNF-α [217,218], RANTES and IP-10 compared to AMs [218]. A recent report suggests that the inhibitory effects of AMs on viral replication could also be mediated by extracellular vesicles acting on epithelial cells [221].Seminar reports showed that wild-type mice injected with supraphysiological doses of GM-CSF [222] or mutant mice overexpressing GM-CSF in the lung [223], were protected from IAV infection. This protective effect was associated with improved lung functions, decreased protein exudates in the bronchoalveolar lavage (BAL), a better clinical recovery and a repolarization of AMs from a M1-like to a M2-like phenotype [222–224]. Furthermore, the protective effects of GM-CSF were abrogated by airway administration of clodronate liposomes [223], suggesting a role for AMs in GM-CSF-mediated protection against IAV. Further supporting their beneficial roles, Schneider and colleagues showed that neonatal adoptive transfers of AM progenitors in *Csf2rb*$^{-/-}$ mice, lacking GM-CSF receptor, prevented severe disease post-IAV, while depletion of AM by clodronate liposomes in wild-type before IAV infection exacerbated morbidity and mortality [214]. Recently, a study showed that an appropriate imprinting of AMs by their niche could contribute to host protection against IAV pathology. Indeed, the authors showed that *Alox15*$^{-/-}$ AMs, deficient in 12- and 15-lipoxygenase, were not properly instructed during the neonatal period by neutrophil-derived eicosanoids (Fig. 5b) and were thus no longer able to control IAV replication later in life, which was associated with increased levels of CCL2, accumulation of monocytes and increased mortality of IAV-infected mice [225].Mouse AMs have been reported to be depleted post-IAV [226,227]. The mechanisms driving AM depletion have been shown to be dependent on IFN- γ in BALB/c mice [226] and may involve AM apoptosis subsequent to a robust anti-viral response [228], inhibition of AM self-renewal capacity by IAV-induced Wnt ligands [229] or modifications of the AM niche triggered by IAV infection of epithelial cells [230]. The extent of AM depletion is thought to be dependent on the host genetic background [226,227]. Indeed, employing a sublethal infection model with the H1N1 PR8 strain, Califano *et al.* reported a massive loss of AMs 7 and 9 days post-IAV in BALB/c mice, but not C57BL/6NCrl mice [226], while Li el al. recently showed that such infection also induced a rapid loss of resident AMs in C57BL/6J mice [227]. We

also consistently observe AM depletion in PR8-infected C57BL/6J mice raised in our animal facilities (unpublished observations). The reasons for these discrepancies remain currently unclear and likely evolve a combination of genetic and environmental factors. In their study, Li et al. further showed that the AM pool was quickly replenished by Siglec-F^{hi} "survivor" AMs (5-10% of original AMs) between day 4 and 15 post-IAV in mice [227]. After viral clearance, AMs were gradually replaced by pro-inflammatory monocyte-derived Siglec-F^{lo} Mo-Macs that would eventually outcompete embryonically-derived AMs on a long-term basis [131,227]. Eventually, the alveolar niche can return to a homeostatic, non-inflammatory state, and repopulated AMs can become similar to the native ones [231,232](Fig. 5d).

Aging can affect AM microenvironment, ontogeny and functions, which might account for the enhanced mortality and morbidity post-IAV in the elderly [227,233–235]. The aging microenvironment can confer resistance of AMs to GM-CSF responsiveness [236], which correlates with decreased AM numbers and proliferative abilities [233]. Aged AMs have also been shown to be impaired in their ability to phagocyte neutrophils compared to young AMs, and high neutrophil counts might account for excessive tissue damage [233]. Finally, embryonically-derived AMs are gradually replaced by bone marrow-derived AMs in aged mice, which can intrinsically contribute to disease severity post-IAV [227].

2.2.2 The enigmatic fate and function of resident interstitial macrophages post-IAV

Lung IMs have been less studied than AMs. To date, most of the studies aiming at addressing the contributions of IMs to disease physiopathology, including IAV-triggered pathology, have faced two main challenges [237]. First, Mo-Macs recruited when homeostasis is broken exhibit a phenotype that can largely overlap the one of IMs. Hence, while it is repeatedly reported that IMs "expand" upon exposure to insults or pathogen-associated molecular patterns [8,238–244], the IM compartment arguably contains a mix of resident IMs and Mo-Macs, and the respective contributions of IMs *vs.* Mo-Macs to disease physiopathology remain often unclear. Second, transgenic tools allowing a specific and efficient tracking or depletion of resident IMs while sparing AMs and Mo-Macs are difficult to obtain. To date, at least three

models of diphteria toxin (DT)-induced bolus IM depletion exist, namely *Lyve1*$^{Cre/GFP}$ *Slco2b1*$^{LSL\text{-}DTR}$[11], *Cd169*^{Cre} *Cx3cr1*$^{LSL\text{-}DTR}$ (NAM-DTR) [245] and *Tmem119*^{Cre} *Cx3cr1*$^{LSL\text{-}DTR}$ (IM^{DTR}) [124]mice. However, IM depletion is transient and rapidly followed by the recruitment of monocytes that refill the empty niche, and it remains to be determined whether DT treatment also targets Mo-Macs when such transgenic mice are subjected to disease models.

In the context of IAV infection, Ural and colleagues depleted NAMs before IAV infection with the H1N1 PR8 strain in C57BL/6 NAM-DTR mice and found that depleted mice displayed increased morbidity at day 12 post-IAV as compared to controls, even though the viral loads were unchanged[11]. As NAMs were the main producers of IL-10, the authors proposed that NAMs can downregulate IAV-triggered inflammatory responses. These data highlight potential beneficial, immunoregulatory functions of IMs after IAV, as shown in other contexts [11,240,246,247] (Fig. 5b). Future investigations comparing different viral strains (e.g., H1N1, H3N2) and mouse strains (e.g., BALB/c, C57BL/6) and employing complementary models of IM-specific targeting along with additional cellular and molecular read-outs of inflammatory and repair responses will help deciphering their roles post-IAV. Along the same line, a model in which resident IMs could be tracked and discriminated from Mo-Macs post-IAV would open many opportunities for more comprehensive molecular, spatial and functional investigations.

2.2.3 Monocytes and Mo-Mac trajectories and functions post-IAV

Monocytes are, along with neutrophils, the first innate cells recruited to the infected lung. Type I IFNs produced early post-IAV can trigger an emergency monopoiesis in the bone marrow, associated with the proliferation of granulocyte-monocyte progenitors (GMPs), their upregulation of the M-CSF receptor and the egress of Ly6C$^+$ monocytes exhibiting increased expression of stem cell antigen-1 (Sca-1) at the expense of dendritic cell differentiation [248–250]. Type I IFN signalling also promotes the differentiation and lung recruitment of CCL2-producing Ly6C$^+$ monocytes, which further facilitates the influx of CCR2$^+$Ly6C$^+$ monocytes into the lung [227,251,252] (Fig. 5b). Type II IFNs have also been shown to regulate inflammatory monocyte recruitment post-IAV [253]. Along with AMs, recruited monocytes orchestrate the acute inflammatory response in part via the activation of NOD-like receptor family pyrin

domain-containing 3 (NLRP3) inflammasome [254]. In lethal models of IAV infection, early NLRP3 inflammasome activity is thought to be protective [255] while an excess of activation may worsen lung damage and increase mortality [256]. Several reports support that the global outcome of $CCR2^+$ monocyte accumulation is detrimental and associated with increased morbidity and mortality [227,257–259]. Deleterious effects of $CCR2^+$ monocytes may be related to an elevated production of iNOS which, unlike for other pathogens, does not display antiviral activity against IAV but rather inhibits an effective adaptive immune response [260].

Upon recruitment, a portion of monocytes can differentiate into Mo-DCs, peaking in the lung at days 7-10 post-IAV [259]. Type I IFN-producing Mo-DCs have been shown to contribute to the antiviral response [261] (Fig. 1b) and ensure appropriate virus-specific $CD8^+$ T cell memory responses [262]. Recruited monocytes can also develop into Mo-Macs that are either short-lived or can establish in particular niches with functional consequences for lung immunity [212,231,263–265]. While Mo-Macs have long been considered as detrimental and pathogenic cells after IAV infection [227,259], their biology is arguably much more complex than previously thought.

During the acute inflammatory phase, IFN- γ -induced Mo-Macs with a pro-inflammatory profile are thought to contribute to efficient viral clearance. They are progressively replaced by pro-resolving Mo-Macs, thereby facilitating tissue healing [164,228,266] (Fig. 1c). The phagocytosis of dying cells, called efferocytosis, is an integral part of the resolution of inflammation [267]. Before cell death, infected cells can release “find-me” signals and cytokines such as macrophage inflammatory protein-1α (MIP1 α), CCL2, CXCL10, able to direct Mo-Macs toward apoptotic cells for engulfment [164,228]. This process contributes to limit the progression of IAV infection in mice by clearing infected cells and promoting a pro-resolving phenotype in efferocytic Mo-Macs [22,268,269]. Degradation of engulfed cells induces a substantial metabolic shift from pro-inflammatory glycolytic pathways towards oxidative phosphorylation pathways associated with anti-inflammatory functions [267,270,271] (Fig. 1c). After H1N1 infection in mice, genes related to anti-inflammatory functions, such as *Arg1*, *Il10*, *Relma* and *Chil3* are upregulated in macrophages as soon as 7 days post-IAV [272]. Of note, the resolution phase post-IAV is characterized by a local type 2 profile, including elevated levels

of IL-13$^+$ type 2 helper T cells, innate lymphoid type 2 cells (ILC2s), IL-4 and IL-13 [272,273], which participate to macrophage reprogramming towards a wound-healing phenotype [274,275]. The receptor for IL-4 and IL-13 (IL4R), starts to be expressed on pro-inflammatory Mo-Macs [276] and its activation triggers expression of Arginase-1, an enzyme competing with IFN- γ -induced iNOS for the common substrate L-Arginine [277]. The Arg-1 product L-ornithine can be further converted into polyamines and proline that can contribute to tissue repair via enhancement of efferocytosis, regulation of cell growth and collagen production[278–280]. GM-CSF, overexpressed by infected alveolar epithelial cells, is also involved in macrophage reprogramming from a pro-inflammatory to a pre-resolving state [222,281] and has been shown to confer protection against lethal IAV infection in mice [223,224]. Whether GM-CSF acts on homeostatic AMs, Mo-Macs, or both, would require further investigations.

2.2.4 Consequences of IAV-shaped Macs for lung immunity

The shaping of the alveolar niche by respiratory infections and the long-term consequences for lung immunity have been elegantly reviewed recently [212]. We will focus here on studies supporting the idea that IAV-induced changes in Macs are associated with short- and long-term modifications in the ability of the host to respond to subsequent insults and stimuli (Fig. 1d). IAV-triggered AM depletion can increase susceptibility to secondary bacterial pneumonia [282]. Moreover, IFN-γ produced by T cells after IAV infection can impair AM antibacterial properties and increases the risk of secondary bacterial infections [283,284]. Such impaired capacity of resident AMs to capture bacteria has been shown to last for months and to rely on SIRP α-dependent immunosuppressive signals released in the local environment leading to immunoparalysis after IAV infection [285]. Influenza-trained AMs have recently been proposed to confer antitumor immunity [286]. Indeed, in a model of B16 melanoma, IAV-trained AM could maintain their phagocytic and cytotoxic potential despite tumor-induced immunosuppression, thereby enabling enhanced antitumor function [286]. However, concerns have been raised as to whether these effects might rather be mediated by recruited Mo-Macs resembling AMs [287]. Mo-Macs replenishing the alveolar spaces post-IAV have been shown to exhibit a more pro-inflammatory phenotype associated with higher glycolytic activity [227] and IL-6 production [264] as compared to AMs, which can confer protection against secondary

bacterial infection one month post-IAV [264] but can also be responsible for increased mortality in recurrent viral infection [227].

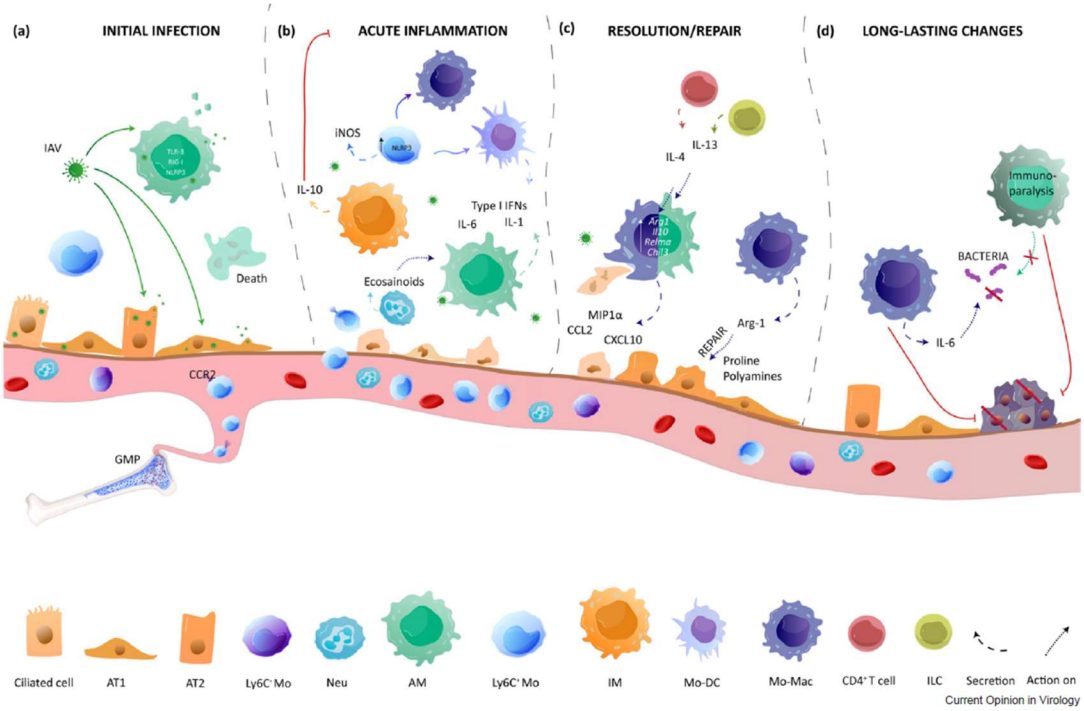

Figure 5 - Monocytes and macrophages after IAV infection

(a) IAV-derived HA proteins can bind to sialylated glycan receptors on lung epithelial cells from the airways and the alveoli. AMs are equipped with the viral RNA sensing machinery and are permissive to IAV, which results in an unproductive infection in a self-limiting disease and can lead to AM death. **(b)** IAV infection can trigger AM activation and production of cytokines, chemokines and type I IFNs, thereby controlling viral spread and coordinate the recruitment of additional inflammatory cells. A proper AM imprinting by neutrophil-derived eicosanoids is essential for AM protective functions post-IAV. The role of IMs in the antiviral response is less clear, with IM-derived IL-10 playing a beneficial role in the downregulation of inflammation. Lung-recruited BM-derived Ly6C+ Mos can activate the NLRP3 pathway and produce elevated amount of iNOS, which can contribute to the acute inflammatory response and, sometimes, to undesirable tissue damage. Ly6C+ Mos can differentiate into type I IFN-producing Mo-DCs or into pro-inflammatory Mo-Macs participating to efficient viral clearance. **(c)** Infected cells can release "find me" signals and cytokines attracting Mo-Macs and inducing their engulfment. Efferocytosis limits viral spread and induces a reprogramming in efferocytic Mo-Macs toward a pro-resolving phenotype associated with upregulation of anti-inflammatory genes as such as Arg1, Il10, Relma and Chil3. Furthermore, during the resolution phase, T cells and ILC2s can produce type 2 cytokines (IL-4 and IL-13) triggering the production of Arginase-1 by Mo-Macs. Arg-1 metabolism results in production of polyamine et proline enhancing cell growth, collagen production and thereby contributing to tissue repair. **(d)** IAV infection leads to long-term consequences for lung immunity. Niche signals produced post-IAV infection induce an immunoparalysis in resident AMs, which exhibit

impaired bacterial phagocytosis, thus enhancing the susceptibility to secondary bacterial infection. Mo-Macs replenishing the alveolar niche post-IAV maintain a proinflammatory phenotype conferring efficient IL-6-dependent protection against bacterial infection but leading to exacerbated lethal response in recurrent viral infection. IAV-instructed Macs can also contribute to protection against tumors by maintaining their phagocytic and cytotoxic potential despite tumor-induced immunosuppression. AT1/2: type 1/2 alveolar epithelial cell; ILC: innate lymphoid cell.

From *Ruscitti, C., Radermecker, C. & Marichal, T. Current Opinion in Virology 66, 101409 (2024)*[211]

3 Lung Repair

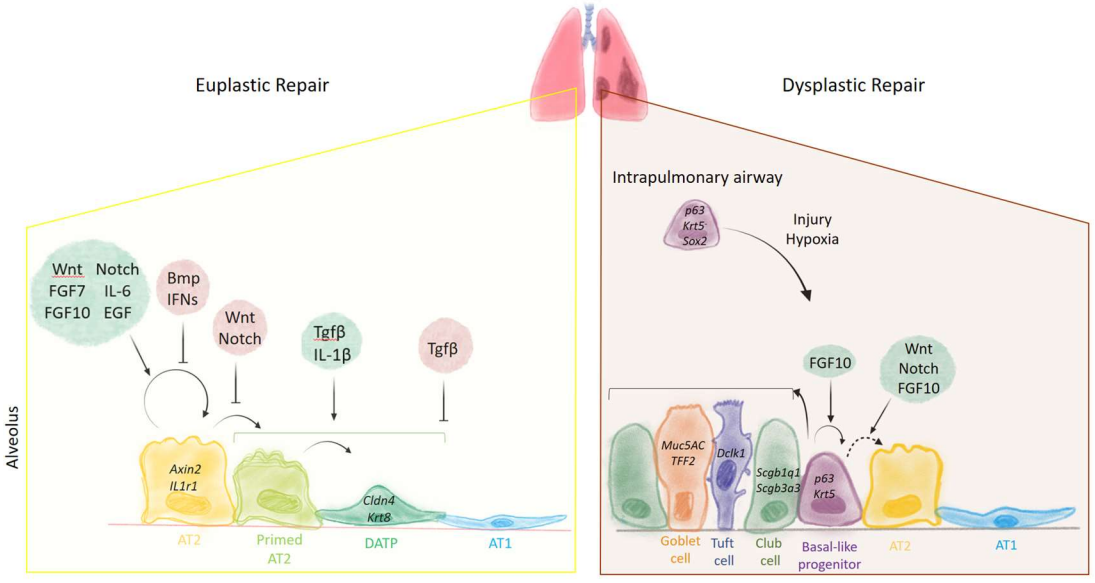

Figure 6 - Regeneration and repair of the alveolar epithelium in homeostasis and after injury

During alveolar epithelial homeostasis or following damage, alveolar type 2 (AT2) epithelial cells play a pivotal role in repair by acting as progenitor cells capable of proliferating and differentiating into alveolar type 1 (AT1) cells. This process is essential for replenishing the AT1 cells, which are crucial for gas exchanges. After injury, AT2 cells proliferate to generate new cells, some of which undergo differentiation into AT1 cells through several intermediate stages. Before acquiring an AT1 profile, AT2 cells are initially primed and then transition into damage-associated transient progenitors (DATPs), marked by the expression of *Cldn4* and *Krt8*. The AT2-to-AT1 differentiation process is regulated by various signaling pathways. Wnt, Notch, FGF7, FGF10, IL-6, and EGF have been shown to support AT2 cell proliferation and survival, whereas BMP and interferons (IFNs) inhibit AT2 replication. While Wnt and Notch promote AT2 proliferation, they simultaneously inhibit AT2 differentiation. Conversely, TGFβ and IL-1β induce AT2 differentiation, though their sustained presence prevents full AT1 maturation. In cases of severe epithelial injury or hypoxia, $p63^{+}$ $Krt5^{-}$ $Sox2^{+}$ basal-like progenitors migrate into the alveoli to restore the epithelial barrier. Only a small fraction of these progenitors differentiates into AT2 cells. Similar to homeostasis, Wnt, Notch, and FGF signals promote the differentiation of basal-like progenitors into AT2 cells. However, more commonly, these airway progenitors give rise to bronchial cell lineages, such as goblet cells (*Muc5Ac, TFF2*), tuft cells (*Dclk1*), and club cells (*Scgb1q1, Scgb3a3*), leading to alveolar bronchiolization, which impairs gas exchange.

AT2: Alveolar type 2 epithelial cell; AT1: Alveolar type 1 epithelial cell; DATP: damage-associated transient progenitor; FGF: Fibroblast growth factor; EGF: Epidermal growth factor; Tgfβ: Transforming growth factor β

Inspired by *Fernanda de Mello Costa, M., Weiner, A. I. & Vaughan, A. E, . Stem Cell Reports 15, 1015–1025 (2020)*[288]

3.1 Lung Alveolar Epithelium Renewal: AT2 as a versatile brick

Under homeostasis, the respiratory parenchyma remains largely inactive, exhibiting a slow turnover rate with an overall renewal rate of 7% of alveoli per year[289]. AT2 cells, which express surfactant protein C (Sftpc), are considered as long-term stem cells during homeostasis and repair due to their capacity for self-renewal and differentiation into AT1 cells[290]. However, the rate at which AT2 cells proliferate and differentiate depends on local demand. In non-injured alveoli, only 1% of mature AT2 cells exhibit such stem cell properties, dividing intermittently every 40 days[291].

Due to the low turnover rate, most studies employ genetic manipulation that deplete alveolar cells to varying degrees in injury models. Specific ablation of AT2 cells in *Sftpc*$^{\text{CreER; Rosa-DTA/Rosa-Tm}}$ mice increases the self-renewal ability of surviving AT2 cells[291]. In the initial days following depletion, AT2 cells undergo expansion, forming densely packed clonal clusters. These clusters subsequently disperse, resulting in a homogeneous distribution of AT2 cells in the surrounding alveoli[291]. The stem cell function of AT2 cells is more broadly induced by AT1 injury, indicating that most AT2 cells possess latent regenerative capacity, which can be activated by dying AT1 cells[292,293]. The exact mechanism by which AT2 cells detect the absence of AT1 cells is unclear, but they might sense the denuded basal lamina, a reduction in cellular contacts with AT1 cells or an increase in mechanical tension[294].

AT2 lineage tracking studies using *Sftpc*$^{\text{CreERT2}}$ combined with clonal expansion analysis by *Rosa-Confetti* multicolor lineage-tracing allele[295] in *Sftpc*$^{\textit{CreER;Rosa-Confetti}}$ shows local clonal expansion of both AT2 and AT1, demonstrating that AT2 can also differentiate in AT1[291]. After acute injury, a specific subset of AT2 cells demonstrates a preferential ability to re-enter the cell cycle, self-renew, and regenerate AT1 cells. This subset, referred to as alveolar epithelial progenitors (**AEPs**)[296], is characterized by the expression of *Axin2*[296,297], a transcriptional target of Wnt signaling involved in AT2-dependent alveolar development during organogenesis. Similarly, a single-cell molecular atlas of the lung identified a Wnt-active AT2 subpopulation that could act as AEPs in humans[298]. Wnt-responsive AT2 cells self-renew in the presence of Wnt signaling but differentiate in its absence[299]. Wnts are secreted glycoproteins that act over

a short range, suggesting that neighboring cells finely regulate AT2 stemness. Platelet-derived growth factor receptor alpha (Pdgfrα)-expressing fibroblasts, which also constitute the mesenchymal alveolar niche, provide juxtacrine Wnt ligands preventing reprogramming into AT1 cells[297]. Dying AT1 cells send mitogenic signals inducing AT2 stem cell proliferation: one AT2 daughter cell remains in the fibroblast niche while the other moves out, losing Wnt signals and differentiating into a new AT1 cell[297]. During injury, ancillary Axin2 stem cells are recruited by autocrine production of Wnts, providing increased sensitivity to mitogens and unlimited proliferation[297]. Thus, Wnt signaling confers stem cell identity to AT2 cells but does not itself activate the stem cells. Similarly, a biphasic temporally regulated Notch activity have been described for AT2 to AT1 transition. At the early phase of repair, high Notch activity is required for the survival of AT2s, however, at the later phase, AT2 Notch activity needs to be downregulated so that these cells can further differentiate into AT1s[300].

Besides Wnt signals, Pdgfrα+ fibroblasts fine-tune renewal through the production of IL-6 and fibroblast growth factors 7 (Fgf7) and 10 (Fgf10), promoting AT2 self-renewal, while Bone Morphogenetic Proteins (Bmp) signaling inhibits AT2 growth[301]. During injury, differentiation is accompanied by downregulation of Bmp signaling, likely due to upregulation of Bmp antagonists, such as follistatin and follistatin-like 1, by stromal cells[292]. Additionally, activated capillary endothelial cells deliver signals sustaining lung alveolar regeneration. Vascular endothelial growth factors and FGF can induce the expression of MMP14 in capillary endothelial cells, which degrades laminin and releases cryptic Epidermal Growth Factor (EGF), thereby inducing AT2 proliferation[302]. Similarly, platelets supply stromal cell-derived factor 1 (SDF-1, also known as CXCL12), triggering CXCR4 and CXCR7 on pulmonary capillary endothelial cells and inducing the production of MMP14[303].

Multiple recent lineage tracing studies propose that AT1 cells could also serve as a cellular origin for regenerating the alveolar epithelium after various alveolar injuries[304,305]. A subgroup of $Hopx^{+}$ AT1 cells might be capable of giving rise to AT2 cells in neonatal alveoli and adults[304,305]. However, a recent publication reported that Hopx-based genetic tools used in previous studies cannot specifically target AT1 cells, sugeesting that AT1 cells cannot de-

differentiate into AT2 cells after lung injury[306]. Thus, whether AT1 plasticity plays a role in alveolar regeneration remains unclear.

Multiple single-cell RNA sequencing from different injury models have identified a transient AT2-AT1 cell state that is a necessary state to transiting into AT1[307–309]. LPS-[310] and bleomycin-[307] induced alveolar injury reveal that AT2 pass through a differentiation trajectory characterized by a proliferation state, cycle arrested state and a final transitional state before acquiring AT1 identity. Choi and collegues[307] suggest that acute damage phase is dominated by 3 sequential transcriptional state: cycling AT2, primed AT2, and damage-associated transient progenitors (DATPs). **Primed AT2s** express canonical levels of AT2 markers together with genes induced by an inflammatory response and the downregulation of AT2 specification genes. **Cycling AT2** cluster appeared strongly related to the primed AT2 cluster, suggesting that differentiation is associated to a cell cycle event. **DAPTs** express *Cldn4* and *Krt8,* share features of the AT1 lineage and are characterized by increased expression of genes associated with arrest of proliferation and IFN-γ signaling pathway[307].

The AT2-AT1 transitional state has also been observed in patients with acute respiratory distress syndrome (ARDS) and diffuse alveolar damage[308,311]. A precise balance of signaling is essential for successful AT2 transdifferentiation. For example, TGF-β signaling is involved in cell cycle arrest and is critical for proliferating AT2 cells to exit the cell cycle, but it must be inactivated to permit AT1 differentiation[310,312]. Persistent TGF-β signaling results in AT2 cells becoming stuck at the intermediate stage, preventing their differentiation into AT1 cells, a condition observed in human pulmonary fibrosis[308,309]. Additionally, IL-1β has been suggested to prime AT2 cells for the DATP transition by enhancing Hif1α-mediated glycolysis, which is instrumental for transitioning into DATPs and the subsequent differentiation into AT1 cells during regeneration. In chronic inflammation, such as in idiopathic pulmonary fibrosis (IPF)[312] or cancer[313], persistent IL-1β stimulation leads to the accumulation of DATPs, associated with failure in AT1 differentiation[307].

Recent spatial transcriptomic and single-cell profiling studies of terminal and respiratory bronchioles in primates and humans have identified a unique alveolar population called AT0.

AT0 cells are present in bronchioles during homeostasis but can differentiate into AT2 cells during injury and have the potential to further differentiate into AT1 or secretory cells. In severe pulmonary fibrosis, AT0 cells convert into secretory cells, forming bronchiolized regions[314].

3.2 "Band aid" basal-like progenitors

Although AT2 cells play a crucial role in alveolar regeneration, their ability to repair the lung barrier is insufficient in cases of extensive alveolar epithelial depletion. In such severe conditions, a suboptimal epithelial repair mechanism is triggered to maintain barrier integrity. In highly damaged areas, hypoxia activates a rare population of airway basal-like progenitors. These progenitors migrate, proliferate in the alveoli, and form clusters known as "pods", identified by the expression of p63 and cytokeratin 5 (Krt5) [315–317]. Lineage tracking analyses have shown that these cells originate from $Sox2^+$ airway epithelial progenitor cells[318]. While classical basal cells ($p63^+$ $Krt5^+$) are confined to the trachea and mainstem bronchi in mice, basal-like progenitors ($p63^+$ $Krt5^{low}$) are primarily located in intrapulmonary airways and upregulate Krt5 after alveolar migration[319]. In larger mammals, including humans, basal $p63^+$ $Krt5^+$ cells persist to the terminal bronchi and likely give rise to $Krt5^+$ pods, although $p63^+$ $Krt5^{low}$ cells have been identified in human distal airways[320].

Intrapulmonary $p63^+$ progenitors can detect disruptions in the alveolar epithelium and rapidly activate to repair epithelial defects[321]. The ultimate fate of $p63^+$ progenitors is still contentious. Some evidence suggests that Krt5+ pods can partially differentiate into functional AT1 and AT2 cells[317], with the extent of differentiation depending on the type of stimulus (10% in influenza A models; 30% in bleomycin models[316]). However, there is growing consensus that $p63^+$ progenitors primarily give rise to bronchial cells including club cells (*Scgb1a1* and *Scgb3a2*), goblet cells (*Muc5AC* and *TFF2*), and tuft cells (*DCLK1*) [316,322]. This process, where bronchial epithelium replaces previously gas-exchanging areas of the lung, is known as alveolar bronchiolization. Dysplastic remodeling associated with $Krt5^+$ pods is observed in humans following viral infections like influenza[323] or COVID-19[324], idiopathic acute lung injury with ARDS[325], and IPF[316].

The signalling mechanisms regulating this regenerative response during repair are not fully understood. One study indicates that Notch signaling is necessary for the initial activation of this pathway[316]. However, persistent Notch signalling is incompatible with differentiation, while increased Wnt signaling can drive an airway cell-to-AT2 transition[316,323]. Notably, post-injury Krt5+ pods are found only in hypoxic regions, suggesting that hypoxia-inducible factor (HIF1α) sensing of local hypoxia coordinates with Notch signaling to regulate p63 activation[323]. Interestingly, hypoxia promotes the differentiation of basal cells toward a neuroendocrine cell fate in a HIF1α-dependent manner. Neuroendocrine cells help protect against injury by secreting calcitonin-related gene peptide[326]. Similar to Wnt signaling, FGF-10 has been shown to contribute to the expansion of $p63^+$ progenitors. However, at later stages after acute damage, FGF10 signalling favours AT2 cell fate over $Krt5^+$ fate[327].

Since intrapulmonary $p63^+$ progenitors migrate into respiratory parenchyma and occupy areas where alveolar repair might occur but do not consistently give rise to functional AT1 and AT2 cells, $p63^+$ progenitors and Krt5 pods are considered contributors to the long-term decline of pulmonary function[288].

3.3 The injured Alveolar Epithelium: Rebuilding from the Rubble

Airway and alveolar epithelia are primary targets of respiratory infections, leading to extensive de-epithelialized zones. The activation of epithelial, endothelial, and stromal cells results in the local production of MMPs and extracellular matrix (ECM) remodeling, which facilitate cell migration[328]. Additionally, macrophages activated by type 2 cytokines can promote TGF-β and Arg-1-induced collagen synthesis and ECM deposition, providing a foundation for newly formed alveoli[329].

Infected epithelial cells play a critical role in amplifying the IFN response by secreting type I and III IFNs along with other inflammatory cytokines[330]. IFN signaling leads to growth arrest in the lung epithelium. Following H3N2 IAV infection, epithelial proliferation drastically decreases in the first 5 days post-infection (p.i.), a period corresponding to tissue injury and maximal IFN production, a strategy aiming at limiting viral replication targets[331]. As

inflammation resolves and IFN levels decrease, epithelial cell proliferation and differentiation progressively increase, particularly in the second week post-infection[331]. Similarly, SARS-CoV-2 infection and consequent IFN activation are associated with decreased proliferation and induction of apoptosis in AT2 cells, a feature observed in severe COVID-19 specimens[332]. Although upregulation of IFNs is crucial for infection control and preventing viral spread, cessation of IFN production is necessary to ensure the epithelial regenerative response. IFN-γ produced during infection also induces the recruitment of CCR2-dependent monocytes[333], often associated with exacerbation of lung injury[160,334]. However, $CCR2^+$ monocytes recruited during the repair phase might play a beneficial role in alveolar regeneration. Lechner and colleagues[293] proposed that 7 days after partial pneumonectomy, AT2 cells and PDGFRA+ fibroblasts increased their expression of CCL2, inducing the recruitment of $CCR2^+CX3CR1^-$ blood monocytes near AT2 cells, at the periphery of the regenerating lung. CCR2-deficient mice exhibited decreased AT2 proliferation and AT2-AT1 differentiation. They also described that lung macrophages assume an M2-like phenotype, expressing *Arg*1, *Retnla/Fizz1*, *Chil3/Ym1*, and *IL-4Rα*, along with matrix metalloproteinases like *MMP2*, *MMP3*, *MMP4*, and *MMP19*, but not *TNF-α*, *IL-1β*, or *IL-6*[293]. After pneumonectomy, this M2-like polarization depends on the activation of IL-13-producing ILC2s that trigger IL-4 receptor alpha (IL4Rα) signaling on recruited monocytes and resident macrophages. The loss of the IL-13-IL-4Rα axis impairs optimal lung growth[293].

Interestingly, Th2 response activation has also been observed in respiratory viral-induced disorders by the X31 H3N2 strain of influenza virus[273]. ILC2 are mainly recruited to the lungs of infected mice as early as day 5 p.i., during the peak of viral load, and reach their modest IL-13 production peak at day 10 p.i., while IL-13-producing T cells increase at days 7 and 10 post-infection[273]. Despite ILC2 expansion in H1N1 influenza infection models[273,335], their repair function does not seem related to IL-13 but to a IL-33-IL33R axis-dependent production of amphiregulin, an EGF family member[335]. Amphiregulin produced by pulmonary ILC2s and regulatory T cells (Treg) is considered a major mediator to restore epithelial integrity and tissue homeostasis after infection[256]. Moreover, natural killer cells, ILCs, and γδ T cells produce IL-22, inducing anti-apoptotic genes in AT2 cells[336].

Other soluble inflammatory factors also influence alveolar epithelial cell behavior. FGF-7 and FGF-10 signaling through the FGFR2 receptor on AT2 cells are crucial for restoring homeostatic alveolar architecture by maintaining AT2 fate. FGFR2-deficient AT2 cells differentiate more readily into AT1 cells, resulting in increased alveolar area with expanded air spaces[337]. Moreover, proinflammatory cytokines have been involved in alveolar epithelial proliferation[338]. Since the denser immune infiltrates accumulate in infected areas, away from sites of alveolar proliferation, the applicability of this finding in vivo could appear paradoxical. The explanation was found in the observation that AT2 proliferation was higher in zones near damaged regions and can be influenced by the nearby inflammatory environment[338]. Stimulation by proinflammatory cytokines like TNFα, IL-1, and IL-17 can increase the size of lung organoids by promoting epithelial cell proliferation[338]. Both IL-1α and IL-1β exhibit proliferative effects on AT2 cells and fibroblasts, supporting alveolar re-epithelialization[338]. The crucial role of IL-1 was further confirmed by Choi and colleagues[307] which found that IL-1β was critical in priming IL-1R^{+} AT2 and induce DATP in bleomycin model. In the same study, *IL1b* transcription increased in pulmonary macrophages on day 14 post-injury, namely during the repair phase. CD45^{+}CD64^{+}Siglec-F^{-}CD11b^{hi} IMs were identified as the main source of IL-1β, with GM-CSF activation specifically augmenting IL-1β expression in these cells[307].

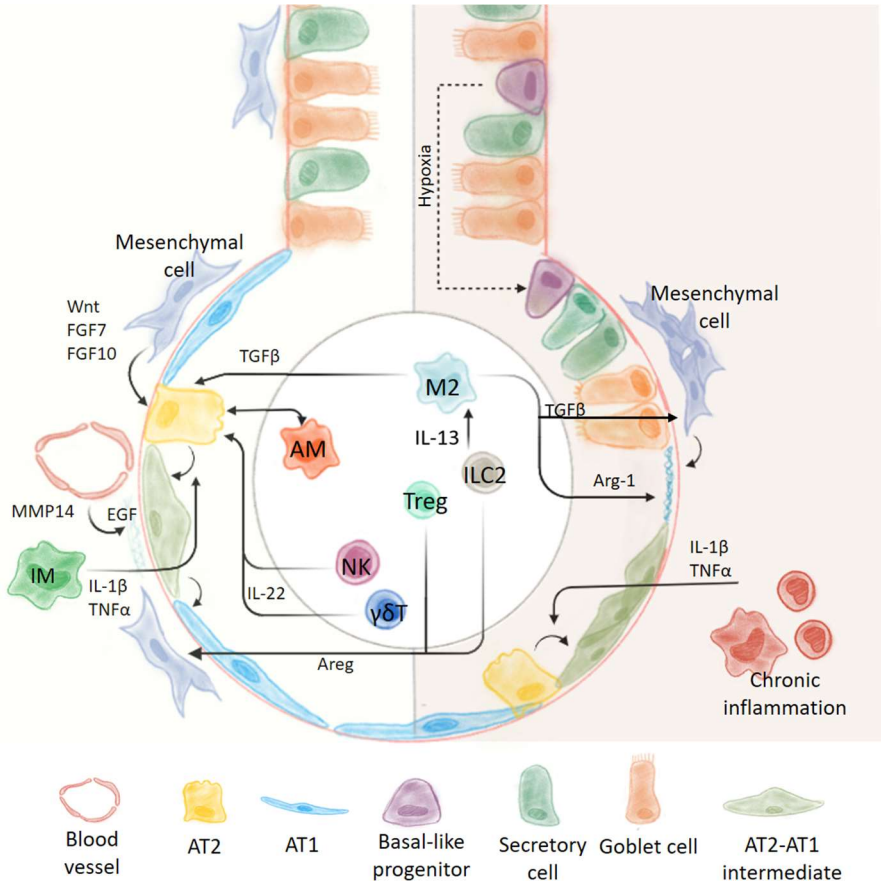

Figure 7- Immune regulation of lung repair

In the alveolar epithelium, AT2 cells act as the primary progenitors of AT1 cells following moderate injury. They respond to various signals, including mesenchymal-derived Wnt proteins, FGF7, and FGF10, which are primarily released by fibroblasts surrounding the alveoli. Immune cells such as macrophages, regulatory T cells, group 2 innate lymphoid cells, γδ T cells, and natural killer cells also enhance epithelial proliferation and differentiation through the secretion of molecular signals. While macrophage-derived IL-1β and TNFα promote AT1 differentiation, chronic inflammation can hinder this process, leading to the abnormal accumulation of transitional AT1-AT2 intermediate cells and increasing the risk of fibrosis. In cases of severe injury, hypoxia triggers the recruitment of basal-like progenitors from the distal airways to help maintain the epithelial barrier. However, these progenitors tend to adopt airway-specific fates upon differentiation, which can result in bronchiolization of the alveolar epithelium and impair normal gas exchange.

AT2: Alveolar type 2 epithelial cell; AT1: Alveolar type 1 epithelial cell; DATP: damage-associated transient progenitor; IM: Interstitial Macrophages; AM: Alveolar Macrophages; NK: Natural Killer cell; Treg: regulatory T cells; ILC: innate lymphoid cells; FGF: Fibroblast growth factor; EGF: Epithelial growth factor; Tgfβ: Transforming growth factor β; Areg: Amphireguline; Arg-1: Arginase 1;

Inspired by *Narasimhan, H., Wu, Y., Goplen, N. P. & Sun, J., Science Immunology* ***7****, eabm7996 (2022)*[339]

In addition, AT2 cells represent the major source of GM-CSF in the lungs[340], which is essential for the development and function of AMs during homeostasis and inflammation[341]. GM-CSF can induce expression of PPAR-γ, crucial for AM development from fetal monocytes and the induction of an immunosuppressive program in AMs[120]. In an IAV infection model, myeloid deficiency of PPAR-γ in *Pparg*$^{\Delta Lyz2}$ transgenic mice resulted in impaired expression of wound-healing-related genes, including epithelial and endothelial growth factors such as *Vegf*, *Egf*, and *Fgf7*, along with impaired tissue repair and diminished AT2 regeneration at days 10 and 15 post-infection[341]. Moreover, during inflammation, TNF-α can stimulate GM-CSF production by AT2 cells, eliciting proliferative signalling in alveolar epithelial cells through autocrine stimulation[340]. Furthermore, macrophages are able to secrete Wnt, which can promote epithelial regeneration[342]. In a hookworm infection model, the depletion of CD68^{+} macrophages leads to dramatic decrease of AT2s and in vitro co-culture of macrophages with both tracheal and AT2s promote epithelial proliferation[343]. One of the demonstrated mechanism of this interaction have been related to the myeloid Trefoil factor family 2 (TFF2), required for expression of myeloid derived Wnts[343].

3.3.1 Lung Post-Acute Infection Chronic Sequelae: A Long-Lasting Worksite

These studies collectively provide evidence that the processes involved in epithelial lung repair are strongly dependent on the initial trigger and the nature of the inflammatory response. For instance, pneumonectomy allows for the conservation of alveolar progenitors at the edge of the excision and is typically used as a classical model to study alveolar regeneration. In contrast, respiratory virus-induced alveolar damage infects mature epithelial cells and potential progenitors, leading to severe epithelial loss. In this case, sub-optimal compensatory tissue repair processes are enabled to rebuild the air-blood barrier.

Several studies report long-term respiratory dysfunction following severe viral-triggered lung injuries. Influenza virus infections lead to a wide range of clinical outcomes, from asymptomatic cases to death. Severe illness results from infection of the lower respiratory tract, causing pneumonia and ARDS. Long-term studies on H1N1 cohorts revealed that 54%

of patients who had been infected with H1N1 exhibited lung disabilities at least one year post-infection[344,345]. Similarly, persistent pathology was observed in individuals infected with H5N1 and H7N9[346,347]. Despite clear anatomical and immune differences, H1N1 infection in mice induces chronic pathology characterized by persistent immune infiltrates and areas of dysplastic repair, lasting at least until day 200 post-infection[322,341].

These chronic sequelae are at least partly attributable to epithelial dysplasia. Not surprisingly, influenza virus infection is used as a model to decipher mechanisms underlying dysplastic repair.

Upon H1N1 IAV infection, $p63^+$ basal progenitors are rapidly recruited and expand in the lung parenchyma[316]. $KRT5^+$ clusters are detectable eleven days post-infection, and the resulting $KRT5^+$ cysts, composed of differentiated secretory cells (CC10+) and other bronchial cells, are maintained until at least day 200 post-infection[316]. Upon migration, p63 progenitors develop into two different patterns depending on their localization and local signals: when seeded in AT2-rich areas, they preferentially engage in AT2 differentiation; when engrafted near other KRT5+ structures, they express KRT5 and CC10. Similar to AT2 cells, regenerative KRT5+ cells depend on Notch activity for their expansion, and Notch inhibition induces the expression of surfactant protein C, suggesting AT2 differentiation. Thus, persistent Notch activity found in cystic epithelium prevents alveolar differentiation. Notch ligands, such as Delta-like 1 (Dll1) and Dll-4, are expressed by M1-like macrophages upon induction of the type-I IFN pathway[348] and hypoxia[349], respectively. The supportive role of pro-inflammatory signals for $KRT5^+$ structures is evident when examining their localization. Computational image analysis of mouse lung sections 14 days post-H1N1 infection defined three zones of injury: severe, damaged, and normal[337]. Severe zones are “alveolar deserts” characterized by the absence of AT1 markers and the presence of rare, highly proliferative non-differentiating AT2 cells. $KRT5^+$ cells are exclusively found in these zones. Damaged zones harbour a dense collection of AT1 cells and proliferating and differentiating AT2 cells, while normal zones consist of homeostatic tissue architecture with regular distribution of AT1 and AT2 cells lining the alveolar wall[337].

While an effective immune response is crucial for eliminating the pathogen and sending pro-repair signals to epithelial cells, dysregulated responses can adversely affect repair and lead to parenchymal abnormalities. Proper regulation and resolution of inflammation after the acute infectious phase are necessary to avoid additional immune-induced tissue damage and abnormal remodelling. Although stemming from different etiologies, most abnormal remodeling processes are associated with persistent inflammation, which maintains the production of growth factors, proteolytic enzymes, and profibrotic cytokines[350].

Dysregulated IFN signaling has been implicated in the pathogenesis of chronic sequelae in COVID-19[351]. Persistent IFN signaling in the post-acute infection phase induces activated macrophages to secrete CCL7, CCL8, and CCL13, contributing to the recruitment and maintenance of CD8+ cells, which in turn secrete IFN-γ[352]. Furthermore, suboptimal alveolar repair may lead to repetitive non-resolving micro-injuries, resulting in the reactivation of immunity[353]. $CD8^+$ resident memory T cells are preferentially localized in the repair foci[354]. Since their activation causes the expression of high levels of cytotoxic molecules, they can amplify the initial epithelial injury and inhibit functional repair[288].

Myeloid cells contribute to fibrotic sequelae after viral infection. Despite the essential role of IL-1β signaling in AT2-AT1 transdifferentiation, chronic inflammatory IL-1β may prevent this differentiation[307]. Persistent inflammation results in the accumulation of alveolar epithelial cell intermediates associated with impaired regeneration[307,308]. Furthermore, IL-1β can induce airway progenitor differentiation into AT2 cells, which, however, maintain some secretory features, further contributing to alveolar bronchiolization[355]. Thus, strict regulation of IL-1β signaling is mandatory for successful lung regeneration.

Type 2-polarized macrophages have been implicated in ECM deposition leading to fibrotic sequelae after influenza virus infection. Their presence at the end of infection and during the early recovery phase is essential for resolving inflammation and inducing wound repair[356]. However, their persistence may induce a fibroproliferative and dysregulated wound healing cascade. Fibroblasts recruited by CCL2 to injured sites are activated by macrophage-derived TGF-β, among other factors, to assume a myofibroblast phenotype[357]. TGF-β has also been

described to promote epithelial transdifferentiation into myofibroblasts, a phenomenon known as epithelial to mesenchymal transition (EMT) [358]. Myofibroblasts express smooth muscle proteins such as α-SMA, promoting their contractility, and produce high levels of ECM, contributing to organ architecture distortion. Furthermore, the persistence of Ly6C^{hi} inflammatory monocytes recruitment to maintain the profibrotic macrophage pool contributes to the progression of pulmonary fibrosis[359].

4 Macrophages in tissue repair

Wound healing involves dynamic cellular proliferation and differentiation, alongside the formation of a new ECM and collagen deposition to support the newly differentiated cells. Multiple cell types are involved in the tightly regulated wound healing response to ensure a rapid resolution of inflammation and prevent pathological scarring in the injured organ. Macrophages play a crucial regulatory role at all stages of inflammation and repair due to their highly flexible programming[164]. Although resident macrophages and recruited monocytes are key drivers of the inflammatory response and contribute to tissue disruption, their impaired activation can hinder wound debridement and extend exposure to pro-inflammatory stimuli, leading to incomplete regeneration.

Two non-exclusive models have been proposed to explain how macrophages interact with resident cell populations to promote tissue repair. In the passive model, during the resolution phase of inflammation, recruited monocytes differentiate into macrophages in response to increasing homeostatic signals from regenerating tissue. This results in macrophages acquiring a phenotype similar to that of tissue-resident macrophages, which aids in normalizing the tissue environment and promoting repair. The second model involves active repair induced by macrophage activation in response to signals from injured tissue. Among these mechanisms, the best studied mechanisms are efferocytosis and type 2 cytokines, both of which can regulate inflammation and stimulate the secretion of pro-repair molecules[360].

4.1 Extinguishing the Inflammatory Fire

The downregulation of inflammatory cell infiltration is a critical initial step in terminating inflammation and initiating new tissue formation. During this resolution phase, macrophages adopt functional profiles that actively cease neutrophil influx. Macrophage-derived **MMPs**, particularly MMP-12, possess pro-reparative properties by cleaving and inactivating pro-inflammatory cytokines[361] and chemokines[362], thus limiting neutrophil recruitment. Additionally, macrophages secrete interleukin-1 receptor antagonist (**IL-1ra**), which blocks IL-1β receptors on alveolar epithelial cells. Blocking IL-1β downregulates alveolar CXCL2 and ICAM1, which can reduce neutrophil recruitment[363]. Moreover, macrophages can promote the apoptosis of neutrophils. Despite neutrophils being short-lived cells, their lifespan is extended by survival signals such as granulocyte-colony stimulating factor (G-CSF) and IL-1β during inflammation[364]. Local IL-1β antagonism by macrophage-derived IL-1ra can suppress the production of these supportive signals and induce neutrophil apoptosis[363]. Similarly, during respiratory infections, lung macrophages express high levels of the death ligand TRAIL[365], which induces neutrophil apoptosis[366]. Active migration of early apoptotic neutrophils via CXCL2 through inflammatory monocytes induces EGF-dependent monocyte differentiation into APCs and facilitates neutrophil efferocytosis[367].

Phagocytosis of apoptotic neutrophils is essential for resolving inflammation[368]. Apoptotic neutrophils signal their presence through "find me" signals, such as fractalkine (CX3CL1) and the nucleotides ATP and uridine 5′ triphosphate (UTP), which are recognized by CX3CR1 and P2Y2 receptors, respectively[369]. Following **efferocytosis**, macrophages undergo functional repolarization and are stimulated to release anti-inflammatory and pro-repair mediators. Neutrophil-fed macrophages increase the secretion of transforming growth factor-beta (TGF-β), IL-10, prostaglandin E2 (PGE2), and platelet-activating factor (PAF) while reducing the release of pro-inflammatory cytokines such as IL-6[370,371]. Additionally, the phagocytosis of cellular debris induces the production of growth factors essential for tissue repair, including VEGF [372] and hepatocyte growth factor (HGF) [373].

Bosurgi and colleagues propose that the macrophage anti-inflammatory program is coordinated by simultaneous signals from type 2 cytokines (IL-4/IL-13) and apoptotic cells. IL-4 receptor activation in BM-derived macrophages is sufficient to induce genes involved in translation, cell proliferation, chemotaxis (e.g., *Ccl2* and *Ccl7*), pattern recognition (e.g., *Clec7a*), and cell adhesion (e.g., *Cdh1*). Conversely, the anti-inflammatory (e.g., *Retnla* and *Chil*) and pro-repair (e.g., *Fn1* and *Ear2*) programs are only activated by co-stimulation with apoptotic neutrophils. Consistent with this, impairment of apoptotic cell signals in *Axl*$^{-/-}$ and *Mertk*$^{-/-}$ mice results in reduced expression of *Retnla*, *Chil3*, and *Arg1*, leading to defective repair in models of helminth[368] infection and colitis[374].

Contrasting with type 1 and type 17 responses, which control microbial infections, **type 2 responses** are often associated with protection against helminth infections. Type 1 pro-inflammatory responses release antimicrobial mediators effective against pathogens but often cause significant collateral tissue damage[375]. In evolutionary terms, type 2 tissue-reconstructive and anti-inflammatory responses are more cost-effective against large, motile targets such as metazoan parasites, which cause direct tissue damage. Thus, type 2 immunity should be viewed not only as an anti-helminth response but also as a tissue repair mechanism[376]. Even after microbial infections, type 1 responses dynamically shift to type 2 tissue-reparative responses, involving many cell types and molecular factors. Epithelial cells release alarmins, such as thymic stromal lymphopoietin, IL-25, and IL-33[377], in response to barrier insults, which activate type 2 cells like ILC2, mast cells, basophils, and eosinophils[378]. Additionally, Th2 lymphocytes, which express the IL-33 receptor (ST2), can be directly activated by IL-33 independently of antigen stimulation[379]. The type 2 response includes classical cytokines such as IL-4, IL-13, IL-5, IL-10, and TGF-β, along with other features associated with inflammation regulation and repair.

The first indication of type 2 involvement in wound repair emerged from observations that IL-4 can induce arginase expression in macrophages, thereby enabling their pro-repair functions through the activation of IL-4Rα signaling[380,381]. Notably, the IL-4R α chain can combine with the common gamma chain to form the type 1 receptor or with IL-13Ra1 to form

the type 2 receptor. IL-4 binds to both types of receptors, whereas IL-13 only utilizes the type 2 receptor. Since many in vivo studies on type 2 responses use *IL-4Rα*$^{-/-}$ transgenic mice[382,383], distinguishing the specific roles of IL-4 and IL-13 in vivo can be challenging[166].

Part of the wound-healing function of **IL-4Rα** signaling involves limiting inflammation to allow repair processes to progress. Activation of IL-4Rα on neutrophils directly reduces their migration, expansion, and production of extracellular traps[384,385]. Additionally, IL-4Ra-activated macrophages suppress signals such as Ccl3 (Mip1α), Ccl4, Ccl2 (MCP-1), Ccl7 (MCP-3), and Cxcl14, which are involved in recruiting innate immune cells[386], and enhance their phagocytic uptake[387]. Moreover, IL-4Rα activation curtails mitochondrial ROS and NO production through a metabolic shift. During the early inflammatory stages, macrophages primarily rely on glycolytic metabolism, but they switch to mitochondrial oxidative phosphorylation during the healing process[388]. Redirecting mitochondrial metabolism toward ATP production prevents tissue-damaging ROS production[389].

Type 2 cytokines also strongly induce the expression of 'resistin-like molecules' (**RELMα**) in macrophages[376]. RELMα, also known as found in inflammatory zone (Fizz1), is a member of a family of cysteine-rich secreted proteins originally identified in the lung[390]. Although induced by IL-4/IL-13, RELMα provides a negative feedback mechanism to suppress type 2 responses, partially through the regulation of $CD4^+$ T cell responses[391,392]. In the N. brasiliensis infection model, IMs, but not AMs, express high levels of RELMα, which is essential for the resolution of inflammation[393].

A significant type 2-induced metabolic pathway conversion involves arginine metabolism. Arginine serves as a substrate for the enzymes iNOS and Arg-1. iNOS, induced by type 1 cytokines, produces NO, a toxic antimicrobial mediator, while **Arg-1** generates metabolites that support cell proliferation and collagen deposition[394]. The high affinity of arginine for Arg-1 results in local depletion of the substrate available for iNOS, thereby controlling inflammation. Arginine is also crucial for activated T cells[394], and its metabolism can suppress T cell responses by inhibiting antigen-specific T cell proliferation[395]. This suppression affects

Th1, Th17, as well as Th2 responses, highlighting Arg-1 role in limiting Th2 responses and preventing organ failure linked to excessive collagen deposition[396] as described below. However, Arg-1 is not a definitive marker of IL-4-responsive macrophages, as it can also be induced by pro-inflammatory signals[397], hypoxic environments[398], and other inflammatory cytokines such as IL-10 and TGF-β[399], indicating a redundancy in Arg-1-dependent inflammation control.

In addition to arginases, other macrophage-derived cytokines can exhibit a dual functionality, contributing to both the resolution of inflammation and tissue repair. Among the most extensively studied examples are TGF-β and IL-10. Unlike most cytokines, **TGF-β** is secreted by virtually all cells in a biologically inactive form known as latent TGF-β. This latent form consists of an amino-terminal latency-associated peptide (LAP) non-covalently associated with the carboxy-terminal mature TGF-β molecule. TGF-β activation involves enzymatic cleavage by proteases and metalloproteases, as well as viral neuraminidases[400]. This pleiotropic molecule is induced by the phagocytosis of apoptotic cells and directly contributes to suppressing local inflammation and promoting wound healing. TGF-β controls T cell differentiation[401], fosters the development of peripheral regulatory T cells[402], and inhibits the pro-inflammatory responses of activated macrophages[403] limiting the secretion of IL-1β, TNF-α, GM-CSF, and IL-8[371,404]. **IL-10** serves as a general suppressive cytokine, inhibiting pro-inflammatory responses from both innate and adaptive immune systems, thereby preventing immune-induced tissue damage[405]. In the skin, IL-10 deficient mice show a prolonged inflammatory response and excessive scar collagen deposition[406]. Similarly, the depletion of airway nerve-associated IM, which are the primary IL-10 producing lung macrophages that expand under inflammatory conditions, leads to worsening clinical conditions and persistent inflammation upon injection of the immunostimulant poly(I:C)[8].

Recently, the role of epithelial growth factor-like **amphiregulin** as a local inflammation suppressor has been described. Macrophages are the main producers of amphiregulin after helminth infection[407] and LPS-induced lung injury[408]. Amphiregulin functions by regulating

Treg activity[401] or by releasing bioactive TGF-β[407], directly contributing to repair by inducing the proliferation of structural cells[409].

After inflammation, recruited monocytes and monocyte-derived macrophages persist in tissues and eventually adopt a transcriptional profile similar to that of native AM, suggesting that signals within the alveolar niche influence the behavior of not only AMs but also other myeloid cells[132]. Notably, alveolar epithelial cells have a direct immunomodulatory effect on macrophages via CD200/CD200R[410], as well as CSF2R/GM-CSF[411] and β-catenin/E-cadherin[412] interactions. The loss of alveolar epithelial cells upon injury, determine the disruption of this crosstalk and contributes to the activation of pro-inflammatory programs in macrophages. During repair, the restoration of the physiological number of AT2 cells re-establishes immunomodulatory immune-epithelial signaling, determining the reduction of IL-6 and TNF-α secretion, thereby facilitating the resolution of inflammation[151].

4.2 Macrophages as Construction Workers

Macrophages adopting a pro-resolving phenotype can secrete molecules that act on structural cells, laying the foundation for tissue repair.

IL-4 enhances the production of **IGF-1**, which stimulates the proliferation and survival of fibroblasts and myofibroblasts, thereby promoting wound closure[383]. Monocyte- and macrophage-derived IGF-1 has been identified as a critical player in the repair of several organs. Furthermore, **RELMα** is involved in directing collagen matrix organization in fibroblasts. RELMα induces fibroblasts to produce lysyl hydroxylase 2 (LH2), an enzyme that directs stable collagen cross-links in the skin[413] and lungs[414]. Although RELMα is primarily derived from macrophages in the skin, it is mainly produced by epithelial cells in the lungs. In this context, Ym1 secreted by macrophages induces RELMα in epithelial cells[414].

IL-13 induces the production of **MMPs** by macrophages[415]. MMPs can degrade almost every component of the extracellular matrix and, although often associated with aberrant remodeling, are crucial for maintaining structural integrity and preventing excessive scar

accumulation in damaged regions. Furthermore, MMP-9, as well as amphiregulin, can activate latent TGF-β, thereby contributing to tissue remodeling[415]. **TGF-β** is implicated in re-epithelialization, tissue angiogenesis, and fibroblast activation. TGF-β induces the migration of epithelial cells at the edge of cutaneous wounds[416] and promotes the expression of VEGF by mesenchymal cells, supporting angiogenesis[417]. It also stimulates fibroblast proliferation, their differentiation into myofibroblasts, and the deposition and remodeling of the extracellular matrix[418]. Although myofibroblast activation and extracellular matrix deposition are crucial for recovering functional structure, their activity must be finely tuned to prevent excessive scar formation. For instance, IFN-γ-stimulated macrophages secrete CXCL10, which inhibits fibroblast chemotaxis[419] and proliferation[420] via the CXCR3 receptor.

In addition to TGF-β, other cytokines act as both inflammatory suppressors and pro-repair factors. **Arg-1** specifically catalyzes the conversion of L-arginine into L-ornithine and urea. L-ornithine can be further metabolized into polyamines such as putrescine, cadaverine, and spermidine, which are involved in tissue repair by inducing epithelial cell proliferation[421]. Furthermore, polyamines can be catalyzed to form L-proline, used by myofibroblasts for collagen formation[422].

Another crucial contribution of macrophages to tissue repair is their involvement in angiogenesis. The sprouting of capillaries from existing blood vessels into the injured area is vital for healing because it supplies nutrients and oxygen to the newly forming tissue. During the early healing stages, macrophages are identified as a major source of **VEGF** in skin repair and promote endothelial cell migration, proliferation, and angiogenesis[388]. Moreover, lung macrophage-derived **IL-1Ra** plays a role in restoring barrier integrity. During inflammation, IL-1β increases alveolar endothelial and epithelial permeability, leading to edema fluid accumulation in the airspaces[423]. IL-1β antagonism by IL-1Ra prevents the disruption of tight junction proteins[363] and increases Na+ channels in epithelial cells, thereby clearing alveolar edema[423].

4.3 Macrophages in Lung Fibrosis: When Things Go Wrong

The abnormal persistence of the lung repair response can lead to pulmonary fibrosis, characterized by irreversible scarring and chronic fibrotic remodeling. Although ECM-producing myofibroblats play an important role as profibrotic effectors, an inadequate macrophage response is also critical in this pathological process.

One commonly used model to understand the biological mechanisms underlying lung fibrosis development is the intratracheal instillation of bleomycin[424]. Bleomycin is a chemotherapeutic antibiotic produced by the bacterium Streptomyces verticillus. Observations that bleomycin-based cancer therapy induces pulmonary fibrosis as a major adverse effect justify its use as a model for pulmonary fibrosis in animals[424]. This model is characterized by an acute inflammatory phase lasting seven days before the induction of the fibrotic phase[425]. However, a significant limitation is the spontaneous reversal of fibrosis that typically occurs 3-4 weeks post-treatment, unlike the irreversible chronic pathology seen in human patients[426].

Lung macrophages have been implicated in the fibrotic phase of the bleomycin model[132,427]. Recent studies have highlighted the differential involvement of alveolar macrophages (AMs) in lung fibrosis based on their origin. The depletion of tissue-resident macrophages before bleomycin instillation has no impact on fibrosis development, supporting that resident AMs are dispensable for this process[132]. In contrast, inducing apoptosis in circulating monocytes to reduce the number of monocyte-derived alveolar macrophages (mo-AMs) ameliorates lung fibrosis[428]. $CD11b^{+}CD64^{+}$ macrophages inhabiting alveolar spaces exhibit high levels of profibrotic cytokines, such as CCL24 and CCL2[428]. CCL24 promotes fibroblast survival, while CCL2 stimulates their proliferation and collagen production[429]. Another study identified a group of fibrosis-specific macrophages with monocyte origin (expressing CXCR1, CCR2, Mafb, and MHC2) and co-expressing CX3CR1 and SiglecF[430]. This transitional population, an intermediate between monocytes and AMs, produces high levels of PDGFA, localizes in fibrotic niches near $PDGFR^{+}$ fibroblasts, and drives fibrosis by inducing their proliferation and

fibrotic scar deposition[430]. Importantly, human fibrosis samples were enriched in Mafb$^+$ macrophages compared to healthy controls, demonstrating the presence of this transitional population in humans[430]. The presence of a heterogeneous AM population correlated with a profibrotic signature in human fibrosis has also been confirmed by other studies[132,244,431] . However, little is known about signals maintaining this population nor if pro-fibrotic AM are the source of the results of the microenvironmental changes.

IMs have also been described as contributors to fibrosis development in both the bleomycin model[11,427] and the radiation-induced lung fibrosis (RIF) model[432]. In both models, IMs overexpress Arg-1 and trigger the differentiation of fibroblasts into myofibroblasts[427,432]. Conversely, the depletion of vessel-associated Lyve1^{hi}MHCII^{lo} IMs ,corresponding to the CD206$^+$ IM subset[12], in the bleomycin model leads to exacerbation of collagen deposition and inflammation[11]. This study suggest that Lyve1^{hi}MHCII^{lo} IMs play an early antifibrotic role by controlling leukocyte migration and persistence in the injured lung[11]. In human samples, IMs have been found to accumulate in fibrotic lungs[433,434]. These macrophages are enriched in profibrotic genes, including *Mertk*, *Lgmn*, *Siglec10*, and *Spp1*[433,434]. Interestingly, macrophages in severe COVID-19 closely resemble lung fibrosis-associated macrophages and express *CD163*, *Lgmn*, and *Spp1*[435]. Spatial transcriptomic analyses revealed that *Spp1*$^+$ macrophages, enriched in samples with higher fibrosis pathology scores, are recruited to the airspaces in the late remodeling stage after fibroblast activation[436]. In the mouse bleomycin model, monocytes have been described to drive pulmonary fibrosis via *Spp1* induction[437]. Intravenous transfer of these bilobed Ceacam1$^+$Msr1$^+$Ly6C$^-$F4/80$^-$Mac1$^+$ monocytes, named segregated-nucleus-containing atypical monocytes (SatM), into SatM-deficient mice was sufficient to restore fibrotic features by inducing *Spp1* in fibroblasts[437]. Notably, *Spp1* codes for osteopontin, a pleiotropic protein that facilitates diverse cellular functions such as macrophage and T-cell migration[438], enhances cell survival[439], induces TGF-β1-dependent myofibroblast differentiation, and promotes proper collagen organization[440]. *Spp1* expression in macrophages is related to a proinflammatory Th1 response, and the persistence of *Spp1*$^+$ cells after injury is correlated with abnormal repair[433,435].

OBJECTIVES

Due to their structure and function, the lungs are continually exposed to airborne particles and pathogens. Among these pathogens, respiratory viruses are a significant cause of mortality, responsible for approximately 2 million deaths annually[441], and they impose a substantial economic burden, exceeding 50 billion USD in the United States[442]. Commonly encountered viral respiratory pathogens include include human coronaviruses, rhinoviruses (RVs), influenza viruses, and respiratory syncytial virus (RSV), which generally cause self-limiting infections confined to the upper respiratory tract, leading to mild symptoms. However, the recent COVID-19 pandemic has highlighted the increasing incidence and prevalence of chronic sequelae following acute viral infections, posing a serious health concern[443]. While the acute effects of various respiratory viral infections have been extensively studied, there is a significant and unmet need to understand the mechanisms leading to chronic symptoms to mitigate these conditions that persistently diminish patients' quality of life. The primary chronic respiratory sequelae result from direct lung infections and the failure of normal repair processes. Despite mild respiratory symptoms during acute infection, viruses can infect the deeper airways and respiratory parenchyma, leaving extensive areas of denuded epithelium to be reconstructed[337]. The outcomes of these repair processes depend on various confounding factors, including age[444], viral tropism[445], and differences in immune responses[446].

Dysregulated immune responses have been implicated in maladaptive tissue remodeling and adverse long-term outcomes after recovery from acute illness, characterized by alveolar bronchiolization, aberrant remodeling, and fibrosis[322,341]. Monocytes and macrophages are crucial immune cells that actively participate to all the phases of respiratory infection. Although their roles during acute infection have been well documented[211], their function in the recovery phase is less understood. In this study, we utilized a clinically relevant murine model of influenza, induced by intranasal infection with the H1N1 PR8 strain, commonly used to model maladaptive repair[288]. By employing advanced technologies such as single-cell RNA sequencing, spatial transcriptomics, metabolic assays, multiplex flow cytometry, and microscopy, we conducted a comprehensive analysis of the myeloid compartment during the early repair phase. Additionally, we used transgenic mice and bone marrow chimera

experiments to further investigate the origin and function of immune populations during the post-infection. This integrative approach facilitated a detailed characterization of immune cells and their functional localization within the injured lung. To assess whether our findings were exclusive to influenza A virus infection, we employed additional injury models: bleomycin-induced lung fibrosis and acetaminophen-induced acute hepatitis. Furthermore, to explore potential therapeutic applications, we evaluated the translational relevance of our findings by characterizing the transcriptome of broncho-alveolar lavage samples from patients with infectious pneumonia.

EXPERIMENTAL SECTION

The findings of this study have been recently published as a research article in the journal *Science Immunology*[159] together with a focus commentary by Chrysante S. Iliakis and Andreas Wack[447] .

Our findings were highlighted on the cover of the August Issue of *Science Immunology*.


Science
Immunology
AUGUST 2024
AAAS

1 Materials and Methods

Mice

All experiments, unless otherwise specified, were performed on age-matched 8–12-wk-old C57BL/6 male and female mice. The following strains of mice were used: CD45.2 wild-type (WT) C57BL/6J (The Jackson Laboratory, #000664); CD45.1 WT (The Jackson Laboratory, #002014); *Cx3cr1*$^{GFP/+}$ [448] (The Jackson Laboratory, #005582); *Ccr2*$^{-/-}$ [449] (The Jackson Laboratory, #004999); *Ms4a3*^{Cre} [235]; *Ly6g*^{CreERT2} [450]; *R26*$^{LSL\text{tdTomato}}$ [451] (The Jackson Laboratory, #007909); *Maf*$^{fl/fl}$ [452], *Mafb*$^{fl/fl}$[124]; *Lyz2*^{Cre} [453] (The Jackson Laboratory, #004781); WT BALB/cJ (The Jackson Laboratory, #000651). CD45.1/CD45.2 WT C57BL/6J were obtained from CD45.1 WT crossed with CD45.2 WT mice. Myeloid-restriced c-Maf and Mafb depletion was achieved by crossing Maf$^{fl/fl}$ and Mafb$^{\mathbf{fl/fl}}$ mice with Lyz2^{Cre} mice. *Ms4a3*^{tdTom} and *Ly6g*^{tdTom} mice were obtained by crossing *R26*$^{LSL\text{tdTomato}}$ with *Ms4a3*^{Cre} and *Ly6g*^{CreERT2} mice, respectively.

Mice were housed under specific pathogen-free conditions and maintained in a 12-h light–dark cycle with food and water ad libitum. All animal experiments described in this study were carried out in an animal biosafety level 3 containment unit. Experiments were reviewed and approved by the Institutional Animal Care and Use Committee of the University of Liège (ethical approval #2276). The 'Guide for the Care and Use of Laboratory Animals,' prepared by the Institute of Laboratory Animal Resources, National Research Council, and published by the National Academy Press, as well as European and local legislations, was followed carefully. Accordingly, the temperature and relative humidity were 21°C and 45-60%, respectively

***In vivo* models of lung injury**

The mouse-adapted influenza strain A/Puerto Rico/8/34 (H1N1; PR8) was kindly provided by F. Trottein (Institut Pasteur, France). The viral stock suspension (10^8 Plaque Forming Units [PFU] ml^{-1}) was diluted and 5 PFU were administered intranasally (i.n.) to isoflurane-anesthetized mice in 50 µl of PBS (Thermo Fisher). Control groups received an equal volume of PBS i.n. for mock infection.

For bleomycin-induced lung injury, isoflurane-anesthetized mice were treated intratracheally (i.t.) with a single instillation of 0.06 IU of bleomycin (Bio-Connect) in a volume of 50µl of PBS. Control animals received 50µl PBS alone.

For acetaminophen-induced liver injury mice were were fasted during of 15 hours with free access to water then injected with 300mg/kg of acetaminophen (Sigma) in NaCl 0.9% (30°C) intraperitoneally. After treatment, free access to food was allowed.

Assessment of viral NS1 mRNA levels

Whole lungs were excised and total mRNA was isolated from homogenized tissues according to the Immgen protocol (www.immgen.org). cDNA was obtained with RevertAid First Strand cDNA Synthesis Kit (Thermo Fisher), and qPCR was performed in duplicate with iTaq Universal SYBR green supermix (BioRad). Primer sequences were as follows: 5′-TTCACCATTGCCTTCTCTTC-3′ and 5′-CCCATTCTCATTACTGCTTC-3′ for viral NS1, 5′-CATGGCTCGCTCGGTGACC-3′ and 5′-AATGTGAGGCGGGTGGAACTG-3′ for housekeeping gene B2m. Expression levels of NS1 were normalized relative B2M control gene.

Bone marrow, blood and tissue cell isolation

Cell isolation was achieved as previously described [124,454]. Briefly, for BM cells, femurs were dissected and cleaned of soft adhering tissue. Distal and proximal ends were opened, and BM cells were flushed out. After centrifugation, cell pellets were re-suspended in ice-cold PBS containing 10mM EDTA and cell suspensions were filtered using a cell strainer (70 µM, Corning) to obtain a single cell suspension. Blood was collected from the tail vein in a 100 mM EDTA(Merck Millipore)-containing tube, and red blood cells were lysed with RBC lysis buffer (ThermoFischer). For the isolation of leucocytes and structural cells, lung vessels were perfused with 5ml PBS through the right ventricle and 1 ml of HBSS (Lonza) containing 0.5 UI dispase II (Sigma-Aldrich), 0.1mg ml^{-1} elastase (MedChemExpress), 0.075 mg ml^{-1} of DNAse (Roche) was injected i.t. before dissecting the lung and digesting it for 30 minutes at 37°C in the same digestion medium. After 30 minutes of digestion, lungs were cut into small pieces with razor blades and further digested for 30 minutes at 37°C in HBSS containing 5% vol/vol FBS (Thermo Fisher), 0.5 UI of dispase II, 0.05 mg ml^{-1} DNAse, 1mg ml^{-1} collagenase A (Roche).

After 30minutes, the cell suspension was flushed using a 18-gauge needle to dissociate aggregates. Ice-cold PBS containing 10mM EDTA was added to stop the digestion process and cell suspensions were filtered using a 70µm cell strainer. Residual red blood cells were lysed with RBC lysis buffer. In all experiments, the number of cells was counted using an automatic cell counter (iPrasense Norma XS).

Leucocyte isolation from the liver was obtained as described elsewhere. After being euthanized, mice were perfused with 10 ml of PSB in right ventricle, the liver middle lobe was dissected and the gallbladder removed. The liver was cut into small pieces with razor blade and digested in 10 ml HBSS supplemented with 0.2mg/ml of collagenase IV (ThermoFisher), 5U/ml of DNase I and 10% FBS at 37°C during 45 minutes in tube rotator. After incubation the homogenized liver solution was filtered through a 70µm cell strainer and washed with 10 ml of PBS 10mM EDTA and centrifuged at 50 rcf for 3 minutes. Aqueous phase was recovered, filtered in a new tube and centrifuged at 400 rfc for 5 minutes. Pellet was suspended in red blood cell lysis buffer, incubated during 2 minutes, then washed with 10 ml of PBS 10mM EDTA and counted using automatic cell counter (iPrasense Norma XS).

Annexin V/Propidium Iodide apoptosis assay

Annexin V/Propidium Iodide apoptosis assay was performed following Rieger et al. protocol. After lung cell isolation, cells were resuspended in Annexin V binding buffer (ThermoFisher) and $2x10^6$ cells were stained with Annexin V-APC and incubated on the dark for 15 minutes at room temperature. Cells were washed with 100 µl of Annexin V binding buffer and 2 µg/ml of PI (ThermoFisher) were added to each sample and incubated in the dark for 15 minutes at room temperature. After having been washed with 500µl of Annexin V buffer, cells were centrifuged and pellet, resuspended in fixative solution of 1% formaldehyde and incubated for 10 minutes on ice. Cells were then washed with PBS, centrifuged, resuspended in PBS supplemented in 50 µg/ml RNase A (Merck Millipore) and incubated for 15 min at 37°C. Cell suspension was washed with PBS, centrifuged and stained for leucocytes markers.

Flow cytometry

Staining reactions were performed in the dark at 4°C for 30 minutes with 2% v/v of Fc block (BD Biosciences) to avoid nonspecific binding. For intracellular stainings, extracellular-stained cells were fixed and permeabilized with the Foxp3/Transcription factor Staining Buffer Set (Thermo Fisher). For EdU stainings, extracellular-stained cells were permeabilized and stained using Click-iT EdU Alexa Fluor 488 Flow Cytometry Assay Kit (Thermo Fisher), according to the manufacturer's instructions.

Cell viability was assessed using 7-AAD (BD Bioscience) or Fixable Viability Dye eFluor™ 780 (Thermo Fisher). Cell suspensions was analysed with a FACSCANTO II or a LSRFortessa (BD Biosciences). Results were analyzed using FlowJo software (Tree Star). For scRNA-seq, transmission electron microscopy, cytologic examination and *ex vivo* experiments, lung myeloid cells were sorted using a FACSAria III (BD Biosciences) or Sony MA900.

In vivo treatments

For EdU incorporation experiments shown in fig. S3, A and B, mice were injected at day 10 post-IAV intraperitoneally (i.p.) with 1 mg EdU (Santa Cruz Biotechnology) in 200 µl PBS 4 h before sacrifice. For experiments addressing the lifespan of $Ly6G^+$ Macs (Fig. 2F), 1mg EdU was injected i.p. twice 5 hours apart at day 7 post-IAV, and EdU incorporation was evaluated in blood leucocytes at day 8 post-IAV. The incorporation of EdU in lung myeloid cells was evaluated at days 10, 14 and 17 post-IAV. Assessment of phagocytic activity was performed as previously described[12]. Briefly, isoflurane-anesthetized mice were instilled i.t. with 2.10^8 pHrodo™ Green E. coli BioParticules (Thermo Fisher) in 100 µl PBS. Lungs were harvested 3 h later for flow cytometry analyses.

Adoptive transfer of $Ly6G^+$Macs

$Ly6G^+$Macs were isolated from CD45.2 wild-type mice at day 10 p.i.. Lung cells suspention was enriched using the CD11b MicroBeads (Miltenyi Biotec) and FACS sorted using a Sony MA900 . Around $3x10^5$ $Ly6G^+$Macs resuspended in 50µl of sterile PBS were instilled in lightly isofluorane anesthetized *Maf/Mafb*^{MyeloKO} mice at days 8, 11, 13, 15 post-IAV. Control *Maf/Mafb*^{MyeloKO} mice and WT mice received PBS at the same time points.

Generation of BM (competitive) chimeras

CD45.2, CD45.1 or CD45.1/CD45.2 WT mice were anesthetized by i.p. injection of 200µl PBS containing ketamine (Nimatek, Dechra, 75mg kg^{-1}) and xylazine (Rompun, Bayer, 10mg kg^{-1}). When mentioned, the thoracic cavity was protected with a 0.6-cm-thick lead cover. Mice were irradiated with two consecutive doses of 6Gy 15 minutes apart. Once recovered from the anaesthesia, mice were reconstituted by intravenous (i.v.) administration of 2.10^6 BM cells from *Ms4a3*^{tdtom} or *Il4ra*$^{-/-}$ mice, for full chimeras. For mixed BM chimeras, mice were reconstituted i.v. with 2.10^6 BM cells consisting of a 1:1 mix of BM cells obtained from the following mice: *Ms4a3*^{tdtom}, *Ccr2*$^{-/-}$, *Cx3cr1*$^{GFP/+}$, *Il4ra*$^{-/-}$, or homozygous *Ly6g*^{CreERT2} mice *(*also called *Ly6g*$^{-/-}$ mice). GM-CSF dependency assay was obtained with the engrafment of a 1:1 mix of CD45.1 *Csf2ra*$^{-/-}$ and CD45.2 *Csf2ra*$^{+/+}$ BM donor cells kindly provided by C. Schneider (University of Zurich, Switzerland) in thorax-protected, lethally irradiated CD45.1/CD45.2 WT mice. From the day of irradiation, mice were treated for 4 weeks with 0.05mg ml^{-1} of enrofloxacin (Baytril, Bayer) in drinking water. Chimerism was assessed by flow cytometry in the blood 4 weeks after irradiation.

scRNA-sequencing and analyses

Mouse scRNA-seq analyses

Lung myeloid cells were FACS-sorted as living singlet $CD45^+$, $F4/80^+$ and/or $CD11b^+$ cells from lung single-cell suspensions pooled from 5 mock-infected and IAV-infected C57BL/6 male WT mice at day 10 post-IAV. For each sample, an aliquot of Trypan blue-treated cells was examined under the microscope for counting, viability and aggregate assessment following FACS sorting. Viability was above 90% for all samples and no aggregates were observed. Cell preparations were centrifuged and pellets were resuspended in calcium- and magnesium-free PBS containing 0.4mg ml^{-1} of UltraPure BSA (Thermo Fisher Scientific).

The 10X Genomics platform (Single Cell 3' Solution) was used. For library preparation, approximately 2,000 (Mock group) and 6,000 (IAV group) cells were loaded into the Chromium Controller, in which they were partitioned, their polyA RNAs captured and barcoded using Chromium Single Cell 3' GEM, Library & Gel Bead Kit v3 (10X Genomics). The cDNAs were amplified and libraries compatible with Illumina sequencers were generated

using Chromium Single Cell 3' GEM, Library & Gel Bead Kit v3 (10X Genomics). The libraries were sequenced on an Illumina NovaSeq sequencer on an SP100 cell flow (Read1: 28 cy, read2: 76 cy, index1: 10cy, index2: 10cy) at a depth of 50,000 reads per cell.

The Cell Ranger (v6.1.2) application (10x Genomics) was used to demultiplex the BCL files into FASTQ files (cellranger mkfastq), to perform alignment (to Cell Ranger mouse genome references 6.1.2 GRCm38/release 102), filtering and unique molecular identifier counting and to produce gene-barcode matrices.

Filtered matrix files were used for further scRNA-seq analyses with R Bioconductor (3.17) and Seurat (4.3.0) (31178118). Briefly, filtered matrices containing cell IDs and feature names in each sample were used to build a Seurat object. We performed quality control by filtering out the cells with less than 200 detected genes, the genes detected in less than three cells and the cells exhibiting more than 10% of mitochondrial genes. Gene counts in each sample were normalized separately by default method 'LogNormalize' with a scale factor of 10,000 and log transformation. Two thousand highly variable features were identified with the 'vst' method. After merging cells from all samples, cell contaminants were removed based on the expression of cell-specific genes, and 12 clusters were identified in the remaining cells using the FindClusters function (15 Principal Components [PC] included and a resolution of 0.7 was selected) and the differentially expressed genes (DEGs) were calculated using the FindAllMarkers function (Seurat package). ScRNA_seq datasets containing steady-state $CD64^+$ lung cells (GSE194021) were integrated with the lung myeloid cells of this study using FindIntegrationAnchors function (Seurat) with anchor.features = 2000.

Single-cell regulatory network inference and clustering analysis

To predict the potential active transcription factors, lung myeloid cells analyzed by scRNA-seg were subjected to SCENIC analysis [455]. The normalized counts, nFeature_RNA and nCount_RNA in the merged Seurat object were used for the initial SCENIC analysis. The genes expressed with a value of 3 in 0.1% of the cells and detected in 1% of the cells were kept, and coexpression network analysis was made with GENIE3 in the SCENIC package. To represent

the SCENIC results, the results of the '3.4_regulonAUC' output were added to the metadata of Seurat object so that regulon AUC scores could be plotted as a heatmap.

Slingshot and tradeSeq pseudotime trajectory analyses

To evaluate trajectory-based differential expression analysis, CD206$^-$ IMs, Ly6G$^+$ Macs, Ly6C$^+$ Mos, iMos, CD206$^+$ IMs and dying Macs were subjected to Slingshot analysis [456]. The trajectories along pseudotime were built using umap embedding from the Seurat object. To compare the expression patterns of DEGs across pseudotime, the counts matrix, pseudotime and cell weights calculated above were then used as input in fitGAM function (tradeSeq package) [457]. The association of average expression of each gene with pseudotime was tested using associationTest and the DEGs between IMs and Ly6G$^+$ Mac trajectories were calculated with the patternTest function. The value of the estimated smoother on a grid of pseudotimes was estimated for each DEG using predictSmooth. The 200 DEGs with the biggest FcMedian and waldStat>200 were annotated as 'changed genes', meaning that their expression patterns were different in IMs and Ly6G$^+$ Mac trajectories, while the 200 genes whose average expression was associated with pseudotime in both lineages were selected based on their Fold change and labeled as 'unchanged genes'. Genes whose expression patterns appeared to be influenced by a small number of cells behaving as outliers were manually removed. Finally, the scaled estimated smoothers calculated by predictSmooth were used to build heat maps with the ComplexHeatmap package [458].

Gene Set Enrichment Analyses (GSEA)

In order to analyse enrichment of published signatures in the scRNA-seq data, the normalized counts were used as expression datasets in GSEA. GSEA was carried out using the GSEA software (version 4.1.0) [459]. We used the hallmark gene sets from the Molecular Signatures Database (MSigDB) to test for enrichment. The analyses involved a gene set permutation method with 1,000 permutations to calculate the enrichment scores.

scRNA-seq of human BALF cells

Chromium Fixed RNA Profiling for multiplexed samples (10X Genomics) was used for scRNA-seq analysis of human BALF cells, allowing the storage of fixed cells and enabling analysis of multiple samples in one single GEM reaction. Fresh samples were directly fixed in a 4% formaldehyde solution after collection for storage at -80°C. For GEM creation, the Multiplex-compatible Chromium Next GEM Single Cell Fixed RNA Human Transcriptome Probe Kit including a Probe Barcode that permits sample multiplexing and subsequent demultiplexing was used. The Cell Ranger (v7.1.0) application (10x Genomics) was used to demultiplex the BCL files into FASTQ files (cellranger mkfastq), to perform alignment (to Cell Ranger human genome reference GRCh38-2020-A), filtering and unique molecular identifier counting and to produce gene-barcode matrices. Filtered matrix files were used for further scRNA-seq analyses. A total of 12 clusters were identified, with 15 PCs included and a resolution of 0.5.

Ly6G$^+$ Mac signature scoring

Orthologous genes of the Ly6G$^+$ Mac signature in humans were manually identified using the gene database of NCBI. The signature was then used to calculate the score for each cell using AddModuleScore function (Seurat). The scores were stored in the seurat object and plotted using FeaturePlot function.

Transmission electron microscopy

FACS-sorted myeloid cell populations or lung tissues from IAV-infected mice at day 10 post-IAV were fixed in 2.5% glutaraldehyde (diluted in Sorensen's buffer: 0.1 M Na2HPO4/NaH2PO4 buffer, pH 7.4) for 1h at 4 °C and postfixed for 30 min in 2% OsO4 (diluted in 0.1 M Sorensen's Buffer). After dehydration in graded ethanol, samples were embedded in Epon resin. Ultrathin sections obtained with a Reichert Ultracut S ultramicrotome (Reichert Technologies) were contrasted with 2% uranyl acetate and 4% lead citrate.

For ultrastructural analyses, random fields of cells were examined under a Jeol TEM JEM-1400 Transmission Electron Microscope at 80 kV, and photographed using an 11-megapixel camera system (Quemesa, Olympus).

Extracellular flux analysis

Oxygen consumption rate (OCR) was measured using Seahorse XF Cell Mito Stress Test (Agilent) according to manufacturer's recommendations and as described previously [460,461]. Briefly, Neu, IM-like cells and Ly6G+ Macs were FACS-sorted at day 10 post-IAV and seeded (10 10^4, 7 10^4 and 8 10^4 cells/well, respectively) in XFp mini-plates (Agilent) pre-coated with CellTak. Cells were kept in unbuffered serum-free DMEM supplemented with pyruvate (1mM), glutamine (2mM), glucose (10mM), at pH 7.4, 37 °C and ambient CO_2 for 1h before the assay. Analysis was performed using the XFp analyser (Seahorse Bioscience) as per manufacturer's instructions. Cells were sequentially challenged with 1 µM oligomycin, 1 µM carbonyl cyanide p-(trifluoromethoxy)phenylhydrazone (FCCP), and rotenone/antimycin mix (0.5 µM each). All results were normalized according to the cell number evaluated by Hoechst (2 mg/mL) incorporation after cold methanol/acetone fixation.

Spatial transcriptomic analyses using Digital Spatial Profiling (DSP)

Five-µm-thick formalin-fixed, paraffin-embedded (FFPE) sections were prepared using the protocol from NanoString Technologies. Briefly, 2 tissue slides, each containing 1 mock and 2 IAV samples harvested 10 days post-IAV, were analyzed. Slides were first stained with antibodies against CD68, Ly6G (clone 1A8), and DNA was visualized with 500 nM Syto83. Mouse Whole Transcriptome Atlas probes targeting more than 19,000 targets were hybridized, and slides were

loaded on the GeoMx DSP. Briefly, entire slides were imaged at x20 magnification, and Regions of Interest (ROIs) were chosen based on serial Hematoxylin & Eosin sections and on morphological markers to select lesional, perilesional and extralesional areas. ROIs were exposed to ultraviolet light, releasing the indexing oligos and collecting them in a 96-well plate for subsequent processing and sequencing, as described [462]. Raw count, third quartile (Q3)–normalized count data of target genes from ROIs were provided by the vendor, which were used as input to downstream analyses. Pairwise differential expression analysis between perilesional, lesional, extralesional and control ROIs were performed using the GeoMx Digital Spatial Profiler Data Analysis Suite (DSPDA version 3.0.0.111). The R script SpatialDecon [463] was loaded into the DSPDA and run using the Mouse Adult Lung profile matrix. For cell

signature scoring, the gene signatures were obtained from scRNA-seq data using the 20 most specific markers obtained using the FindAllMarkers function (Seurat package), genes were then ordered according to their average log_2FC. Lung myeloid cell signature scores were obtained from our oqn scRNA-seq datasets, while the AT2, primed AT2, DATPs and AT1 signature score were calculated from previously published data [464] using the same procedure. The signatures were then used to calculate the score for each cell type using the simpleScore function (singscore package) [465] on the ranked gene expression matrix.

Cytologic examination

Cytologic examination of FACS-sorted neutrophils, iMo, IM-like and Ly6G$^+$Macs at 10 days p.i. was performed on cytospin preparations stained with Hemacolor (Merck KgaA). Sections were examined with a Echo Revolve microscope.

Immunofluorescence

Immunofluorescence stainings of mouse lungs were performed as previously described[124]. Briefly, lungs from WT or *Cx3cr1*$^{GFP/+}$ mice were perfused with 5 ml PBS through the right ventricle then with 5 ml paraformaldehyde (PFA) 4% (Thermo Fisher) in PBS, and lungs were collected. Lungs were fixed for 4 h in 4% PAF at 4 °C, then cryoprotected overnight in 30% sucrose (VWR) in PBS at 4 °C, followed by embedding in optimal cutting temperature compound (OCT) (VWR) and stored at −80 °C.

For staining of lungs from *Cx3cr1*$^{GFP/+}$ mice (Fig. 3H), 7-µm-thick sections were left in a methanol 100% (Merck) bath at −20 °C for 20 min prior to be stained for 2h at room temperature with a rabbit anti-GFP antibody (ThermoFischer, dilution 1:200) and a rat anti-mouse Ly6G (BDBioscience, dilution 1:50). After washing samples with PBS, a secondary anti-rat AF594 (Invitrogen, dilution 1:1000) was added in blocking buffer and incubated for 2 h in the dark at room temperature.

For stainings of WT lungs (Fig. 3O and fig. S6), 7-µm-thick sections were left in a methanol 100% (Merck) bath at −20 °C for 20 min prior to be stained overnight at 4°C in blocking buffer (PBS with 0.3% Triton X-100 [Merck], 2% donkey serum [Merck]) with the following antibodies: rabbit anti-mouse pSPC (Abcam, dilution 1:200); rat anti-mouse Ly6G

(BDBioscience, dilution 1:50). After washing samples with PBS, secondary antibodies (anti-rabbit AF532; anti-rat AF594 [Invitrogen], dilutions 1:1000) were added in blocking buffer and incubated for 2 h in the dark at room temperature. Samples were washed with PBS and incubated with directly-coupled antibodies (eFluor570-Ki-67 [Invitrogen, dilution 1:200]; anti-mouse AF700-MHC-II [ThermoFischer, dilution 1:100]; anti-mouse Superbright432-Pdpn [ThermoFischer, dilution 1:200]) in blocking buffer for 6h at 4 °C.

Finally, all samples were washed one last time with PBS and were mounted with 10 µl ProLong Antifade reagent (Invitrogen) containing 0.1% Sytox blue nucleic acid stain (Invitrogen) on glass slides and stored at room temperature in the dark overnight.

For stainings of lung human tissues, lungs were FFPE and 4-µm-thick lung sections were cut for immunofluorescence staining. After deparaffinization and rehydration, tissue sections were boiled for 20 min in 10-mM citrate carbonate buffer for antigen retrieval (Zytomed) containing 0.05 % Tween (Acros Organics). Lung sections were permeabilized in PBS 0.5% Triton X-100 for 10 minutes. Samples were incubated with blocking buffer (PBS with 0.3% Triton, 2% BSA and 2% donkey serum [Sigma-Aldrich]) for 1h at room temperature and stained in blocking buffer with the primary antibody (rabbit anti-mouse CXCR4 [AbCam, dilution 1:50]) overnight at 4°C. After washing samples with PBS, slides were incubated with a secondary donkey anti-rabbit IgG antibody conjugated with AlexaFluor 532 (dilution 1:1000) for 1 hour followed by a PBS wash and a staining with AF649-conjugated anti-human CD68 antibody (SantaCruz) for 6 hours at 4°C. Finally, samples were mounted with 10 µl of ProLong Antifade reagent containing 0.1% Sytox blue nucleic acid on glass slides.

All images were acquired on an LSM 980 with Airyscan 2 inverted confocal microscope (Zeiss) using a LD C-Apochromat ×40/1.1 W objective and Zen Black software.

Histology

Seven-µm-thick sections from frozen lung tissues obtained from mock- and IAV-infected mice at day 20 post-IAV were mounted onto glass slides and stained with Hematoxylin & Eosin (H&E) or periodic-acid Schiff (PAS). The slides were scanned with an Axioscan 7 scanner (Zeiss, Germany). Whole slide images were analysed with an open-source automated software

analysis program for digital pathology (QuPath version 0.4.3). Briefly, lesional areas were determined manually and automated tissue detection was performed in the lesional area to correct for alveolar blank spaces. Thereafter, built-in algorithms for pixel classification of QuPath and machine learning were used on PAS sections and a threshold was determined to quantify % of mucus$^+$ cells within the lesional area.

***Ex vivo* experiments**

For *ex vivo* stimulation and co-culture experiments, single cell suspensions isolated from IAV-infected lungs of WT or *Ly6g*^{tdTom} mice at day 10 post-IAV were enriched in CD11b$^+$ cells by a magnetic-activated cell sorting (MACS) using CD11b MicroBeads (Myltenyi). Cells were then stained and FACS-sorted using the gating strategy shown in Fig. 1A. After sorting, cells were counted, spinned down, and either directly added to the co-culture with MLE-12 cells, or seeded in 96 wells at a concentration 5 10^4 cells/well in complete RPMI (ThermoFischer), containing 1mM sodium pyruvate, 1% v/v MEM non-essential amino acids, 50 U ml−1 Penicillin-Streptomycin and 10% v/v % FBS. For stimulation experiments, recombinant mouse GM-CSF (20 ng/mL, Peprotech), mouse M-CSF (20 ng/mL, Peprotech), mouse IL-4 (20 ng/mL, Peprotech) or mouse IL-13 (20 ng/mL, Peprotech) were added. When required, Cre-ERT2 activation was achieved by adding 0.02 mg ml^{-1} of 4-hydroxytamoxifen (Sigma-Aldrich). After 18 hours of culture, cell supernatants were collected (conditioned medium, CM) and cells were harvested for flow cytometry phenotyping. For the visualisation of tdTomato induction in tamoxifen-treated iMos from *Ly6g*^{tdTom} mice by confocal microscopy, iMos were seeded and cultured in 8-chambers slides (Nunc Lab-Tek II Chamber Slide system, Sigma) precoated with poly-D-lysin hydrobromide (Sigma). Cells were incubated in complete RPMI containing 0.02 mg ml^{-1} 4-hydroxytamoxifen and 20ng ml^{-1} GM-CSF or vehicle. Supernatants were removed and chambers were rinsed with PBS. Slides were then fixed with paraformaldehyde 10% for 10 minutes, rinsed twice with PBS and mounted with ProLong Antifade reagent with DAPI (ThermoFisher). Images were acquired as above.

Proteome profiler (R&D) was performed on CM from Ly6G$^+$Macs cultured for 18h in complete RPMI with or without 20ng ml^{-1} IL-4 and 20ng ml^{-1} IL-13 treatment. The assay was performed

following the manufacturer's instructions and was analysed using the Protein Array Analyzer plug-in for ImageJ.

Murine lung epithelial (MLE)-12 cells were cultured in DMEM/F12 (ThermoFisher) complemented with 1% Insulin-Transferrin-Selenium (ITS-G) (ThermoFisher), L-glutamine 2mM (ThermoFisher), FBS 2% and HEPES 10mM (ThermoFisher). Cells were incubated at 37 °C in a humidified atmosphere containing 5% CO2. Cells were passaged at 80–90% confluence using 0.05% Trypsin-EDTA (ThermoFisher). Experiments were performed with passage numbers ranging from 4 to 6. Scratch Wound Assay were performed using IncucyteS3 (Sartorius). MLE-12 cells were seeded in 96-well (Sartorius) at density of 4 10^4 cells/well and incubated 24h in DMEM/F12 medium. An open wound area was created in the cell monolayer using the IncuCyte ® Wound Maker tool, washed with PBS and subsequently co-cultured with 5 x 10^4 Neu, IM-like cells, iMos or Ly6G$^+$ Macs, or incubated with CM from unpulsed or IL-4/IL-13-pulsed Ly6G$^+$ Macs. Complete DMEM medium containing 20ng ml^{-1} IL-4 and 20ng ml^{-1} IL-13 was used as control. Cells were imaged after wounding every 3h using the IncuCyte live cell imaging system at x10 magnification. For each time point, relative wound closure was calculated using the Scratch Wound analyses pipeline of the IncuCyte software.

Human BALFs

The use of human BALF cells was approved in 2022 by the Ethics Reviewing Board of the University Hospital of Liege, Belgium (ref. 2022/159). The characteristics of the patients are summarized in Table S1. Human BALFs were processed directly after collection. For flow cytometry, the BALF was centrifuged at 1,400 rpm for 10 minutes. The cell pellet was suspended and filtered in a PBS solution containing 10 mM EDTA and red blood cells were lysed with RBC lysis buffer. Cells were stained as above, washed with PBS and fixed with PAF 4% in PBS during 20 min before being analyzed by a LSRFortessa (BD Biosciences). For scRNA-seq, see section *scRNA-seq of human BALF cells* above.

Statistical analysis

Graphs were prepared with GraphPad Prism 9 (GraphPad software) or R Bioconductor (3.5.1) [329]. No statistical methods were used to pre-determine sample sizes but our sample sizes are

similar to those reported in previous publications [124,239,454,466]. Data distribution was assumed to be normal when parametric tests were performed. Data from independent experiments were pooled for analysis in each data panel, unless otherwise indicated. No data were excluded from the analyses. Statistical analyses were performed with Prism 9 (GraphPad software), and with R Bioconductor (3.5.1) [329] and Seurat [467] for scRNA-seq data, respectively. The statistical analyses performed for each experiment are indicated in the respective figure legends. We considered a *P* value lower than 0.05 to be significant (*, $P < 0.05$; **, $P < 0.01$; ***, $P < 0.001$; ****, $P < 0.0001$; ns, not significant).

Data and code availability

Mouse and human scRNA-seq data have been deposited in the GEO and are available under GEO accession number GSE244765. All original codes have been deposited at Zenodo and are available via this link: https://zenodo.org/records/11354523.

Reagents and antibodies

Reagents	Source	Cat. number
5-Ethynyl-2′-deoxyuridine	Santa Cruz Biotechnology	sc-284628
(Z)-4-Hydroxytamoxifen	Sigma-Aldrich	H7904
10X RBC Lysis Buffer (Multi-species)	Thermo Fisher Scientific	15270658
2-Mercaptoethanol	Thermo Fisher Scientific	21985023
Acetaminophen	Sigma-Aldrich	A7085
Agilent Seahorse XF Base Medium	Agilent	102353-100
Binding Buffer for Annexin V	Thermo Fisher Scientific	BMS500BB
Bleomycin sulfate - 10 mg	BIO-CONNECT	HY-17565
CD11b MicroBeads, human and mouse	Miltenyi Biotec	130-097-142
Cell-Tak™ Cell and Tissue Adhesive, 1 mg	Corning	354240
Click-iT™ Plus EdU Alexa Fluor™ 488 Flow Cytometry Assay Kit	Thermo Fisher Scientific	C10632
Collagenase A	Roche	10103578001
Collagenase IV	Thermo Fisher Scientific	17104019
Dispase® II protease	Sigma-Aldrich	D4693-1G
DMEM/F-12, no phenol red	Thermo Fisher Scientific	21041025
DNase I	Roche	11284932001
Donkey serum	Sigma-Aldrich	D9663
DPBS	Thermo Fisher Scientific	14190094
eBioscience™ Foxp3 / Transcription Factor Staining Buffer Set	Thermo Fisher Scientific	00-5523-00
Elastase from porcine pancreas	MedChemExpress	HY-P2974
Epoxy Embedding Medium kit	Sigma-Aldrich	45359
Fetal Bovine Serum	Thermo Fisher Scientific	A3160801
Formaldehyde, Extra Pure, Solution 37-41%, SLR, Fisher Chemical™	Thermo Fisher Scientific	F/1501/PB15
Hanks Balanced Salt Solution (HBSS)	Lonza	10-508F
Hemacolor	Sigma-Aldrich	111674
HEPES (1 M)	Thermo Fisher Scientific	15630080
Incucyte® Imagelock 96-well Plate	Sartorius	BA-04856
Insulin-Transferrin-Selenium (ITS -G) (100X)	Thermo Fisher Scientific	41400045
iTaq Universal SYBR Green Supermix	BioRad	1725120
L-Glutamine (200 mM)	Thermo Fisher Scientific	25030081
MEM Non-Essential Amino Acids Solution (100X)	Thermo Fisher Scientific	11140050
Méthanol	MerkMillipore	67-56-1

Milieu RPMI 1640		Thermo Fisher Scientific	21875091
Nimatek		Dechra	804132
Nunc® Lab-Tek® Chamber Slide™ system		Sigma-Aldrich	C7182
Penicillin-Streptomycin (10,000 U/mL)		Thermo Fisher Scientific	15140122
pHrodo™ Green E. coli BioParticles™ Conjugate for Phagocytosis		Thermo Fisher Scientific	P35366
Poly-D-lysine hydrobromide		Sigma-Aldrich	P6407
ProLong™ Diamond Antifade Mountant		Thermo Fisher Scientific	P36961
ProLong™ Gold Antifade Mountant with DNA Stain DAPI		Thermo Fisher Scientific	P36931
Propidium Iodide		Thermo Fisher Scientific	P1304MP
Proteome Profiler Mouse XL Cytokine Array		R&D	ARY028
Recombinant Murine GM-CSF		Preprotech	315-03
Recombinant Murine IL-13		Preprotech	210-13
Recombinant Murine IL-4		Preprotech	214-14
Recombinant Murine M-CSF		Preprotech	315-02
RevertAid First Strand cDNA Synthesis Kit		Thermo Fisher Scientific	K1621
RNase A Solution		Merck Millipore	70856
Rompun Sol Inj 2%		Bayer	76901
Sucrose		VWR	57-50-1
SYTOX™ Blue Nucleic Acid Stain		Thermo Fisher Scientific	S11348
Tissue-Tek® O.C.T. Compound		VWR	4583
Titriplex® III		Merck Millipore,	1084181000
TRITON® X-100 Detergent		Merck Millipore	648466
Trypsin-EDTA (0.05%), phenol red		Thermo Fisher Scientific	25300062
Tween 20		Acros Organics	AC233360010
UltraPure™ BSA (50 mg/mL)		Thermo Fisher Scientific	AM2616
Zytomed Systems HIER Citrate Buffer pH 6,0 (10 X)		Zytomed	ZUC028-500
Antibodies (Mouse)			
Annexin V	APC	Thermo Fisher Scientific	A35110
Arg 1	APC	Thermo Fisher Scientific	17-3697-82
CD115	APC	Invitrogen	17-1152-82
CD11b	BUV395	BD Bioscience	563553
CD11b	APC	Thermo Fisher	17-0112-83
CD11c	APC-Cy7	BD Bioscience	561241
CD124 (IL4Ra)	PE	BD Bioscience	561695
CD170 (Siglec F)	PE	BD Bioscience	552126

CD170 (Siglec F)	FITC	Biolegend	155503
CD184 (CXCR4)	APC	Thermo Fisher	17-9991-82
CD31	APC	Thermo Fisher	17-0311-82
CD326 (Epcam)	BV510	BD Bioscience	563216
CD45.1	APC	BD Bioscience	558701
CD45.2	V500	BD Bioscience	562129
CD45.2	BUV395	BD Bioscience	564616
CD45.2	FITC	BD Bioscience	561874
CD64	BV421	Biolegend	139309
Cmaf	PE	Thermo Fisher	12-9855-42
CXCR4	Purified	AbCam	ab124824
F4/80	BV650	Biolegend	123149
Ki-67	eFluor™ 570,	Thermo Fisher	41-5698-82
Ly-6C	Texas Red	BD Bioscience	562728
Ly-6G	PE/Cy7	BD Bioscience	560601
Ly-6G	Purified	BD Bioscience	551559
MHC II (IA/IE)	Alexa Fluor 700	Thermo Fisher	56-5321-82
MHC II (IA/IE)	Percp Cy5.5	Sony	1138130
Osteopontin	PE	R&D	IC808P
Podoplanin	Superbright 436	Thermo Fisher	62-5381-82
Prosurfactant Protein C antibody	Purified	AbCam	ab211326
Secondary antibodies			
Goat anti-Rabbit IgG (H+L) Cross-Adsorbed Secondary Antibody,	Alexa Fluor™ 532	Invitrogen	A-11009
Goat anti-Rabbit IgG (H+L) Highly Cross-Adsorbed Secondary Antibody	Alexa Fluor™ 488	Invitrogen	A-11034
GFP Polyclonal Antibody	Alexa Fluor™ 488	Invitrogen	A-21311

2 Results

2.1 Lung Ly6G$^+$ Macs emerge in the early recovery phase post-IAV infection

To investigate the dynamic of myeloid cell responses after lung injury, we performed time-course flow cytometry studies in a clinically relevant mouse model of lung infectious injury following IAV infection [468]. Eight to twelve weeks-old C57BL/6 wild-type (WT) mice were infected intranasally (i.n.) with 5 plaque-forming units (PFU) of IAV H1N1 strain PR8/34, which triggered self-limiting disease with a peak in viral RNA at day 5 post-IAV and viral clearance at day 10 post-IAV (fig. S1, A and B). In this model, Ly6G$^+$CD11b$^+$CD64$^-$ neutrophils (Neu) increased at day 5 post-IAV and returned to baseline by day 15 (Fig. 1, A and B). A partial loss of Ly6G$^-$CD64$^+$SiglecF$^+$CD11c$^+$ AM was observed between day 5 and day 10 post-IAV, which was restored at day 15 post-IAV, as described [227] (Fig. 1, A and B). The numbers of CD64$^-$Ly6C$^-$ monocytes (Ly6C$^-$ Mo) remained stable over the course of infection, unlike those of classical CD64$^-$Ly6C$^+$ Mo (Ly6C$^+$ Mo) and inflammatory CD64$^+$Ly6C$^+$ monocytes (iMo) that peaked around day 5 post-IAV (Fig. 1, A and B). Macrophages (Macs) resembling IM (IM-like), defined as F4/80$^+$CD11b$^+$Ly6G$^-$SiglecF$^-$Ly6C$^-$CD64$^+$ cells and likely encompassing resident IM and recruited Mo-Macs, increased over time (Fig. 1, A and B). We also observed emergence, from day 5 onwards, of a distinct population of IAV-triggered Ly6G$^+$CD11b$^+$CD64$^+$ Macs that fell in the classical Ly6G$^+$CD11b$^+$ neutrophil gate but were clearly distinct from neutrophils based on their elevated CD64 expression (Fig. 1, C and D), which we call Ly6G$^+$ Macs hereafter. Ly6G$^+$ Macs were absent in the blood (Fig. 1E), peaked at day 10 post-IAV in the lung and could still be detected at days 15 and 20 post-IAV (Fig. 1D). Morphologically, Ly6G$^+$ Macs analyzed at day 10 post-IAV exhibited a kidney-shaped nucleus, like iMo, and possessed numerous cytoplasmic vacuolated structures and a cell membrane rich in protrusions (Fig. 1F and fig. S1C). Phenotypically, Ly6G$^+$ Macs were F4/80^{hi}SiglecF^{lo}CD11c^{lo} (fig. S1, D and E) and expressed high levels of the chemokine receptor CXCR4, of type II major histocompatibility complex (MHC-II), of CD101 and of CD319, a regulator of Mac functions [469,470] (Fig. 1, G and H).

However, Ly6G$^+$ Macs exhibited low expression of the neutrophil activation marker CD177 (Fig. 1, G and H).

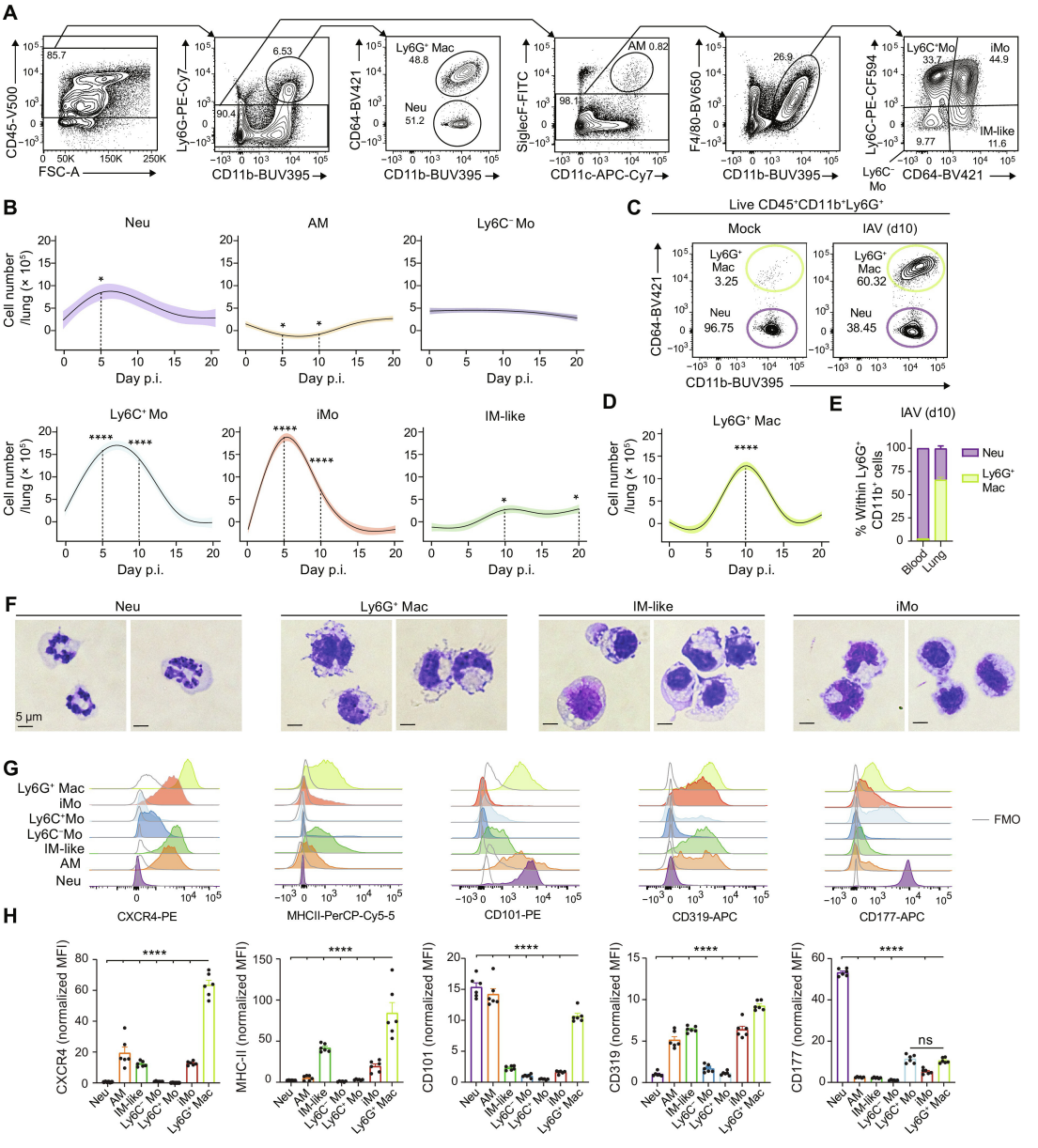

Fig. 1. Ly6G$^+$ Macs culminate during the early recovery phase post-IAV infection

(**A**) Representative flow cytometry gating strategy showing live CD45$^+$CD11b$^+$Ly6G$^+$CD64$^-$ neutrophils(Neu),CD45$^+$CD11b$^+$Ly6G$^+$CD64$^+$macrophages(Ly6G$^+$Mac),CD45$^+$Ly6G$^-$CD11c$^+$SiglecF$^+$alveol armacrophages(AM),CD45$^+$Ly6G$^-$SiglecF$^-$F4/80$^+$CD11b$^+$Ly6C$^+$CD64$^-$monocytes(Ly6C$^+$Mo),CD45$^+$Ly6G$^-$S iglecF$^-$F4/80$^+$CD11b$^+$Ly6C$^-$CD64$^-$monocytes(Ly6C$^-$Mo), CD45$^+$Ly6G$^-$SiglecF$^-$F4/80$^+$CD11b$^+$Ly6C$^+$CD64$^+$ inflammatory monocytes (iMo) and CD45$^+$Ly6G$^-$SiglecF$^-$F4/80$^+$CD11b$^+$Ly6C$^-$CD64$^+$ IM-like cells in lungs

of C57BL/6 wild-type (WT) mice at day 10 post-IAV. (**B**) Time course of absolute numbers of Neu, AM, Ly6C$^-$ Mo, Ly6C$^+$ Mo, iMo and IM-like cells quantified by flow cytometry at days 0, 5, 10, 15 and 20 post-IAV in WT mice. (**C**) Representative contour plots of CD64 and CD11b expression within lung CD45$^+$CD11b$^+$Ly6G$^+$ cells at day 10 p.i. in mock-infected or IAV-infected WT mice. (**D**) Time course of absolute numbers of Ly6G$^+$ Macs quantified by flow cytometry, as in (B). (**E**) Percentage of Neu and Ly6G$^+$ Macs within Ly6G$^+$CD11b$^+$ cells quantified by flow cytometry in the blood and lungs of WT mice at day 10 post-IAV. (**F**) Photographs of Neu, Ly6G$^+$ Macs, IM-like cells and iMo sorted by FACS from IAV-infected WT mice at day 10 p.i.. Pictures are representative of 1 of 3 independent sorting experiments, each giving similar results. (**G**) Representative histograms of CXCR4, MHC-II, CD101, CD319 and CD177 expression in the indicated myeloid cell populations, quantified by flow cytometry at day 10 post-IAV in WT mice. (**H**) Quantification of expression of the indicated markers, as in (G). (B,D) Data show mean (centerline) ± SEM (colored area) and are pooled from 2-3 independent experiments (*n*=6 mice per time point); (E,H) mean + SEM and are pooled from 2 independent experiments (*n*=5-6 mice). (B,D,H) *P* values were calculated using a one-way ANOVA with Dunnett's post hoc tests. *, *P*<0.05; ***, *P*<0.001; ****, *P*<0.0001. FMO, fluorescence minus one; ns, not significant; p.i., post-infection. (F) Scale bars: 5 μm.

Next, we performed single cell (sc) RNA-sequencing (scRNA-seq) analyses of lung myeloid cells at day 10 post-IAV. Lung CD45$^+$F4/80$^+$ and/or CD11b$^+$ cells were sorted from five mock-infected and 5 IAV-infected mice and were subjected to sc droplet encapsulation [471], scRNA-seq and quality control filtering. The curated data were integrated with a published dataset of steady-state lung monocytes and IM[124] and projected to global and condition-specific uniform manifold approximation and projection (UMAP) plots (Fig. 2A). Myeloid cells from mock-infected mice mainly comprised clusters annotated as AM (*Chil3, Ear1, Fapb1*; C6), Ly6C$^-$ Mo (*Ace, Nr4a1, Fcgr4*; C3), Ly6C$^+$ Mo (*Ccr2, Ly6c2*; C4) and dendritic cells (DC; *H2-Ab1, Cd209a, Flt3;* C9) (Fig. 2A-C and fig. S2A). Few cycling Macs (*Birc5, Top2a, Mki67*; C11) were also detected in mock-infected mice, along with few CD206$^-$ IM (*C1qa, C1qc, H2-Ab1, Cd74, Tmem119;* C1) and CD206$^+$ IM (*C1qa, C1qc, Mrc1, Maf;* C8) [124] (Fig. 2A-C and fig. S2A). Ten days post-IAV, AM (C6) disappeared, a small cluster of IAV-associated AM was present instead (*Chil3, Ear1, Ear 2*; C12), Neu were recruited (*S100a8, S100a9, Mmp9*; C7), and IM (C1, C8) and iMo (*Ccr2, Ly6c2, Irf7*; C5) expanded (Fig. 2A-C and fig. S2A). Of note, clusters C2 and C10 were specifically triggered by IAV. C10 had an elevated content in mitochondrial genes and low numbers of detected genes (fig. S2B) and was therefore annotated as dying Macs. C2 expressed significantly higher levels of cathepsins (*Ctsb, Ctsz*), galectins (*Lgals1, Lgals3*), Arginase-1 (*Arg1*) and osteopontin (*Spp1*) as compared to the other clusters (Fig. 2D).

Intracellular flow cytometry staining for Arginase-1 and osteopontin showed that the combined expression of these two proteins was restricted to Ly6G$^+$ Macs at day 10 post-IAV (Fig. 2, E and F), supporting that C2 corresponded to Ly6G$^+$ Macs identified by flow cytometry. Of note, Ly6G$^+$ Macs expressed high levels of *Csf1r* and *Slamf7* (coding for CD319) but did not express any of the neutrophil-related transcripts *Csf3r*, *S100a8, S100a9, Mmp8, Mmp9, Mpo, Slpi* or *Cd177* (fig. S2, A and C). *Ly6g* transcripts were not detectable in Neu nor Ly6G$^+$ Macs (fig. S2, A and C). Ly6G$^+$ Macs (C2) displayed both "M1-like" or "M2-like" signature scores and genes and could not be categorized as such on the basis of their expression profile (fig. S2, D and E). Together, our data show that a phenotypically and transcriptionally distinct subset of Ly6G$^+$ Macs emerges during a specific time window corresponding to early weight recovery post-IAV.

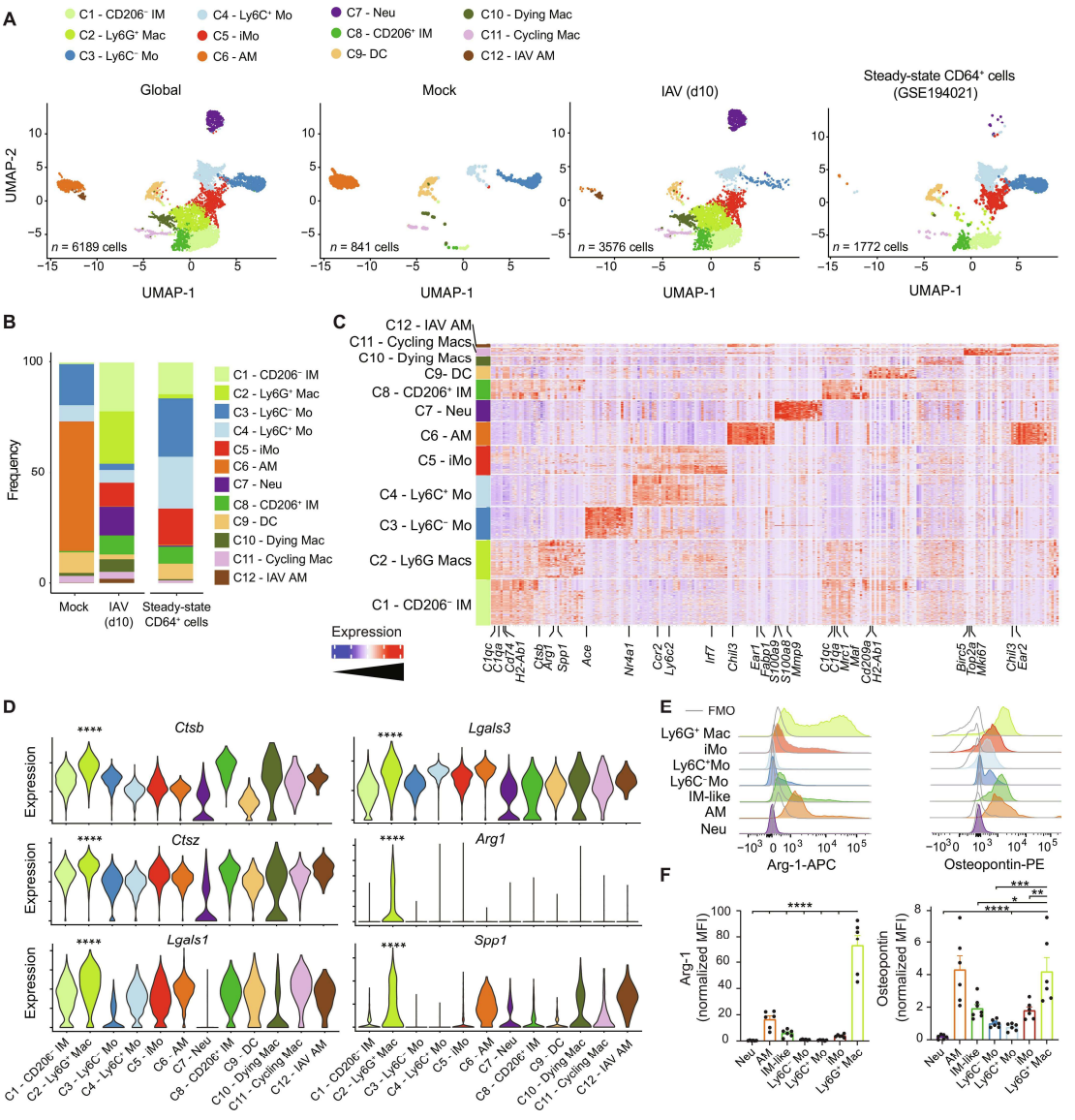

Fig. 2. Ly6G⁺ Macs are transcriptionally distinct from other lung myeloid cells at day 10 post-IAV

(A) UMAP plots of scRNA-seq data depicting the transcriptional identity of FACS-sorted lung live CD45⁺F4/80⁺ and/or CD11b⁺ cells from mock- or IAV-infected WT mice 10 days p.i. (pooled from 5 mice per conditions), merged with a published dataset of steady-state lung monocytes and IMs[124]. (**B**) Frequency of each cluster within each experimental condition, as in (A). (**C**) Heatmap depicting the single cell expression of the most upregulated genes within each cluster. (**D**) Expression of the indicated genes within each cluster, as depicted by violin plots (height: expression; width: abundance of cells). (**E**) Representative histograms of intracellular Arg-1 and osteopontin expression in the indicated lung myeloid cell populations, quantified by flow cytometry at day 10 post-IAV in WT mice. (**F**) Quantification of Arg-1 and osteopontin expression, as in (E). (F) Data show mean + SEM and are pooled from 2 independent experiments (*n*=6 mice). *P* values were calculated using (D) a Wilcoxon rank sum test and

compare C2 vs. all other clusters or (F) a one-way ANOVA with Dunnett's post hoc tests. *, $P<0.05$; **, $P<0.01$; ***, $P<0.001$; ****, $P<0.0001$. FMO, fluorescence minus one; p.i., post-infection.

2.2 Ly6G$^+$ Macs arise from recruited monocytes and are partially dependent on GM-CSF receptor signaling

We next investigated the origin of Ly6G$^+$ Macs and asked whether they could expand via local proliferation. We observed that the percentage of cells positive for the proliferation Ki67 was very low in Ly6G$^+$ Macs (fig. S3A). Next, we treated mice at day 10 post-IAV intraperitoneally (i.p.) with 5-ethynyl-2′-deoxyuridine (EdU) 4 hours before analysis. While the percentage of EdU$^+$ cells was higher in AM compared to all other lung myeloid cells, indicative of active proliferation, virtually no EdU$^+$ cells were detected in Ly6G$^+$ Macs, ruling out their active proliferation (fig. S3, B and C). Third, we assessed whether Ly6G$^+$ Macs arose from the BM or from local progenitor monocytes[240]. We generated chimeric mice in which lethally irradiated, thorax-protected CD45.2 WT mice were reconstituted with BM cells from *Ms4a3*^{Cre}*R26*$^{LSL\text{tdTomato}}$ mice (subsequently referred to as *Ms4a3*^{tdTom}), in which the progeny of granulocyte monocyte progenitors (GMPs) is constitutively labelled [235]. At week 4 after transfer, the percentages of tdTomato$^+$ blood Ly6C$^+$ Mo was around 50%, while the percentages of tdTomato$^+$ lung AM and IM were very low, confirming efficient reconstitution and thorax protection (fig. S3, D-G). At day 10 post-IAV, we found that the percentage of tdTomato$^+$ Ly6G$^+$ Macs was similar to that of Ly6C$^+$ Mo (fig. S3, H and I), consistent with a major contribution of BM-derived GMPs, but not local progenitors, to Ly6G$^+$ Macs.

The kinetics of Ly6G$^+$ Mac emergence post-IAV was comparable but delayed compared to that of Ly6C$^+$ Mo and iMo, consistent with the idea that recruited Ly6C$^+$ Mo could give rise to Ly6G$^+$ Macs. Supporting this, Slingshot trajectory analyses of the scRNA-seq data identified two main trajectories starting from Ly6C$^+$ Mo, transiting through iMo to give rise to either IM-like cells or Ly6G$^+$ Macs [456] (Fig. 3A). Genes that exhibited the same pattern of downregulation along pseudotime in each trajectory encompassed the classical monocyte-associated genes *Ccr2* and *Ly6c2* (Fig. 3B). We also found, in both trajectories, a time-restricted upregulation of interferon-stimulated genes (*Ifi209, Ifitm3, Ifi47, Isg15*) that likely corresponded to

transitioning iMo (Fig. 3B). Finally, trajectory-specific genes were gradually and specifically upregulated along pseudotime in the IM-like (e.g., *C1qa, C1qc, C1qb, Mrc1, Cd74, H2-Ab1, H2-Eb1*) or the Ly6G$^+$ Mac (e.g., *Arg1, Spp1, Ccl2, Ccl7, Ctsb*) trajectories (Fig. 3B).

Next, we infected the monocyte fate-mapper mice *Ms4a3^{tdTom}* [235] and *Cx3cr1^{GFP}* [82] with IAV and found that, at day 10 post-IAV, Ly6G$^+$ Macs were Tomato$^+$ and GFP^{hi}, respectively, consistent with their GMP-derived monocytic origin (Fig. 3, C and D). To address the dependency of Ly6G$^+$ Mac on Ccr2-dependent BM-derived Ly6C$^+$ Mo [472], we generated BM competitive chimeras in which lethally irradiated CD45.1/CD45.2 WT mice were engrafted with a 1:1 mix of CD45.2 *Ccr2$^{-/-}$* and CD45.2 *Ms4a3^{tdTom}* BM cells. At week 4 after reconstitution, most blood Ly6C$^+$ Mo were of donor Tomato$^+$ origin, as expected (fig. S3, J and K) [472]. At day 10 post-IAV, the majority of Ly6G$^+$ Macs was also of donor *Ms4a3^{tdTom}* origin, indicating their dependency on Ccr2 (Fig. 3, E and F).

We next sought to assess the fate and lifespan of Ly6G$^+$ Macs. The abundance of Ly6G$^+$ Macs during a limited time window post-IAV suggested that they might be short-lived. In line with this, trajectory analyses in Fig. 3A suggested that Ly6G$^+$ Macs (C2) gave rise to Macs with low RNA content (C10) (fig. S2B). We performed EdU pulse experiments at day 7 post-IAV and found that Ly6G$^+$ Macs staining positive for EdU at day 10 post-IAV were completely cleared from the lung at day 17 (Fig. 3G). Annexin V/Propidium iodide (PI) staining at day 10 post-IAV further supported that Ly6C$^+$ Mo transitioning to iMo and differentiating into Ly6G$^+$ Macs became progressively more sensitive to death, with a substantial portion of Ly6G$^+$ Macs being either early or late apoptotic (Annexin V$^+$/PI$^{+/-}$), or necrotic (Annexin V$^-$/PI$^+$) (Fig. 3H and fig. S3L). Hence, our data show that Ly6G$^+$ Macs represent a short-lived Mac subset arising from Ccr2-dependent Ly6C$^+$ Mo.

The Ly6G signal on Ly6G$^+$ Macs, considered to be neutrophil-specific, was unexpected and required careful validation. First, we verified that the Ly6G fluorescence intensity was virtually absent in unstained or isotype antibody (Ab)-stained CD11b$^+$ cells from IAV-infected WT mice (fig. S4A). Second, we evaluated whether Ly6G$^+$ Mac precursors, namely iMo, could intrinsically upregulate Ly6G on their surface when isolated from the lungs of IAV-infected

mice at day 10 post-IAV. We found that iMo from IAV-infected mice and stimulated *ex vivo* with GM-CSF, and to a less extent with M-CSF, upregulated Ly6G protein on their surface (Fig. 3, I and J). Importantly, we also found that lung iMo isolated from IAV-infected *Ly6g*^{CreERT2}*R26*^{LSL}tdTomato mice (*Ly6g*^{tdTom}) treated with tamoxifen and stimulated with GM-CSF ex vivo became tdTomato$^+$, indicative of active *Ly6g* gene transcription in monocytic cells (Fig. 3, K and L). These data demonstrate that Ly6G can be actively expressed by Mo-Macs.

Given the ability of GM-CSF to trigger Ly6G expression on lung iMo isolated from IAV-infected mice, we assessed the dependency of Ly6G$^+$ Macs on GM-CSF receptor signaling *in vivo*. We generated BM competitive chimeras in which thorax-protected, lethally irradiated CD45.1/CD45.2 WT mice were engrafted with a 1:1 mix of CD45.1 *Csf2ra*$^{-/-}$ and CD45.2 *Csf2ra*$^{+/+}$ BM donor cells. At week 4 after reconstitution, blood Neu and Mo of donor origin arose equally from CD45.1 *Csf2ra*$^{-/-}$ and CD45.2 *Csf2ra*$^{+/+}$ BM cells (fig. S4, B and C). At day 10 post-IAV, we found that CD45.2 *Csf2ra*$^{+/+}$ BM cells had a competitive advantage over CD45.1 *Csf2ra*$^{-/-}$ BM cells to become Ly6G$^+$ Macs, which was not observed among most other lung myeloid cells (Fig. 3M and fig. S4C-E), and the percentage of Arg-1$^+$ cells was lower in *Csf2ra*$^{-/-}$ Ly6G$^+$ Macs as compared to *Csf2ra*$^{-/-}$ Ly6G$^+$ Macs (Fig. 3, N and O), indicating their partial dependency on GM-CSF receptor signaling.

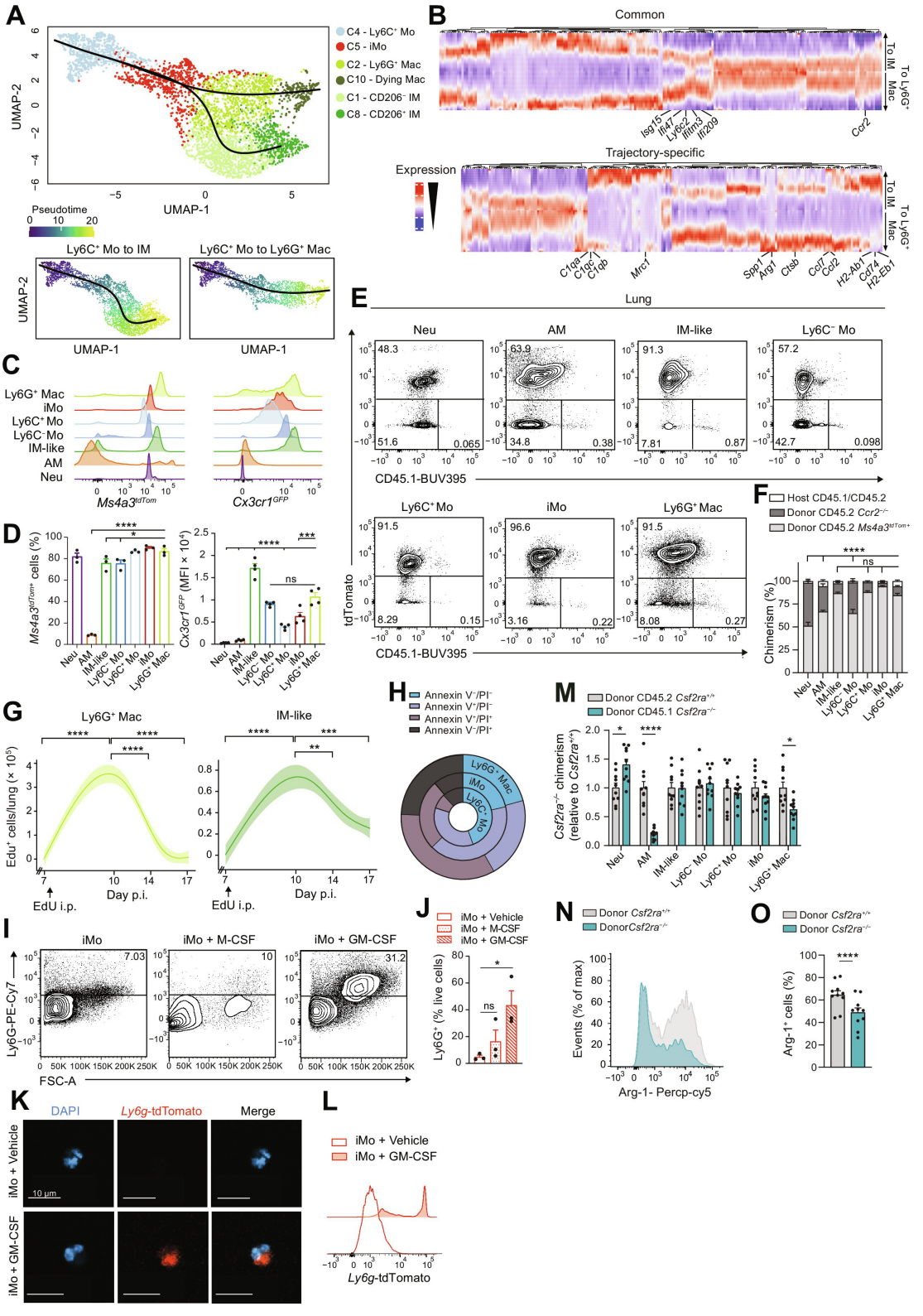
A
UMAP-2
UMAP-1
Pseudotime
C4 - Ly6C⁺ Mo
C5 - iMo
C2 - Ly6G⁺ Mac
C10 - Dying Mac
C1 - CD206⁻ IM
C8 - CD206⁺ IM
Ly6C⁺ Mo to IM
Ly6C⁺ Mo to Ly6G⁺ Mac
B
Common
To IM
To Ly6G⁺ Mac
Isg15
Ifit47
Lyve2
Ifitm3
Ifi209
Ccr2
Trajectory-specific
Expression
C1qa
C1qc
C1qb
Mrc1
Spp1
Arg1
Ctsb
Ccl7
Ccl2
H2-Ab1
Cd74
H2-Eb1
C
Ly6G⁺ Mac
iMo
Ly6C⁺ Mo
Ly6C⁻ Mo
IM-like
AM
Neu
Ms4a3tdTom
Cx3cr1GFP
D
Ms4a3tdTom+ cells (%)
Cx3cr1GFP (MFI x 10⁴)
ns
E
Lung
Neu
AM
IM-like
Ly6C⁻ Mo
Ly6C⁺ Mo
iMo
Ly6G⁺ Mac
CD45.1-BUV395
tdTomato
F
Host CD45.1/CD45.2
Donor CD45.2 Ccr2⁻/⁻
Donor CD45.2 Ms4a3tdTom+
Chimerism (%)
G
Ly6G⁺ Mac
IM-like
Edu⁺ cells/lung (× 10⁵)
Day p.i.
EdU i.p.
H
Annexin V⁻/PI⁻
Annexin V⁺/PI⁻
Annexin V⁺/PI⁺
Annexin V⁻/PI⁺
I
iMo
iMo + M-CSF
iMo + GM-CSF
Ly6G-PE-Cy7
FSC-A
J
iMo + Vehicle
iMo + M-CSF
iMo + GM-CSF
Ly6G⁺ (% live cells)
K
DAPI
Ly6g-tdTomato
Merge
iMo + Vehicle
iMo + GM-CSF
10 µm
L
iMo + Vehicle
iMo + GM-CSF
Ly6g-tdTomato
M
Donor CD45.2 Csf2ra+/+
Donor CD45.1 Csf2ra−/−
Csf2ra−/− chimerism (relative to Csf2ra+/+)
N
Donor Csf2ra+/+
DonorCsf2ra−/−
Events (% of max)
Arg-1- Percp-cy5
O
Donor Csf2ra+/+
Donor Csf2ra−/−
Arg-1⁺ cells (%)

Fig. 3. IAV-triggered Ly6G$^+$ Macs are recruited from classical monocytes and are short-lived. (**A**) UMAP plot depicting the transcriptional identity and cell trajectories (top), and pseudotime trajectory values (below) of lung Ly6C$^+$ Mo, iMo, Ly6G$^+$ Mac, dying Mac, CD206$^-$ IM and CD206$^+$ IM, as in Fig. 2A, evaluated by Slingshot trajectory analyses. (**B**) Heatmap plot depicting the differentially expressed genes along pseudotime evaluated by tradeSeq in the trajectory starting from Ly6C$^+$ Mo and ending either in IM or in Ly6G$^+$ Mac. (**C**) Representative histograms of tdTomato (left) and GFP (right) expression in the indicated myeloid cell populations, quantified by flow cytometry at day 10 post-IAV in *Ms4a3^{tdTom}* and *Cx3Cr1^{GFP}* mice, respectively. (**D**) Quantification of tdTomato$^+$ cells (left) and GFP expression (right), as in (C). (**E**) Representative tdTomato and CD45.1 contour plots and (**F**) bar graph showing % of host, donor *Ccr2$^{-/-}$* and donor *Ms4a3^{tdTom+}* chimerism in the indicated cell populations from lethally-irradiated CD45.1/CD45.2 mice reconstituted with a 1:1 mix of CD45.2 *Ccr2$^{-/-}$* and *Ms4a3^{tdTom+}* BM cells, infected with IAV 4 weeks later and evaluated at day 10 post-IAV. (**G**) Time course of absolute numbers of EdU$^+$ Ly6G$^+$ Macs and EdU$^+$ IM-like cells quantified by flow cytometry at days 7, 10, 14 and 17 post-IAV in EdU-pulsed WT mice at day 7 post-IAV. (**H**) Pie chart representation of the mean frequency of Annexin V and PI negative and/or positive fractions within lung Ly6C$^+$ Mo, iMo and Ly6G$^+$ Macs, quantified at day 10 post-IAV in WT mice. (**I**) Representative Ly6G and FSC contour plots and (**J**) bar graph showing % of Ly6G$^+$ cells within lung iMo sorted from WT mice at day 10 post-IAV and cultured 18 hours *ex vivo* with vehicle, M-CSF or GM-CSF. (**K**) Representative confocal microscopy pictures and (**L**) representative flow cytometry histograms of tdTomato expression within lung iMo sorted from *Ly6g^{tdTom}* mice at day 10 post-IAV and treated *ex vivo* with tamoxifen and GM-CSF or vehicle for 18 hours. (**M**) Bar graph showing donor *Csf2ra$^{-/-}$* chimerism relative to donor *Csf2ra$^{+/+}$* chimerism in the indicated cell populations from thorax-protected, lethally-irradiated CD45.1/CD45.2 mice reconstituted with a 1:1 mix of CD45.1 *Csf2ra$^{-/-}$* and CD45.2 *Csf2ra$^{+/+}$* BM cells, infected with IAV 4 weeks later and evaluated at day 10 post-IAV. (**N**) Representative histograms and (**O**) quantification of Arg-1$^+$ cells (%) in Ly6G$^+$ Macs from donor *Csf2ra$^{+/+}$* and *Csf2ra$^{-/-}$* BM cells, as in (M). Data show (D,F,J,M,O) mean + SEM and (D,F) are representative of 1 of 3 independent experiments (*n*=3-4 mice), (J) are pooled from 3 independent sorting experiments, each dot representing one biological replicate, (M,O) are pooled from 2 independent experiments (*n*=10 mice); (G) mean (centerline) ± SEM (colored area) and are pooled from 2 independent experiments (*n*=6 mice per time point). *P* values compare CD45.2 donor *Ccr2$^{-/-}$* chimerism in (F). *P* values were calculated using (D) a one-way ANOVA with Dunnett's post hoc tests, (F) a two-way ANOVA with Tukey's post hoc tests, (G,J) a one-way ANOVA with Tukey's post hoc tests, (M) a two-way ANOVA with Sidak's post hoc tests, (O) a two-tailed Student's *t* test. *, *P*<0.05; ***, *P*<0.001; ****, *P*<0.0001. FMO, fluorescence minus one; ns, not significant.

2.3 Ly6G$^+$ Macs exhibit distinct ultrastructural features associated with elevated metabolic and phagocytic abilities

Gene Set Enrichment Analyses (GSEA) of the transcriptomic profile of Ly6G$^+$ Macs (C2) compared to all other clusters identified a response to interferon-□ and cytokines, chemotactic and viral processes, an active metabolic state, a highly developed endomembrane system and elevated phagocytic abilities in Ly6G$^+$ Macs (Fig. 4A). We

analyzed FACS-sorted Ly6G$^+$ Macs by transmission electron microscopy at day 10 post-IAV and found that they exhibited a kidney-shaped nucleus, microvilli-rich membrane, secretory granules and a cytoplasm rich in rugous endoplasmic reticulum (RER), Golgi apparatus, lysosomes and autophagy vacuoles, distinguishing them from Neu, Ly6C$^+$ Mo and IM-like cells (Fig. 4B). The morphology of Ly6G$^+$ Macs was reminiscent to that of an atypical population of monocytes, called SatM monocytes, which arise from particular GMPs during the fibrotic phase in lungs post-bleomycin, contribute to fibrosis and were regulated by CCAAT/enhancer binding protein β (C/EBPβ) [437]. We conducted a single-cell regulatory network inference and clustering (SCENIC) analysis [455] and found that C/EBPβ activity was lower in Ly6G$^+$ Macs compared to Ly6C$^-$ Mo, Ly6C$^+$ Mo, iMo and Neu (fig. S5A). Moreover, we generated a SatM signature score based on the genes unregulated in SatM monocytes[437], mapped such score to our scRNA-seq data and found that Ly6G$^+$ Macs displayed a lower SatM score compared to IM, Ly6C$^+$ Mo, Ly6C$^-$ Mo or iMo (fig. S5, B and C), supporting that Ly6G$^+$ Macs are not dependent on C/EBPβ and are transcriptionally distinct from SatM monocytes[437].

Next, we characterized the metabolic profile of Ly6G$^+$ Macs using a metabolic flux assay and found that the extracellular acidification rate (ECAR) was higher in Ly6G$^+$ Mac compared to IM-like cells, both at baseline and under stress, supporting that the glycolytic pathway was highly active in Ly6G$^+$ Macs (Fig. 4C). Moreover, while the basal mitochondrial oxygen consumption rate (OCR) was similar between Ly6G$^+$ Mac and IM-like cells, the OCR under stress conditions was higher in Ly6G$^+$ Macs compared to IM-like cells (Fig. 4D), supporting that they possessed a high metabolic potential (Fig. 4E).

We administered infected mice with fluorescently-labeled E. coli particles intratracheally (i.t.) at day 10 post-IAV and confirmed that Ly6G$^+$ Macs were highly

phagocytic compared to Neu, Ly6C$^+$ Mo, IM-like cells and AM (Fig. 4, F and G). Hence, we asked whether Ly6G$^+$ Macs could perform efferocytosis *in vivo*. To this end, we infected BM competitive chimeras in which lethally irradiated CD45.2 WT mice were engrafted with a 1:1 mix of *Cx3cr1*$^{GFP/+}$ and *Ms4a3*^{tdTom} BM cells. Of note, at day 10 post-IAV, 60% of *Cx3cr1*$^{GFP/+}$ Ly6G$^+$ Macs were also tdTomato$^+$ (Fig. 4, H and I and fig. S6, A-C), demonstrating that they were highly potent in engulfing myeloid cells *in vivo.* To assess whether Ly6G molecules could be transferred from Neu to Ly6G$^+$ Macs during efferocytosis, we infected BM competitive chimeras in which lethally irradiated CD45.1/CD45.2 WT mice were engrafted with a 1:1 mix of *Cx3cr1*$^{GFP/+}$ cells and *Ly6g*$^{-/-}$ (i.e., homozygous *Ly6g*^{CreERT2} mice) [450] or *Ly6g*$^{+/+}$ BM cells. At day 10 post-IAV, we found that the levels of Ly6G on *Cx3cr1*$^{GFP+}$ Ly6G$^+$ Macs from *Cx3cr1*$^{GFP+}$: *Ly6g*$^{-/-}$ BM chimeric mice, in which half of the Neu were *Ly6g*$^{-/-}$, were similar to those from *Cx3cr1*$^{GFP+}$: *Ly6g*$^{+/+}$ BM chimeric mice, supporting no evidence for a Ly6G transfer from Neu to Ly6G$^+$ Macs (fig. S6, D and E). Together, these data show that IAV-triggered Ly6G$^+$ Macs are characterized by metabolic, morphological and efferocytic properties distinct from other lung myeloid cells.

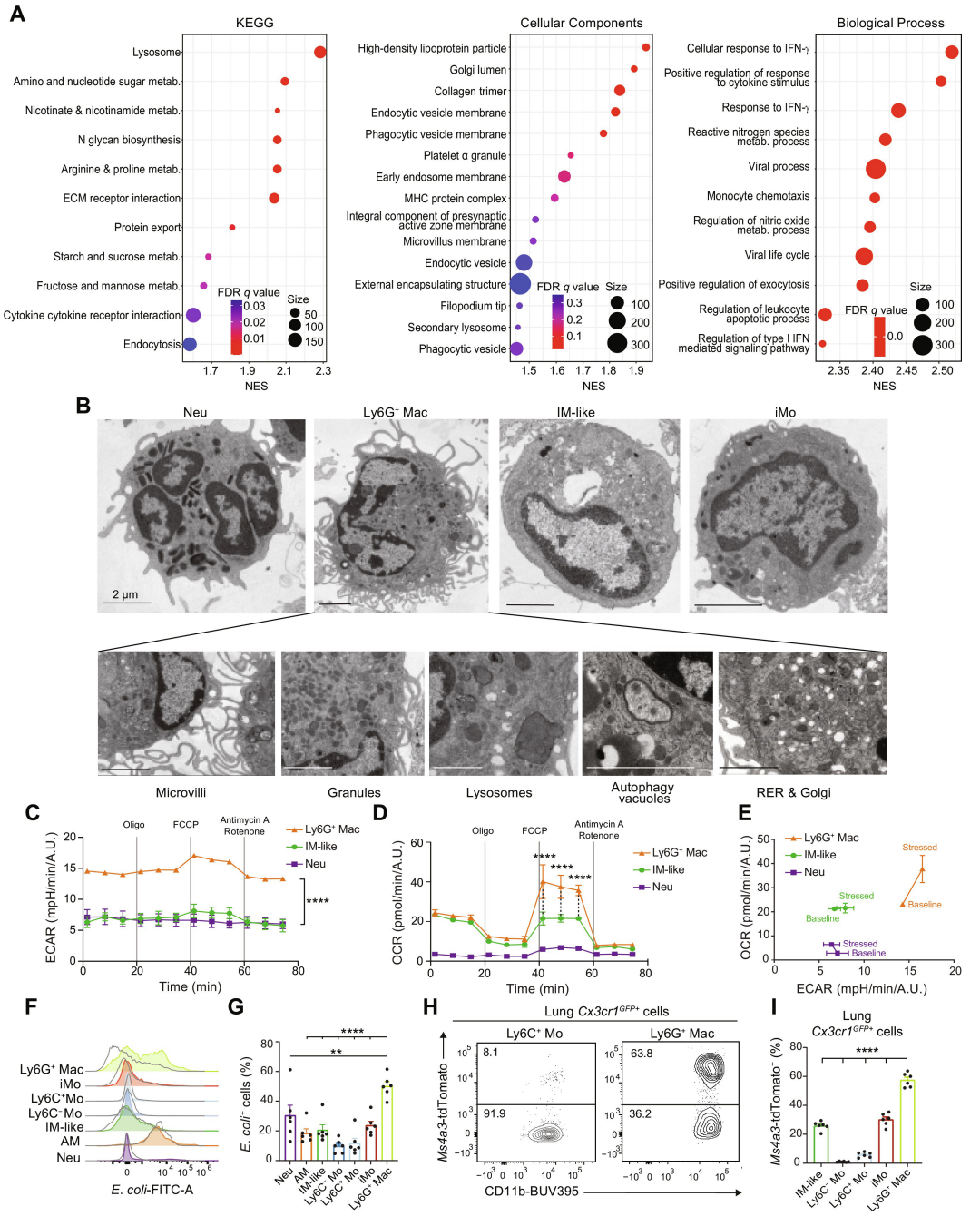

Fig. 4. Ly6G⁺ Macs exhibit an atypical morphology and possess distinct metabolic, phagocytic and efferocytic capabilities.

(**A**) GSEA analyses of Ly6G⁺ Mac (C2) profile compared to other clusters using KEGG, Cellular Components and Biological Process gene sets. The Normalized Enrichment Score (NES), False Discovery Rate (FDR) and the size of the gene set are shown for each process. (**B**) Representative transmission

electron microscopy pictures of Neu, Ly6G$^+$ Mac, IM-like cells and iMo FACS-sorted from lungs of WT mice at day 10 post-IAV. (**C**) Extracellular acidification rate (ECAR) of FACS-sorted Ly6G$^+$ Mac, Neu and IM-like cells, as in (B), quantified at baseline and under stress over time using a Seahorse assay. (**D**) Oxygen consumption rate (OCR) of Ly6G$^+$ Mac, Neu and IM-like cells, as in (C). (**E**) ECAR and OCR of Ly6G$^+$ Macs, Neu and IM-like cells, as in (C,D). (**F**) Representative histograms of E. coli-FITC signal in the indicated myeloid cell populations, quantified by flow cytometry at day 10 post-IAV and 3 hours after i.t. injection of E. coli-FITC particles. Non-injected mice were used as controls (grey line). (**G**) Quantification of E. coli-FITC$^+$ cells, as in (F). (**H**) Representative tdTomato and CD11b contour plots of and (**I**) bar graph showing % of tdTomato$^+$ cells in the indicated *Cx3cr1*$^{GFP+}$ donor cell populations from lethally-irradiated CD45.2 WT mice reconstituted with a 1:1 mix of CD45.2 *Cx3cr1*$^{GFP+}$ and *Ms4a3*$^{tdTom+}$ BM cells, infected with IAV 4 weeks later and evaluated at day 10 post-IAV. Data show (C,D) mean ± SEM and are representative of 1 of 3 independent experiments, each giving similar results; (G,I) mean + SEM and are pooled from 2 independent experiments (n=6 mice). P values (C,D) compare Ly6G$^+$ Macs vs. IM-like cells or Neu and were calculated using a two-way ANOVA with Bonferroni's post hoc tests; (G,I) were calculated using a one-way ANOVA with Dunnett's post hoc tests. **, P<0.01; ****, P<0.0001. (B) Scale bars: 2 µm.

2.4 Ly6G$^+$ Macs populate the alveolar lumen of perilesional regenerating areas

Next, we investigated the localization and the spatial organization of Ly6G$^+$ Macs. First, we performed confocal microscopy staining of lung sections of infected *Cx3cr1*^{GFP} mice at day 10 post-IAV. By defining Ly6G$^+$ Macs as cells double positive for Ly6G and GFP, we found that they were located in the alveolar lumen (Fig. 5A), which was also confirmed by *in situ* electron microscopy (Fig. 5B).

To further investigate the spatial distribution of Ly6G$^+$ Macs and the molecular signatures of Ly6G$^+$ Macs-rich areas, we performed spatial transcriptomic analyses using GeoMx Digital Spatial Profiler (DSP), which allows whole-genome transcript analyses within regions of interest (ROIs). Lung sections from 2 mock- and 4 IAV-infected mice were collected at day 10 post-IAV, stained with anti-CD68 and anti-Ly6G antibodies, and ROIs were selected in control lungs (4 ROIs), extralesional zones (4 ROIs), intralesional zones (5 ROIs) and zones rich in Ly6G$^+$CD68$^+$ cells that were mostly located in the periphery of consolidated areas (perilesional, 11 ROIs) (Fig. 5C and fig. S7A). Unsupervised principal component (PC) analysis showed that perilesional ROIs

were separated from the other regions (Fig. 5D). Volcano plot representation of the differentially expressed (DE) genes between conditions and the heatmap of the 522 significantly upregulated genes in perilesional areas compared to the other areas supported that perilesional areas were transcriptionally very active (fig. S7, B and C). General cellular deconvolution indicated that perilesional zones were also enriched in tissue Macs as compared to the other regions (fig. S7D). We next mapped cell signature scores of lung myeloid cell populations analyzed by scRNA-seq to the ROIs and confirmed that perilesional zones were enriched in Ly6G$^+$ Mac compared to the other zones (Fig. 5E and fig. S7E). GSEA analyses indicated that perilesional areas were enriched in biological responses related to cytoskeleton activity, epithelial cell migration and elevated metabolic activity compared to intralesional areas, consistent with intense remodeling activities (Fig. 5F).

Next, we took advantage of a publicly available scRNA-seq dataset of alveolar epithelial cell states present during alveolar regeneration after bleomycin-induced lung injury [464] and containing type 1 and type 2 alveolar epithelial cells (AT1 and AT2, respectively), as well as transitional states appearing during AT2 to AT1 differentiation, called primed AT2 and damage-associated transient progenitors (DATPs) [464]. By mapping the signature scores of such transitional epithelial cell states to the ROIs, we found that Ly6G$^+$ Mac-rich perilesional zones were enriched in primed AT2 and DATPs compared to control and intralesional zones (fig. S7, F and G). Accordingly, the Ly6G$^+$ Mac score correlated positively with those of primed AT2 and DATPs (Fig. 5G). We also confirmed by confocal microscopy that Ly6G$^+$ Macs were particularly abundant in the periphery of consolidated areas and clustered with AT2 cells, while intralesional consolidated areas, which exhibited low levels of staining for AT1 and AT2, contained few Ly6G$^+$ Macs (Fig. 5H and fig. S8). Altogether, these data are consistent with perilesional areas serving as the site of active epithelial

regeneration post IAV, and that Ly6G$^+$ Macs, which cluster in such areas, contribute to this process

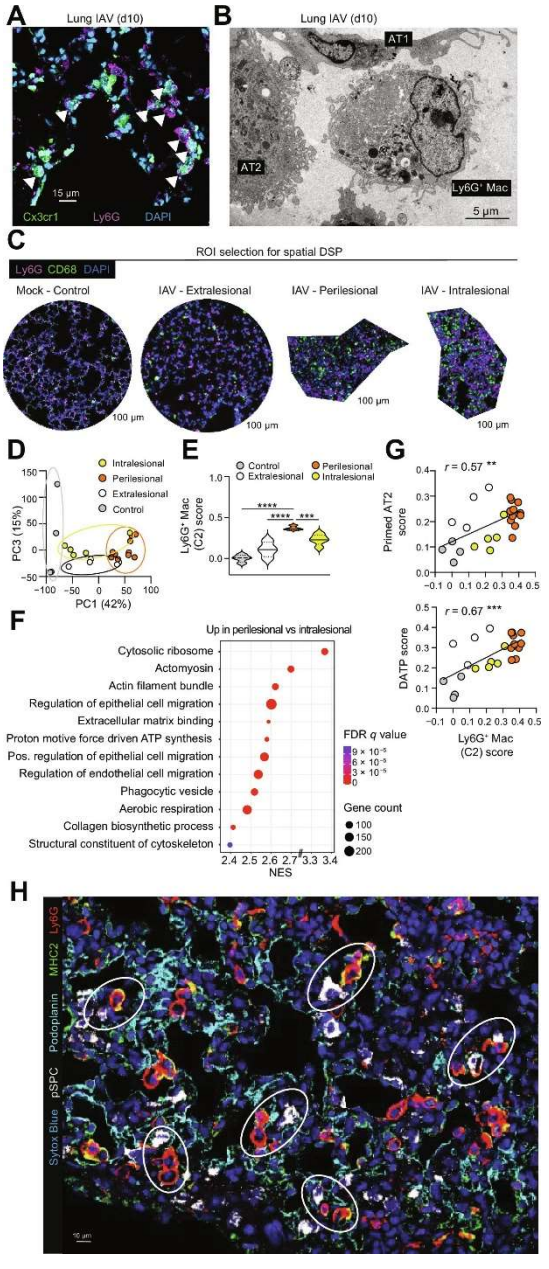

Fig. 5. Ly6G$^+$ Macs populate the alveoli of perilesional regenerating areas.

(**A**) Representative confocal microscopy picture of lung sections from *Cx3cr1^{GFP}* mice at day 10 post-IAV, with Ly6G$^+$ Macs identified as Ly6G$^+$*Cx3cr1^{GFP+}* cells. (**B**) Representative *in situ* electron microscopy picture of Ly6G$^+$ Macs in the vicinity of AT2 and AT1 cells, identified on lung sections from WT mice at day 10 post-IAV. (**C**) Representative examples of regions of interest (ROIs) selected on lung sections from mock- or IAV-infected WT mice at day 10 post-IAV stained with anti-Ly6G and anti-CD68 antibodies. (**D**) Unsupervised Principal Component (PC) analysis of the ROIs analyzed by DSP. Percentages indicate the variability explained by each component. (**E**) Ly6G$^+$ Mac signature score within control, extralesional, perilesional and intralesional ROIs, as depicted by violin plots (height: scores; width: abundance of cells). (**F**) GSEA analysis of perilesional ROIs compared to intralesional ROIs using Cellular Components, Molecular Function and Biological Process gene sets. The Normalized Enrichment Score (NES), False Discovery Rate (FDR) and the size of the gene set are shown for each process. (**G**) Correlation of Ly6G$^+$ Mac score with primed AT2 (top) and DATP (bottom) scores of the ROIs. (**H**) Representative picture of perilesional Ly6G$^+$ Macs (i.e., Ly6G$^+$MHC-II$^+$ cells), pSPC$^+$ AT2 and podoplanin$^+$ AT1 identified by confocal microscopy on lung sections from WT mice at day 10 post-IAV. (A,B,H) Pictures are representative of one of 6 mice, each giving similar results. (E) *P* values were calculated using a one-way ANOVA with Tukey's post hoc tests. (G) The correlation analysis used was parametric Pearson correlation coefficient. **, $P<0.01$; ***, $P<0.001$. Scale bars: (A) 15, (B) 5, (C) 100, (D) 10 µm.

2.5 Ly6G$^+$ Macs promote alveolar epithelial regeneration through IL-4R signaling

To formally assess the function of Ly6G$^+$ Macs *in vivo*, we aimed to generate a transgenic mouse strain in which Ly6G$^+$ Mac differentiation was impaired. Thus, we applied the SCENIC algorithm to our scRNA-seq data to map gene regulatory networks and predict transcription factor activities in Ly6G$^+$ Macs [455]. Of note, c-Maf and MafB exhibited a high regulon activity in Ly6G$^+$ Macs and IM-like cells, as described[124], but not in other lung myeloid cells (Fig. 6A and fig. S9). Elevated c-Maf and MafB protein levels were also detected in Ly6G$^+$ Macs at day 10 post-IAV by flow cytometry (Fig. 6, B and C), and *Maf* and *Mafb* transcript levels were elevated in lung Ly6G$^+$ Mac-rich perilesional areas of IAV-infected mice (Fig. 6D). We generated mice with myeloid-restricted *Maf* and *Mafb* deficiency by crossing *Maf* and *Mafb* floxed mice (*Maf*/*Mafb*$^{fl/fl}$) with mice constitutively expressing Cre recombinase under the control of the lysozyme M promoter (*Lyz2*^{Cre}), called *Maf/Mafb*^{MyeloKO} mice hereafter. At day 10 post-IAV, *Maf/Mafb*^{MyeloKO} mice showed a virtual absence of Ly6G$^+$ Macs, while numbers of Neu, AM, IM-like cells, Ly6C$^+$ Mo and iMo were similar and numbers of Ly6C$^-$ Mo were higher compared to control mice (Fig. 6E). Hence, we employed this model to address the consequences of Ly6G$^+$ Mac deficiency on viral control, morbidity and alveolar epithelial repair following IAV infection.

We assessed the levels of lung mRNA coding for the non-structural influenza protein NS1 post-IAV and found that they were not significantly different between *Maf/Mafb*^{MyeloKO} and controls and returned to baseline at day 10 post-IAV (Fig. 6F), supporting that Ly6G$^+$ Macs did not substantially influence host viral control. However, *Maf/Mafb*^{MyeloKO} mice lost more weight post-IAV compared to controls (Fig. 6G), suggestive of a more severe IAV-induced pathology. Histopathological analyses of lung sections at day 20 post-IAV indicated broader lesional areas in *Maf/Mafb*^{MyeloKO}

mice compared to controls, as well as more pronounced dysplastic repair and bronchiolization of the alveoli, based on quantification of mucus area in lung lesional areas (Fig. 6H-J). These results suggested that, in the absence of Ly6G$^+$ Macs, the classical pathway of alveolar epithelial regeneration involving progenitor AT2 expansion and differentiation towards AT1 [230,473] was defective and compensated by dysplastic repair. Next, we evaluated the numbers of AT1, AT2 and regenerating AT2 (regAT2) at day 20 post-IAV in *Maf/Mafb*^{MyeloKO} and control mice by flow cytometry and observed a significant decrease in the numbers of AT2 and regAT2 in *Maf/Mafb*^{MyeloKO} mice compared to controls (Fig. 6, K and L), confirming that AT2 were less able to expand and differentiate into AT1 in the absence of Ly6G$^+$ Macs. Of note, i.t. transfer of Ly6G$^+$ Macs isolated from lungs of WT mice at day 10 post-IAV into IAV-infected *Maf/Mafb*^{MyeloKO} mice partially improved weight recovery and restored numbers of AT2 to the levels observed in IAV-infected control mice (Fig. 6, M and N). These results suggest that Ly6G$^+$ Macs are key players of euplastic epithelial regeneration after IAV-induced lung injury.

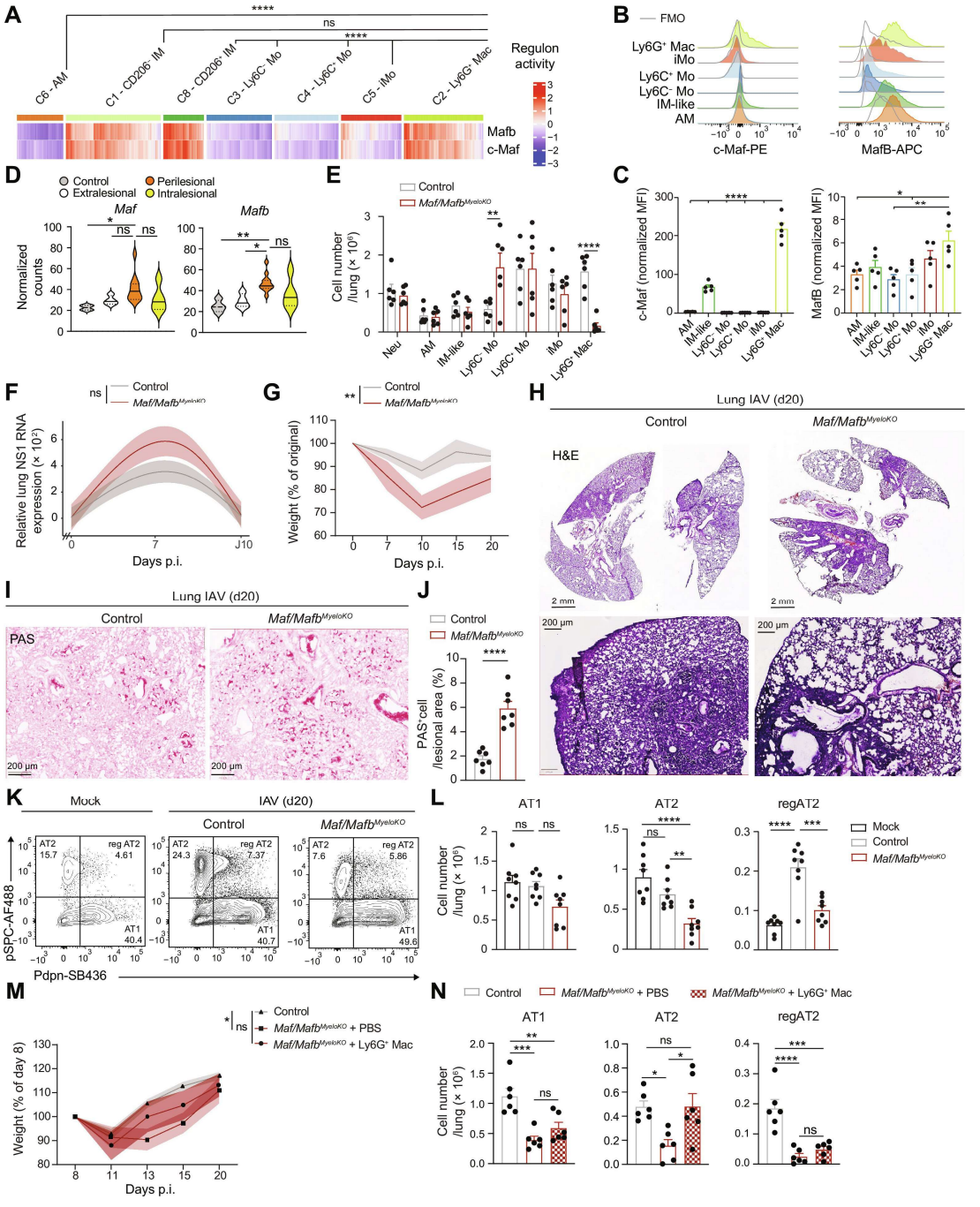

Fig. 6. C-Maf/MafB-dependent Ly6G$^+$ Macs promote euplastic alveolar epithelial regeneration.

(**A**) Heatmap depicting predicted activities of c-Maf and MafB across lung myeloid cells post-IAV, evaluated by SCENIC analysis of the scRNA-seq data, as in Fig. 2A. (**B**) Representative histograms of intracellular c-Maf and MafB expression in the indicated lung myeloid cell populations, quantified at day 10 post-IAV. (**C**) Quantification of expression of intracellular c-Maf and MafB, as in (B). (**D**)

Expression of *Maf* and *Mafb* within control, extralesional, perilesional and intralesional ROIs, as depicted by violin plots (height: normalized counts; width: abundance of cells). (**E**) Absolute numbers of the indicated lung myeloid cell populations, quantified at day 10 post-IAV in control and *Maf/Mafb*^{MyeloKO} mice. (**F**) Time course of relative lung NS1 RNA expression, assessed by RT-qPCR at days 0, 7 and 10 post-IAV in control and *Maf/Mafb*^{MyeloKO} mice. (**G**) Time course of weight, expressed as the % of the original weight at day 0 and assessed at days 0, 7, 10, 15, 20 post-IAV in control and *Maf/Mafb*^{MyeloKO} mice. (**H-I**) Representative (H) Hematoxylin & Eosin and (I) Periodic Acid Schiff (PAS, bottom) pictures of lung sections of control and *Maf/Mafb*^{MyeloKO} mice at day 20 post-IAV. Pictures are representative of 1 of 7 mice analyzed. (**J**) Percentage of PAS$^+$ cells in lung lesional areas of control and *Maf/Mafb*^{MyeloKO} mice at day 20 post-IAV. (**K**) Representative pSPC and Pdpn contour plots of CD45$^-$ CD31$^-$EpCam$^+$ cells in mock- or IAV-infected mice at day 20 post-IAV. (**L**) Absolute numbers of pSPC$^+$Pdpn$^-$ AT2, pSPC$^-$Pdpn$^+$ AT1 and pSPC$^+$Pdpn$^+$ regenerating AT2 (reg AT2), quantified as in (K). (**M**) Time course of weight, expressed as the % of the original weight at day 8 and assessed at days 8, 11, 13, 15 and 20 post-IAV in control mice, in *Maf/Mafb*^{MyeloKO} mice instilled i.t. at days 8, 11, 13 and 15 post-IAV with PBS or with 3 x 10^5 Ly6G$^+$ Macs isolated from WT mice at day 10 post-IAV. (**N**) Absolute numbers of pSPC$^+$Pdpn$^-$ AT2, pSPC$^-$Pdpn$^+$ AT1 and pSPC$^+$Pdpn$^+$ regenerating AT2 (reg AT2), quantified at day 20 post-IAV, as in (M). (C,E,J,L,N) Data show mean + SEM and are pooled from 2 independent experiments (C:*n*=5 mice; E,N: *n*=6 mice/group; J: *n*=7 mice/group; L: *n*=8 mice/group). (F,G,M) Data show mean (centerline) ± SEM (colored area) and are pooled from 2-3 independent experiments (F: *n*=10 mice/group; G: *n*=7 mice/group; M: *n*=6 mice/group). *P* values were calculated using (A) a Wilcoxon rank sum test, (C) a one-way ANOVA with Dunnett's post hoc tests, (D,L) a one-way ANOVA with Tukey's post hoc tests, (E,F,G,M) a two-way ANOVA with Sidak's post hoc tests, (J) a two-tailed Student's *t* test, *, *P<0.05;* **, *P*<0.01; ***, *P*<0.001; ****, *P*<0.0001. FMO, fluorescence minus one; ns, not significant; p.i., post-infection. Scale bars: (H, top) 2 mm, (H, bottom; I) 200 µm.

To determine whether Ly6G$^+$ Mac-rich perilesional areas were imprinted by a type 2 reparative environment [274,474,475], we mapped a type 2 signature score based on genes involved in IL-4 receptor downstream signaling pathways to the DSP spatial transcriptomic data and found that perilesional areas exhibited the highest type 2 score as compared to the other ROIs (Fig. 7A). Hence, we asked whether IL-4 receptor signaling, whose activation is known to induce a repair phenotype in Macs [274,474,475], was involved in Ly6G$^+$ Mac identity and function. First, we found that Ly6G$^+$ Macs expressed high levels of the IL-4 receptor □ chain (IL-4Rα) (Fig. 7, B and C). Next, we generated BM competitive chimeras in which lethally irradiated CD45.1/CD45.2 WT mice were engrafted with a 1:1 mix of CD45.2 *Il4ra*$^{-/-}$ and CD45.2 *Ms4a3*^{tdTom} BM cells. At week 4 after reconstitution, efficient BM reconstitution was confirmed in the blood (fig. S10, A and B). At day 10 post-IAV, we found that Ly6G$^+$ Macs of donor *Ms4a3*^{tdTom}

origin exhibited a competitive advantage over those of donor *Il4ra*$^{-/-}$ origin, which was not observed among other lung myeloid cells (Fig. 7D and fig. S10, C and D), and the remaining *Il4ra*$^{-/-}$ Ly6G^{+} Macs were impaired in their ability to express Arg-1 (Fig. 7, E and F). Finally, WT chimeric mice fully reconstituted with *Il4ra*$^{-/-}$ or WT BM cells were generated (*Il4ra*$^{-/-}$ BM -> WT or WT BM -> WT, respectively) and infected with IAV. We found, like in *Maf/Mafb*^{MyeloKO} mice, that *Il4ra*$^{-/-}$ BM -> WT mice had an impaired recovery post-IAV compared to WT BM -> WT mice (Fig. 7G). These data suggest that Ly6G^{+} Macs exert their function via IL-4R-dependent pathways, at least in part.

Finally, we asked whether Ly6G^{+} Macs could directly influence AT2 fate and whether cell-cell contacts were needed. To this end, we performed a scratch assay *in vitro* using the MLE-12 mouse AT2 cell line and evaluated the confluence of AT2 cells 12 hours post-scratch in the presence or absence of Ly6G^{+} Macs isolated from infected lung at day 10 post-IAV. Co-culture with Ly6G^{+} Macs, but not with Neu, IM-like cells or iMo was associated with an increase in cell confluence (Fig. 7H), indicating that Ly6G^{+} Macs can directly and specifically promote wound healing in vitro. A similar scratch assay was also performed using conditioned medium (CM) from FACS-sorted Ly6G^{+} Macs that were cultured overnight with or without the type 2 cytokines IL-4 and IL-13. In this setting, CM from IL-4/13-pulsed Ly6G^{+} Macs could promote wound healing compared to control medium (containing only IL-4 and IL-13) or CM from unpulsed Ly6G^{+} Macs (Fig. 7, I and J). We performed proteome profiling on such CM and found that Ly6G^{+} Macs were highly potent in secreting soluble factors, among which were chemokines (CCL5, CXCL16, CCL12, CXCL10), cytokines (TNF-α, IL-10, IL-1□) and osteopontin, some of which were increased upon IL-4R activation (Fig. 7K). Some of the molecules detected in the CM of Ly6G^{+} Macs had their transcript levels significantly upregulated in Ly6G^{+} Macs (C2) as compared to other clusters (fig. S11).

Altogether, our data demonstrate that Ly6G$^+$ Macs can release soluble factors upon IL-4 receptor triggering that act directly on AT2 to promote epithelial regeneration (fig. S12).

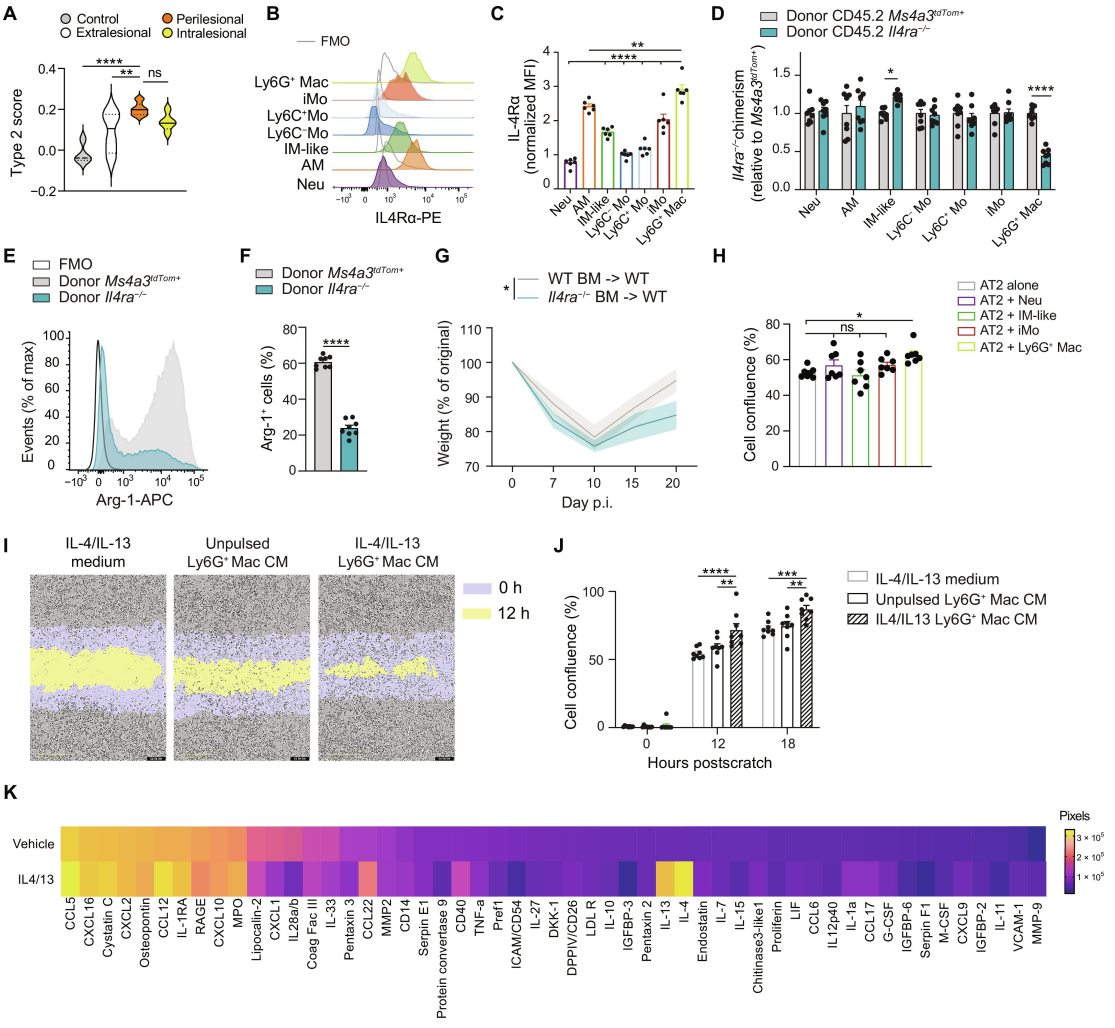

Fig. 7. IL-4R-dependent Ly6G$^+$ Macs release soluble factors that improve alveolar regeneration from AT2 cells

(**A**) Type 2 signature score within control, extralesional, perilesional and intralesional ROIs, as depicted by violin plots (height: scores; width: abundance of cells). (**B**) Representative histograms of IL-4R expression in the indicated lung myeloid cell populations, quantified at day 10 post-IAV. (**C**) Quantification of IL-4R expression, as in (H). (**D**) Bar graph showing donor *Il4ra*$^{-/-}$ chimerism relative to donor *Ms4a3*$^{tdTom+}$ chimerism in the indicated cell populations from lethally-irradiated CD45.1 mice reconstituted with a 1:1 mix of CD45.2 *Il4ra*$^{-/-}$ and *Ms4a3*$^{tdTom+}$ BM cells, infected with IAV 4 weeks later and evaluated at day 10 post-IAV. (**E**) Representative histograms and (**F**) quantification of Arg-1$^+$

cells (%) in Ly6G$^+$ Macs from donor *Il4ra*$^{-/-}$ or *Ms4a3*$^{tdTom+}$ BM cells, as in (F). (**G**) Time course of weight, expressed as the % of the original weight at day 0 and assessed at days 0, 7, 10, 15, 20 post-IAV in lethally-irradiated CD45.1/CD45.2 WT mice reconstituted with CD45.2 *Il4ra*$^{-/-}$ BM cells (*Il4ra*$^{-/-}$ BM -> WT) or CD45.2 WT BM cells (WT BM -> WT) and infected with IAV 4 weeks later. (**H**) Cell confluence of AT2 cells (MLE-12) quantified 12 hours after a standardized scratch by live cell analysis when AT2 cells were co-cultured in the presence of Neu, IM-like cells, iMo or Ly6G$^+$ Macs isolated from the lungs of WT mice at day 10 post-IAV. (**I**) Representative picture of cell confluence of AT2 cells at 0 and 12 hours post-scratch when AT2 cells were cultured with IL-4/13 or with conditioned medium (CM) of unpulsed or IL-4/13-pulsed Ly6G$^+$ Macs isolated from the lungs of WT mice at day 10 post-IAV. (**J**) Bar graph of cell confluence of AT2 cells quantified 0, 12 and 18 hours after scratch, as in (K). (**K**) Heatmap showing the proteome profiling of CM of vehicle and IL-4/13-treated Ly6G$^+$ Macs isolated from the lungs of WT mice at day 10 post-IAV. (C,D,F,H,J) Data show mean + SEM and (C,D,F) are pooled from 2 independent experiments (C: *n*=6 mice; D,F: *n*= 8 mice); (H,J) are pooled from 3 independent sorting experiments. (G) Data show mean (centerline) ± SEM (colored area) and are pooled from 2 independent experiments (*n*=6 mice per group). *P* values were calculated using (C) a one-way ANOVA with Dunnett's post hoc tests, (D,G) a two-way ANOVA with Sidak's post hoc tests, (F) a two-tailed Student's *t* test, (H) a one-way or (J) a two-way ANOVA with Tukey's post hoc tests. *, *P<0.05;* **, *P*<0.01; ****, *P*<0.0001. FMO, fluorescence minus one; ns, not significant; p.i., post-infection.

2.6 Ly6G$^+$ Macs belong to a conserved host response to injury across organs, triggers and species

We evaluated whether Ly6G$^+$ Macs were specifically recruited in the IAV model or were also triggered in other models of injury. First, we used a model of non-infectious lung injury based on bleomycin (bleo) instillation and performed time-course flow cytometry analyses. Ly6G$^+$ Macs expressing high levels of Arg-1 and CXCR4 were mostly present between day 7 and day 14 post-bleo, which correlated with signs of epithelial damage, as reflected by the decrease in numbers of AT1 and AT2 (Fig. 8A-E). We also found similar Ly6G$^+$ Macs peaking at days 1 and 2 post-treatment in an acute model of acetaminophen-induced liver injury, which correlated with the release of alanine aminotransaminase (ALT) in plasma (Fig. 8F-I). Our data thus suggested that Ly6G$^+$ Macs are a component of a conserved response to tissue damage, regardless of the organ or trigger.

Finally, we asked whether Macs sharing a similar transcriptomic signature were also present in the broncho-alveolar lavage fluid (BALF) of diseased humans. We

performed scRNA-seq analyses of BALF cells from 7 patients with a suspicion of pneumonia and manually annotated the cell clusters based on the most upregulated genes (Fig. 8, J and K and fig. S13). Next, we mapped a Ly6G$^+$ Mac score based on orthologous genes in humans to the BALF cells and found that cells exhibiting the highest Ly6G$^+$ Mac score belonged to the same cluster C9 identified as Mo-Macs based on their high expression of monocyte genes and their low expression of AM-associated genes (Fig. 8, L and M). SCENIC analyses [455] predicted higher MAF and MAFB activities in the Mo-Mac cluster compared to other clusters (Fig. 8N), further supporting that the airspace of human pneumonia lungs contains Mo-Macs that are transcriptionally similar to mouse Ly6G$^+$ Macs.

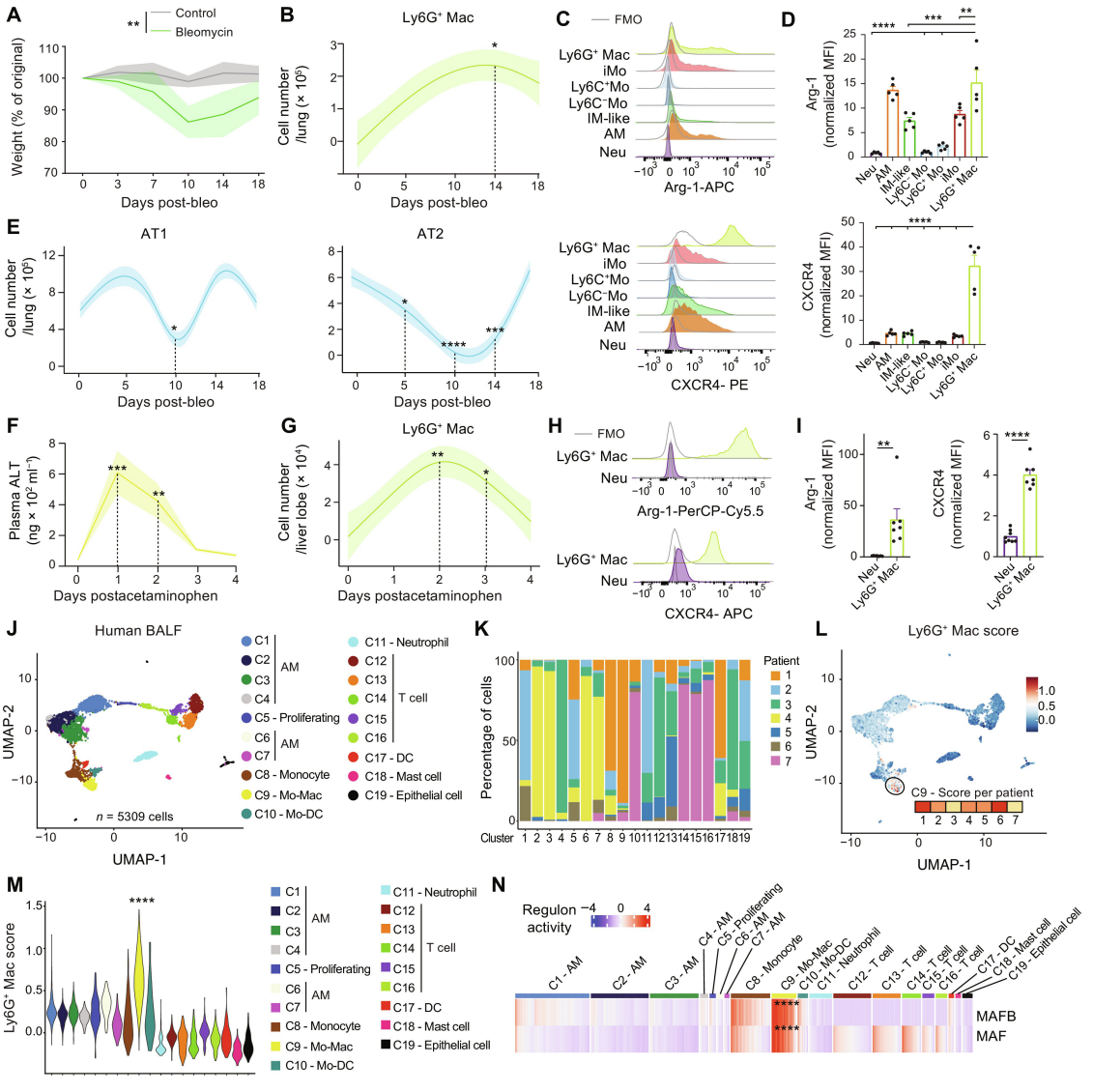

Fig. 8. Ly6G⁺ Macs are triggered by other insults and have a human counterpart

(**A**) Time course of weight, expressed as the % of the original weight at day 0 and assessed at days 0, 3, 7, 10, 14 and 18 post-injection in C57BL/6 WT mice instilled i.t. with bleomycin (bleo). (**B**) Time course of absolute numbers of lung Ly6G⁺ Macs quantified at days 0, 5, 10, 14 and 18 post-bleo in WT mice. (**C**) Representative histograms of intracellular Arg-1 and CXCR4 expression in the indicated lung myeloid cell populations, quantified at day 14 post-bleo. (**D**) Quantification of intracellular Arg-1 and CXCR4 expression, as in (C). (**E**) Time course of absolute numbers of pSPC⁻Pdpn⁺ AT1 and pSPC⁺Pdpn⁻ AT2, quantified at days 0, 7, 10, 14 and 18 post-bleo. (**F**) Amount of alanine aminotransferase (ALT) in the plasma of WT mice injected i.p. with acetaminophen at days 0, 1, 2, 3 and 4 post-injection. (**G**) Time course of absolute numbers of liver Ly6G⁺ Macs quantified at days 0, 1, 2, 3 and 4 post-acetominophen. (**H**) Representative histograms of intracellular Arg-1 and CXCR4 expression in liver neutrophils (Neu) and Ly6G⁺ Macs, quantified at day 1 post-acetominophen. (**I**) Quantification of intracellular Arg-1 and

CXCR4 expression, as in (H). (**J**) UMAP plot depicting the transcriptional identity of human BALF cells collected from 7 patients suspected of pneumonia and analyzed by scRNA-seq. Annotations of cell clusters are shown. (**K**) Representation of each patient within each cluster, shown as frequency. (**L**) UMAP feature plot, as in (J), according to the Ly6G^{+} Mac signature score. The score level in cluster C9 is shown for each patient. (**M**) Ly6G^{+} Mac signature score of single cells within each cluster, as depicted by violin plots (height: score; width: abundance of cells). (**N**) Heatmap depicting predicted activities of MAFB and MAF across BALF cell populations, evaluated by SCENIC analysis of the scRNA-seq data shown in (**J**). (A,B,E,F,G) Data show mean (centerline) ± SEM (colored area) and are pooled from 2 independent experiments (*n*=5-6 mice). (D,I) Data show mean + SEM and are pooled from 2 independent experiments (*n*=5-7 mice). *P* values were calculated using (A) a two-way ANOVA, (B,D,E,F,G) a one-way ANOVA with Dunnett's post hoc tests, (I) a two-tailed Student's *t* test or (M,N) a Wilcoxon rank sum test. (M) *P* values compare C9 vs. all other clusters. *, *P<0.05;* **, *P*<0.01; ***, *P*<0.001; ****, *P*<0.0001. FMO, fluorescence minus one.

2.7 Supplementary Figures

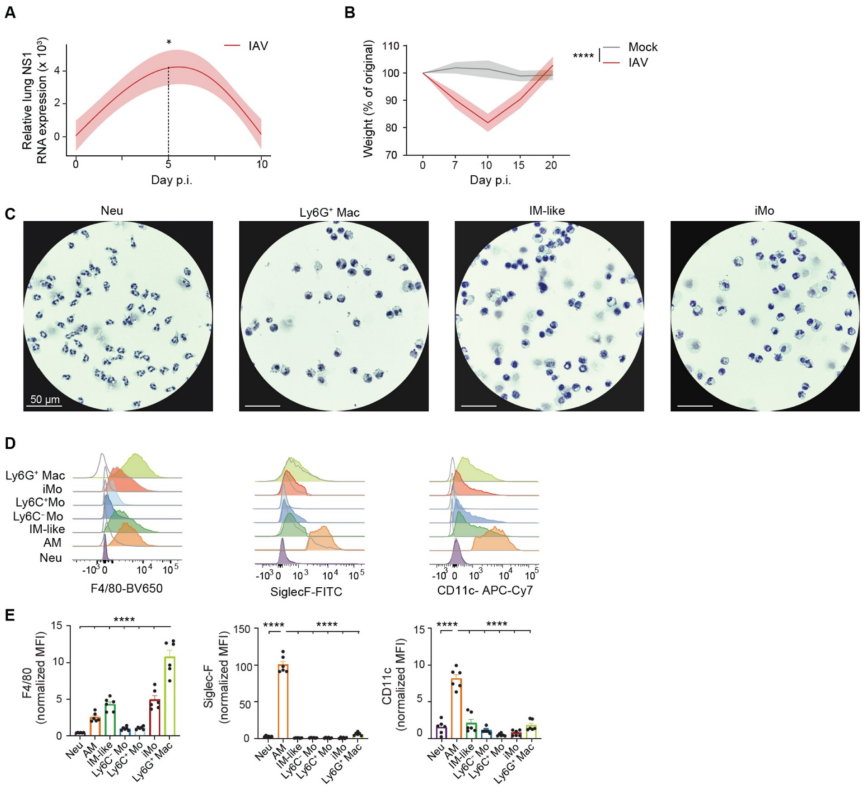

Fig. S1. Morphology and phenotype of lung myeloid cells at day 10 post-IAV

(A) Time course of relative lung NS1 RNA expression, assessed by RT-qPCR at days 0, 5 and 10 post-IAV in WT mice. (B) Time course of weight, expressed as the % of the original weight at day 0 and assessed at days 0, 7, 10, 15 and 20 post-IAV in WT mice. (C) Photographs of Neu, Ly6G+ Macs, IM-like cells and iMo sorted by FACS from IAV-infected WT mice at day 10 p.i.. Pictures are representative of 1 of 3 independent sorting experiments, each giving similar results. (D) Representative histograms of F4/80, SiglecF and CD11c expression in the indicated myeloid cell populations, quantified by flow cytometry at day 10 post-IAV in WT mice. (E) Quantification of expression of the indicated markers, as in (D). (A,B) Data show mean (centerline) ± SEM (colored area) and are pooled from 2 independent experiments (n=6-7 mice per time point). (E) Data show mean + SEM and are pooled from 2 independent experiments (n= 6 mice). P values compare day 5 vs. day 0 in (A) and were calculated using (A,D) a one-way ANOVA with Dunnett's post hoc tests or (B) a two-way ANOVA. *, P<0.05; ****, P<0.0001. p.i., post-infection. (C) Scale bar: 50 µm.

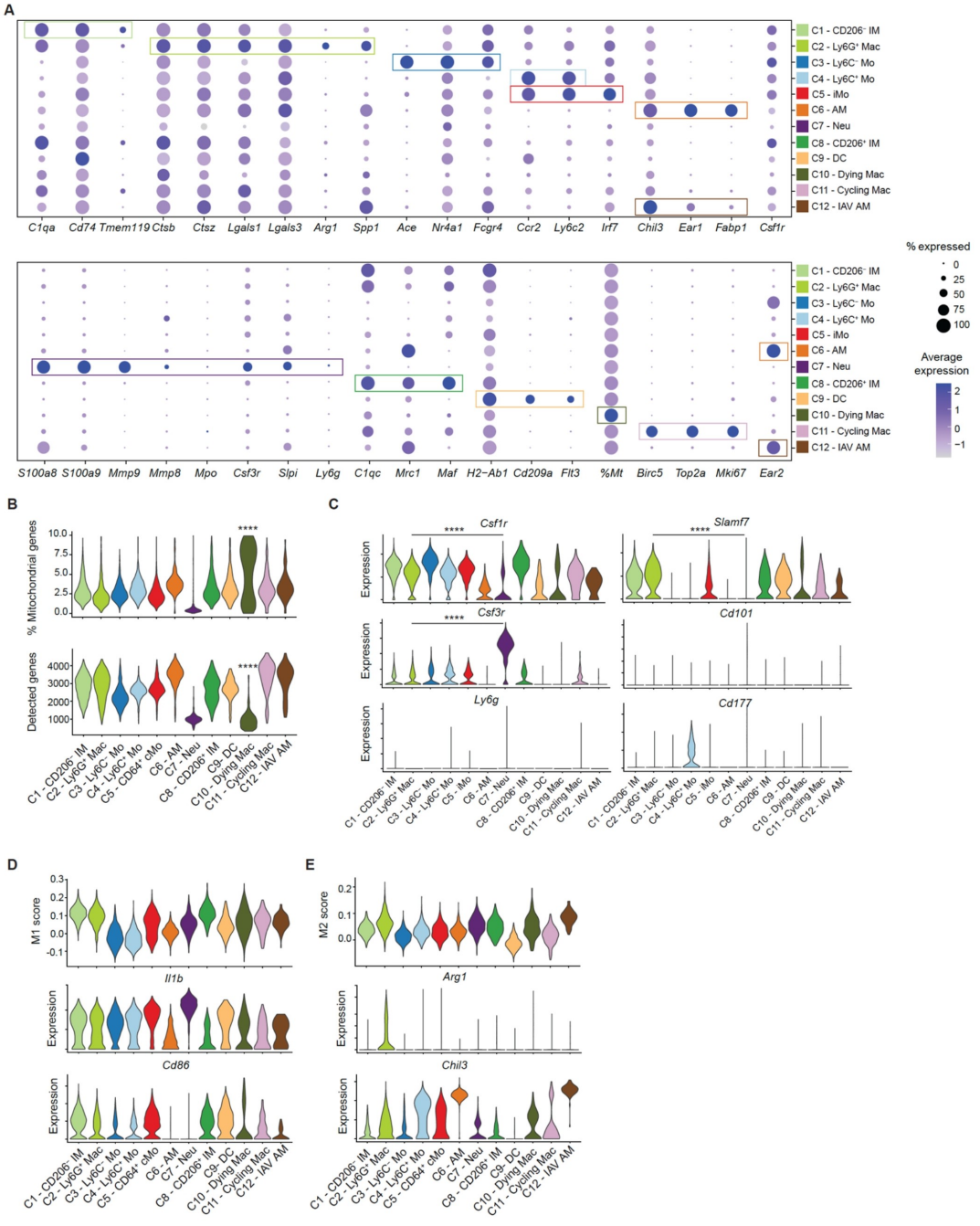

Fig. S2. Gene expression in and features of myeloid cell clusters identified by scRNA-seq at day 10 post-IAV. (**A**) Dot plots showing average expression of the indicated genes and % of cells expressing the genes within each cluster, related to Fig. 2A. (**B**) Percentage of mitochondrial genes (top) and number of detected genes (bottom) within each cluster, as depicted by violin plots (width: abundance of cells). (**C**) Expression of the indicated genes within each cluster, as depicted by violin plots (height: gene

expression; width: abundance of cells). (**D**) M1 signature score (top) and expression of M1-related genes within each cluster, as depicted by violin plots (height: M1 score or gene expression; width: abundance of cells). (**E**) M2 signature score (top) and expression of M2-related genes within each cluster, as depicted by violin plots (height: M2 score or gene expression; width: abundance of cells). *P* values compare (B) C10 – dyings Macs *vs.* all other clusters or (C) C2 – Ly6G+ Macs *vs.* C7 – Neutrophils and were calculated using a Wilcoxon rank sum test. ****, *P*<0.0001.

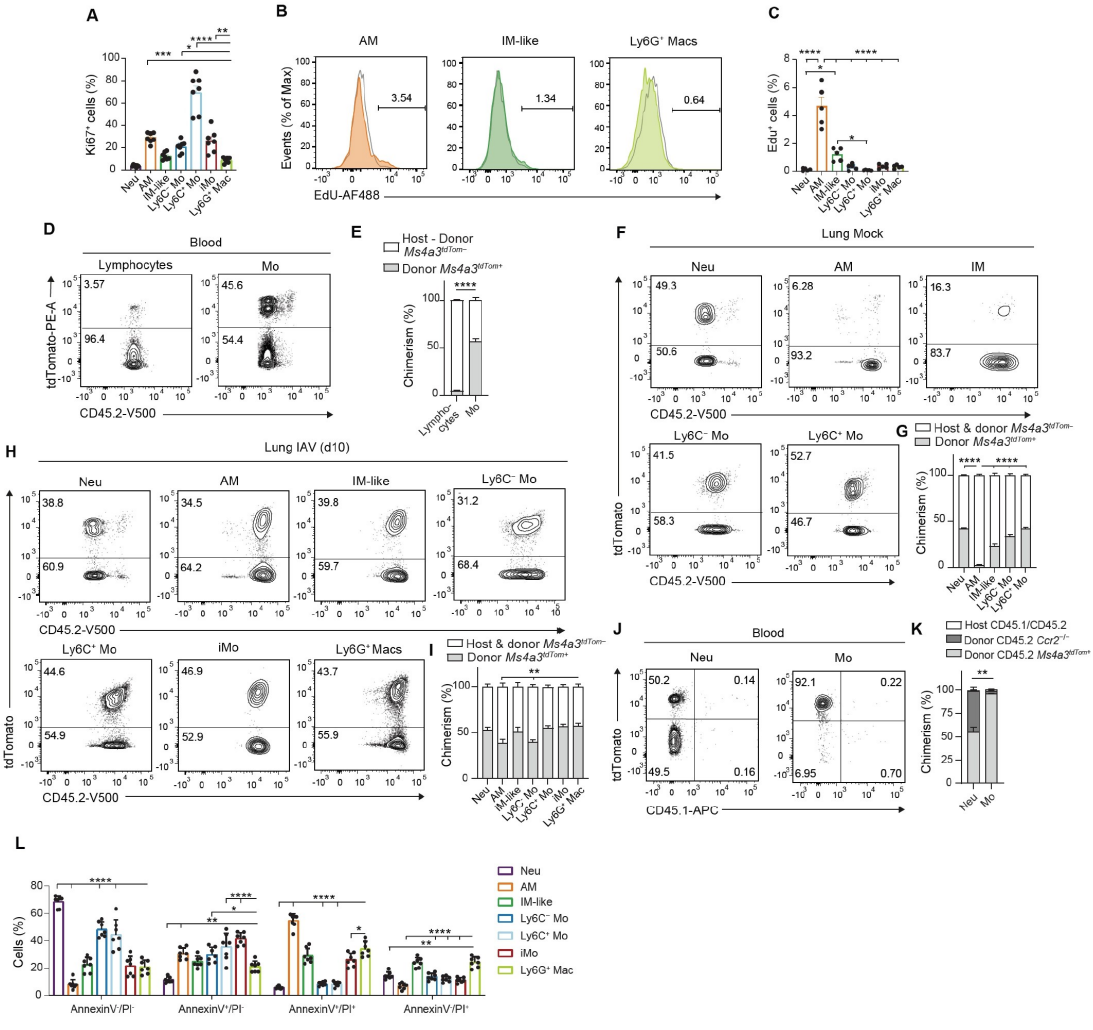

Fig. S3. Ly6G+ Macs do not proliferate, are short-lived and arise from recruited BM-derived monocytes post-IAV. (**A**)

Bar graphs showing the % of Ki67+ cells in the indicated lung myeloid cell populations, as quantified by flow cytometry in lungs of WT mice at day 10 post-IAV. (**B**) Representative histograms of EdU levels in AMs, IM-like cells and Ly6G+ Macs from EdU-pulsed WT mice at day 10 post-IAV. Unpulsed mice were

used as controls (grey line). (**C**) Bar graphs showing the % of EdU+ cells in the indicated lung myeloid cell populations, as in (B). (**D**) Representative tdTomato and CD45.2 contour plots and (**E**) bar graph showing % of host and donor *Ms4a3tdTom–* chimerism and donor *Ms4a3tdTom+* chimerism of blood lymphocytes and monocytes (Mo) from lethally-irradiated thorax-protected WT mice reconstituted with *Ms4a3*$^{tdTom+}$ BM donor cells, evaluated by flow cytometry 4 weeks after reconstitution. (**F**) Representative tdTomato and CD45.2 contour plots and (**G**) bar graph showing % of host and donor *Ms4a3tdTom–* chimerism and donor *Ms4a3tdTom+* chimerism of the indicated lung myeloid cell populations, as in (D-E), evaluated by flow cytometry 4 weeks after reconstitution and 10 days after mock infection. (**H**) Representative tdTomato and CD45.2 contour plots and (**I**) bar graphs showing % of host + donor *Ms4a3tdTom-* chimerism and donor *Ms4a3tdTom+* chimerism of the indicated lung myeloid cell populations, as in (F-G), evaluated by flow cytometry 4 weeks after reconstitution and 10 days after IAV infection. (**J**) Representative tdTomato and CD45.1 contour plots and (**K**) bar graph showing % of host CD45.1/CD45.2, CD45.2 donor *Ccr2*$^{-/-}$ and *Ms4a3*$^{tdTom+}$ chimerism of blood neutrophils (Neu) and Mo from lethally-irradiated CD45.1/CD45.2 mice reconstituted with a 1:1 mix of CD45.2 *Ccr2–/–* and *Ms4a3*$^{tdTom+}$ BM cells, evaluated by flow cytometry 4 weeks after reconstitution. (**L**) Bar graph showing the frequency of Annexin V and PI negative and/or positive fractions within the indicated lung myeloid cell populations, quantified by flow cytometry at day 10 post-IAV in WT mice. (A,C,E,G,I,K,L) Data show mean + SEM and are pooled from 2 independent experiments (n=4-10 mice). *P* values compare donor *Ms4a3tdTom+* chimerism in (D,F,H,J) and were calculated using (A,C) a one-way ANOVA with Dunnett's post hoc tests, (E,K) a two-way ANOVA with Sida's post hoc tests or (G,I,L) a two-way ANOVA with Tukey's post hoc tests. *, $P<0.05$; **, $P<0.01$; ****, $P<0.0001$.

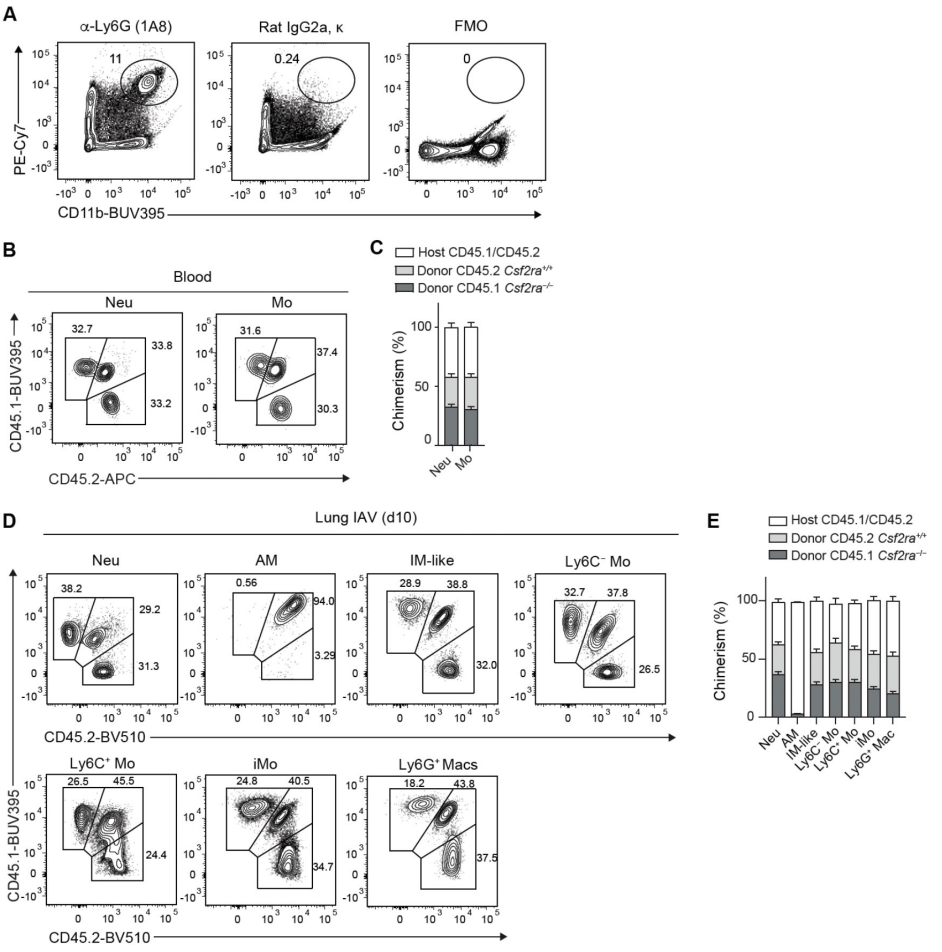

Fig. S4. Specificity of the anti-Ly6G staining and analysis of IAV-infected *Csf2ra–/–*: *Csf2ra+/+* mixed BM chimeras

(A) Representative contour plots of PE-Cy7 and CD11b expression within lung live CD45+ cells in IAV-infected WT mice at day 10 post-IAV. Plots are representative of 1 of 6 mice analyzed, each giving similar results. (B) Representative CD45.1 and CD45.2 contour plots and (C) bar graph showing % of host CD45.1/CD45.2, CD45.2 donor *Csf2ra*$^{-/-}$ and CD45.1 *Csf2ra*$^{+/+}$ chimerism of blood neutrophils (Neu) and monocytes (Mo) from thorax-protected, lethally-irradiated CD45.1/CD45.2 mice reconstituted with a 1:1 mix of CD45.2 *Csf2ra*$^{-/-}$ and CD45.1 *Csf2ra+/+* BM cells, evaluated by flow cytometry 4 weeks after reconstitution. (D) Representative CD45.1 and CD45.2 contour plots and (E) bar graph showing % of host CD45.1/CD45.2, donor CD45.1 *Csf2ra–/–* and donor CD45.2 *Csf2ra+/+* chimerism of the indicated lung myeloid cell populations, as in (B-C), infected with IAV 4 weeks later and evaluated at day 10 post-IAV. (C,E) Data show mean + SEM and are pooled from 2 independent experiments (*n*=10 mice).

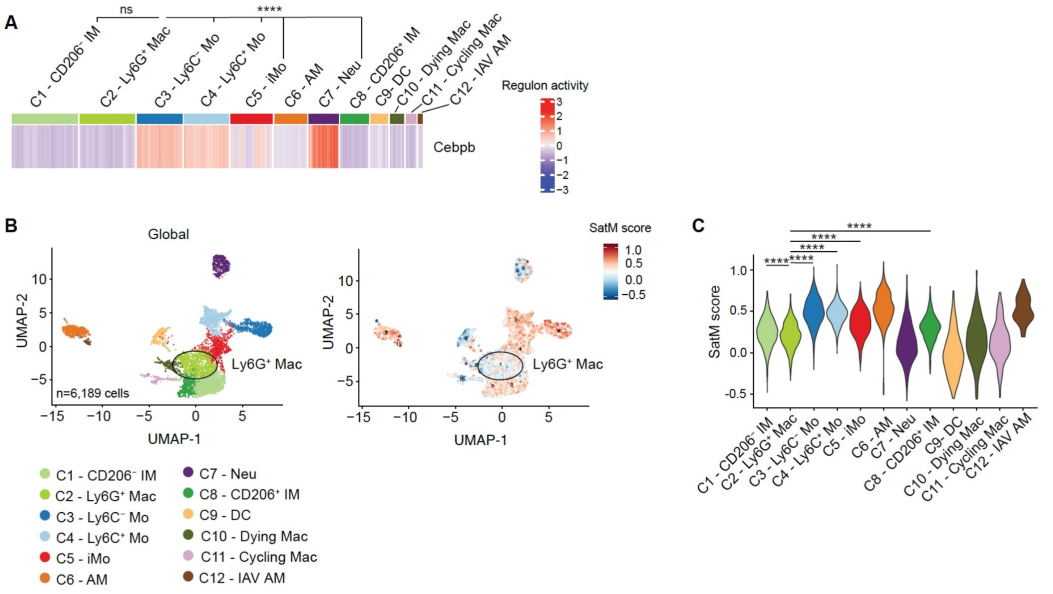

Fig. S5. Transcriptomic comparison of Ly6G+ Macs and SatM monocytes

(**A**) Heatmap depicting predicted activities of Cebpb across lung myeloid cells post-IAV, evaluated by SCENIC analysis of the scRNA-seq data shown in Fig. 2A. (**B**) UMAP plots of scRNA-seq data depicting (left) the transcriptional identity of sorted lung live CD45+F4/80+ and/or CD11b+ cells from mockor IAV-infected WT mice 10 days post-infection (5 mice per time points), merged with a published dataset of steady-state lung monocytes and IMs (*69*), and (right) a SatM monocyte signature score (*35*). (C) SatM monocyte signature score within each scRNA-seq cluster, as depicted by violin plots (height: score; width: abundance of cells). (A,C) *P* values were calculated using a Wilcoxon rank sum test. ****, *P*<0.0001. ns, not significant.

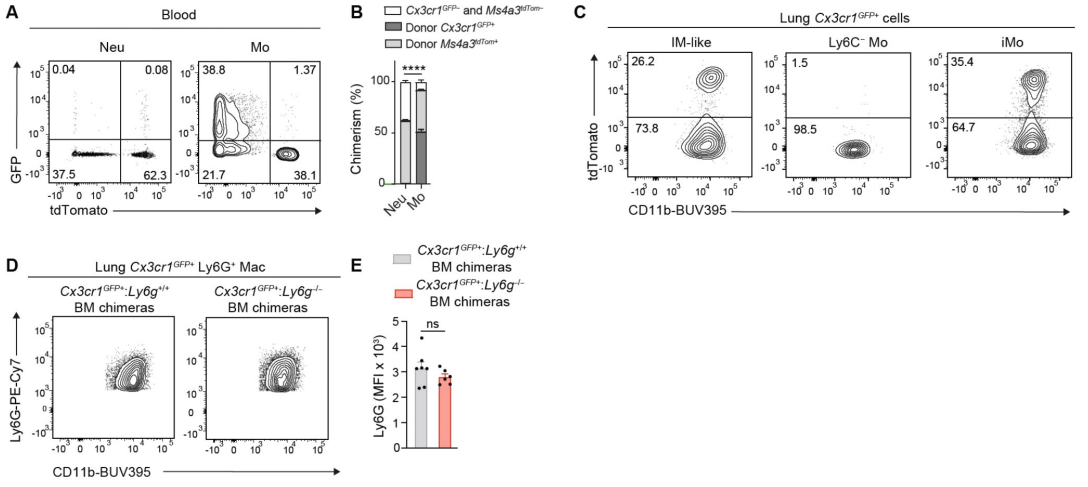

Fig. S6. Efferocytic abilities of lung myeloid cells post-IAV

(**A**) Representative GFP and tdTomato contour plots and (**B**) bar graph showing chimerism of *Cx3cr1*$^{GFP-}$*Ms4a3*$^{tdTom-}$, donor *Cx3cr1*$^{GFP+}$ and donor *Ms4a3tdTom+* cells in blood neutrophils (Neu) and monocytes (Mo) from lethally-irradiated CD45.2 WT mice reconstituted with a 1:1 mix of CD45.2 *Cx3cr1*$^{GFP+}$ and *Ms4a3*$^{tdTom+}$ BM cells, evaluated by flow cytometry 4 weeks after reconstitution. (**C**) Representative tdTomato and CD11b contour plots of the indicated lung *Cx3cr1*$^{GFP+}$ donor cell populations from lethally-irradiated CD45.2 WT mice reconstituted with a 1:1 mix of CD45.2 *Cx3cr1*$^{GFP+}$ and *Ms4a3*$^{tdTom+}$ BM cells, infected with IAV 4 weeks later and evaluated at day 10 post-IAV. (**D**) Representative Ly6G and CD11b contour plots of lung *Cx3cr1*$^{GFP+}$ Ly6G^{+} Macs from lethally-irradiated CD45.1/CD45.2 mice reconstituted with a 1:1 mix of CD45.2 *Cx3cr1*$^{GFP+}$ and *Ly6g*$^{+/+}$ (left) or *Ly6g*$^{-/-}$ (right) BM cells, infected with IAV 4 weeks later and evaluated at day 10 post-IAV. (**E**) Bar graph showing Ly6G expression levels in lung *Cx3cr1*$^{GFP+}$ Ly6G+ Macs, as in (D). (B,E) Data show mean + SEM and are pooled from 2 independent experiments (B: *n*=14 mice; E: *n*=6 mice). (B) *P* values compare donor *Cx3cr1*^{GFP} chimerism and were calculated using a two-way ANOVA with Sidak's post hoc tests. (E) *P* values were calculated using a two-tailed Student's *t* test. ns, not significant.

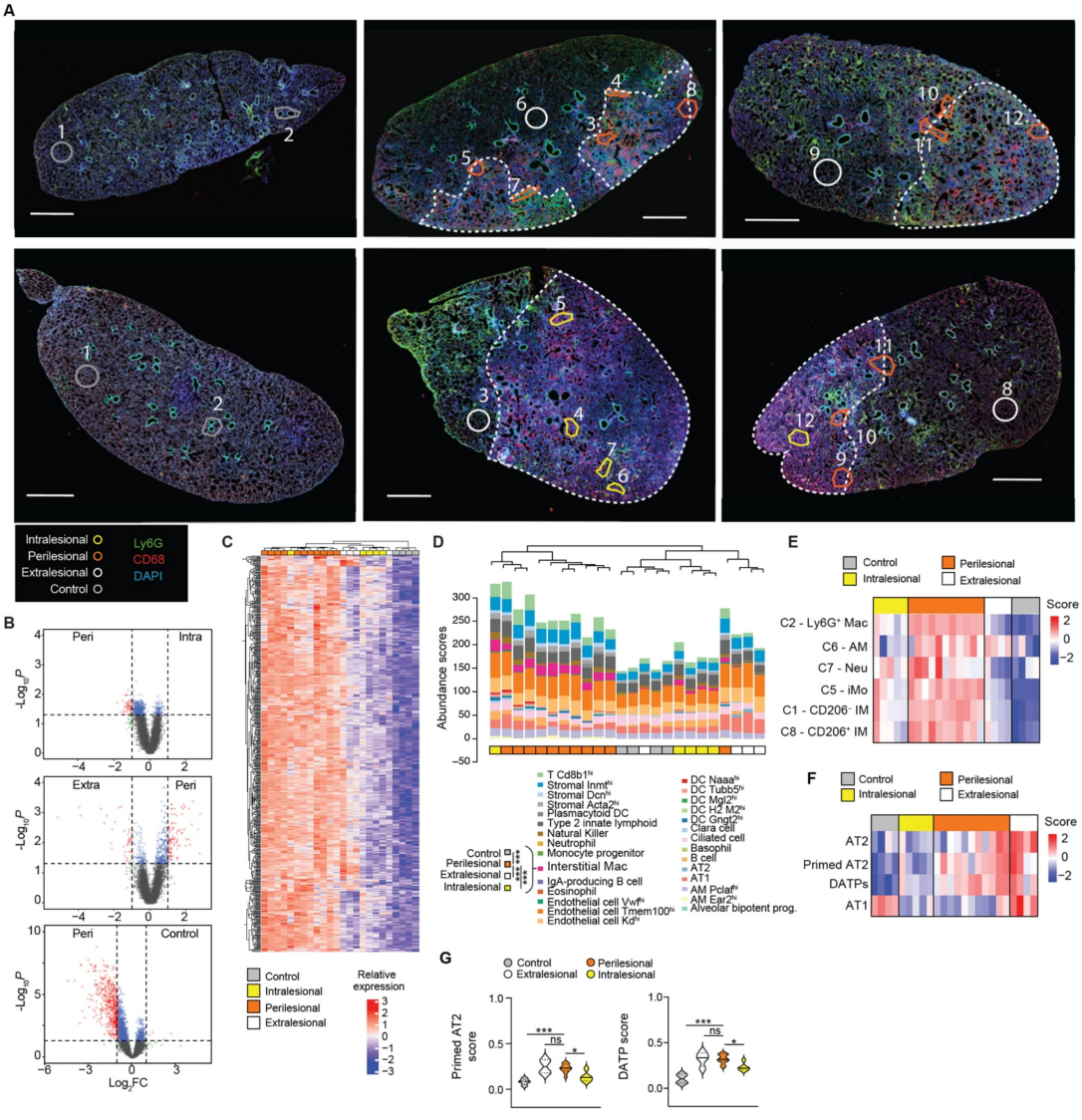

Fig. S7. Identification of Ly6G+ Macs-AT2 clusters by confocal microscopy in lung perilesional areas post-IAV

(A) Selection of regions of interest (ROIs) on lung sections from mock- or IAV-infected WT mice at day 10 post-IAV, stained with anti-Ly6G and anti-CD68 antibodies. (**B**) Volcano Plot depicting the differentially expressed genes (DEGs) between perilesional (Peri) and intralesional (Intra) areas (top), extralesional (Extra) and Peri areas (middle), and Peri and control areas (bottom). (**C**) Heatmap depicting the significantly upregulated genes in Peri areas as compared to Intra areas. (**D**) Cell deconvolution of the ROIs and abundance score of cell populations in individual ROIs using SpatialDecon algorithm. (**E**) Heatmap showing the signature score of the indicated myeloid cell populations within individual ROIs, inferred from the scRNA-seq data presented in Fig. 2A. (**F**) Heatmap showing the signature score of transitional epithelial cell states during AT2-mediated regeneration

after bleomycin-induced lung injury, inferred from previously published scRNA-seq data (*38*). (G) Primed AT2 (left) and DATPs (right) signature scores within control, extralesional, perilesional and intralesional ROIs, as in (F), as depicted by violin plots (height: scores; width: abundance of cells). *P* values were calculated using (D) a two-way ANOVA with Tukey's post-hoc tests or (G) a one-way ANOVA with Tukey's post-hoc tests. *, $P<0.05$; ***, $P<0.001$. ns, not significant.

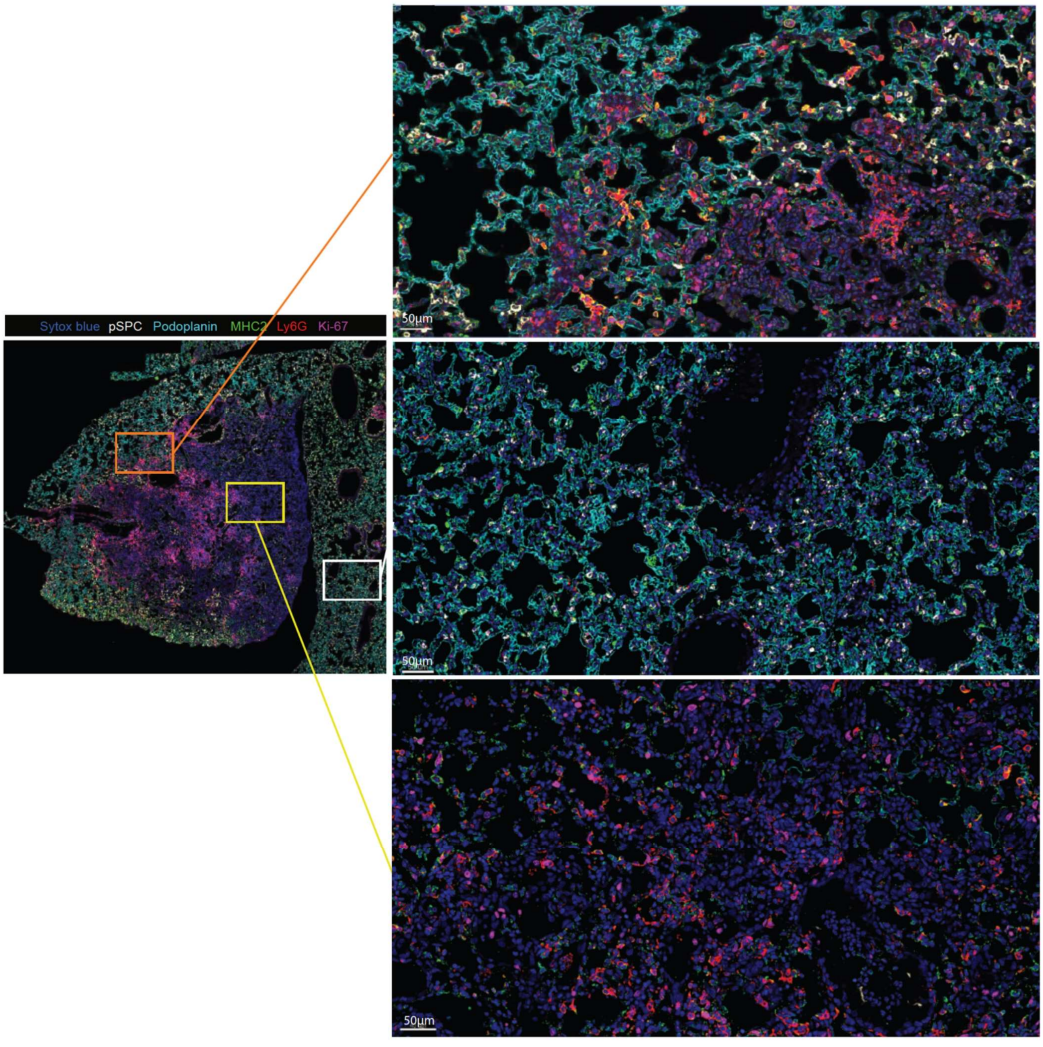

Fig. S8. Ly6G+ Macs cluster with AT2 cells in perilesional areas

Representative highresolution confocal laser scanning microscopy picture of a lung section from an IAV-infected WT mouse at day 10 post-IAV. Zooms of perilesional (orange) and intralesional (yellow) areas are shown. Pictures are representative of 1 of 6 mice analyzed, each of them giving similar results. Scale bar: 50 µm.

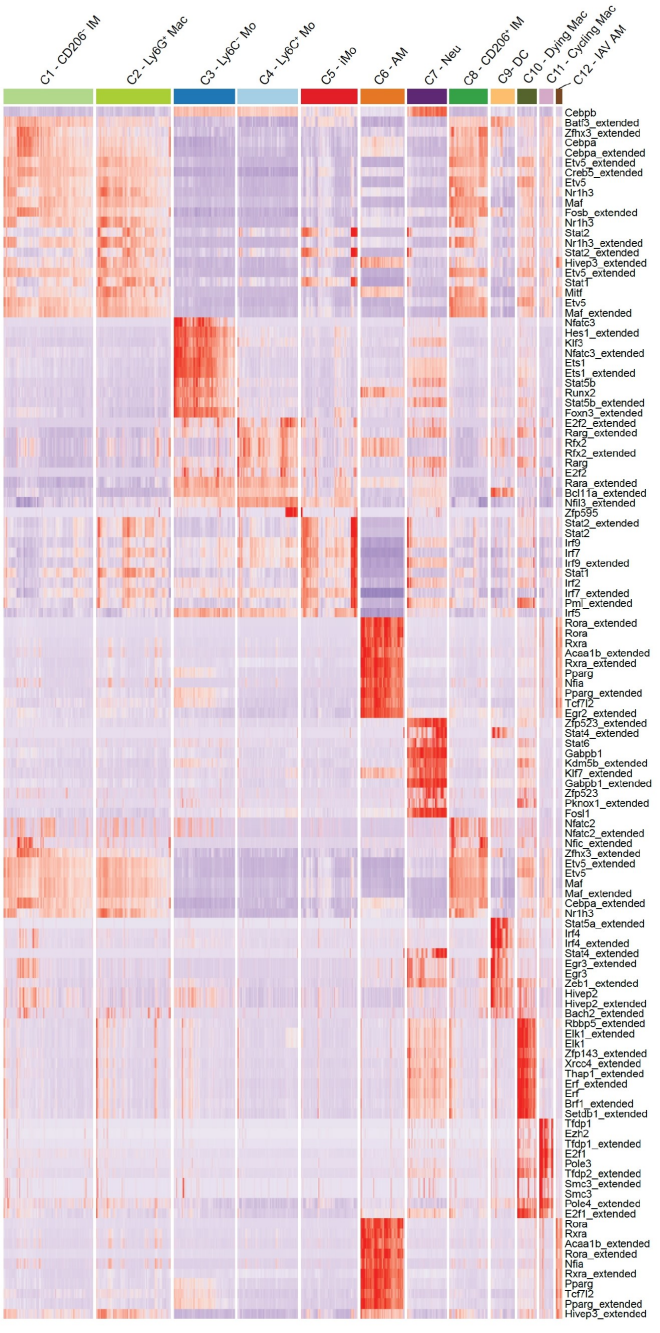

Fig. S9. SCENIC analysis of lung myeloid cells at day 10 post-IAV

Heat map depicting predicted transcription factor (TF) activities across lung myeloid cells at day 10 post-IAV, as assessed by SCENIC analysis of the scRNA-seq data shown in Fig. 2A.

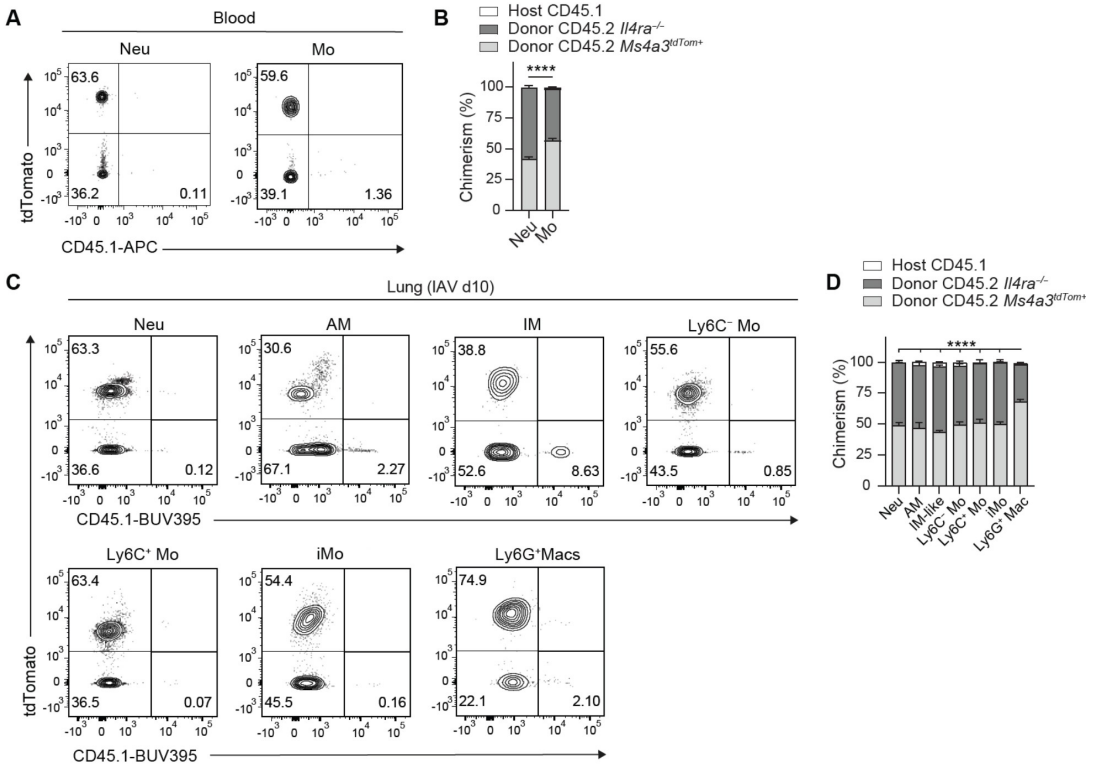

Fig. S10. Analysis of IAV-infected *Il4ra*$^{-/-}$:*Il4ra*$^{+/+}$ mixed BM chimeras

(**A**) Representative tdTomato and CD45.1 contour plots and (**B**) bar graph showing % of host CD45.1, donor CD45.2 *Il4ra*$^{-/-}$ and donor CD45.2 *Ms4a3*$^{tdTom+}$ chimerism of blood neutrophils (Neu) and monocytes (Mo) from lethally-irradiated CD45.1 mice reconstituted with a 1:1 mix of CD45.2 *Il4ra*$^{-/-}$ and ^{Ms4a3tdTom}+ BM cells, evaluated 4 weeks after transplantation by flow cytometry. (**C**) Representative tdTomato and CD45.1 contour plots and (**D**) bar graph showing % of host CD45.1, donor CD45.2 *Il4ra*$^{-/-}$ and *Ms4a3*$^{tdTom+}$ chimerism of the indicated lung myeloid cell populations from lethally-irradiated CD45.1 mice reconstituted with a 1:1 mix of CD45.2 *Il4ra–/–* and *Ms4a3*$^{tdTom+}$ BM cells, infected with IAV 4 weeks later and evaluated at day 10 post-IAV. (B,D) Data show mean + SEM and are pooled from 2 independent experiments (B: *n*=4 mice; D: *n*=8 mice). (B,D) *P* values compare donor CD45.2 *Il4ra*$^{-/-}$ chimerism and were calculated using (B) a two-way ANOVA with Sidak's post hoc tests or (D) a two-way ANOVA with Tukey's post hoc tests. ***, *P*<0.001; ****, *P*<0.0001.

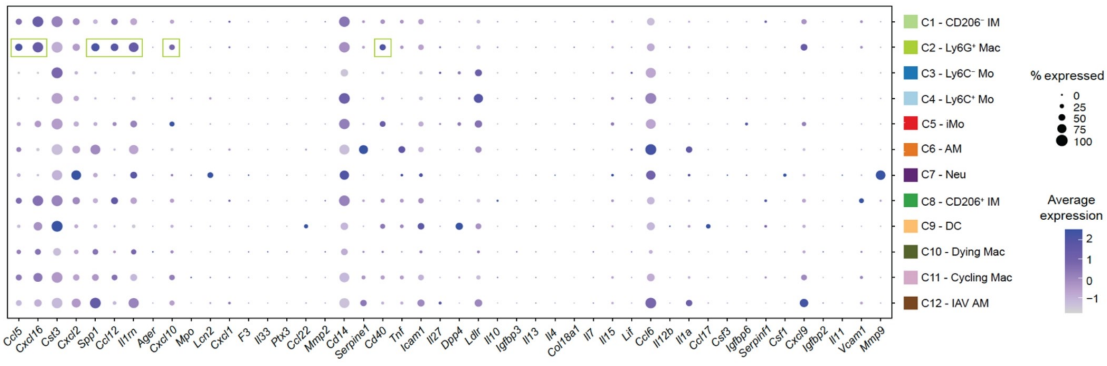

Fig. S11. Gene expression in myeloid cell clusters identified by scRNA-seq at day 10 post- IAV

Dot plots showing average expression of the indicated genes and % of cells expressing the genes within each cluster, related to Fig. 7K and 2A. Dot plots framed in green indicated gene that are significantly (P<0.0001) upregulated in C2 - Ly6G$^+$ Macs as compared to other clusters. P values were calculated using a Wilcoxon rank sum test

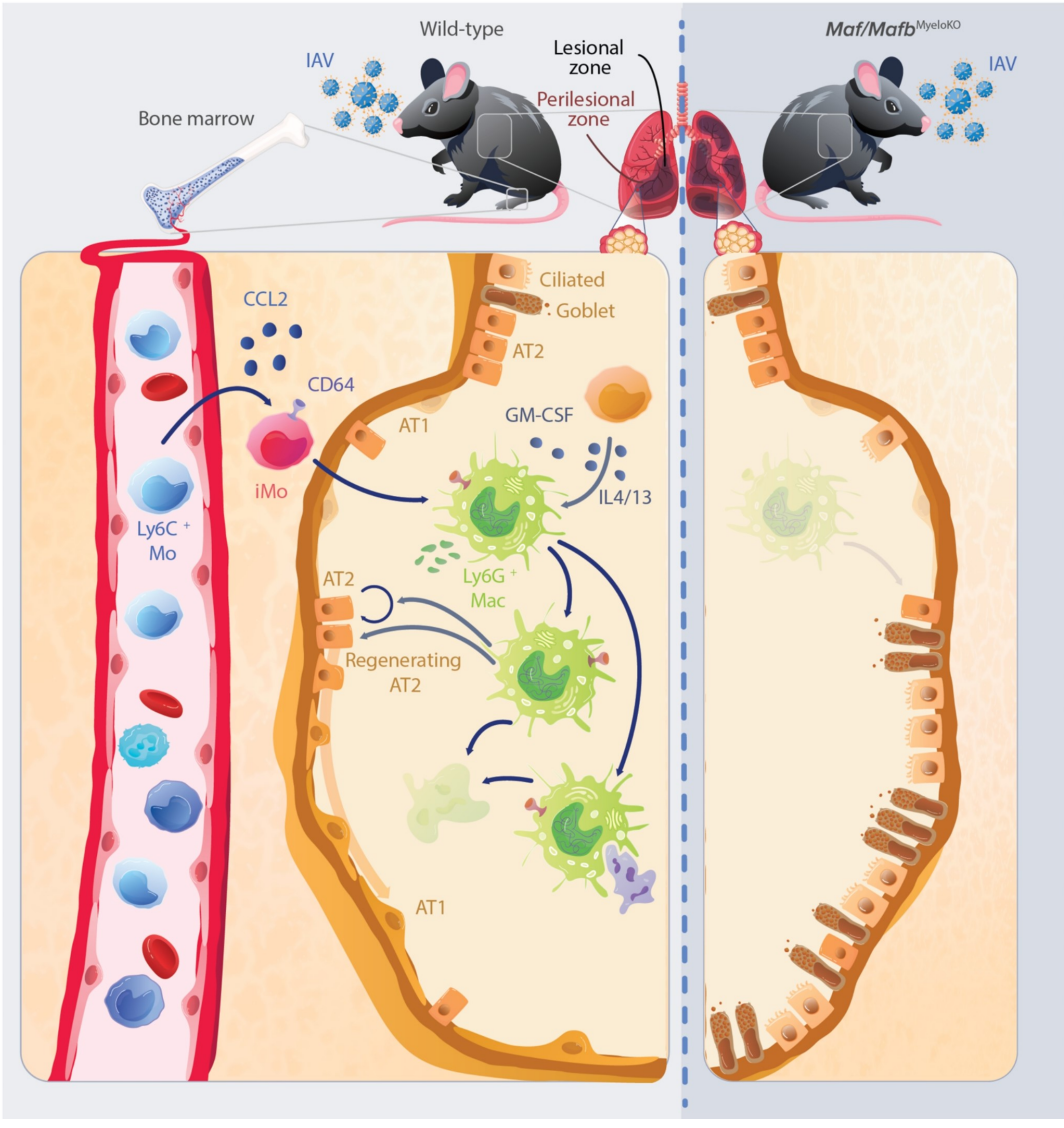

Fig. S12. Proposed model of Ly6G+ Mac-mediated alveolar epithelial regeneration after IAVtriggered Injury

In mice, an atypical population of Ly6G+ Macs is recruited from BM-derived Ccr2-dependent monocytes during the early recovery phase of IAV infection. Ly6G+ Macs exhibit atypical ultrastructural features, are metabolically very active and short-lived, and are endowed with powerful phagocytic and efferocytic capabilities. They inhabit the alveolar spaces of lung perilesional areas, where they promote euplastic alveolar regeneration and AT2-to-AT1 differentiation via IL-4R-dependent mechanisms and soluble factors. In the absence of Ly6G+ Macs, *Maf/MafB*^{MyeloKO} mice exhibit exacerbated morbidity, pathology and dysplastic bronchiolization of the alveoli.

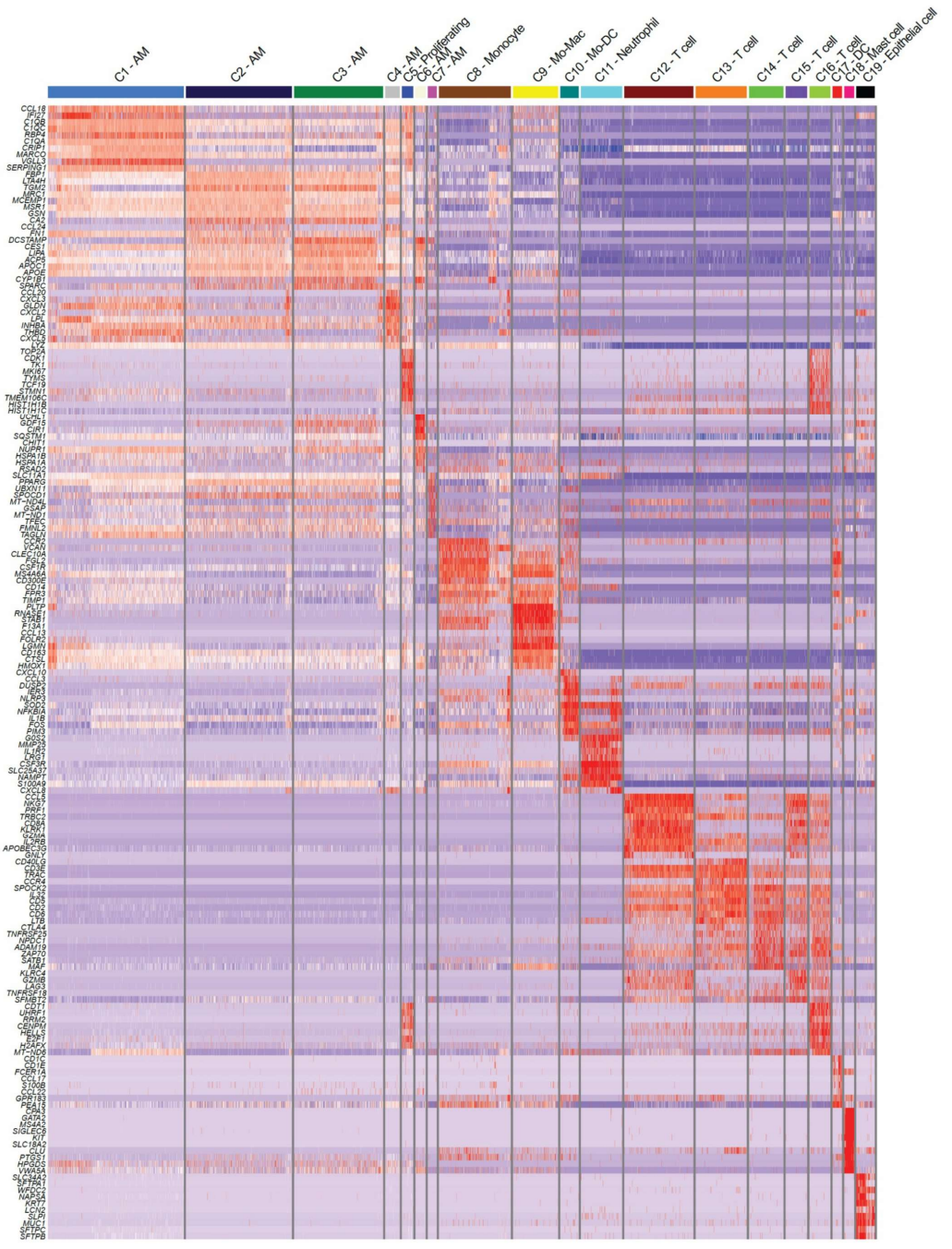

Fig. S13. Transcriptomic identities of human BALF single cells analyzed by scRNA-seq

Heatmap depicting the single cell expression of the 20 most upregulated genes within each cluster of human BALF cells analyzed by scRNA-seq, as shown in Fig. 8J.

Patient	Gender	Age	Disease status	Number of BALF cells analyzed
1	**M**	50	Bacterial pneumonia	858
2	**F**	63	Immunosuppressed, bacterial pneumonia	1,032
3	**M**	58	Interstitial pneumonia, metapneumovirus and cytomegalovirus infections	811
4	**M**	60	Pneumonia	1,445
5	**M**	71	Lung fibrosis and bacterial bronchopneumonia	311
6	**F**	62	Pneumonia	289
7	**M**	71	Immunosuppressed, bronchopneumonia	563

Table S1. Characteristics of patients from whom originate the BALF cells analyzed by scRNA-seq

DISCUSSION & PERSPECTIVES

1 Discussion

Throughout the human lifespan, the lungs fulfil the crucial function of performing gas exchanges between the external environment and the body's internal circulatory system. This complex process is made possible thanks to the lung's highly specialized architecture, which allows for the continuous flow of thousands of liters of air in and out of the body. Effective gas exchange is achieved through a combination of factors, including an extensive epithelial surface area, a dense capillary network, combined with the lung elastic properties, which enable substantial changes in air volume during respiration. Due to their continuous exposure to the external, non-sterile environment, the lungs, particularly their mucosal surfaces, are susceptible to damage from pathogens, toxins, or irritants. While minor injuries can be swiftly repaired through regenerative processes, extensive damage can alter cellular organization and functions, resulting in compromised lung function. Various factors, including the extent of damage and the intensity and duration of the local immune response, influence the outcome of the lung repair process. In this study, we focused on the role of myeloid cells in lung repair post-injury. Using a comprehensive multimodal approach, we examined the dynamic behavior of innate immune cells and specifically investigated a transient, previously unidentified population of Ly6G-expressing macrophages appearing during the early recovery phase, i.e., after the peak of acute inflammation. We initially employed a clinically relevant influenza infection model, known for causing extensive epithelial damage, and validated our findings using models of bleomycin-induced lung injury and acetaminophen-induced acute hepatitis. Furthermore, we explored the translational potential of our findings by analyzing broncho-alveolar lavage fluids from patients with infectious pneumonia. Deep characterization was conducted through an integrative approach that combined single-cell RNA sequencing, spatial transcriptomics, multiplex cytometry, microscopy, gene targeting, and both *ex vivo* and *in vivo* experiments. During the early recovery phase following influenza A virus infection, classical monocyte-derived $Ly6G^+$ macrophages were transiently recruited into the alveoli of perilesional, epithelial-regenerating areas. Such $Ly6G^+$ macrophages were highly metabolically active, exhibiting robust phagocytosis and efferocytosis capabilities, and

they underwent rapid cell death. Under the influence of IL-4 and GM-CSF receptor signaling, these macrophages could fully differentiate and interacted with epithelial cells to support AT2 cell-dependent euplastic alveolar repair.

Among the most unexpected features of these macrophages was the unanticipated expression of the Ly6G receptor, which has traditionally been thought to be exclusively expressed by neutrophils[476]. Ly6G is part of the Ly6/uPAR family[477] and is encoded solely in mice, although it exhibits structural and functional similarities with CD177, which is expressed on neutrophils in both humans and mice[478]. The function of Ly6G remains unclear, but it appears to be involved in neutrophil beta-2 integrin (CD18)-dependent migration[479]. Despite the elevated levels of Ly6G protein expression, *Ly6g* transcripts were not detected by scRNA-seq in either neutrophils or Ly6G$^+$ macrophages. Of note, neutrophils are thought to acquire Ly6G during their maturation in the bone marrow and *Ly6g* transcripts are not detectable in circulating blood neutrophils[480]. The absence of *Ly6g* transcripts in Ly6G$^+$ macrophages is somehow surprising as Ly6G expression is acquired in the lung and should therefore have been captured by scRNA-seq. One possible explanation is that the sequencing depth of the scRNA-seq experiment might not have been sufficient to sequence lowly expressed *Ly6g* transcripts, even though this remains speculative. Our phagocytosis experiments, corroborated by another study showing substantial neutrophil efferocytosis after influenza infection[367], demonstrated that inflammatory Ly6C$^+$CD64$^+$ monocytes, which we showed were direct progenitors of Ly6G$^+$ macrophages, as well as Ly6G$^+$ macrophages, were capable of actively phagocytosing other Ms4a3-labeled myeloid cells (Fig. 4I). However, the possibility of Ly6G transfer following the engulfment of neutrophils was ruled out by the observation that the levels of Ly6G expression in Ly6G$^+$ macrophages was unaffected by the presence of Ly6G-deficient neutrophils (Fig. S6). Furthermore, Ly6G protein expression (Fig. 3I, G) and the activation of *Ly6g* transcription in GM-CSF-stimulated inflammatory monocytes (Fig. 3K, L) supported the hypothesis that the precursors of Ly6G$^+$ macrophages were capable of encoding and translating Ly6G protein. Nonetheless, the possibility that neutrophil efferocytosis by inflammatory monocytes leads to genomic DNA transfer[367], resulting in transcription of *Ly6g*, cannot be excluded. Lim and colleagues demonstrated that the

phagocytosis of Cre-expressing neutrophils could induce the expression of a fluorescent protein in reporter bone marrow-derived macrophages via genetic recombination[367]. In this context, *ex vivo* hydroxytamoxifen stimulation of FACS-sorted inflammatory monocytes from *Ly6g*^{tdTom} mice could result in *Ly6g* transcription and the acquisition of tomato fluorescence, as observed in Fig. 3K. A more in-depth transcriptomic analysis or assessing a different time point may be required to detect *Ly6g* mRNA in Ly6G$^+$ macrophages. Notably, for experiments involving Ly6G antibodies, we used the 1A8 clone, which specifically recognizes Ly6G but not Ly6C, unlike other clones[481]. In most studies aimed at elucidating the role of macrophages, Ly6G has been used as a marker to remove neutrophils within the CD11b$^+$ population before gating on macrophages. Our study challenges this approach, as Ly6G$^+$ macrophages could have previously been excluded from such analyses[447]. To circumvent this issue, one could identify macrophages upstream of neutrophils, and the combined use of Ly6G and CD177 would be more appropriate for accurately identifying neutrophil populations by flow cytometry. Trzebanski and colleagues suggested that GMP-derived monocytes can also express CD177 in both bone marrow and blood[111]. Interestingly, after influenza A infection, it has been shown that CD206$^+$ interstitial macrophages are predominantly GMP-derived, with MDP progenitors replenish this population only 23 days post-infection[111]. Similarly, in our study, Ly6C$^+$ monocytes at 10 day post-infection expressed high levels of *Cd177*, *Chil3*, *Mmp8,* and *Sell*, which are characteristic of GMP-derived monocytes, and exhibited high tomato fluorescence in *Ms4a3*^{tdTom} mice. Furthermore, Trzebanski and colleagues identified interstitial macrophages as SiglecF$^-$CD11b$^+$CD64$^+$ cells[111] and likely included the Ly6G$^+$ population within the interstitial macrophage gate. Collectively, these observations suggest that Ly6G$^+$ macrophages derive from GMP progenitors, which may partially explain their neutrophil-like characteristics.

In addition to expressing Ly6G, Ly6G$^+$ macrophages were characterized by a combination of features from both M1 and M2 polarized macrophages (Fig. S2 D, E). These dual characteristics are likely attributable to the specific spatiotemporal context in which Ly6G$^+$ macrophages differentiate. In the initial days following infection, IFNγ signals[482] predominate and gradually decline after the peak of infection[273]. Consequently, recruited monocytes and

monocyte-derived macrophages differentiate in a type 1 cytokine-rich environment, retaining markers of this imprinting (Fig 4 A- Biological Processes). Ly6G$^+$ macrophages begin their differentiation during the resolution phase of inflammation when inflammatory signals are waning but still present in the injured tissues. Furthermore, although the pro-inflammatory signals are diminished in the infected areas, they persist, albeit at lower levels, in perilesional zones where Ly6G$^+$ macrophages differentiate[338]. Thus, it is unsurprising to observe activation of genes associated with the IFN-γ response in these macrophages (Fig. 4 A, Biological processes). Concurrently, a type 2 response begins to develop during the resolution phase of infection[273]. Notably, *in vitro* co-stimulation of macrophages with type 1 (LPS) and type 2 (IL-4) stimuli results in a distinct macrophage polarization[483]. Macrophages stimulated with LPS/IL-4 indeed express both M1- and M2-associated genes, show higher expression of Arg-1 compared to IL-4-stimulated macrophages, and exhibit high activation levels of both glycolysis and oxidative phosphorylation[483]. Similar characteristics were observed in Ly6G$^+$ macrophages, suggesting that the simultaneous presence of type 1 and type 2 cytokines is critical for their differentiation. A similar environment has also been reported to activate wound-healing macrophages in the liver following bacterial infection[484]. In cases of Listeria monocytogenes infection, type 1 inflammatory responses and monocyte recruitment are initiated, while recruited basophils secrete high levels of IL-4[484]. These sequential activations promote the transition of recruited monocytes into pro-repair macrophages that can restore tissue homeostasis[484]. Interestingly, repair-promoting macrophages following liver injury share similar characteristics and origins with Ly6G$^+$ macrophages. Specifically, pro-repair macrophages express high levels of CD11b and differentiate from CCR2-dependent Ly6C$^+$ monocytes. Depletion of CD11b$^+$ macrophages[485] or of CCR2[486] during the late stages of inflammation results in impaired repair. In cases of acute liver injury caused by acetaminophen, a reduced number of circulating monocytes is observed in patients with the poorest outcomes[487]. Furthermore, the phenotype of pro-resolving liver macrophages correlates with IL-4R activation[10] and efferocytosis activity[488]. It would be interesting to assess Ly6G expression in such pro-resolving macrophages, and whether they are similar to the Ly6G$^+$ macrophages observed after acetaminophen-induced liver injury (Fig. 8 F-I).

Ly6G$^+$ macrophages rely, at least in part, on GM-CSF receptor signaling for their differentiation and Arg-1 production (Fig. 5 M-L). GM-CSF has been reported to orchestrate immune responses towards both pro-inflammatory and anti-inflammatory phenotypes[411]. It can induce the secretion of high levels of pro-inflammatory cytokines (IL-1, IL-6, and TNF) and chemokines (CCL2, IL-8, and CCL17) [489], which further recruit other leukocytes to the sites of inflammation thereby contributing to chronic inflammation in autoimmune diseases[490]. GM-CSF also plays a critical role in viral clearance by promoting the migration and antigen presentation by DCs, leading to the recruitment of antigen-specific T cells[491]. Additionally, pro-inflammatory cytokines derived from macrophages can induce GM-CSF expression in lung epithelium[340], endothelium[492], fibroblasts[493], and CD4$^+$ T cells[494], thereby amplifying the inflammatory response. Conversely, other studies have suggested that GM-CSF contributes to immunomodulation by dampening M1-like polarization[222], inducing tolerogenic DCs[495], and restoring lung barrier integrity by promoting epithelial proliferation[496]. Moreover, defects in GM-CSF production appear to be involved in the pathogenesis of pulmonary fibrosis following bleomycin administration[497] or radiation-induced injury[498]. Understanding the role of GM-CSF during influenza A virus infection is arguably complex and influenced by the timing of observation, as well as the models used for GM-CSF overexpression or suppression. Furthermore, most studies have concentrated on the role of GM-CSF during the infection phase rather than during recovery. The regulatory effects of GM-CSF may also depend on the concentration of the growth factor and the concurrent presence of other cytokines. Given the spatial association between Ly6G$^+$ macrophages and AT2 in remodelling zones (Fig. 5H), surviving or newly generated AT2 cells could serve as a source of GM-CSF and exert immunoregulatory effects specifically within the repairing alveoli. Further investigation using spatial biology tools is essential to better elucidate this pathway and optimize the clinical application of inhaled GM-CSF, as previously suggested[499].

The temporal restriction of Ly6G$^+$ macrophages to the repair phase in models of IAV infection, bleomycin-induced injury, and acetaminophen-induced liver injury suggests that these cells play a critical role in repair and restoration of homeostasis. Their functions likely include the control of inflammation. Ly6G$^+$ macrophages are highly efficient phagocytes, capable of

rapidly engulfing cells and other particles (Fig. 4 F-I). Efferocytosis can play a dual role, both aiding in the resolution of inflammation and contributing to the development of a regenerative phenotype in Ly6G$^+$ macrophages. Apoptotic cells provide a key source of arginine, which is initially metabolized by Arginase-1 into urea and ornithine, with the latter being further converted into polyamines. Among these polyamines, intracellular putrescine promotes signaling pathways that induce changes in the actin cytoskeleton, thereby further enhancing phagocytic activity[278]. Other polyamines, such as spermidine and spermine, are essential for downregulating pro-inflammatory cytokines, including IL-1β and IL-6[500]. Furthermore, Arginase-1 deficiency in myeloid cells has been linked to defective efferocytosis[278]. Of note, Ly6G$^+$ macrophages express high levels of Arginase-1 (Fig.2 D-F), suggesting its involvement in processing efferocytosis-derived arginine and facilitating morphological and functional changes induced by arginine metabolites. Notably, the observed inverse relationship between the number of neutrophils and Ly6G$^+$ macrophages suggests that Ly6G$^+$ macrophages may play a key role in reducing neutrophil numbers, potentially through neutrophil efferocytosis. While neutrophils can leave the site of injury and migrate to other organs for clearance, a process known as reverse migration[501], this phenomenon has not been observed in the trachea following influenza infection[367]. Interestingly, despite the accumulation of apoptotic neutrophils during active influenza infection, neutrophil death and efferocytosis were not detectable at the site of injury[367]. This has been attributed to the migration of early apoptotic neutrophils towards CXCL2-secreting monocytes/macrophages[367]. Ly6G$^+$ macrophages have been shown to secrete high levels of CXCL2 (Fig. 7K; Fig. S11) and may facilitate neutrophil clearance by attracting them away from injury zones to areas where they can be phagocytosed.

In addition, Ly6G$^+$ macrophages can secrete a broad range of chemokines (Fig. 7K; Fig. S11) that are involved in the migration of innate and adaptive immune cells, which can contribute to directing pro-inflammatory cells out of inflamed areas. This mechanism represents a potential immunoregulatory strategy, as the persistence of pro-inflammatory cells in injured areas can be detrimental and lead to further tissue damage. Moreover, Ly6G$^+$ macrophages produce high levels of IL-1Ra, CD28, and Arg-1, which are associated with anti-inflammatory

activities[422,502–504]. IL-1Ra acts as a competitive receptor antagonist of IL-1β and plays a significant role in mitigating IL-1β-driven inflammation. IL-1Ra can reduce IL-1β-induced production of pro-inflammatory cytokines, such as IL-1β, TNF-α, IL-6, and IL-12, and promotes the polarization of anti-inflammatory macrophages[505]. IL-1Ra also inhibits the migration and maturation of dendritic cells and promotes the expansion of immunosuppressive T cells[506], thereby contributing to the modulation of inflammation. Additionally, the administration of IL-1Ra has been shown to prevent lung damage and extracellular matrix deposition in mice exposed to bleomycin or silica[503] and may similarly aid in lung preservation in influenza infection models. Furthermore, the high metabolic activity of Ly6G$^+$ macrophages could lead to competition with local CD4+ T cells and myofibroblasts for critical amino acids, thereby slowing local cell proliferation and limiting maladaptive collagen deposition[391]. Arginine consumption through Arg-1 secretion could further contribute to this nutrient competition. These observations suggest that Ly6G$^+$ macrophages play a crucial role in controlling inflammation following viral clearance. Notably, although IL-1β transcripts were identified in Ly6G$^+$ macrophages through single-cell RNA sequencing, the corresponding protein was undetectable in the supernatant of both unstimulated and IL-4/IL-13-stimulated Ly6G$^+$ macrophages.

The transient presence of Ly6G$^+$ macrophages aligns with their specialized function, which needs to be synchronized with the early resolution phase of inflammation. A substantial portion of Ly6G$^+$ macrophages undergo cell death via apoptosis or necrosis. Pyroptosis, a form of necrosis triggered by inflammatory signals, have been involved in tissue repair. In fact, supernatant of pyrolytic cells induce fibroblast and macrophage migration and promote wound closure in vivo and in vitro[507]. It cannot be excluded that pyroptosis of Ly6G$^+$ macrophages allows the delivery of pro-repair secretome in alveolar spaces, further enhancing epithelial repair. Fas-dependent programmed cell death of CD11b$^+$ recruited macrophages in the airway appears necessary for resolving inflammation following H1N1 infection[125]. Similarly, the induction of apoptosis in macrophages protects against fibrosis development in the bleomycin model[428]. Moreover, the phagocytosis of Ly6G$^+$ macrophages apoptotic bodies from Ly6G$^+$ macrophages could further promote an efferocytosis-induced

anti-inflammatory shift[508] of this cells through autologous feedback. Another factor likely contributing to their decline is linked to the microenvironmental changes post-infection. As Ly6G$^+$ macrophages partially depend on IL-4Rα signaling, the presence of type 2 cytokines is crucial for their differentiation. Following infection, T cell responses and IL-13 production increase by day 5 and return to baseline by day 15 post-infection (p.i.) [273], paralleling the kinetics of Ly6G$^+$ macrophages (Fig. 1D). The absence of type 2 cytokines beyond day 15 p.i. may inhibit further differentiation of Ly6G$^+$ macrophages.

Beyond their anti-inflammatory roles, Ly6G$^+$ macrophages support alveolar regeneration by locally supporting AT2 cells. In vitro wound healing assays with conditioned medium (Fig. 7I and J), along with their alveolar localization (Fig. 5A, B, and H), both suggest that these macrophages secrete soluble factors that directly influence AT2 cells. In vitro studies have shown that primary rat AT2 and MLE12 cells secrete high levels of CXCL12 following scratch wounding assays[509]. Ly6G$^+$ macrophages express high levels of CXCR4 (Fig. 1G), which may help direct them towards the damaged AT2 cells. Additionally, as AT2 cells also express CXCR4, which enhances their migration[509], high concentrations of CXCL12 could facilitate the colocalization of Ly6G$^+$ macrophages and AT2 cells. Notably, lung epithelial cell proliferation begins gradually after the peak of infection and reaches its maximum around day 10 post-infection[331], following the kinetics of Ly6G$^+$ macrophages. This observation suggests that Ly6G$^+$ macrophages can promote alveolar progenitor cell proliferation. In vitro experiments (Fig. 7I and J) demonstrated that the conditioned medium from IL-4/IL-13 stimulated Ly6G$^+$ macrophages could accelerate wound closure, indicating that these macrophages secrete soluble factors that induce AT2 proliferation. The specific molecular pathways through which Ly6G$^+$ macrophages support AT2 cells remain to be elucidated. Of note, Ly6G$^+$ macrophages produce, albeit in limited amount, TNF-α, which is known to induce alveolar epithelial cells to produce GM-CSF, acting as an autocrine growth factor to stimulate epithelial cell proliferation[340,510]. Furthermore, since IFN-γ signals inhibit AT2 proliferation[331], Ly6G$^+$ macrophages may indirectly support alveolar proliferation by modulating antiviral inflammation. Additionally, IL-1β signaling can regulate AT2 cells by promoting their priming and initiating their differentiation into AT1 cells[307]. However, chronic inflammation

characterized by persistent IL-1β can lead to the accumulation of alveolar epithelial intermediate cells and impede their terminal differentiation into mature AT1 cells. The adoptive transfer of Ly6G$^+$ macrophages into *Maf/Mafb*^{MyeloKO} mice could specifically restore AT2 but not AT1 numbers (Fig. 6N). It is therefore possible that Ly6G$^+$ macrophages act directly or indirectly to enhance AT2 proliferation, which is critical in the early post-infection phase for recovery from virus-induced loss of alveolar progenitors. In this context, restricting AT2 differentiation into AT1 cells by blocking the IL-1 receptor on AT2 cells might prioritize initial proliferation over differentiation. Conversely, Ly6G$^+$ macrophages could modulate inflammation and help regulate IL-1β production by inflammatory cells, thereby permitting the terminal differentiation of AT1 cells.

A notable characteristic of Ly6G$^+$ macrophages is their pro-repair profile combined with the high expression of osteopontin transcripts (i.e., *Spp1*) and protein (i.e. Opn) (Fig. 2D-F; Fig. 7K). Opn is a cytokine primarily involved in type 1-dependent responses, such as infections and autoimmune disorders[438,511]. Elevated circulating osteopontin levels have been associated with the severity of various inflammatory conditions, including cancer[512], cardiovascular[513], and respiratory diseases[514], and has been proposed as a biomarker for COVID-19, with levels directly correlating with disease severity[515,516]. High Opn levels are also linked to fibrosis[517]. However, we argue that the expression and secretion of Opn by Ly6G$^+$ macrophages must be considered within the context of early tissue repair. Opn is recognized as a key factor in pro-fibrotic responses due to its ability to induce fibroblast proliferation, extracellular matrix accumulation, and matrix metalloproteinase (MMP) production. Although chronic pro-fibrotic responses can be detrimental, Opn plays a crucial role in providing structural support for epithelial growth and migration during tissue repair, as observed in skin wounds[518]. Furthermore, Opn facilitates migration of both immune[519,520] and epithelial cells[521,522] through integrin and CD44-mediated pathways. Given that CD44 is expressed by a subset of AT2 cells with stem cell properties[523], Opn may assist in directing progenitor cells to regenerating areas for priming. Additionally, Opn has been shown to protect cells from apoptosis[524,525], which could help to prevent AT2 cell loss post-infection. While typically associated with inflammatory responses, Opn may also exert protective effects

in tissues by inhibiting the expression of iNOS [526]. Since nitric oxide (NO) is a potent inducer of Opn in macrophages[527], this negative feedback loop could mitigate NO-mediated tissue damage. Therefore, within the context of tissue repair, localized and transient osteopontin production may support epithelial repair by reducing inflammation, providing structural support, and preventing epithelial cell apoptosis.

Current therapeutic options targeting functional lung regeneration after acute injury remain limited. The most effective strategy to mitigate chronic sequelae following respiratory viral infections is prevention. While vaccination campaigns have proven effective in preventing severe diseases, the rapid genetic recombination of viruses necessitates ongoing epidemiological surveillance to anticipate the emergence of new variants. Moreover, therapeutic interventions to promote repair of established lung damage are scarce. Direct pharmacological stimulation of AT2 cell proliferation has not shown favourable outcomes in clinical studies. For instance, intravenous administration of FGF7 in patients with ARDS failed to yield any clinical or physiological benefits[528,529]. Similarly, the efficacy of cell-based therapies remains unproven. Trials involving mesenchymal stromal cell (MSC) transfer, which aim to foster a favourable environment for lung repair through their immunomodulatory and epithelial support functions[530], have been conducted in patients with various respiratory conditions, including COPD[531], IPF[532], and COVID-19[533], but have yielded inconsistent and generally unconvincing results. A major challenge in cell therapy is that cells are introduced into a non-homeostatic tissue environment dominated by inflammatory signals, altered oxygen levels, and mechanical forces[534]. Given the variability of these conditions among patients and stages of disease progression, the behavior of transferred plastic cells, such as MSCs or pluripotent stem cells, is difficult to predict. In the context of viral infections, which are known to induce long-term lung dysplasia and diminish quality of life, particularly in the elderly, new therapeutic strategies could focus on preventing abnormal remodelling. This approach should address both the persistent activation of the immune response and aberrant signaling to mesenchymal cells, acknowledging the interconnected nature of these processes. In this study, we identified the pivotal role of $Ly6G^+$ macrophages in limiting virus-induced lung dysplasia. These cells can reduce inflammation, phagocytose other immune cells, and

support AT2 cells. Due to their unique pro-repair properties, Ly6G$^+$ macrophages may represent a promising therapeutic target. Of note, transcriptomic analyses of BALF from patients with pneumonia have identified Ly6G$^+$ macrophage-like cells in humans. Although these findings are preliminary and warrant further investigations, they suggest that these macrophages could be manipulated to improve lung repair outcomes following acute infectious lung injury. While a cell therapy based on Ly6G$^+$ macrophages, as demonstrated in adoptive transfer experiments (Fig. 6M, N), could be an option, its practical application in clinical settings is unfeasible for several reasons. First, Ly6G$^+$ macrophages cannot be differentiated *ex vivo* from blood or bone marrow monocytes: their development involves a continuum of signals influenced by tightly regulated sequences of events that shape their identity. *Ex vivo* differentiation using a simplified panel of cytokines and growth factors would likely result in incomplete macrophage maturation. Second, due to their metabolic and morphological characteristics, Ly6G$^+$ macrophages are fragile and short-lived, requiring an impractically high number of cells for effective transfer. Third, these macrophages are specifically localized at the periphery of damaged zones, making intravenous administration unsuitable and necessitating local injection. However, local injection does not ensure uniform cell distribution within the airways, and cells may preferentially migrate to healthy areas with larger bronchi lumens and better ventilation. For these reasons, the amplification of Ly6G$^+$ macrophages-like cells *in vivo* might be a more adequate approach.

Given the partial dependence of Ly6G$^+$ macrophages on GM-CSF and IL-4, the combined administration of these molecules could promote their amplification. Recombinant GM-CSF, marketed as Sargramostim, is an FDA-approved drug for multiple respiratory diseases and is currently being tested as a therapy for lung proteinosis with encouraging results[535,536]. In other lung diseases, intravenous GM-CSF treatment has shown clinical improvement in patients with sepsis-associated respiratory dysfunction[537] but not in those with ALI[510]. These variable outcomes may be due to the high GM-CSF concentrations required in the alveoli which could be not reach by intravenous administration. In addition, systemic administration of GM-CSF may affect the differentiation of bone marrow progenitors towards the neutrophil lineage and promote the mobilization of immune cells into the bloodstream, thereby

enhancing the activation of inflammation[538]. While these effects provide a rationale for the therapeutic use of GM-CSF in cancer and treatment-resistant infections[538], the non-specific activation of the immune system may be an undesirable off-target effect in the context of lung tissue repair. Altogether, these evidences suggest that inhalation may be a preferable delivery method. It is important to note that lung barrier integrity can be compromised by infections and inflammation, which may lead to systemic dispersion of locally delivered molecules and insufficient local persistence. Consequently, current animal models are exploring strategies to enhance GM-CSF bioavailability. For example, Subramanian and colleagues have conjugated murine GM-CSF to nanocrystals to increase its size and facilitate retention in the alveolar space[539]. Most studies exploring the benefits of GM-CSF in infection-induced lung injury have focused on pretreatment before infection onset. GM-CSF pretreatment has been shown to confer protection and reduce mortality against both influenza and secondary bacterial pneumonia[214,223,540]. However, less is known about GM-CSF administration post-infection. In a clinical study, six patients with pneumonia-associated ARDS received 125 µg of Sargramostim via nebulization every 48 hours for 10 days. Treated patients demonstrated improved oxygenation, increased lung compliance, and reduced morbidity[252]. Additionally, GM-CSF has shown benefits for patients with COVID-19-induced acute hypoxic respiratory failure[499]. The Sargramostim to treat patients with acute hypoxic respiratory failure due to COVID-19 (SARPAC) trial was conducted on 80 patients who received 125 µg of inhaled Sargramostim twice daily for 5 days, with intravenous administration of 125 µg/m^2 body surface for patients requiring mechanical ventilation. The treatment resulted in improved alveolar gas exchange without increasing inflammatory cytokines[499]. Although these studies primarily targeted the inflammatory rather than the repair phase post-injury, they support that inhaled Sargramostim might be a safe and beneficial treatment for infected patients.

Regarding IL-4R signaling, most current studies focused on lung fibrosis or asthma, conditions in which type 2 responses play a detrimental role[541]. In these contexts, antibodies against IL-4, IL-13, or IL-4R have been beneficial in reducing eosinophilia, airway hyperresponsiveness[542–544], and collagen deposition[545]. IL-4R signaling has also been

implicated in wound healing in the skin and heart. Topical administration of IL-4 has been shown to accelerate healing of excisional skin wounds in mice[546], and IL-4 therapy post-myocardial infarction has promoted pro-reparative macrophages and reduced infarct size[547].

Further studies are needed to validate the feasibility and clinical relevance of these protocols, as well as to optimize the timing and duration of treatment. The potential for administering IL-4/IL-13 and GM-CSF via aerosol[535,548] should be considered to achieve deeper distribution within the lung alveoli and minimize systemic side effects. Given that IL-4 signaling is a key driver of collagen deposition, stimulation of this pathway should be limited to a brief period during the resolution of inflammation to prevent excessive myofibroblast activation and the establishment of fibrosis.

Our study faced significant challenges due to the highly dynamic changes occurring in the tissue during the early recovery phase. During this period, viral particles remain present in the lung, and although decreasing, the antiviral response is still active. Concurrently, more peripheral, less damaged areas of the lung begin to undergo reorganization. Consequently, the microenvironmental signals are in constant modification, as are the cells that depend on such signals. We selected day 10 for most of the characterization of Ly6G$^+$ macrophages because they are particularly abundant at this time point, which coincides with complete viral clearance and the beginning of clinical recovery. It is possible that this population exhibits different phenotypic and functional characteristics if observed at earlier or later time points. This dynamic differentiation likely contributes to functional repair. This is evident from the adoptive transfer of Ly6G$^+$ macrophages in *Maf/Mafb*^{MyeloKO} mice (Figure 5 M, N). In this experiment, the artificial persistence of Ly6G$^+$ macrophages, which were FACS-sorted from day 10 post-infection and maintained until 15 days post-infection, facilitated the restoration of AT2 cells but not of regenerating AT2 cells. These data suggest that the reduction in Ly6G$^+$ macrophages and/or changes in their secretome are necessary to allow AT2 differentiation. Moreover, the dysplastic changes observed in Maf/Mafb^{MyeloKO} mice may be due to the absence of Ly6G$^+$ macrophages or to alterations in the functions of other macrophage populations. cMaf and Mafb have been implicated in the identity and function of IMs under

steady-state conditions[124], and their transcriptional activity is predicted to be highly active in IMs following IAV infection (Fig. 6 A). Although the number of IMs is not altered in these transgenic mice, their functional properties may be modified, which may result in reduced anti-inflammatory activity and contribute to the exacerbation of clinical symptoms and tissue damage observed in these mice. Nonetheless, the role of Ly6G$^+$ macrophages has been further supported by complementary adoptive transfer experiments. The development of transgenic mice with a more specific targeting of Ly6G$^+$macrophages could be considered as a strategy to minimize disruption to other macrophage populations.

While the pivotal role of Ly6G$^+$ macrophages in promoting tissue repair during influenza infection is well-supported, their function in other types of lung injury or in different organs remains less understood. We observed the presence of Ly6G$^+$ macrophages following lung and liver damage induced by bleomycin and acetaminophen, respectively. The kinetics and phenotype of these cells closely resemble those seen during influenza infection: they emerge after epithelial damage (Fig. 8 B, G) and exhibit high expression of Arg-1 and CXCR4 (Fig. 8 C, D, H, I). Future studies in Ly6G$^+$ macrophage-deficient mice, combined with in-depth characterization, are needed to provide stronger evidence for the conserved function of these macrophages across different injury types and tissues. To further investigate the generalizability of these macrophages in lung repair, additional models, including infections with more virulent influenza strains, COVID-19, bacterial infections, or chemically induced lung damage, should be explored. Extending the research to other tissues where macrophages are known to play a reparative role, such as skin[549], hearth[550] and bone[551], could offer broader insights. Notably, immune responses vary across mouse strains, with C57BL/6 mice displaying a Th1- and M1-dominant response, whereas BALB/c mice show a Th2- and M2-dominant profile[552,553]. It would be valuable to determine whether genetic background also influences Ly6G$^+$ macrophage behavior during tissue repair.

Another significant challenge lies in identifying Ly6G$^+$ macrophages-like cells in human bronchoalveolar lavage fluid. While single-cell RNA sequencing suggests their presence in pneumonia patients, flow cytometry and immunofluorescence (IF) have proven identification

challenges. Since in mouse our gate strategy is based on the coexpression of CD64 (or CD68 in IF) and Ly6G, and Ly6G is not expressed in humans, alternative markers must be identified. A deeper comparative analysis of human and mouse single-cell RNA data may reveal surface markers useful for identifying these Ly6G$^+$ macrophage-like cells in humans and allow the characterization of their profile and function *ex vivo*.

Our study identified growth factors involved in the identity and function of Ly6G$^+$ macrophages, opening potential therapeutic avenues for reducing chronic inflammation and promoting epithelial repair. However, despite the importance of GM-CSF and IL-4/IL-13 in supporting these macrophages, further evidence is needed to confirm their ability to expand Ly6G$^+$ macrophages *in vivo*. Combined intratracheal administration of GM-CSF and IL-4/IL-13 in H1N1-infected mice could help evaluate the effects of the drugs administration on other immune and structural cells and therapeutic benefits. Additionally, comparing the effects of GM-CSF combined with IL-4 or IL-13 could pinpoint which IL-4R signaling pathways most effectively enhance the function of Ly6G$^+$ macrophages.

Our work lays the groundwork for further research into the interactions between structural and immune cells during infection and tissue repair. Firstly, of particular interest is the discovery that Ly6G$^+$ macrophages secrete molecules that support alveolar AT2 cells. A deeper investigation combining transcriptomic data from scRNA-seq of myeloid cells and spatial transcriptomics from this study, along with data from other influenza infection studies[554], may shed light on the molecular mechanisms underlying this repair function. The *in vivo* and *in vitro* testing of these identified pathways could lead to the identification of key therapeutic targets. Secondly, while the focus has been on Ly6G$^+$ macrophages over and after infection, other myeloid populations also demonstrated interesting characteristics. For example, interstitial macrophages were found to be enriched in areas of tissue damage, coinciding with increased nerve innervation. Recent studies suggest that nociceptors play a role in modulating immune responses during influenza infections, with nociceptor-deficient mice showing exacerbated lung pathology due to disrupted recruitment of neutrophils and monocytes[555]. Given that IM are immunomodulatory and interact with nerves[8], further

investigation into the reciprocal regulation of IM and nerves in viral-induced disorders is warranted. Thirdly, this study highlights the importance of microanatomical niches in shaping the identity of recruited monocyte-derived macrophages, pointing to an overlooked diversity of macrophages in injured lungs. In this prospective, mirroring the studies investigating the origins, the molecular regulation and functional diversity of lung tissue-resident macrophages, future works will focus on defining the identity of monocyte-derived macrophages in various lung injury models. By inducing epithelial or endothelial damage and examining the resulting microenvironmental changes, this project aims to map the genetic and epigenetic pathways that govern monocyte differentiation and identity, while identifying the specific niches that influence their development and function.

In conclusion, our work identifies a previously unrecognized macrophage population that resides in remodeling alveolar spaces during the early recovery phase. This macrophage population contributes to lung repair by reducing inflammation, clearing inflammatory cells, and supporting AT2 cell-dependent alveolar regeneration thus representing an attractive therapeutic target for treating lung damage.

2 Serendipity

Serendipity — the fact of finding interesting or valuable things by chance - was the thread running through the entirety of this study. The discovery of Ly6G+ macrophages and the subsequent research were all the result of a random but fortunate observation. At the start of my PhD training, we were investigating the kinetics of allergy-favoring CXCR4^{hi} neutrophils, a particular population previously described by our lab[454]. Coraline Radermecker and colleagues indeed demonstrated that the recruitment of CD45^{+}CD11b^{+}Ly6G^{+}CXCR4^{hi} neutrophils was necessary and sufficient to trigger allergic airway inflammation through the release of neutrophil extracellular traps (NETs), which facilitated allergen uptake by dendritic cells. These neutrophils were known to be recruited in response to low levels of LPS (simulating a hygienic environment), to influenza virus infection, and ozone exposure, i.e., risk factors for the development of allergic asthma. Notably, NET-prone CXCR4^{hi} neutrophils appeared at the peak of inflammation in an influenza virus infection model in BALB/c mice. Interestingly, in C57BL/6 mice, the initial peak of CXCR4^{hi} neutrophils during active infection was followed by a second peak corresponding to the resolution phase of the infection. The presence of CXCR4^{hi} neutrophils during the resolution phase was unexpected, as this particular neutrophil activation state was typically associated with acute inflammatory conditions. For several months, our research focused on characterizing this unusual neutrophil population, adhering to the widely accepted notion that Ly6G was an unmistakable marker of neutrophils. Further flow cytometry analyses revealed that these “neutrophils” expressed atypical surface markers, such as high levels of MHC-II, F4/80, and CD64. As a matter of fact, the deeper we delved into characterizing this atypical population, the more inconsistencies arose. The breakthrough came when we examined cytospin slides of FACS-sorted cells. While the CD45^{+}CD11b^{+}Ly6G^{+}CXCR4^{-} population displayed all the classical morphological features of neutrophils, the CXCR4^{+} cells displayed features of macrophages. This observation prompted us to reconsider our view of these Ly6G^{+}CD64^{+} cells. Still perplexed by the macrophage expression of Ly6G and by their hybrid properties (e.g., Ly6G^{+}CD64^{+} cells possessed secretory granules similar to those of neutrophils), we named these cells “Motrophils,” a diminutive of MOnocyte and neuTROPHIL. Although the functional

significance of Ly6G expression was secondary to the repair properties of Ly6G$^+$ macrophages discovered in this study, we made considerable efforts to confirm – or not - the true expression of this marker by macrophages, likely as a form of self-reassurance. Finally, the decision to rename them “Ly6G$^+$ macrophages” reflected our method of distinguishing them from other macrophages and moved beyond the need to explain why they expressed this receptor.

Hearing about the macrophage-intrinsic Ly6G expression, some of our peers were incredulous and very dubitative, and told us that "It's hard to find something new these days". I firmly believe that, if scientists embrace the opportunity to view biology from different perspectives, the pursuit of science would become far more rewarding and enjoyable.

REFERENCES

1. Mizgerd, J. P. & Skerrett, S. J. Animal models of human pneumonia. *Am. J. Physiol. Lung Cell. Mol. Physiol.* **294**, L387-398 (2008).
2. Petersson, J. & Glenny, R. W. Gas Exchange in the Lung. *Semin. Respir. Crit. Care Med.* **44**, 555–568 (2023).
3. Ganesan, S., Comstock, A. T. & Sajjan, U. S. Barrier function of airway tract epithelium. *Tissue Barriers* **1**, e24997 (2013).
4. Knudsen, L. & Ochs, M. The micromechanics of lung alveoli: structure and function of surfactant and tissue components. *Histochem. Cell Biol.* **150**, 661–676 (2018).
5. Weaver, T. E. & Conkright, J. J. Function of surfactant proteins B and C. *Annu. Rev. Physiol.* **63**, 555–578 (2001).
6. Huang, X., Cao, M. & Xiao, Y. Alveolar macrophages in pulmonary alveolar proteinosis: origin, function, and therapeutic strategies. *Front. Immunol.* **14**, 1195988 (2023).
7. Kawano, H. *et al.* IL-10-producing lung interstitial macrophages prevent neutrophilic asthma. *Int. Immunol.* **28**, 489–501 (2016).
8. Ural, B. B. *et al.* Identification of a nerve-associated, lung-resident interstitial macrophage subset with distinct localization and immunoregulatory properties. *Sci. Immunol.* **5**, eaax8756 (2020).
9. Aegerter, H., Lambrecht, B. N. & Jakubzick, C. V. Biology of lung macrophages in health and disease. *Immunity* **55**, 1564–1580 (2022).
10. Hume, P. S. *et al.* Localization of Macrophages in the Human Lung via Design-based Stereology. *Am. J. Respir. Crit. Care Med.* **201**, 1209–1217 (2020).
11. Chakarov, S. *et al.* Two distinct interstitial macrophage populations coexist across tissues in specific subtissular niches. *Science* **363**, eaau0964 (2019).
12. Schyns, J. *et al.* Non-classical tissue monocytes and two functionally distinct populations of interstitial macrophages populate the mouse lung. *Nat. Commun.* **10**, 3964 (2019).
13. Shi, T., Denney, L., An, H., Ho, L.-P. & Zheng, Y. Alveolar and lung interstitial macrophages: Definitions, functions, and roles in lung fibrosis. *J. Leukoc. Biol.* **110**, 107–114 (2021).
14. Medzhitov, R. Charles A. Janeway, Jr. 1943-2003. *Nat. Immunol.* **4**, 502–502 (2003).
15. Carton, Y. *Innate Immunity: From Louis Pasteur to Jules Hoffmann*. (Elsevier, 2019).
16. Buchmann, K. Evolution of Innate Immunity: Clues from Invertebrates via Fish to Mammals. *Front. Immunol.* **5**, 459 (2014).
17. Desjardins, M., Houde, M. & Gagnon, E. Phagocytosis: the convoluted way from nutrition to adaptive immunity. *Immunol. Rev.* **207**, 158–165 (2005).

18. Uribe-Querol, E. & Rosales, C. Phagocytosis: Our Current Understanding of a Universal Biological Process. *Front. Immunol.* **11**, 1066 (2020).
19. Mallat, M., Marín-Teva, J. L. & Chéret, C. Phagocytosis in the developing CNS: more than clearing the corpses. *Curr. Opin. Neurobiol.* **15**, 101–107 (2005).
20. Arandjelovic, S. & Ravichandran, K. S. Phagocytosis of apoptotic cells in homeostasis. *Nat. Immunol.* **16**, 907–917 (2015).
21. Wynn, T. A. & Vannella, K. M. Macrophages in Tissue Repair, Regeneration, and Fibrosis. *Immunity* **44**, 450–462 (2016).
22. Kourtzelis, I., Hajishengallis, G. & Chavakis, T. Phagocytosis of Apoptotic Cells in Resolution of Inflammation. *Front. Immunol.* **11**, (2020).
23. Rabinovitch, M. Professional and non-professional phagocytes: an introduction. *Trends Cell Biol.* **5**, 85–87 (1995).
24. Bilej, M., De Baetselier, P. & Beschin, A. Antimicrobial defense of the earthworm. *Folia Microbiol. (Praha)* **45**, 283–300 (2000).
25. Metchnikoff, E. *Lectures on the Comparative Pathology of Inflammation Delivered at the Pasteur Institute in 1891*. (Рипол Классик, 1893).
26. Metchnikoff, E. L'immunité dans les maladies infectieuses. *Sem. Médicale* **12**, 469 (1892).
27. Krombach, F. *et al.* Cell size of alveolar macrophages: an interspecies comparison. *Environ. Health Perspect.* **105**, 1261–1263 (1997).
28. Lendeckel, U., Venz, S. & Wolke, C. Macrophages: shapes and functions. *ChemTexts* **8**, 12 (2022).
29. Bain, C. C. & Schridde, A. Origin, Differentiation, and Function of Intestinal Macrophages. *Front. Immunol.* **9**, 2733 (2018).
30. Mylvaganam, S., Freeman, S. A. & Grinstein, S. The cytoskeleton in phagocytosis and macropinocytosis. *Curr. Biol.* **31**, R619–R632 (2021).
31. Hanna, R. N. *et al.* Patrolling monocytes control tumor metastasis to the lung. *Science* **350**, 985–990 (2015).
32. Nimmerjahn, A., Kirchhoff, F. & Helmchen, F. Resting microglial cells are highly dynamic surveillants of brain parenchyma in vivo. *Science* **308**, 1314–1318 (2005).
33. Chieppa, M., Rescigno, M., Huang, A. Y. C. & Germain, R. N. Dynamic imaging of dendritic cell extension into the small bowel lumen in response to epithelial cell TLR engagement. *J. Exp. Med.* **203**, 2841–2852 (2006).

34. Doodnauth, S. A., Grinstein, S. & Maxson, M. E. Constitutive and stimulated macropinocytosis in macrophages: roles in immunity and in the pathogenesis of atherosclerosis. *Philos. Trans. R. Soc. B Biol. Sci.* **374**, 20180147 (2019).
35. Wang, S. *et al.* Two-component macrophage model for active phagocytosis with pseudopod formation. *Biophys. J.* **123**, 1069–1084 (2024).
36. Pikkarainen, T., Brännström, A. & Tryggvason, K. Expression of Macrophage MARCO Receptor Induces Formation of Dendritic Plasma Membrane Processes*. *J. Biol. Chem.* **274**, 10975–10982 (1999).
37. Orbach, R. & Su, X. Surfing on Membrane Waves: Microvilli, Curved Membranes, and Immune Signaling. *Front. Immunol.* **11**, (2020).
38. Davidson, A. J. & Wood, W. Macrophages Use Distinct Actin Regulators to Switch Engulfment Strategies and Ensure Phagocytic Plasticity In Vivo. *Cell Rep.* **31**, 107692 (2020).
39. Kress, H. *et al.* Filopodia act as phagocytic tentacles and pull with discrete steps and a load-dependent velocity. *Proc. Natl. Acad. Sci. U. S. A.* **104**, 11633–11638 (2007).
40. Singer, I. I. *et al.* CCR5, CXCR4, and CD4 Are Clustered and Closely Apposed on Microvilli of Human Macrophages and T Cells. *J. Virol.* **75**, 3779–3790 (2001).
41. Quantitation of L-selectin distribution on human leukocyte microvilli by immunogold labeling and electron microscopy. - R E Bruehl, T A Springer, D F Bainton, 1996. https://journals.sagepub.com/doi/10.1177/44.8.8756756.
42. Erlandsen, S. L., Hasslen, S. R. & Nelson, R. D. Detection and spatial distribution of the beta 2 integrin (Mac-1) and L-selectin (LECAM-1) adherence receptors on human neutrophils by high-resolution field emission SEM. *J. Histochem. Cytochem.* **41**, 327–333 (1993).
43. De Duve, C., Pressman, B. C., Gianetto, R., Wattiaux, R. & Appelmans, F. Tissue fractionation studies. 6. Intracellular distribution patterns of enzymes in rat-liver tissue. *Biochem. J.* **60**, 604–617 (1955).
44. Settembre, C., Fraldi, A., Medina, D. L. & Ballabio, A. Signals for the lysosome: a control center for cellular clearance and energy metabolism. *Nat. Rev. Mol. Cell Biol.* **14**, 283–296 (2013).
45. Braulke, T. & Bonifacino, J. S. Sorting of lysosomal proteins. *Biochim. Biophys. Acta* **1793**, 605–614 (2009).
46. Conner, S. D. & Schmid, S. L. Regulated portals of entry into the cell. *Nature* **422**, 37–44 (2003).
47. Wang, Y. *et al.* Clec7a expression in inflammatory macrophages orchestrates progression of acute kidney injury. *Front. Immunol.* **13**, 1008727 (2022).

48. Haider, M. *et al.* The pattern recognition receptors dectin-2, mincle, and FcRγ impact the dynamics of phagocytosis of Candida, Saccharomyces, Malassezia, and Mucor species. *PloS One* **14**, e0220867 (2019).
49. Asano, K., Kikuchi, K. & Tanaka, M. CD169 macrophages regulate immune responses toward particulate materials in the circulating fluid. *J. Biochem. (Tokyo)* **164**, 77–85 (2018).
50. Canton, J., Neculai, D. & Grinstein, S. Scavenger receptors in homeostasis and immunity. *Nat. Rev. Immunol.* **13**, 621–634 (2013).
51. Anderson, C. L., Shen, L., Eicher, D. M., Wewers, M. D. & Gill, J. K. Phagocytosis mediated by three distinct Fc gamma receptor classes on human leukocytes. *J. Exp. Med.* **171**, 1333–1345 (1990).
52. van Spriel, A. B. *et al.* Effective phagocytosis and killing of Candida albicans via targeting FcgammaRI (CD64) or FcalphaRI (CD89) on neutrophils. *J. Infect. Dis.* **179**, 661–669 (1999).
53. Elliott, M. R., Koster, K. M. & Murphy, P. S. Efferocytosis signaling in the regulation of macrophage inflammatory responses. *J. Immunol. Baltim. Md 1950* **198**, 1387–1394 (2017).
54. Canton, J. *et al.* Calcium-sensing receptors signal constitutive macropinocytosis and facilitate the uptake of NOD2 ligands in macrophages. *Nat. Commun.* **7**, 11284 (2016).
55. Redka, D. S., Gütschow, M., Grinstein, S. & Canton, J. Differential ability of proinflammatory and anti-inflammatory macrophages to perform macropinocytosis. *Mol. Biol. Cell* **29**, 53–65 (2018).
56. Swanson, J. A. Shaping cups into phagosomes and macropinosomes. *Nat. Rev. Mol. Cell Biol.* **9**, 639–649 (2008).
57. Pacitto, R., Gaeta, I., Swanson, J. A. & Yoshida, S. CXCL12-induced macropinocytosis modulates two distinct pathways to activate mTORC1 in macrophages. *J. Leukoc. Biol.* **101**, 683–692 (2017).
58. Condon, N. D. *et al.* Macropinosome formation by tent pole ruffling in macrophages. *J. Cell Biol.* **217**, 3873–3885 (2018).
59. von Delwig, A. *et al.* Inhibition of macropinocytosis blocks antigen presentation of type II collagen in vitro and in vivoin HLA-DR1 transgenic mice. *Arthritis Res. Ther.* **8**, R93 (2006).
60. Yoshida, S., Pacitto, R., Inoki, K. & Swanson, J. Macropinocytosis, mTORC1 and cellular growth control. *Cell. Mol. Life Sci.* **75**, 1227–1239 (2018).
61. Sahu, R. *et al.* Microautophagy of cytosolic proteins by late endosomes. *Dev. Cell* **20**, 131–139 (2011).
62. Kaushik, S. & Cuervo, A. M. Chaperone-mediated autophagy: a unique way to enter the lysosome world. *Trends Cell Biol.* **22**, 407–417 (2012).

63. Hollenstein, D. M. & Kraft, C. Autophagosomes are formed at a distinct cellular structure. *Curr. Opin. Cell Biol.* **65**, 50–57 (2020).
64. Delgado, M. A., Elmaoued, R. A., Davis, A. S., Kyei, G. & Deretic, V. Toll-like receptors control autophagy. *EMBO J.* **27**, 1110–1121 (2008).
65. Travassos, L. H. *et al.* Nod1 and Nod2 direct autophagy by recruiting ATG16L1 to the plasma membrane at the site of bacterial entry. *Nat. Immunol.* **11**, 55–62 (2010).
66. Lupfer, C. *et al.* Receptor interacting protein kinase 2-mediated mitophagy regulates inflammasome activation during virus infection. *Nat. Immunol.* **14**, 480–488 (2013).
67. Castillo, E. F. *et al.* Autophagy protects against active tuberculosis by suppressing bacterial burden and inflammation. *Proc. Natl. Acad. Sci. U. S. A.* **109**, E3168-3176 (2012).
68. Chang, C.-P., Su, Y.-C., Lee, P.-H. & Lei, H.-Y. Targeting NFKB by autophagy to polarize hepatoma-associated macrophage differentiation. *Autophagy* **9**, 619–621 (2013).
69. Chang, C.-P., Su, Y.-C., Hu, C.-W. & Lei, H.-Y. TLR2-dependent selective autophagy regulates NF-κB lysosomal degradation in hepatoma-derived M2 macrophage differentiation. *Cell Death Differ.* **20**, 515–523 (2013).
70. Miao, Y., Li, G., Zhang, X., Xu, H. & Abraham, S. N. A TRP Channel Senses Lysosome Neutralization by Pathogens to Trigger Their Expulsion. *Cell* **161**, 1306–1319 (2015).
71. Haka, A. S. *et al.* Exocytosis of macrophage lysosomes leads to digestion of apoptotic adipocytes and foam cell formation. *J. Lipid Res.* **57**, 980–992 (2016).
72. Tancini, B. *et al.* Lysosomal Exocytosis: The Extracellular Role of an Intracellular Organelle. *Membranes* **10**, 406 (2020).
73. Underhill, D. M. & Goodridge, H. S. Information processing during phagocytosis. *Nat. Rev. Immunol.* **12**, 492–502 (2012).
74. Lavin, Y. *et al.* Tissue-resident macrophage enhancer landscapes are shaped by the local microenvironment. *Cell* **159**, 1312–1326 (2014).
75. Okabe, Y. & Medzhitov, R. Tissue-specific signals control reversible program of localization and functional polarization of macrophages. *Cell* **157**, 832–844 (2014).
76. Hoeffel, G. *et al.* C-Myb+ Erythro-Myeloid Progenitor-Derived Fetal Monocytes Give Rise to Adult Tissue-Resident Macrophages. *Immunity* **42**, 665–678 (2015).
77. Florent Ginhoux *et al.* Fate Mapping Analysis Reveals That Adult Microglia Derive from Primitive Macrophages. *Science* **330**, 841–845 (2010).

78. van Furth, R. & Cohn, Z. A. The origin and kinetics of mononuclear phagocytes. *J. Exp. Med.* **128**, 415–435 (1968).
79. Alliot, F., Godin, I. & Pessac, B. Microglia derive from progenitors, originating from the yolk sac, and which proliferate in the brain. *Brain Res. Dev. Brain Res.* **117**, 145–152 (1999).
80. Kennedy, D. W. & Abkowitz, J. L. Kinetics of central nervous system microglial and macrophage engraftment: analysis using a transgenic bone marrow transplantation model. *Blood* **90**, 986–993 (1997).
81. Parwaresch, M. R. & Wacker, H. H. Origin and kinetics of resident tissue macrophages. Parabiosis studies with radiolabelled leucocytes. *Cell Tissue Kinet.* **17**, 25–39 (1984).
82. Simon Yona *et al.* Fate Mapping Reveals Origins and Dynamics of Monocytes and Tissue Macrophages under Homeostasis. *Immunity* **38**, 79–91 (2013).
83. Hashimoto, D. *et al.* Tissue-resident macrophages self-maintain locally throughout adult life with minimal contribution from circulating monocytes. *Immunity* **38**, 792–804 (2013).
84. Müller, A. M., Medvinsky, A., Strouboulis, J., Grosveld, F. & Dzierzak, E. Development of hematopoietic stem cell activity in the mouse embryo. *Immunity* **1**, 291–301 (1994).
85. Tavian, M., Robin, C., Coulombel, L. & Péault, B. The human embryo, but not its yolk sac, generates lympho-myeloid stem cells: mapping multipotent hematopoietic cell fate in intraembryonic mesoderm. *Immunity* **15**, 487–495 (2001).
86. Ginhoux, F., Lim, S., Hoeffel, G., Low, D. & Huber, T. Origin and differentiation of microglia. *Front. Cell. Neurosci.* **7**, (2013).
87. Ginhoux, F. & Merad, M. Ontogeny and homeostasis of Langerhans cells. *Immunol. Cell Biol.* **88**, 387–392 (2010).
88. Palis, J., Robertson, S., Kennedy, M., Wall, C. & Keller, G. Development of erythroid and myeloid progenitors in the yolk sac and embryo proper of the mouse. *Dev. Camb. Engl.* **126**, 5073–5084 (1999).
89. Cumano, A. & Godin, I. Ontogeny of the Hematopoietic System. *Annu. Rev. Immunol.* **25**, 745–785 (2007).
90. Naito, M., Yamamura, F., Nishikawa, S. & Takahashi, K. Development, differentiation, and maturation of fetal mouse yolk sac macrophages in cultures. *J. Leukoc. Biol.* **46**, 1–10 (1989).
91. Faust, N., Huber, M. C., Sippel, A. E. & Bonifer, C. Different macrophage populations develop from embryonic/fetal and adult hematopoietic tissues. *Exp. Hematol.* **25**, 432–444 (1997).

92. Ramsay, R. G. & Gonda, T. J. MYB function in normal and cancer cells. *Nat. Rev. Cancer* **8**, 523–534 (2008).
93. Schulz, C. *et al.* A lineage of myeloid cells independent of Myb and hematopoietic stem cells. *Science* **336**, 86–90 (2012).
94. Mass, E. *et al.* Specification of tissue-resident macrophages during organogenesis. *Science* **353**, aaf4238 (2016).
95. Distribution of blood monocytes between a marginating and a circulating pool. *J. Exp. Med.* **163**, 474 (1986).
96. Swirski, F. K. *et al.* Identification of splenic reservoir monocytes and their deployment to inflammatory sites. *Science* **325**, 612–616 (2009).
97. Geissmann, F., Jung, S. & Littman, D. R. Blood monocytes consist of two principal subsets with distinct migratory properties. *Immunity* **19**, 71–82 (2003).
98. Liu, Z. *et al.* Fate Mapping via Ms4a3-Expression History Traces Monocyte-Derived Cells. *Cell* **178**, 1509-1525.e19 (2019).
99. Hoffman, D. *et al.* A non-classical monocyte-derived macrophage subset provides a splenic replication niche for intracellular Salmonella. *Immunity* **54**, 2712-2723.e6 (2021).
100. Jakubzick, C. *et al.* Minimal differentiation of classical monocytes as they survey steady-state tissues and transport antigen to lymph nodes. *Immunity* **39**, 599–610 (2013).
101. Zhang, P. *et al.* Enhancement of hematopoietic stem cell repopulating capacity and self-renewal in the absence of the transcription factor C/EBP alpha. *Immunity* **21**, 853–863 (2004).
102. Fogg, D. K. *et al.* A Clonogenic Bone Marrow Progenitor Specific for Macrophages and Dendritic Cells. *Science* **311**, 83–87 (2006).
103. Auffray, C. *et al.* CX3CR1+ CD115+ CD135+ common macrophage/DC precursors and the role of CX3CR1 in their response to inflammation. *J. Exp. Med.* **206**, 595–606 (2009).
104. Hettinger, J. *et al.* Origin of monocytes and macrophages in a committed progenitor. *Nat. Immunol.* **14**, 821–830 (2013).
105. Iwasaki, H. & Akashi, K. Myeloid Lineage Commitment from the Hematopoietic Stem Cell. *Immunity* **26**, 726–740 (2007).
106. Carlin, L. M. *et al.* Nr4a1-dependent Ly6C(low) monocytes monitor endothelial cells and orchestrate their disposal. *Cell* **153**, 362–375 (2013).
107. Gamrekelashvili, J. *et al.* Regulation of monocyte cell fate by blood vessels mediated by Notch signalling. *Nat. Commun.* **7**, 12597 (2016).

108. Thierry, G. R. *et al.* Non-classical monocytes scavenge the growth factor CSF1 from endothelial cells in the peripheral vascular tree to ensure survival and homeostasis. *Immunity* **0**, (2024).
109. Yáñez, A. *et al.* Granulocyte-Monocyte Progenitors and Monocyte-Dendritic Cell Progenitors Independently Produce Functionally Distinct Monocytes. *Immunity* **47**, 890-902.e4 (2017).
110. Weinreb, C., Rodriguez-Fraticelli, A., Camargo, F. D. & Klein, A. M. Lineage tracing on transcriptional landscapes links state to fate during differentiation. *Science* **367**, eaaw3381 (2020).
111. Trzebanski, S. *et al.* Classical monocyte ontogeny dictates their functions and fates as tissue macrophages. *Immunity* S1074-7613(24)00224–3 (2024) doi:10.1016/j.immuni.2024.04.019.
112. Bain, C. C. *et al.* Constant replenishment from circulating monocytes maintains the macrophage pool in the intestine of adult mice. *Nat. Immunol.* **15**, 929–937 (2014).
113. Tamoutounour, S. *et al.* Origins and Functional Specialization of Macrophages and of Conventional and Monocyte-Derived Dendritic Cells in Mouse Skin. *Immunity* **39**, 925–938 (2013).
114. Epelman, S. *et al.* Embryonic and Adult-Derived Resident Cardiac Macrophages Are Maintained through Distinct Mechanisms at Steady State and during Inflammation. *Immunity* **40**, 91–104 (2014).
115. Calderon, B. *et al.* The pancreas anatomy conditions the origin and properties of resident macrophages. *J. Exp. Med.* **212**, 1497–1512 (2015).
116. Kaplan, D. H. Ontogeny and function of epidermal murine Langerhans cells. *Nat. Immunol.* **18**, 1068–1075 (2017).
117. Guilliams, M. *et al.* Alveolar macrophages develop from fetal monocytes that differentiate into long-lived cells in the first week of life via GM-CSF. *J. Exp. Med.* **210**, 1977–1992 (2013).
118. Izquierdo, H. M. *et al.* Von Hippel-Lindau Protein Is Required for Optimal Alveolar Macrophage Terminal Differentiation, Self-Renewal, and Function. *Cell Rep.* **24**, 1738–1746 (2018).
119. Gschwend, J. *et al.* Alveolar macrophages rely on GM-CSF from alveolar epithelial type 2 cells before and after birth. *J. Exp. Med.* **218**, e20210745 (2021).
120. Schneider, C. *et al.* Induction of the nuclear receptor PPAR-γ by the cytokine GM-CSF is critical for the differentiation of fetal monocytes into alveolar macrophages. *Nat. Immunol.* **15**, 1026–1037 (2014).
121. Yu, X. *et al.* The Cytokine TGF-β Promotes the Development and Homeostasis of Alveolar Macrophages. *Immunity* **47**, 903-912.e4 (2017).
122. Soucie, E. L. *et al.* Lineage-specific enhancers activate self-renewal genes in macrophages and embryonic stem cells. *Science* **351**, aad5510 (2016).

123. Gomez Perdiguero, E. *et al.* Tissue-resident macrophages originate from yolk-sac-derived erythro-myeloid progenitors. *Nature* **518**, 547–551 (2015).
124. Vanneste, D. *et al.* MafB-restricted local monocyte proliferation precedes lung interstitial macrophage differentiation. *Nat. Immunol.* **24**, 827–840 (2023).
125. Janssen, W. J. *et al.* Fas determines differential fates of resident and recruited macrophages during resolution of acute lung injury. *Am. J. Respir. Crit. Care Med.* **184**, 547–560 (2011).
126. Machiels, B. *et al.* A gammaherpesvirus provides protection against allergic asthma by inducing the replacement of resident alveolar macrophages with regulatory monocytes. *Nat. Immunol.* **18**, 1310–1320 (2017).
127. Sabatel, C. *et al.* Exposure to Bacterial CpG DNA Protects from Airway Allergic Inflammation by Expanding Regulatory Lung Interstitial Macrophages. *Immunity* **46**, 457–473 (2017).
128. Lavine, K. J. *et al.* Distinct macrophage lineages contribute to disparate patterns of cardiac recovery and remodeling in the neonatal and adult heart. *Proc. Natl. Acad. Sci. U. S. A.* **111**, 16029–16034 (2014).
129. Tran, S. *et al.* Impaired Kupffer Cell Self-Renewal Alters the Liver Response to Lipid Overload during Non-alcoholic Steatohepatitis. *Immunity* **53**, 627-640.e5 (2020).
130. Fengqi Li *et al.* Monocyte-derived alveolar macrophages autonomously determine severe outcome of respiratory viral infection. *Sci. Immunol.* **7**, (2022).
131. Aegerter, H. *et al.* Influenza-induced monocyte-derived alveolar macrophages confer prolonged antibacterial protection. *Nat. Immunol.* **21**, 145–157 (2020).
132. Misharin, A. V. *et al.* Monocyte-derived alveolar macrophages drive lung fibrosis and persist in the lung over the life span. *J. Exp. Med.* **214**, 2387–2404 (2017).
133. Bian, Z. *et al.* Deciphering human macrophage development at single-cell resolution. *Nature* **582**, 571–576 (2020).
134. Mass, E., Nimmerjahn, F., Kierdorf, K. & Schlitzer, A. Tissue-specific macrophages: how they develop and choreograph tissue biology. *Nat. Rev. Immunol.* **23**, 563–579 (2023).
135. Boyce, B. F., Yao, Z. & Xing, L. Osteoclasts have Multiple Roles in Bone in Addition to Bone Resorption. *Crit. Rev. Eukaryot. Gene Expr.* **19**, 171–180 (2009).
136. Terpstra, V. & van Berkel, T. J. Scavenger receptors on liver Kupffer cells mediate the in vivo uptake of oxidatively damaged red blood cells in mice. *Blood* **95**, 2157–2163 (2000).
137. Muller, P. A., Matheis, F. & Mucida, D. Gut Macrophages: Key Players in Intestinal Immunity and Tissue Physiology. *Curr. Opin. Immunol.* **62**, 54–61 (2020).

138. García-Fojeda, B., Minutti, C. M., Montero-Fernández, C., Stamme, C. & Casals, C. Signaling Pathways That Mediate Alveolar Macrophage Activation by Surfactant Protein A and IL-4. *Front. Immunol.* **13**, 860262 (2022).

139. Chinnery, H. R., McMenamin, P. G. & Dando, S. J. Macrophage physiology in the eye. *Pflugers Arch.* **469**, 501–515 (2017).

140. M, K.-S. & S, A. Synovial tissue macrophages: friend or foe? *RMD Open* **3**, (2017).

141. Maloy, K. J. & Powrie, F. Intestinal homeostasis and its breakdown in inflammatory bowel disease. *Nature* **474**, 298–306 (2011).

142. McGaha, T. L., Chen, Y., Ravishankar, B., van Rooijen, N. & Karlsson, M. C. I. Marginal zone macrophages suppress innate and adaptive immunity to apoptotic cells in the spleen. *Blood* **117**, 5403–5412 (2011).

143. Franken, L., Schiwon, M. & Kurts, C. Macrophages: sentinels and regulators of the immune system. *Cell. Microbiol.* **18**, 475–487 (2016).

144. Leach, S. M. *et al.* Human and Mouse Transcriptome Profiling Identifies Cross-Species Homology in Pulmonary and Lymph Node Mononuclear Phagocytes. *Cell Rep.* **33**, 108337 (2020).

145. Gautier, E. L. *et al.* Gene-expression profiles and transcriptional regulatory pathways that underlie the identity and diversity of mouse tissue macrophages. *Nat. Immunol.* **13**, 1118–1128 (2012).

146. Kitamura, T. *et al.* Idiopathic pulmonary alveolar proteinosis as an autoimmune disease with neutralizing antibody against granulocyte/macrophage colony-stimulating factor. *J. Exp. Med.* **190**, 875–880 (1999).

147. Huffman Reed, J. A. *et al.* GM-CSF enhances lung growth and causes alveolar type II epithelial cell hyperplasia in transgenic mice. *Am. J. Physiol.* **273**, L715-725 (1997).

148. Gautier, E. L. *et al.* Systemic analysis of PPARγ in mouse macrophage populations reveals marked diversity in expression with critical roles in resolution of inflammation and airway immunity. *J. Immunol. Baltim. Md 1950* **189**, 2614–2624 (2012).

149. Holmskov, U., Thiel, S. & Jensenius, J. C. Collections and ficolins: humoral lectins of the innate immune defense. *Annu. Rev. Immunol.* **21**, 547–578 (2003).

150. Janssen, W. J. *et al.* Surfactant Proteins A and D Suppress Alveolar Macrophage Phagocytosis via Interaction with SIRPα. *Am. J. Respir. Crit. Care Med.* **178**, 158–167 (2008).

151. Snelgrove, R. J. *et al.* A critical function for CD200 in lung immune homeostasis and the severity of influenza infection. *Nat. Immunol.* **9**, 1074–1083 (2008).

152. Morris, D. G. *et al.* Loss of integrin alpha(v)beta6-mediated TGF-beta activation causes Mmp12-dependent emphysema. *Nature* **422**, 169–173 (2003).
153. Murray, P. J. The primary mechanism of the IL-10-regulated antiinflammatory response is to selectively inhibit transcription. *Proc. Natl. Acad. Sci. U. S. A.* **102**, 8686–8691 (2005).
154. Krysko, D. V., D'Herde, K. & Vandenabeele, P. Clearance of apoptotic and necrotic cells and its immunological consequences. *Apoptosis Int. J. Program. Cell Death* **11**, 1709–1726 (2006).
155. Hussell, T. & Bell, T. J. Alveolar macrophages: plasticity in a tissue-specific context. *Nat. Rev. Immunol.* **14**, 81–93 (2014).
156. Franke-Ullmann, G. *et al.* Characterization of murine lung interstitial macrophages in comparison with alveolar macrophages in vitro. *J. Immunol.* **157**, 3097–3104 (1996).
157. Legrand, C. *et al.* Lung Interstitial Macrophages Can Present Soluble Antigens and Induce Foxp3+ Regulatory T Cells. *Am. J. Respir. Cell Mol. Biol.* **70**, 446–456 (2024).
158. Li, X. *et al.* Coordinated chemokine expression defines macrophage subsets across tissues. *Nat. Immunol.* **25**, 1110–1122 (2024).
159. Ruscitti, C. *et al.* Recruited atypical Ly6G+ macrophages license alveolar regeneration after lung injury. *Sci. Immunol.* **9**, eado1227 (2024).
160. Coates, B. M. *et al.* Inflammatory Monocytes Drive Influenza A Virus–Mediated Lung Injury in Juvenile Mice. *J. Immunol.* **200**, 2391–2404 (2018).
161. Chen, S. T. *et al.* A shift in lung macrophage composition is associated with COVID-19 severity and recovery. *Sci. Transl. Med.* **14**, eabn5168 (2022).
162. Zhang, M. *et al.* Multiomic analysis of monocyte-derived alveolar macrophages in idiopathic pulmonary fibrosis. *J. Transl. Med.* **22**, 598 (2024).
163. L, van de L. *et al.* Yolk Sac Macrophages, Fetal Liver, and Adult Monocytes Can Colonize an Empty Niche and Develop into Functional Tissue-Resident Macrophages. *Immunity* **44**, (2016).
164. Mosser, D. M. & Edwards, J. P. Exploring the full spectrum of macrophage activation. *Nat. Rev. Immunol.* **8**, 958–969 (2008).
165. O'Shea, J. J. & Murray, P. J. Cytokine Signaling Modules in Inflammatory Responses. *Immunity* **28**, 477–487 (2008).
166. Allen, J. E. IL-4 and IL-13: Regulators and Effectors of Wound Repair. *Annu. Rev. Immunol.* **41**, 229–254 (2023).

167. Ginhoux, F., Schultze, J. L., Murray, P. J., Ochando, J. & Biswas, S. K. New insights into the multidimensional concept of macrophage ontogeny, activation and function. *Nat. Immunol.* **17**, 34–40 (2016).
168. Murray, P. J. Macrophage Polarization. *Annu. Rev. Physiol.* **79**, 541–566 (2017).
169. Pérez, S. & Rius-Pérez, S. Macrophage Polarization and Reprogramming in Acute Inflammation: A Redox Perspective. *Antioxid. Basel Switz.* **11**, 1394 (2022).
170. Strizova, Z. *et al.* M1/M2 macrophages and their overlaps - myth or reality? *Clin. Sci. Lond. Engl. 1979* **137**, 1067–1093 (2023).
171. Liu, R., Sheng, Z., Huang, C., Wang, D. & Li, F. Influenza D virus. *Curr. Opin. Virol.* **44**, 154–161 (2020).
172. Planer, J. D. & Morrisey, E. E. After the Storm: Regeneration, Repair, and Reestablishment of Homeostasis Between the Alveolar Epithelium and Innate Immune System Following Viral Lung Injury. *Annu. Rev. Pathol.* **18**, 337–359 (2023).
173. Krammer, F. *et al.* Influenza. *Nat. Rev. Dis. Primer* **4**, 3 (2018).
174. Uyeki, T. M., Hui, D. S., Zambon, M., Wentworth, D. E. & Monto, A. S. Influenza. *Lancet Lond. Engl.* **400**, 693–706 (2022).
175. Shinya, K. *et al.* Avian flu: influenza virus receptors in the human airway. *Nature* **440**, 435–436 (2006).
176. Dou, D., Revol, R., Östbye, H., Wang, H. & Daniels, R. Influenza A Virus Cell Entry, Replication, Virion Assembly and Movement. *Front. Immunol.* **9**, 1581 (2018).
177. Atkin-Smith, G. K., Duan, M., Chen, W. & Poon, I. K. H. The induction and consequences of Influenza A virus-induced cell death. *Cell Death Dis.* **9**, 1002 (2018).
178. Schulz, O. *et al.* Toll-like receptor 3 promotes cross-priming to virus-infected cells. *Nature* **433**, 887–892 (2005).
179. Lund, J. M. *et al.* Recognition of single-stranded RNA viruses by Toll-like receptor 7. *Proc. Natl. Acad. Sci. U. S. A.* **101**, 5598–5603 (2004).
180. Pichlmair, A. *et al.* RIG-I-mediated antiviral responses to single-stranded RNA bearing 5'-phosphates. *Science* **314**, 997–1001 (2006).
181. Ichinohe, T., Pang, I. K. & Iwasaki, A. Influenza virus activates inflammasomes via its intracellular M2 ion channel. *Nat. Immunol.* **11**, 404–410 (2010).
182. Pothlichet, J. *et al.* Type I IFN Triggers RIG-I/TLR3/NLRP3-dependent Inflammasome Activation in Influenza A Virus Infected Cells. *PLOS Pathog.* **9**, e1003256 (2013).

183. Schneider, W. M., Chevillotte, M. D. & Rice, C. M. Interferon-stimulated genes: a complex web of host defenses. *Annu. Rev. Immunol.* **32**, 513–545 (2014).

184. Julkunen, I. *et al.* Molecular pathogenesis of influenza A virus infection and virus-induced regulation of cytokine gene expression. *Cytokine Growth Factor Rev.* **12**, 171–180 (2001).

185. Mendelson, M. *et al.* NKp46 O-glycan sequences that are involved in the interaction with hemagglutinin type 1 of influenza virus. *J. Virol.* **84**, 3789–3797 (2010).

186. Hashimoto, G., Wright, P. F. & Karzon, D. T. Antibody-dependent cell-mediated cytotoxicity against influenza virus-infected cells. *J. Infect. Dis.* **148**, 785–794 (1983).

187. van de Sandt, C. E., Kreijtz, J. H. C. M. & Rimmelzwaan, G. F. Evasion of influenza A viruses from innate and adaptive immune responses. *Viruses* **4**, 1438–1476 (2012).

188. GeurtsvanKessel, C. H. *et al.* Dendritic cells are crucial for maintenance of tertiary lymphoid structures in the lung of influenza virus-infected mice. *J. Exp. Med.* **206**, 2339–2349 (2009).

189. Tate, M. D. *et al.* The Role of Neutrophils during Mild and Severe Influenza Virus Infections of Mice. *PLoS ONE* **6**, e17618 (2011).

190. Tate, M. D., Brooks, A. G. & Reading, P. C. The role of neutrophils in the upper and lower respiratory tract during influenza virus infection of mice. *Respir. Res.* **9**, 57 (2008).

191. Narasaraju, T. *et al.* Excessive neutrophils and neutrophil extracellular traps contribute to acute lung injury of influenza pneumonitis. *Am. J. Pathol.* **179**, 199–210 (2011).

192. Hufford, M. M. *et al.* Influenza-Infected Neutrophils within the Infected Lungs Act as Antigen Presenting Cells for Anti-Viral CD8+ T Cells. *PLoS ONE* **7**, e46581 (2012).

193. Hashimoto, Y., Moki, T., Takizawa, T., Shiratsuchi, A. & Nakanishi, Y. Evidence for phagocytosis of influenza virus-infected, apoptotic cells by neutrophils and macrophages in mice. *J. Immunol. Baltim. Md 1950* **178**, 2448–2457 (2007).

194. Bradley, L. M., Douglass, M. F., Chatterjee, D., Akira, S. & Baaten, B. J. G. Matrix metalloprotease 9 mediates neutrophil migration into the airways in response to influenza virus-induced toll-like receptor signaling. *PLoS Pathog.* **8**, e1002641 (2012).

195. Tumpey, T. M., Chen, S. H., Oakes, J. E. & Lausch, R. N. Neutrophil-mediated suppression of virus replication after herpes simplex virus type 1 infection of the murine cornea. *J. Virol.* **70**, 898–904 (1996).

196. Whitmire, J. K., Tan, J. T. & Whitton, J. L. Interferon-γ acts directly on CD8+ T cells to increase their abundance during virus infection. *J. Exp. Med.* **201**, 1053–1059 (2005).

197. Nakanishi, Y., Lu, B., Gerard, C. & Iwasaki, A. CD8(+) T lymphocyte mobilization to virus-infected tissue requires CD4(+) T-cell help. *Nature* **462**, 510–513 (2009).

198. Topham, D. J., Tripp, R. A. & Doherty, P. C. CD8+ T cells clear influenza virus by perforin or Fas-dependent processes. *J. Immunol. Baltim. Md 1950* **159**, 5197–5200 (1997).

199. van Domselaar, R. & Bovenschen, N. Cell death-independent functions of granzymes: hit viruses where it hurts. *Rev. Med. Virol.* **21**, 301–314 (2011).

200. La Gruta, N. L., Turner, S. J. & Doherty, P. C. Hierarchies in cytokine expression profiles for acute and resolving influenza virus-specific CD8+ T cell responses: correlation of cytokine profile and TCR avidity. *J. Immunol. Baltim. Md 1950* **172**, 5553–5560 (2004).

201. Dunbar, P., Wein, A. N., McMaster, S. R., Hayward, S. L. & Kohlmeier, J. E. Tissue-resident monocytes promote the establishment of lung-resident CD8 T cell memory following influenza infection. *J. Immunol.* **196**, 68.7 (2016).

202. Valkenburg, S. A. *et al.* Early priming minimizes the age-related immune compromise of $CD8^+$ T cell diversity and function. *PLoS Pathog.* **8**, e1002544 (2012).

203. Pape, K. A., Khoruts, A., Mondino, A. & Jenkins, M. K. Inflammatory cytokines enhance the in vivo clonal expansion and differentiation of antigen-activated CD4+ T cells. *J. Immunol. Baltim. Md 1950* **159**, 591–598 (1997).

204. Szabo, S. J. *et al.* A novel transcription factor, T-bet, directs Th1 lineage commitment. *Cell* **100**, 655–669 (2000).

205. Zhu, J. & Paul, W. E. Heterogeneity and plasticity of T helper cells. *Cell Res.* **20**, 4–12 (2010).

206. Swain, S. L., McKinstry, K. K. & Strutt, T. M. Expanding roles for $CD4^+$ T cells in immunity to viruses. *Nat. Rev. Immunol.* **12**, 136–148 (2012).

207. Rangel-Moreno, J. *et al.* B cells promote resistance to heterosubtypic strains of influenza via multiple mechanisms. *J. Immunol. Baltim. Md 1950* **180**, 454–463 (2008).

208. Gerhard, W. The role of the antibody response in influenza virus infection. *Curr. Top. Microbiol. Immunol.* **260**, 171–190 (2001).

209. Mozdzanowska, K., Maiese, K., Furchner, M. & Gerhard, W. Treatment of influenza virus-infected SCID mice with nonneutralizing antibodies specific for the transmembrane proteins matrix 2 and neuraminidase reduces the pulmonary virus titer but fails to clear the infection. *Virology* **254**, 138–146 (1999).

210. Seibert, C. W. *et al.* Recombinant IgA is sufficient to prevent influenza virus transmission in guinea pigs. *J. Virol.* **87**, 7793–7804 (2013).

211. Ruscitti, C., Radermecker, C. & Marichal, T. Journey of monocytes and macrophages upon influenza A virus infection. *Curr. Opin. Virol.* **66**, 101409 (2024).
212. Rodriguez-Rodriguez, L., Gillet, L. & Machiels, B. Shaping of the alveolar landscape by respiratory infections and long-term consequences for lung immunity. *Front. Immunol.* **14**, (2023).
213. Li, H., Wang, A., Zhang, Y. & Wei, F. Diverse roles of lung macrophages in the immune response to influenza A virus. *Front. Microbiol.* **14**, 1260543 (2023).
214. Schneider, C. *et al.* Alveolar macrophages are essential for protection from respiratory failure and associated morbidity following influenza virus infection. *PLoS Pathog.* **10**, e1004053 (2014).
215. Kumagai, Y. *et al.* Alveolar Macrophages Are the Primary Interferon-α Producer in Pulmonary Infection with RNA Viruses. *Immunity* **27**, 240–252 (2007).
216. Essers, M. A. G. *et al.* IFNα activates dormant haematopoietic stem cells in vivo. *Nature* **458**, 904–908 (2009).
217. Riel, D. van *et al.* Highly Pathogenic Avian Influenza Virus H5N1 Infects Alveolar Macrophages without Virus Production or Excessive TNF-Alpha Induction. *PLOS Pathog.* **7**, e1002099 (2011).
218. Yu, W. C. L. *et al.* Viral replication and innate host responses in primary human alveolar epithelial cells and alveolar macrophages infected with influenza H5N1 and H1N1 viruses. *J. Virol.* **85**, 6844–6855 (2011).
219. Londrigan, S. L. *et al.* Infection of Mouse Macrophages by Seasonal Influenza Viruses Can Be Restricted at the Level of Virus Entry and at a Late Stage in the Virus Life Cycle. *J. Virol.* **89**, 12319–12329 (2015).
220. Tumpey, T. M. *et al.* Pathogenicity of influenza viruses with genes from the 1918 pandemic virus: functional roles of alveolar macrophages and neutrophils in limiting virus replication and mortality in mice. *J. Virol.* **79**, 14933–14944 (2005).
221. Schneider, D. J. *et al.* Alveolar macrophage-derived extracellular vesicles inhibit endosomal fusion of influenza virus. *EMBO J.* **39**, e105057 (2020).
222. Halstead, E. S. *et al.* GM-CSF overexpression after influenza a virus infection prevents mortality and moderates M1-like airway monocyte/macrophage polarization. *Respir. Res.* **19**, 3 (2018).
223. Huang, F.-F. *et al.* GM-CSF in the lung protects against lethal influenza infection. *Am. J. Respir. Crit. Care Med.* **184**, 259–268 (2011).
224. Sever-Chroneos, Z. *et al.* GM-CSF modulates pulmonary resistance to influenza A infection. *Antiviral Res.* **92**, 319–328 (2011).

225. Pernet, E. *et al.* Neonatal imprinting of alveolar macrophages via neutrophil-derived 12-HETE. *Nature* **614**, 530–538 (2023).
226. Califano, D., Furuya, Y. & Metzger, D. W. Effects of Influenza on Alveolar Macrophage Viability Are Dependent on Mouse Genetic Strain. *J. Immunol. Baltim. Md 1950* **201**, 134–144 (2018).
227. Li, F. *et al.* Monocyte-derived alveolar macrophages autonomously determine severe outcome of respiratory viral infection. *Sci. Immunol.* **7**, eabj5761 (2022).
228. Hofmann, P. *et al.* Susceptibility of mononuclear phagocytes to influenza A virus infection and possible role in the antiviral response. *J. Leukoc. Biol.* **61**, 408–414 (1997).
229. Zhu, B. *et al.* Uncoupling of macrophage inflammation from self-renewal modulates host recovery from respiratory viral infection. *Immunity* **54**, 1200-1218.e9 (2021).
230. Planer, J. D. & Morrisey, E. E. After the Storm: Regeneration, Repair, and Reestablishment of Homeostasis Between the Alveolar Epithelium and Innate Immune System Following Viral Lung Injury. *Annu. Rev. Pathol.* **18**, 337–359 (2023).
231. Guilliams, M. & Svedberg, F. R. Does tissue imprinting restrict macrophage plasticity? *Nat. Immunol.* **22**, 118–127 (2021).
232. Park, M. D., Silvin, A., Ginhoux, F. & Merad, M. Macrophages in health and disease. *Cell* **185**, 4259–4279 (2022).
233. Wong, C. K. *et al.* Aging Impairs Alveolar Macrophage Phagocytosis and Increases Influenza-Induced Mortality in Mice. *J. Immunol. Baltim. Md 1950* **199**, 1060–1068 (2017).
234. McQuattie-Pimentel, A. C. *et al.* The lung microenvironment shapes a dysfunctional response of alveolar macrophages in aging. *J. Clin. Invest.* **131**, 140299 (2021).
235. Liu, Z. *et al.* Fate Mapping via Ms4a3-Expression History Traces Monocyte-Derived Cells. *Cell* **178**, 1509-1525.e19 (2019).
236. McQuattie-Pimentel, A. C. *et al.* The lung microenvironment shapes a dysfunctional response of alveolar macrophages in aging. *J. Clin. Invest.* **131**, (2021).
237. Schyns, J., Bureau, F. & Marichal, T. Lung Interstitial Macrophages: Past, Present, and Future. *J Immunol Res* **2018**, 5160794 (2018).
238. Misharin, A. V. *et al.* Monocyte-derived alveolar macrophages drive lung fibrosis and persist in the lung over the life span. *J. Exp. Med.* **214**, 2387–2404 (2017).
239. Schyns, J. *et al.* Non-classical tissue monocytes and two functionally distinct populations of interstitial macrophages populate the mouse lung. *Nat. Commun.* **10**, 3964 (2019).

240. Sabatel, C. *et al.* Exposure to Bacterial CpG DNA Protects from Airway Allergic Inflammation by Expanding Regulatory Lung Interstitial Macrophages. *Immunity* **46**, 457–473 (2017).
241. Corry, J. *et al.* Infiltration of inflammatory macrophages and neutrophils and widespread pyroptosis in lung drive influenza lethality in nonhuman primates. *PLoS Pathog.* **18**, e1010395 (2022).
242. Zhou, B. *et al.* The angiocrine Rspondin3 instructs interstitial macrophage transition via metabolic-epigenetic reprogramming and resolves inflammatory injury. *Nat. Immunol.* **21**, 1430–1443 (2020).
243. Ogawa, T., Shichino, S., Ueha, S., Bando, K. & Matsushima, K. Profibrotic properties of C1q+ interstitial macrophages in silica-induced pulmonary fibrosis in mice. *Biochem. Biophys. Res. Commun.* **599**, 113–119 (2022).
244. Aran, D. *et al.* Reference-based analysis of lung single-cell sequencing reveals a transitional profibrotic macrophage. *Nat. Immunol.* **20**, 163–172 (2019).
245. Ural, B. B. *et al.* Identification of a nerve-associated, lung-resident interstitial macrophage subset with distinct localization and immunoregulatory properties. *Sci. Immunol.* **5**, eaax8756 (2020).
246. Bedoret, D. *et al.* Lung interstitial macrophages alter dendritic cell functions to prevent airway allergy in mice. *J Clin Invest* **119**, 3723–38 (2009).
247. Kawano, H. *et al.* IL-10-producing lung interstitial macrophages prevent neutrophilic asthma. *Int. Immunol.* **28**, 489–501 (2016).
248. Essers, M. A. G. *et al.* IFNalpha activates dormant haematopoietic stem cells in vivo. *Nature* **458**, 904–908 (2009).
249. Lin, S.-J. *et al.* Type I Interferon Orchestrates Demand-Adapted Monopoiesis during Influenza A Virus Infection via STAT1-Mediated Upregulation of Macrophage Colony-Stimulating Factor Receptor Expression. *J. Virol.* **97**, e00102-23 (2023).
250. Beshara, R. *et al.* Alteration of Flt3-Ligand-dependent de novo generation of conventional dendritic cells during influenza infection contributes to respiratory bacterial superinfection. *PLoS Pathog.* **14**, e1007360 (2018).
251. Seo, S.-U. *et al.* Type I interferon signaling regulates Ly6C(hi) monocytes and neutrophils during acute viral pneumonia in mice. *PLoS Pathog.* **7**, e1001304 (2011).
252. Herold, S. *et al.* Alveolar epithelial cells direct monocyte transepithelial migration upon influenza virus infection: impact of chemokines and adhesion molecules. *J. Immunol. Baltim. Md 1950* **177**, 1817–1824 (2006).

253. Schmit, T. *et al.* Interferon-γ promotes monocyte-mediated lung injury during influenza infection. *Cell Rep.* **38**, 110456 (2022).

254. Allen, I. C. *et al.* The NLRP3 inflammasome mediates in vivo innate immunity to influenza A virus through recognition of viral RNA. *Immunity* **30**, 556–565 (2009).

255. Thomas, P. G. *et al.* The intracellular sensor NLRP3 mediates key innate and healing responses to influenza A virus via the regulation of caspase-1. *Immunity* **30**, 566–575 (2009).

256. Coates, B. M. *et al.* Inhibition of the NOD-Like Receptor Protein 3 Inflammasome Is Protective in Juvenile Influenza A Virus Infection. *Front. Immunol.* **8**, 782 (2017).

257. Wei, X., Narasimhan, H., Zhu, B. & Sun, J. Host Recovery from Respiratory Viral Infection. *Annu. Rev. Immunol.* (2023) doi:10.1146/annurev-immunol-101921-040450.

258. Dawson, T. C., Beck, M. A., Kuziel, W. A., Henderson, F. & Maeda, N. Contrasting effects of CCR5 and CCR2 deficiency in the pulmonary inflammatory response to influenza A virus. *Am. J. Pathol.* **156**, 1951–1959 (2000).

259. Lin, K. L., Suzuki, Y., Nakano, H., Ramsburg, E. & Gunn, M. D. CCR2+ monocyte-derived dendritic cells and exudate macrophages produce influenza-induced pulmonary immune pathology and mortality. *J. Immunol. Baltim. Md 1950* **180**, 2562–2572 (2008).

260. Karupiah, G., Chen, J. H., Mahalingam, S., Nathan, C. F. & MacMicking, J. D. Rapid interferon gamma-dependent clearance of influenza A virus and protection from consolidating pneumonitis in nitric oxide synthase 2-deficient mice. *J. Exp. Med.* **188**, 1541–1546 (1998).

261. Cao, W. *et al.* Rapid differentiation of monocytes into type I IFN-producing myeloid dendritic cells as an antiviral strategy against influenza virus infection. *J. Immunol. Baltim. Md 1950* **189**, 2257–2265 (2012).

262. Cruz, J. L. G. *et al.* Monocyte-derived dendritic cells enhance protection against secondary influenza challenge by controlling the switch in CD8+ T-cell immunodominance. *Eur. J. Immunol.* **47**, 345–352 (2017).

263. Aegerter, H., Lambrecht, B. N. & Jakubzick, C. V. Biology of lung macrophages in health and disease. *Immunity* **55**, 1564–1580 (2022).

264. Aegerter, H. *et al.* Influenza-induced monocyte-derived alveolar macrophages confer prolonged antibacterial protection. *Nat. Immunol.* **21**, 145–157 (2020).

265. Machiels, B. *et al.* A gammaherpesvirus provides protection against allergic asthma by inducing the replacement of resident alveolar macrophages with regulatory monocytes. *Nat Immunol* **18**, 1310–1320 (2017).

266. Stout, R. D. *et al.* Macrophages sequentially change their functional phenotype in response to changes in microenvironmental influences. *J. Immunol. Baltim. Md 1950* **175**, 342–349 (2005).

267. Schilperoort, M. *et al.* The role of efferocytosis-fueled macrophage metabolism in the resolution of inflammation. *Immunol. Rev.* (2023) doi:10.1111/imr.13214.

268. Watanabe, Y., Hashimoto, Y., Shiratsuchi, A., Takizawa, T. & Nakanishi, Y. Augmentation of fatality of influenza in mice by inhibition of phagocytosis. *Biochem. Biophys. Res. Commun.* **337**, 881–886 (2005).

269. Fujimoto, I., Pan, J., Takizawa, T. & Nakanishi, Y. Virus clearance through apoptosis-dependent phagocytosis of influenza A virus-infected cells by macrophages. *J. Virol.* **74**, 3399–3403 (2000).

270. Diskin, C. & Pålsson-McDermott, E. M. Metabolic Modulation in Macrophage Effector Function. *Front. Immunol.* **9**, (2018).

271. Zhang, S. *et al.* Efferocytosis Fuels Requirements of Fatty Acid Oxidation and the Electron Transport Chain to Polarize Macrophages for Tissue Repair. *Cell Metab.* **29**, 443-456.e5 (2019).

272. Chen, W. H. *et al.* Potential Role for Alternatively Activated Macrophages in the Secondary Bacterial Infection During Recovery from Influenza. *Immunol. Lett.* **141**, 227–234 (2012).

273. Li, B. W. S. *et al.* T cells and ILC2s are major effector cells in influenza-induced exacerbation of allergic airway inflammation in mice. *Eur. J. Immunol.* **49**, 144–156 (2019).

274. Wynn, T. A. & Vannella, K. M. Macrophages in Tissue Repair, Regeneration, and Fibrosis. *Immunity* **44**, 450–62 (2016).

275. Gieseck, R. L., Wilson, M. S. & Wynn, T. A. Type 2 immunity in tissue repair and fibrosis. *Nat. Rev. Immunol.* **18**, 62–76 (2018).

276. O'Brien, E. M. & Spiller, K. L. Pro-inflammatory polarization primes Macrophages to transition into a distinct M2-like phenotype in response to IL-4. *J. Leukoc. Biol.* **111**, 989–1000 (2022).

277. Modolell, M., Corraliza, I. M., Link, F., Soler, G. & Eichmann, K. Reciprocal regulation of the nitric oxide synthase/arginase balance in mouse bone marrow-derived macrophages by TH 1 and TH 2 cytokines. *Eur. J. Immunol.* **25**, 1101–1104 (1995).

278. Yurdagul, A. *et al.* Macrophage Metabolism of Apoptotic Cell-Derived Arginine Promotes Continual Efferocytosis and Resolution of Injury. *Cell Metab.* **31**, 518-533.e10 (2020).

279. Baek, A. R. *et al.* Spermidine attenuates bleomycin-induced lung fibrosis by inducing autophagy and inhibiting endoplasmic reticulum stress (ERS)-induced cell death in mice. *Exp. Mol. Med.* **52**, 2034–2045 (2020).

280. Karna, E., Szoka, L., Huynh, T. Y. L. & Palka, J. A. Proline-dependent regulation of collagen metabolism. *Cell. Mol. Life Sci.* **77**, 1911–1918 (2020).

281. Ito, Y. *et al.* Influenza induces IL-8 and GM-CSF secretion by human alveolar epithelial cells through HGF/c-Met and TGF-α/EGFR signaling. *Am. J. Physiol. Lung Cell. Mol. Physiol.* **308**, L1178-1188 (2015).

282. Ghoneim, H. E., Thomas, P. G. & McCullers, J. A. Depletion of alveolar macrophages during influenza infection facilitates bacterial superinfections. *J. Immunol. Baltim. Md 1950* **191**, 1250–1259 (2013).

283. Sun, K. & Metzger, D. W. Inhibition of pulmonary antibacterial defense by interferon-gamma during recovery from influenza infection. *Nat. Med.* **14**, 558–564 (2008).

284. Verma, A. K. *et al.* IFN-γ transforms the transcriptomic landscape and triggers myeloid cell hyperresponsiveness to cause lethal lung injury. *Front. Immunol.* **13**, 1011132 (2022).

285. Roquilly, A. *et al.* Alveolar macrophages are epigenetically altered after inflammation, leading to long-term lung immunoparalysis. *Nat. Immunol.* **21**, 636–648 (2020).

286. Wang, T. *et al.* Influenza-trained mucosal-resident alveolar macrophages confer long-term antitumor immunity in the lungs. *Nat. Immunol.* **24**, 423–438 (2023).

287. Iliakis, C. S. *et al.* The role of recruitment versus training in influenza-induced lasting changes to alveolar macrophage function. *Nat. Immunol.* **24**, 1639–1641 (2023).

288. Fernanda de Mello Costa, M., Weiner, A. I. & Vaughan, A. E. Basal-like Progenitor Cells: A Review of Dysplastic Alveolar Regeneration and Remodeling in Lung Repair. *Stem Cell Rep.* **15**, 1015–1025 (2020).

289. Desai, T. J., Brownfield, D. G. & Krasnow, M. A. Alveolar progenitor and stem cells in lung development, renewal and cancer. *Nature* **507**, 190–194 (2014).

290. Rock, J. R. *et al.* Multiple stromal populations contribute to pulmonary fibrosis without evidence for epithelial to mesenchymal transition. *Proc. Natl. Acad. Sci.* **108**, E1475–E1483 (2011).

291. Barkauskas, C. E. *et al.* Type 2 alveolar cells are stem cells in adult lung. *J. Clin. Invest.* **123**, 3025–3036 (2013).

292. Chung, M.-I., Bujnis, M., Barkauskas, C. E., Kobayashi, Y. & Hogan, B. L. M. Niche-mediated BMP/SMAD signaling regulates lung alveolar stem cell proliferation and differentiation. *Dev. Camb. Engl.* **145**, dev163014 (2018).

293. Lechner, A. J. *et al.* Recruited Monocytes and Type 2 Immunity Promote Lung Regeneration following Pneumonectomy. *Cell Stem Cell* **21**, 120-134.e7 (2017).

294. Liu, Z. *et al.* MAPK-Mediated YAP Activation Controls Mechanical-Tension-Induced Pulmonary Alveolar Regeneration. *Cell Rep.* **16**, 1810–1819 (2016).
295. Snippert, H. J. *et al.* Intestinal Crypt Homeostasis Results from Neutral Competition between Symmetrically Dividing Lgr5 Stem Cells. *Cell* **143**, 134–144 (2010).
296. Zacharias, W. J. *et al.* Regeneration of the lung alveolus by an evolutionarily conserved epithelial progenitor. *Nature* **555**, 251–255 (2018).
297. Nabhan, A. N., Brownfield, D. G., Harbury, P. B., Krasnow, M. A. & Desai, T. J. Single-cell Wnt signaling niches maintain stemness of alveolar type 2 cells. *Science* **359**, 1118–1123 (2018).
298. Travaglini, K. J. *et al.* A molecular cell atlas of the human lung from single-cell RNA sequencing. *Nature* **587**, 619–625 (2020).
299. Frank, D. B. *et al.* Emergence of a Wave of Wnt Signaling that Regulates Lung Alveologenesis by Controlling Epithelial Self-Renewal and Differentiation. *Cell Rep.* **17**, 2312–2325 (2016).
300. Finn, J. *et al.* Dlk1-Mediated Temporal Regulation of Notch Signaling Is Required for Differentiation of Alveolar Type II to Type I Cells during Repair. *Cell Rep.* **26**, 2942-2954.e5 (2019).
301. Zepp, J. A. *et al.* Distinct Mesenchymal Lineages and Niches Promote Epithelial Self-Renewal and Myofibrogenesis in the Lung. *Cell* **170**, 1134-1148.e10 (2017).
302. Ding, B.-S. *et al.* Endothelial-derived inductive angiocrine signals initiate and sustain regenerative lung alveolarization. *Cell* **147**, 539–553 (2011).
303. Rafii, S. *et al.* Platelet-derived SDF-1 primes the pulmonary capillary vascular niche to drive lung alveolar regeneration. *Nat. Cell Biol.* **17**, 123–136 (2015).
304. Jain, R. *et al.* Plasticity of Hopx(+) type I alveolar cells to regenerate type II cells in the lung. *Nat. Commun.* **6**, 6727 (2015).
305. Penkala, I. J. *et al.* Age-dependent alveolar epithelial plasticity orchestrates lung homeostasis and regeneration. *Cell Stem Cell* **28**, 1775-1789.e5 (2021).
306. Liu, K. *et al.* Tracing the origin of alveolar stem cells in lung repair and regeneration. *Cell* **187**, 2428-2445.e20 (2024).
307. Choi, J. *et al.* Inflammatory Signals Induce AT2 Cell-Derived Damage-Associated Transient Progenitors that Mediate Alveolar Regeneration. *Cell Stem Cell* **27**, 366-382.e7 (2020).
308. Strunz, M. *et al.* Alveolar regeneration through a Krt8+ transitional stem cell state that persists in human lung fibrosis. *Nat. Commun.* **11**, 3559 (2020).

309. Jiang, P. *et al.* Ineffectual Type 2-to-Type 1 Alveolar Epithelial Cell Differentiation in Idiopathic Pulmonary Fibrosis: Persistence of the KRT8hi Transitional State. *Am. J. Respir. Crit. Care Med.* **201**, 1443–1447 (2020).

310. Riemondy, K. A. *et al.* Single-cell RNA sequencing identifies TGF-β as a key regenerative cue following LPS-induced lung injury. *JCI Insight* **4**, (2019).

311. Chen, J., Wu, H., Yu, Y. & Tang, N. Pulmonary alveolar regeneration in adult COVID-19 patients. *Cell Res.* **30**, 708–710 (2020).

312. Wu, H. *et al.* Progressive Pulmonary Fibrosis Is Caused by Elevated Mechanical Tension on Alveolar Stem Cells. *Cell* **180**, 107-121.e17 (2020).

313. Conway, E. M. *et al.* Macrophages, Inflammation, and Lung Cancer. *Am. J. Respir. Crit. Care Med.* **193**, 116–130 (2016).

314. Kadur Lakshminarasimha Murthy, P. *et al.* Human distal lung maps and lineage hierarchies reveal a bipotent progenitor. *Nature* **604**, 111–119 (2022).

315. Kumar, P. A. *et al.* Distal airway stem cells yield alveoli in vitro and during lung regeneration following H1N1 influenza infection. *Cell* **147**, 525–538 (2011).

316. Vaughan, A. E. *et al.* Lineage-negative progenitors mobilize to regenerate lung epithelium after major injury. *Nature* **517**, 621–625 (2015).

317. Zuo, W. *et al.* p63+Krt5+ distal airway stem cells are essential for lung regeneration. *Nature* **517**, 616–620 (2015).

318. Ray, S. *et al.* Rare SOX2+ Airway Progenitor Cells Generate KRT5+ Cells that Repopulate Damaged Alveolar Parenchyma following Influenza Virus Infection. *Stem Cell Rep.* **7**, 817–825 (2016).

319. Yang, Y. *et al.* Spatial-Temporal Lineage Restrictions of Embryonic p63+ Progenitors Establish Distinct Stem Cell Pools in Adult Airways. *Dev. Cell* **44**, 752-761.e4 (2018).

320. Smirnova, N. F. *et al.* Detection and quantification of epithelial progenitor cell populations in human healthy and IPF lungs. *Respir. Res.* **17**, 83 (2016).

321. Yee, M. *et al.* Alternative Progenitor Lineages Regenerate the Adult Lung Depleted of Alveolar Epithelial Type 2 Cells. *Am. J. Respir. Cell Mol. Biol.* **56**, 453–464 (2017).

322. Kanegai, C. M. *et al.* Persistent Pathology in Influenza-Infected Mouse Lungs. *Am. J. Respir. Cell Mol. Biol.* **55**, 613–615 (2016).

323. Xi, Y. *et al.* Local lung hypoxia determines epithelial fate decisions during alveolar regeneration. *Nat. Cell Biol.* **19**, 904–914 (2017).

324. Kathiriya, J. J. *et al.* Human alveolar type 2 epithelium transdifferentiates into metaplastic KRT5+ basal cells. *Nat. Cell Biol.* **24**, 10–23 (2022).
325. Taylor, M. S. *et al.* Delayed Alveolar Epithelialization: A Distinct Pathology in Diffuse Acute Lung Injury. *Am. J. Respir. Crit. Care Med.* **197**, 522–524 (2018).
326. Shivaraju, M. *et al.* Airway stem cells sense hypoxia and differentiate into protective solitary neuroendocrine cells. *Science* **371**, 52–57 (2021).
327. Yuan, T. *et al.* FGF10-FGFR2B Signaling Generates Basal Cells and Drives Alveolar Epithelial Regeneration by Bronchial Epithelial Stem Cells after Lung Injury. *Stem Cell Rep.* **12**, 1041–1055 (2019).
328. Basil, M. C. *et al.* The Cellular and Physiological Basis for Lung Repair and Regeneration: Past, Present, and Future. *Cell Stem Cell* **26**, 482–502 (2020).
329. Cheng, P., Li, S. & Chen, H. Macrophages in Lung Injury, Repair, and Fibrosis. *Cells* **10**, 436 (2021).
330. Wang, J. *et al.* Differentiated Human Alveolar Type II Cells Secrete Antiviral IL-29 (IFN-λ1) in Response to Influenza A Infection. *J. Immunol. Baltim. Md 1950* **182**, 1296–1304 (2009).
331. Major, J. *et al.* Type I and III interferons disrupt lung epithelial repair during recovery from viral infection. *Science* **369**, 712–717 (2020).
332. Katsura, H. *et al.* Human Lung Stem Cell-Based Alveolospheres Provide Insights into SARS-CoV-2-Mediated Interferon Responses and Pneumocyte Dysfunction. *Cell Stem Cell* **27**, 890-904.e8 (2020).
333. Schmit, T. *et al.* Interferon (IFN)-γ promotes monocyte-mediated lung injury during influenza infection. *Cell Rep.* **38**, 110456 (2022).
334. Lin, S.-J. *et al.* The pathological effects of CCR2+ inflammatory monocytes are amplified by an IFNAR1-triggered chemokine feedback loop in highly pathogenic influenza infection. *J. Biomed. Sci.* **21**, 99 (2014).
335. Monticelli, L. A. *et al.* Innate lymphoid cells promote lung tissue homeostasis following acute influenza virus infection. *Nat. Immunol.* **12**, 1045–1054 (2011).
336. Ivanov, S. *et al.* Interleukin-22 Reduces Lung Inflammation during Influenza A Virus Infection and Protects against Secondary Bacterial Infection. *J. Virol.* **87**, 6911–6924 (2013).
337. Liberti, D. C. *et al.* Alveolar epithelial cell fate is maintained in a spatially restricted manner to promote lung regeneration after acute injury. *Cell Rep.* **35**, (2021).
338. Katsura, H., Kobayashi, Y., Tata, P. R. & Hogan, B. L. M. IL-1 and TNFα Contribute to the Inflammatory Niche to Enhance Alveolar Regeneration. *Stem Cell Rep.* **12**, 657–666 (2019).

339. Narasimhan, H., Wu, Y., Goplen, N. P. & Sun, J. Immune determinants of chronic sequelae after respiratory viral infection. *Sci. Immunol.* **7**, eabm7996 (2022).
340. Cakarova, L. *et al.* Macrophage tumor necrosis factor-alpha induces epithelial expression of granulocyte-macrophage colony-stimulating factor: impact on alveolar epithelial repair. *Am. J. Respir. Crit. Care Med.* **180**, 521–532 (2009).
341. Huang, S. *et al.* PPAR-γ in Macrophages Limits Pulmonary Inflammation and Promotes Host Recovery following Respiratory Viral Infection. *J. Virol.* **93**, e00030-19 (2019).
342. Saha, S. *et al.* Macrophage-derived extracellular vesicle-packaged WNTs rescue intestinal stem cells and enhance survival after radiation injury. *Nat. Commun.* **7**, 13096 (2016).
343. Hung, L.-Y. *et al.* Macrophages promote epithelial proliferation following infectious and non-infectious lung injury through a Trefoil factor 2-dependent mechanism. *Mucosal Immunol.* **12**, 1 (2018).
344. Luyt, C.-E. *et al.* Long-term Outcomes of Pandemic 2009 Influenza A(H1N1)-Associated Severe ARDS. *CHEST* **142**, 583–592 (2012).
345. Liu, W., Peng, L., Liu, H. & Hua, S. Pulmonary Function and Clinical Manifestations of Patients Infected with Mild Influenza A Virus Subtype H1N1: A One-Year Follow-Up. *PloS One* **10**, e0133698 (2015).
346. Chen, J. *et al.* Long term outcomes in survivors of epidemic Influenza A (H7N9) virus infection. *Sci. Rep.* **7**, 17275 (2017).
347. Lu, P. *et al.* Radiological features of lung changes caused by avian influenza subtype A H5N1 virus: report of two severe adult cases with regular follow-up. *Chin. Med. J. (Engl.)* **123**, 100–104 (2010).
348. Ito, T. *et al.* The Critical Role of Notch Ligand Delta-like 1 in the Pathogenesis of Influenza A Virus (H1N1) Infection. *PLoS Pathog.* **7**, e1002341 (2011).
349. Ortiz-Masiá, D. *et al.* M1 Macrophages Activate Notch Signalling in Epithelial Cells: Relevance in Crohn's Disease. *J. Crohns Colitis* **10**, 582–592 (2016).
350. Huang, W. J. & Tang, X. X. Virus infection induced pulmonary fibrosis. *J. Transl. Med.* **19**, 496 (2021).
351. Phetsouphanh, C. *et al.* Immunological dysfunction persists for 8 months following initial mild-to-moderate SARS-CoV-2 infection. *Nat. Immunol.* **23**, 210–216 (2022).
352. Grant, R. A. *et al.* Circuits between infected macrophages and T cells in SARS-CoV-2 pneumonia. *Nature* **590**, 635–641 (2021).

353. Chambers, R. C. & Mercer, P. F. Mechanisms of alveolar epithelial injury, repair, and fibrosis. *Ann. Am. Thorac. Soc.* 12 Suppl 1, S16-20 (2015).

354. Takamura, S. *et al.* Specific niches for lung-resident memory CD8+ T cells at the site of tissue regeneration enable CD69-independent maintenance. *J. Exp. Med.* 213, 3057–3073 (2016).

355. Choi, J. *et al.* Release of Notch activity coordinated by IL-1β signalling confers differentiation plasticity of airway progenitors via Fosl2 during alveolar regeneration. *Nat. Cell Biol.* 23, 953–966 (2021).

356. Shirey, K. A. *et al.* Control of RSV-induced lung injury by alternatively activated macrophages is IL-4R alpha-, TLR4-, and IFN-beta-dependent. *Mucosal Immunol.* 3, 291–300 (2010).

357. Lech, M. & Anders, H.-J. Macrophages and fibrosis: How resident and infiltrating mononuclear phagocytes orchestrate all phases of tissue injury and repair. *Biochim. Biophys. Acta BBA - Mol. Basis Dis.* 1832, 989–997 (2013).

358. Byrne, A. J., Mathie, S. A., Gregory, L. G. & Lloyd, C. M. Pulmonary macrophages: key players in the innate defence of the airways. *Thorax* 70, 1189–1196 (2015).

359. Gibbons, M. A. *et al.* Ly6Chi Monocytes Direct Alternatively Activated Profibrotic Macrophage Regulation of Lung Fibrosis. *Am. J. Respir. Crit. Care Med.* 184, 569–581 (2011).

360. Watanabe, S., Alexander, M., Misharin, A. V. & Budinger, G. R. S. The role of macrophages in the resolution of inflammation. *J. Clin. Invest.* 129, 2619–2628 (2019).

361. Bellac, C. L. *et al.* Macrophage matrix metalloproteinase-12 dampens inflammation and neutrophil influx in arthritis. *Cell Rep.* 9, 618–632 (2014).

362. McQuibban, G. A. *et al.* Matrix metalloproteinase processing of monocyte chemoattractant proteins generates CC chemokine receptor antagonists with anti-inflammatory properties in vivo. *Blood* 100, 1160–1167 (2002).

363. Herold, S. *et al.* Exudate Macrophages Attenuate Lung Injury by the Release of IL-1 Receptor Antagonist in Gram-negative Pneumonia. *Am. J. Respir. Crit. Care Med.* 183, 1380–1390 (2011).

364. Kantari, C., Pederzoli-Ribeil, M. & Witko-Sarsat, V. The Role of Neutrophils and Monocytes in Innate Immunity. in *Contributions to Microbiology* (eds. Egesten, A., Schmidt, A. & Herwald, H.) 118–146 (KARGER, Basel, 2008). doi:10.1159/000136335.

365. Herold, S. *et al.* Lung epithelial apoptosis in influenza virus pneumonia: the role of macrophage-expressed TNF-related apoptosis-inducing ligand. *J. Exp. Med.* 205, 3065–3077 (2008).

366. McGrath, E. E. *et al.* TNF-related apoptosis-inducing ligand (TRAIL) regulates inflammatory neutrophil apoptosis and enhances resolution of inflammation. *J. Leukoc. Biol.* **90**, 855–865 (2011).

367. Lim, K. *et al.* In situ neutrophil efferocytosis shapes T cell immunity to influenza infection. *Nat. Immunol.* **21**, 1046–1057 (2020).

368. Bosurgi, L. *et al.* Macrophage function in tissue repair and remodeling requires IL-4 or IL-13 with apoptotic cells. *Science* **356**, 1072–1076 (2017).

369. Soehnlein, O. & Lindbom, L. Phagocyte partnership during the onset and resolution of inflammation. *Nat. Rev. Immunol.* **10**, 427–439 (2010).

370. Medeiros, A. I., Serezani, C. H., Lee, S. P. & Peters-Golden, M. Efferocytosis impairs pulmonary macrophage and lung antibacterial function via PGE2/EP2 signaling. *J. Exp. Med.* **206**, 61–68 (2009).

371. Fadok, V. A. *et al.* Macrophages that have ingested apoptotic cells in vitro inhibit proinflammatory cytokine production through autocrine/paracrine mechanisms involving TGF-beta, PGE2, and PAF. *J. Clin. Invest.* **101**, 890–898 (1998).

372. Golpon, H. A. *et al.* Life after corpse engulfment: phagocytosis of apoptotic cells leads to VEGF secretion and cell growth. *FASEB J. Off. Publ. Fed. Am. Soc. Exp. Biol.* **18**, 1716–1718 (2004).

373. Amano, H. *et al.* Essential Contribution of Monocyte Chemoattractant Protein-1/C-C Chemokine Ligand-2 to Resolution and Repair Processes in Acute Bacterial Pneumonia. *J. Immunol.* **172**, 398–409 (2004).

374. Bosurgi, L. *et al.* Paradoxical role of the proto-oncogene Axl and Mer receptor tyrosine kinases in colon cancer. *Proc. Natl. Acad. Sci. U. S. A.* **110**, 13091–13096 (2013).

375. Graham, A., Allen, J. & Read, A. Evolutionary Causes and Consequences of Immunopathology. *Annu Rev Ecol Evol Syst* **36**, 373–97 (2005).

376. Allen, J. & Wynn, T. Evolution of Th2 Immunity: A Rapid Repair Response to Tissue Destructive Pathogens. *PLoS Pathog.* **7**, e1002003 (2011).

377. Duchesne, M., Okoye, I. & Lacy, P. Epithelial cell alarmin cytokines: Frontline mediators of the asthma inflammatory response. *Front. Immunol.* **13**, (2022).

378. Koyasu, S. & Moro, K. Type 2 innate immune responses and the natural helper cell. *Immunology* **132**, 475–481 (2011).

379. Lee, H.-G., Cho, M.-J. & Choi, J.-M. Bystander CD4+ T cells: crossroads between innate and adaptive immunity. *Exp. Mol. Med.* **52**, 1255–1263 (2020).

380. Albina, J. E., Mills, C. D., Henry, W. L. & Caldwell, M. D. Temporal expression of different pathways of 1-arginine metabolism in healing wounds. *J. Immunol. Baltim. Md 1950* **144**, 3877–3880 (1990).
381. Loke, P. *et al.* IL-4 dependent alternatively-activated macrophages have a distinctive in vivo gene expression phenotype. *BMC Immunol.* **3**, 7 (2002).
382. Herbert, D. R. *et al.* Alternative Macrophage Activation Is Essential for Survival during Schistosomiasis and Downmodulates T Helper 1 Responses and Immunopathology. *Immunity* **20**, 623–635 (2004).
383. Chen, F. *et al.* An essential role for TH2-type responses in limiting acute tissue damage during experimental helminth infection. *Nat. Med.* **18**, 260–266 (2012).
384. Impellizzieri, D. *et al.* IL-4 receptor engagement in human neutrophils impairs their migration and extracellular trap formation. *J. Allergy Clin. Immunol.* **144**, 267-279.e4 (2019).
385. Woytschak, J. *et al.* Type 2 Interleukin-4 Receptor Signaling in Neutrophils Antagonizes Their Expansion and Migration during Infection and Inflammation. *Immunity* **45**, 172–184 (2016).
386. Thomas, G. D. *et al.* The biology of nematode- and IL4Rα-dependent murine macrophage polarization in vivo as defined by RNA-Seq and targeted lipidomics. *Blood* **120**, e93–e104 (2012).
387. Daseke, M. J. *et al.* Exogenous IL-4 shuts off pro-inflammation in neutrophils while stimulating anti-inflammation in macrophages to induce neutrophil phagocytosis following myocardial infarction. *J. Mol. Cell. Cardiol.* **145**, 112–121 (2020).
388. Willenborg, S. *et al.* CCR2 recruits an inflammatory macrophage subpopulation critical for angiogenesis in tissue repair. *Blood* **120**, 613–625 (2012).
389. Galván-Peña, S. & O'Neill, L. A. J. Metabolic Reprograming in Macrophage Polarization. *Front. Immunol.* **5**, (2014).
390. Holcomb, I. N. *et al.* FIZZ1, a novel cysteine-rich secreted protein associated with pulmonary inflammation, defines a new gene family. *EMBO J.* **19**, 4046–4055 (2000).
391. Pesce, J. T. *et al.* Retnla (Relmα/Fizz1) Suppresses Helminth-Induced Th2-Type Immunity. *PLoS Pathog.* **5**, e1000393 (2009).
392. Nair, M. G. *et al.* Alternatively activated macrophage-derived RELM-α is a negative regulator of type 2 inflammation in the lung. *J. Exp. Med.* **206**, 937–952 (2009).
393. Krljanac, B. *et al.* RELMα-expressing macrophages protect against fatal lung damage and reduce parasite burden during helminth infection. *Sci. Immunol.* **4**, eaau3814 (2019).
394. Martí I Líndez, A.-A. & Reith, W. Arginine-dependent immune responses. *Cell. Mol. Life Sci. CMLS* **78**, 5303–5324 (2021).

395. Rodriguez, P. C. *et al.* L-arginine consumption by macrophages modulates the expression of CD3 zeta chain in T lymphocytes. *J. Immunol. Baltim. Md 1950* **171**, 1232–1239 (2003).

396. Pesce, J. T. *et al.* Arginase-1-expressing macrophages suppress Th2 cytokine-driven inflammation and fibrosis. *PLoS Pathog.* **5**, e1000371 (2009).

397. Dichtl, S. *et al.* Lactate and IL6 define separable paths of inflammatory metabolic adaptation. *Sci. Adv.* **7**, eabg3505 (2021).

398. Colegio, O. R. *et al.* Functional polarization of tumour-associated macrophages by tumour-derived lactic acid. *Nature* **513**, 559–563 (2014).

399. Iniesta, V. *et al.* Arginase I induction in macrophages, triggered by Th2-type cytokines, supports the growth of intracellular Leishmania parasites. *Parasite Immunol.* **24**, 113–118 (2002).

400. Travis, M. A. & Sheppard, D. TGF-β Activation and Function in Immunity. *Annu. Rev. Immunol.* **32**, 51–82 (2014).

401. Gorelik, L., Fields, P. E. & Flavell, R. A. Cutting edge: TGF-beta inhibits Th type 2 development through inhibition of GATA-3 expression. *J. Immunol. Baltim. Md 1950* **165**, 4773–4777 (2000).

402. Yamagiwa, S., Gray, J. D., Hashimoto, S. & Horwitz, D. A. A role for TGF-beta in the generation and expansion of CD4+CD25+ regulatory T cells from human peripheral blood. *J. Immunol. Baltim. Md 1950* **166**, 7282–7289 (2001).

403. Li, M. O., Wan, Y. Y., Sanjabi, S., Robertson, A.-K. L. & Flavell, R. A. Transforming growth factor-beta regulation of immune responses. *Annu. Rev. Immunol.* **24**, 99–146 (2006).

404. McDonald, P. P., Fadok, V. A., Bratton, D. & Henson, P. M. Transcriptional and translational regulation of inflammatory mediator production by endogenous TGF-beta in macrophages that have ingested apoptotic cells. *J. Immunol. Baltim. Md 1950* **163**, 6164–6172 (1999).

405. Ouyang, W., Rutz, S., Crellin, N. K., Valdez, P. A. & Hymowitz, S. G. Regulation and Functions of the IL-10 Family of Cytokines in Inflammation and Disease. *Annu. Rev. Immunol.* **29**, 71–109 (2011).

406. Eming, S. A. *et al.* Accelerated Wound Closure in Mice Deficient for Interleukin-10. *Am. J. Pathol.* **170**, 188–202 (2007).

407. Minutti, C. M. *et al.* A Macrophage-Pericyte Axis Directs Tissue Restoration via Amphiregulin-Induced Transforming Growth Factor Beta Activation. *Immunity* **50**, 645-654.e6 (2019).

408. Xu, Y. *et al.* Classically Activated Macrophages Protect against Lipopolysaccharide-induced Acute Lung Injury by Expressing Amphiregulin in Mice. *Anesthesiology* **124**, 1086–1099 (2016).

409. Kaiser, K. A., Loffredo, L. F., Santos-Alexis, K. de los, Ringham, O. R. & Arpaia, N. Regulation of the alveolar regenerative niche by amphiregulin-producing regulatory T cells. *J. Exp. Med.* **220**, e20221462 (2022).

410. Manich, G. *et al.* Role of the CD200-CD200R Axis During Homeostasis and Neuroinflammation. *Neuroscience* **405**, 118–136 (2019).

411. Bhattacharya, P. *et al.* Dual Role of GM-CSF as a Pro-Inflammatory and a Regulatory Cytokine: Implications for Immune Therapy. *J. Interferon Cytokine Res.* **35**, 585–599 (2015).

412. Van den Bossche, J., Malissen, B., Mantovani, A., De Baetselier, P. & Van Ginderachter, J. A. Regulation and function of the E-cadherin/catenin complex in cells of the monocyte-macrophage lineage and DCs. *Blood* **119**, 1623–1633 (2012).

413. Knipper, J. A. *et al.* Interleukin-4 Receptor α Signaling in Myeloid Cells Controls Collagen Fibril Assembly in Skin Repair. *Immunity* **43**, 803–816 (2015).

414. Sutherland, T. E. *et al.* Ym1 induces RELMα and rescues IL-4Rα deficiency in lung repair during nematode infection. *PLOS Pathog.* **14**, e1007423 (2018).

415. Lee, C. G. *et al.* Interleukin-13 induces tissue fibrosis by selectively stimulating and activating transforming growth factor beta(1). *J. Exp. Med.* **194**, 809–821 (2001).

416. Jeong, H.-W. & Kim, I.-S. TGF-beta1 enhances betaig-h3-mediated keratinocyte cell migration through the alpha3beta1 integrin and PI3K. *J. Cell. Biochem.* **92**, 770–780 (2004).

417. Pertovaara, L. *et al.* Vascular endothelial growth factor is induced in response to transforming growth factor-beta in fibroblastic and epithelial cells. *J. Biol. Chem.* **269**, 6271–6274 (1994).

418. Deng, Z. *et al.* TGF-β signaling in health, disease, and therapeutics. *Signal Transduct. Target. Ther.* **9**, 1–40 (2024).

419. Tager, A. M. *et al.* Inhibition of pulmonary fibrosis by the chemokine IP-10/CXCL10. *Am. J. Respir. Cell Mol. Biol.* **31**, 395–404 (2004).

420. Jiang, D. *et al.* Regulation of pulmonary fibrosis by chemokine receptor CXCR3. *J. Clin. Invest.* **114**, 291–299 (2004).

421. Nakamura, A. *et al.* Symbiotic polyamine metabolism regulates epithelial proliferation and macrophage differentiation in the colon. *Nat. Commun.* **12**, 2105 (2021).

422. Caldwell, R. W., Rodriguez, P. C., Toque, H. A., Narayanan, S. P. & Caldwell, R. B. Arginase: A Multifaceted Enzyme Important in Health and Disease. *Physiol. Rev.* **98**, 641–665 (2018).

423. Marunaka, Y. *et al.* Regulation of Epithelial Sodium Transport via Epithelial Na+ Channel. *J. Biomed. Biotechnol.* **2011**, 978196 (2011).

424. Jenkins, R. G. *et al.* An Official American Thoracic Society Workshop Report: Use of Animal Models for the Preclinical Assessment of Potential Therapies for Pulmonary Fibrosis. *Am. J. Respir. Cell Mol. Biol.* **56**, 667–679 (2017).

425. Izbicki, G., Segel, M. J., Christensen, T. G., Conner, M. W. & Breuer, R. Time course of bleomycin-induced lung fibrosis. *Int. J. Exp. Pathol.* **83**, 111–119 (2002).

426. Chua, F., Gauldie, J. & Laurent, G. J. Pulmonary fibrosis: searching for model answers. *Am. J. Respir. Cell Mol. Biol.* **33**, 9–13 (2005).

427. Libório-Ramos, S., Barbosa-Matos, C., Fernandes, R., Borges-Pereira, C. & Costa, S. Interstitial Macrophages Lead Early Stages of Bleomycin-Induced Lung Fibrosis and Induce Fibroblasts Activation. *Cells* **12**, 402 (2023).

428. McCubbrey, A. L. *et al.* Deletion of c-FLIP from CD11bhi Macrophages Prevents Development of Bleomycin-induced Lung Fibrosis. *Am. J. Respir. Cell Mol. Biol.* (2017) doi:10.1165/rcmb.2017-0154OC.

429. Moore, B. B. *et al.* CCR2-Mediated Recruitment of Fibrocytes to the Alveolar Space after Fibrotic Injury. *Am. J. Pathol.* **166**, 675–684 (2005).

430. Aran, D. *et al.* Reference-based analysis of lung single-cell sequencing reveals a transitional profibrotic macrophage. *Nat. Immunol.* **20**, 163–172 (2019).

431. Adams, T. S. *et al.* Single-cell RNA-seq reveals ectopic and aberrant lung-resident cell populations in idiopathic pulmonary fibrosis. *Sci. Adv.* **6**, eaba1983 (2020).

432. Meziani, L. *et al.* CSF1R inhibition prevents radiation pulmonary fibrosis by depletion of interstitial macrophages. *Eur. Respir. J.* **51**, 1702120 (2018).

433. Morse, C. *et al.* Proliferating SPP1/MERTK-expressing macrophages in idiopathic pulmonary fibrosis. *Eur. Respir. J.* **54**, 1802441 (2019).

434. Single Cell RNA-seq and Mass Cytometry Reveals a Novel and a Targetable Population of Macrophages in Idiopathic Pulmonary Fibrosis | bioRxiv. https://www.biorxiv.org/content/10.1101/2021.01.04.425268v1.

435. Wendisch, D. *et al.* SARS-CoV-2 infection triggers profibrotic macrophage responses and lung fibrosis. *Cell* **184**, 6243-6261.e27 (2021).

436. Vannan, A. *et al.* Image-based spatial transcriptomics identifies molecular niche dysregulation associated with distal lung remodeling in pulmonary fibrosis. *BioRxiv Prepr. Serv. Biol.* 2023.12.15.571954 (2023) doi:10.1101/2023.12.15.571954.

437. Satoh, T. *et al.* Identification of an atypical monocyte and committed progenitor involved in fibrosis. *Nature* **541**, 96–101 (2017).

438. Ashkar, S. *et al.* Eta-1 (osteopontin): an early component of type-1 (cell-mediated) immunity. *Science* **287**, 860–864 (2000).

439. Lin, Y.-H. *et al.* Coupling of Osteopontin and Its Cell Surface Receptor CD44 to the Cell Survival Response Elicited by Interleukin-3 or Granulocyte-Macrophage Colony-Stimulating Factor. *Mol. Cell. Biol.* **20**, 2734–2742 (2000).

440. Lenga, Y. *et al.* Osteopontin expression is required for myofibroblast differentiation. *Circ. Res.* **102**, 319–327 (2008).

441. GBD 2015 LRI Collaborators. Estimates of the global, regional, and national morbidity, mortality, and aetiologies of lower respiratory tract infections in 195 countries: a systematic analysis for the Global Burden of Disease Study 2015. *Lancet Infect. Dis.* **17**, 1133–1161 (2017).

442. Fendrick, A. M., Monto, A. S., Nightengale, B. & Sarnes, M. The Economic Burden of Non–Influenza-Related Viral Respiratory Tract Infection in the United States. *Arch. Intern. Med.* **163**, 487–494 (2003).

443. Nalbandian, A. *et al.* Post-acute COVID-19 syndrome. *Nat. Med.* **27**, 601–615 (2021).

444. Hernandez-Vargas, E. A. *et al.* Effects of Aging on Influenza Virus Infection Dynamics. *J. Virol.* **88**, 4123–4131 (2014).

445. Xie, Y., Choi, T. & Al-Aly, Z. Long-term outcomes following hospital admission for COVID-19 versus seasonal influenza: a cohort study. *Lancet Infect. Dis.* **24**, 239–255 (2024).

446. Nguyen, T. H. O., Rowntree, L. C., Chua, B. Y., Thwaites, R. S. & Kedzierska, K. Defining the balance between optimal immunity and immunopathology in influenza virus infection. *Nat. Rev. Immunol.* 1–16 (2024) doi:10.1038/s41577-024-01029-1.

447. Iliakis, C. S. & Wack, A. Never trust a single myeloid marker: Ly6G on repair-promoting lung macrophages. *Sci. Immunol.* **9**, eadq7306 (2024).

448. Jung, S. *et al.* Analysis of fractalkine receptor CX(3)CR1 function by targeted deletion and green fluorescent protein reporter gene insertion. *Mol Cell Biol* **20**, 4106–14 (2000).

449. Boring, L. *et al.* Impaired monocyte migration and reduced type 1 (Th1) cytokine responses in C-C chemokine receptor 2 knockout mice. *J. Clin. Invest.* **100**, 2552–2561 (1997).

450. Ballesteros, I. *et al.* Co-option of Neutrophil Fates by Tissue Environments. *Cell* **183**, 1282-1297.e18 (2020).

451. Madisen, L. *et al.* A robust and high-throughput Cre reporting and characterization system for the whole mouse brain. *Nat. Neurosci.* **13**, 133–140 (2010).
452. Wende, H. *et al.* The transcription factor c-Maf controls touch receptor development and function. *Science* **335**, 1373–1376 (2012).
453. Clausen, B. E., Burkhardt, C., Reith, W., Renkawitz, R. & Forster, I. Conditional gene targeting in macrophages and granulocytes using LysMcre mice. *Transgenic Res* **8**, 265–77 (1999).
454. Radermecker, C. *et al.* Locally instructed CXCR4hi neutrophils trigger environment-driven allergic asthma through the release of neutrophil extracellular traps. *Nat. Immunol.* **20**, 1444–1455 (2019).
455. Aibar, S. *et al.* SCENIC: single-cell regulatory network inference and clustering. *Nat. Methods* **14**, 1083–1086 (2017).
456. Street, K. *et al.* Slingshot: cell lineage and pseudotime inference for single-cell transcriptomics. *BMC Genomics* **19**, 477 (2018).
457. Van den Berge, K. *et al.* Trajectory-based differential expression analysis for single-cell sequencing data. *Nat. Commun.* **11**, 1201 (2020).
458. Gu, Z., Eils, R. & Schlesner, M. Complex heatmaps reveal patterns and correlations in multidimensional genomic data. *Bioinforma. Oxf. Engl.* **32**, 2847–2849 (2016).
459. Subramanian, A. *et al.* Gene set enrichment analysis: a knowledge-based approach for interpreting genome-wide expression profiles. *Proc Natl Acad Sci U A* **102**, 15545–50 (2005).
460. Nokin, M.-J. *et al.* Hormetic potential of methylglyoxal, a side-product of glycolysis, in switching tumours from growth to death. *Sci. Rep.* **7**, 11722 (2017).
461. Rademaker, G. *et al.* Myoferlin controls mitochondrial structure and activity in pancreatic ductal adenocarcinoma, and affects tumor aggressiveness. *Oncogene* **37**, 4398–4412 (2018).
462. Dinnon, K. H. *et al.* SARS-CoV-2 infection produces chronic pulmonary epithelial and immune cell dysfunction with fibrosis in mice. *Sci. Transl. Med.* **14**, eabo5070 (2022).
463. Danaher, P. *et al.* Advances in mixed cell deconvolution enable quantification of cell types in spatial transcriptomic data. *Nat. Commun.* **13**, 385 (2022).
464. Choi, J. *et al.* Inflammatory Signals Induce AT2 Cell-Derived Damage-Associated Transient Progenitors that Mediate Alveolar Regeneration. *Cell Stem Cell* **27**, 366-382.e7 (2020).
465. Foroutan, M. *et al.* Single sample scoring of molecular phenotypes. *BMC Bioinformatics* **19**, 404 (2018).

466. Scott, C. L. *et al.* Bone marrow-derived monocytes give rise to self-renewing and fully differentiated Kupffer cells. *Nat Commun* **7**, 10321 (2016).
467. Stuart, T. *et al.* Comprehensive Integration of Single-Cell Data. *Cell* **177**, 1888-1902.e21 (2019).
468. Herold, S., Becker, C., Ridge, K. M. & Budinger, G. R. S. Influenza virus-induced lung injury: pathogenesis and implications for treatment. *Eur. Respir. J.* **45**, 1463–1478 (2015).
469. Chen, J. *et al.* SLAMF7 is critical for phagocytosis of haematopoietic tumour cells via Mac-1 integrin. *Nature* **544**, 493–497 (2017).
470. Wu, Y. *et al.* SLAMF7 regulates the inflammatory response in macrophages during polymicrobial sepsis. *J. Clin. Invest.* **133**, e150224 (2023).
471. Zheng, G. X. *et al.* Massively parallel digital transcriptional profiling of single cells. *Nat Commun* **8**, 14049 (2017).
472. Serbina, N. V. & Pamer, E. G. Monocyte emigration from bone marrow during bacterial infection requires signals mediated by chemokine receptor CCR2. *Nat Immunol* **7**, 311–7 (2006).
473. Adamson, I. Y. & Bowden, D. H. The type 2 cell as progenitor of alveolar epithelial regeneration. A cytodynamic study in mice after exposure to oxygen. *Lab. Investig. J. Tech. Methods Pathol.* **30**, 35–42 (1974).
474. Minutti, C. M. *et al.* Local amplifiers of IL-4Rα-mediated macrophage activation promote repair in lung and liver. *Science* **356**, 1076–1080 (2017).
475. Bosurgi, L. *et al.* Macrophage function in tissue repair and remodeling requires IL-4 or IL-13 with apoptotic cells. *Science* **356**, 1072–1076 (2017).
476. Fleming, T. J., Fleming, M. L. & Malek, T. R. Selective expression of Ly-6G on myeloid lineage cells in mouse bone marrow. RB6-8C5 mAb to granulocyte-differentiation antigen (Gr-1) detects members of the Ly-6 family. *J. Immunol. Baltim. Md 1950* **151**, 2399–2408 (1993).
477. Upadhyay, G. Emerging Role of Lymphocyte Antigen-6 Family of Genes in Cancer and Immune Cells. *Front. Immunol.* **10**, 819 (2019).
478. Stroncek, D. F. Neutrophil-specific antigen HNA-2a, NB1 glycoprotein, and CD177. *Curr. Opin. Hematol.* **14**, 688–693 (2007).
479. Wang, J.-X. *et al.* Ly6G ligation blocks recruitment of neutrophils via a β2-integrin–dependent mechanism. *Blood* **120**, 1489–1498 (2012).
480. Boivin, G. *et al.* Durable and controlled depletion of neutrophils in mice. *Nat. Commun.* **11**, 2762 (2020).

481. Daley, J. M., Thomay, A. A., Connolly, M. D., Reichner, J. S. & Albina, J. E. Use of Ly6G-specific monoclonal antibody to deplete neutrophils in mice. *J. Leukoc. Biol.* **83**, 64–70 (2008).

482. Schmit, T. *et al.* Interferon-γ promotes monocyte-mediated lung injury during influenza infection. *Cell Rep.* **38**, 110456 (2022).

483. Ishida, K. *et al.* Induction of unique macrophage subset by simultaneous stimulation with LPS and IL-4. *Front. Immunol.* **14**, 1111729 (2023).

484. Blériot, C. *et al.* Liver-resident macrophage necroptosis orchestrates type 1 microbicidal inflammation and type-2-mediated tissue repair during bacterial infection. *Immunity* **42**, 145–158 (2015).

485. Duffield, J. S. *et al.* Selective depletion of macrophages reveals distinct, opposing roles during liver injury and repair. *J. Clin. Invest.* **115**, 56–65 (2005).

486. Mitchell, C. *et al.* Dual Role of CCR2 in the Constitution and the Resolution of Liver Fibrosis in Mice. *Am. J. Pathol.* **174**, 1766–1775 (2009).

487. Antoniades, C. G. *et al.* Source and characterization of hepatic macrophages in acetaminophen-induced acute liver failure in humans. *Hepatol. Baltim. Md* **56**, 735–746 (2012).

488. Horst, A. K., Tiegs, G. & Diehl, L. Contribution of Macrophage Efferocytosis to Liver Homeostasis and Disease. *Front. Immunol.* **10**, (2019).

489. Hamilton, J. A. GM-CSF in inflammation. *J. Exp. Med.* **217**, e20190945 (2020).

490. Lotfi, N. *et al.* Roles of GM-CSF in the Pathogenesis of Autoimmune Diseases: An Update. *Front. Immunol.* **10**, (2019).

491. Lee, S.-J. *et al.* Local administration of granulocyte macrophage colony-stimulating factor induces local accumulation of dendritic cells and antigen-specific CD8+ T cells and enhances dendritic cell cross-presentation. *Vaccine* **33**, 1549–1555 (2015).

492. Burg, J., Krump-Konvalinkova, V., Bittinger, F. & Kirkpatrick, C. J. GM-CSF expression by human lung microvascular endothelial cells: in vitro and in vivo findings. *Am. J. Physiol. Lung Cell. Mol. Physiol.* **283**, L460-467 (2002).

493. Fitzgerald, S. M. *et al.* GM-CSF induction in human lung fibroblasts by IL-1beta, TNF-alpha, and macrophage contact. *J. Interferon Cytokine Res. Off. J. Int. Soc. Interferon Cytokine Res.* **23**, 57–65 (2003).

494. Komuczki, J. *et al.* Fate-Mapping of GM-CSF Expression Identifies a Discrete Subset of Inflammation-Driving T Helper Cells Regulated by Cytokines IL-23 and IL-1β. *Immunity* **50**, 1289-1304.e6 (2019).

495. Ganesh, B. B., Cheatem, D. M., Sheng, J. R., Vasu, C. & Prabhakar, B. S. GM-CSF-induced CD11c+CD8a—dendritic cells facilitate Foxp3+ and IL-10+ regulatory T cell expansion resulting in suppression of autoimmune thyroiditis. *Int. Immunol.* **21**, 269 (2009).
496. Sturrock, A. *et al.* GM-CSF provides autocrine protection for murine alveolar epithelial cells from oxidant-induced mitochondrial injury. *Am. J. Physiol.-Lung Cell. Mol. Physiol.* **302**, L343–L351 (2012).
497. Christensen, P. J. *et al.* Role of diminished epithelial GM-CSF in the pathogenesis of bleomycin-induced pulmonary fibrosis. *Am. J. Physiol. Lung Cell. Mol. Physiol.* **279**, L487-495 (2000).
498. Li, N., Zhang, L., Li, H. & Fang, B. Administration of granulocyte colony-stimulating factor ameliorates radiation-induced hepatic fibrosis in mice. *Transplant. Proc.* **42**, 3833–3839 (2010).
499. Bosteels, C. *et al.* Loss of GM-CSF-dependent instruction of alveolar macrophages in COVID-19 provides a rationale for inhaled GM-CSF treatment. *Cell Rep. Med.* **3**, 100833 (2022).
500. McCubbrey, A. L. *et al.* Polyamine import and accumulation causes immunomodulation in macrophages engulfing apoptotic cells. *Cell Rep.* **38**, 110222 (2022).
501. de Oliveira, S., Rosowski, E. E. & Huttenlocher, A. Neutrophil migration in infection and wound repair: going forward in reverse. *Nat. Rev. Immunol.* **16**, 378–391 (2016).
502. Estrada-Capetillo, L. *et al.* CD28 is expressed by macrophages with anti-inflammatory potential and limits their T-cell activating capacity. *Eur. J. Immunol.* **51**, 824–834 (2021).
503. Piguet, P. F., Vesin, C., Grau, G. E. & Thompson, R. C. Interleukin 1 receptor antagonist (IL-1ra) prevents or cures pulmonary fibrosis elicited in mice by bleomycin or silica. *Cytokine* **5**, 57–61 (1993).
504. Freeman, B. D. & Buchman, T. G. Interleukin-1 receptor antagonist as therapy for inflammatory disorders. *Expert Opin. Biol. Ther.* **1**, 301–308 (2001).
505. Chamberlain, C. S. *et al.* Interleukin-1 Receptor Antagonist Modulates Inflammation and Scarring after Ligament Injury. *Connect. Tissue Res.* **55**, 177–186 (2014).
506. Iizasa, H. *et al.* Exacerbation of granuloma formation in IL-1 receptor antagonist-deficient mice with impaired dendritic cell maturation associated with Th2 cytokine production. *J. Immunol. Baltim. Md 1950* **174**, 3273–3280 (2005).
507. Mehrotra, P. *et al.* Oxylipins and metabolites from pyroptotic cells act as promoters of tissue repair. *Nature* **631**, 207–215 (2024).
508. Saas, P., Vetter, M., Maraux, M., Bonnefoy, F. & Perruche, S. Resolution therapy: Harnessing efferocytic macrophages to trigger the resolution of inflammation. *Front. Immunol.* **13**, (2022).

509. Ghosh, M. C., Makena, P. S., Gorantla, V., Sinclair, S. E. & Waters, C. M. CXCR4 regulates migration of lung alveolar epithelial cells through activation of Rac1 and matrix metalloproteinase-2. *Am. J. Physiol. - Lung Cell. Mol. Physiol.* **302**, L846–L856 (2012).

510. Paine, R. *et al.* A randomized trial of recombinant human granulocyte-macrophage colony stimulating factor for patients with acute lung injury. *Crit. Care Med.* **40**, 90–97 (2012).

511. Jansson, M., Panoutsakopoulou, V., Baker, J., Klein, L. & Cantor, H. Cutting edge: Attenuated experimental autoimmune encephalomyelitis in eta-1/osteopontin-deficient mice. *J. Immunol. Baltim. Md 1950* **168**, 2096–2099 (2002).

512. Yan, Z., Hu, X., Tang, B. & Deng, F. Role of osteopontin in cancer development and treatment. *Heliyon* **9**, e21055 (2023).

513. Kölmel, S. *et al.* Potential Involvement of Osteopontin in Inflammatory and Fibrotic Processes in Pulmonary Embolism and Chronic Thromboembolic Pulmonary Hypertension. *Thromb. Haemost.* **119**, 1332–1346 (2019).

514. O'Regan, A. The Role of osteopontin in lung disease. *Cytokine Growth Factor Rev.* **14**, 479–488 (2003).

515. Pappas, A. G. *et al.* High Plasma Osteopontin Levels Are Associated with Serious Post-Acute-COVID-19-Related Dyspnea. *J. Clin. Med.* **13**, 392 (2024).

516. Tonello, S. *et al.* Baseline Plasma Osteopontin Protein Elevation Predicts Adverse Outcomes in Hospitalized COVID-19 Patients. *Viruses* **15**, 630 (2023).

517. Tang, Z., Xia, Z., Wang, X. & Liu, Y. The critical role of osteopontin (OPN) in fibrotic diseases. *Cytokine Growth Factor Rev.* **74**, 86–99 (2023).

518. Wang, W. *et al.* Osteopontin activates mesenchymal stem cells to repair skin wound. *PLOS ONE* **12**, e0185346 (2017).

519. Hirano, Y. *et al.* Neutralization of osteopontin attenuates neutrophil migration in sepsis-induced acute lung injury. *Crit. Care* **19**, 53 (2015).

520. Giachelli, C. M., Lombardi, D., Johnson, R. J., Murry, C. E. & Almeida, M. Evidence for a role of osteopontin in macrophage infiltration in response to pathological stimuli in vivo. *Am. J. Pathol.* **152**, 353–358 (1998).

521. Tuck, A. B., Hota, C., Wilson, S. M. & Chambers, A. F. Osteopontin-induced migration of human mammary epithelial cells involves activation of EGF receptor and multiple signal transduction pathways. *Oncogene* **22**, 1198–1205 (2003).

522. Wu, J. & Wang, Z. Osteopontin improves adhesion and migration of human primary renal cortical epithelial cells during wound healing. *Oncol. Lett.* **12**, 4556–4560 (2016).
523. Chen, Q. *et al.* CD44high alveolar type II cells show stem cell properties during steady-state alveolar homeostasis. *Am. J. Physiol. Lung Cell. Mol. Physiol.* **313**, L41–L51 (2017).
524. Ophascharoensuk, V. *et al.* Obstructive uropathy in the mouse: Role of osteopontin in interstitial fibrosis and apoptosis. *Kidney Int.* **56**, 571–580 (1999).
525. Burdo, T. H., Wood, M. R. & Fox, H. S. Osteopontin prevents monocyte recirculation and apoptosis. *J. Leukoc. Biol.* **81**, 1504–1511 (2007).
526. Rollo, E. E., Laskin, D. L. & Denhardt, D. T. Osteopontin inhibits nitric oxide production and cytotoxicity by activated RAW264.7 macrophages. *J. Leukoc. Biol.* **60**, 397–404 (1996).
527. Guo, H., Cai, C. Q., Schroeder, R. A. & Kuo, P. C. Osteopontin is a negative feedback regulator of nitric oxide synthesis in murine macrophages. *J. Immunol. Baltim. Md 1950* **166**, 1079–1086 (2001).
528. McAuley, D. F. *et al.* Keratinocyte growth factor for the treatment of the acute respiratory distress syndrome (KARE): a randomised, double-blind, placebo-controlled phase 2 trial. *Lancet Respir. Med.* **5**, 484–491 (2017).
529. Kim, Y.-S. *et al.* The role of FGF-2 in smoke-induced emphysema and the therapeutic potential of recombinant FGF-2 in patients with COPD. *Exp. Mol. Med.* **50**, 150 (2018).
530. Behnke, J. *et al.* MSC Based Therapies-New Perspectives for the Injured Lung. *J. Clin. Med.* **9**, 682 (2020).
531. Armitage, J. *et al.* Mesenchymal stromal cell infusion modulates systemic immunological responses in stable COPD patients: a phase I pilot study. *Eur. Respir. J.* **51**, 1702369 (2018).
532. Chambers, D. C. *et al.* A phase 1b study of placenta-derived mesenchymal stromal cells in patients with idiopathic pulmonary fibrosis. *Respirol. Carlton Vic* **19**, 1013–1018 (2014).
533. Meng, F. *et al.* Human umbilical cord-derived mesenchymal stem cell therapy in patients with COVID-19: a phase 1 clinical trial. *Signal Transduct. Target. Ther.* **5**, 172 (2020).
534. Abreu, S. C. *et al.* Lung inflammatory environments differentially alter mesenchymal stromal cell behavior. *Am. J. Physiol. Lung Cell. Mol. Physiol.* **317**, L823–L831 (2019).
535. Campo, I. *et al.* Inhaled recombinant GM-CSF reduces the need for whole lung lavage and improves gas exchange in autoimmune pulmonary alveolar proteinosis patients. *Eur. Respir. J.* **63**, 2301233 (2024).

536. Tazawa, R. *et al.* Inhaled GM-CSF for Pulmonary Alveolar Proteinosis. *N. Engl. J. Med.* **381**, 923–932 (2019).

537. Presneill, J. J., Harris, T., Stewart, A. G., Cade, J. F. & Wilson, J. W. A randomized phase II trial of granulocyte-macrophage colony-stimulating factor therapy in severe sepsis with respiratory dysfunction. *Am. J. Respir. Crit. Care Med.* **166**, 138–143 (2002).

538. Lazarus, H. M., Ragsdale, C. E., Gale, R. P. & Lyman, G. H. Sargramostim (rhu GM-CSF) as Cancer Therapy (Systematic Review) and An Immunomodulator. A Drug Before Its Time? *Front. Immunol.* **12**, 706186 (2021).

539. Subramaniam, R. *et al.* Delivery of GM-CSF to Protect against Influenza Pneumonia. *PLOS ONE* **10**, e0124593 (2015).

540. Subramaniam, R. *et al.* Protecting against post-influenza bacterial pneumonia by increasing phagocyte recruitment and ROS production. *J. Infect. Dis.* **209**, 1827–1836 (2014).

541. León, B. & Ballesteros-Tato, A. Modulating Th2 Cell Immunity for the Treatment of Asthma. *Front. Immunol.* **12**, (2021).

542. Tomkinson, A. *et al.* A murine IL-4 receptor antagonist that inhibits IL-4- and IL-13-induced responses prevents antigen-induced airway eosinophilia and airway hyperresponsiveness. *J. Immunol. Baltim. Md 1950* **166**, 5792–5800 (2001).

543. Castro, M. *et al.* Dupilumab Efficacy and Safety in Moderate-to-Severe Uncontrolled Asthma. *N. Engl. J. Med.* **378**, 2486–2496 (2018).

544. Papi, A. *et al.* Dupilumab sustains lung function improvements in patients with moderate-to-severe asthma. *Respir. Med.* **224**, (2024).

545. Chung, S. I. *et al.* IL-13 is a therapeutic target in radiation lung injury. *Sci. Rep.* **6**, 39714 (2016).

546. Salmon-Ehr, V. *et al.* Implication of interleukin-4 in wound healing. *Lab. Investig. J. Tech. Methods Pathol.* **80**, 1337–1343 (2000).

547. Shintani, Y. *et al.* IL-4 as a Repurposed Biological Drug for Myocardial Infarction through Augmentation of Reparative Cardiac Macrophages: Proof-of-Concept Data in Mice. *Sci. Rep.* **7**, 6877 (2017).

548. Shi, H. Z. *et al.* Effect of inhaled interleukin-4 on airway hyperreactivity in asthmatics. *Am. J. Respir. Crit. Care Med.* **157**, 1818–1821 (1998).

549. Hassanshahi, A. *et al.* Macrophage-Mediated Inflammation in Skin Wound Healing. *Cells* **11**, 2953 (2022).

550. Gao, Y., Qian, N., Xu, J. & Wang, Y. The Roles of Macrophages in Heart Regeneration and Repair After Injury. *Front. Cardiovasc. Med.* **8**, 744615 (2021).

551. Frade, B. B., Dias, R. B., Gemini Piperni, S. & Bonfim, D. C. The role of macrophages in fracture healing: a narrative review of the recent updates and therapeutic perspectives. *Stem Cell Investig.* **10**, 4 (2023).

552. Fornefett, J. *et al.* Comparative analysis of humoral immune responses and pathologies of BALB/c and C57BL/6 wildtype mice experimentally infected with a highly virulent Rodentibacter pneumotropicus (Pasteurella pneumotropica) strain. *BMC Microbiol.* **18**, 45 (2018).

553. Mills, C. D., Kincaid, K., Alt, J. M., Heilman, M. J. & Hill, A. M. M-1/M-2 Macrophages and the Th1/Th2 Paradigm1. *J. Immunol.* **164**, 6166–6173 (2000).

554. Kasmani, M. Y. *et al.* A spatial sequencing atlas of age-induced changes in the lung during influenza infection. *Nat. Commun.* **14**, 6597 (2023).

555. Yang, D. *et al.* Vagal TRPV1 + sensory neurons regulate myeloid cell dynamics and protect against influenza virus infection. *BioRxiv Prepr. Serv. Biol.* 2024.08.21.609013 (2024) doi:10.1101/2024.08.21.609013.

PUBLICATION LIST

Ruscitti, C. , Abinet, J., Maréchal, P., Meunier, M., de Meeûs, C., Vanneste, D., Janssen, P., Dourcy, M., Thiry, M., Bureau, F., Schneider, C., Machiels, B., Hidalgo, A. , Ginhoux, F., Dewals, B. G., Guiot, J., Schleich, F., Garigliany, M.-M. , Bellahcène, A. , Radermecker, C., Marichal, T., (2024) Recruited atypical Ly6G^{+} macrophages license alveolar regeneration after lung injury. *Sci. Immunol.* 9, eado1227.

Ruscitti, C.* , Radermecker, C.* , & Marichal, T.*. (2024). Journey of monocytes and macrophages upon influenza A virus infection. Current Opinion in Virology, 66, 101409.* These authors have contributed equally to this work.

Vanneste, D., Bai, Q., Hasan, S., Peng, W., Pirottin, D., Schyns, J., Maréchal, P., **Ruscitti, C**., Meunier, M., Liu, Z., Legrand, C., Fievez, L., Ginhoux, F., Radermecker, C., Bureau, F., & Marichal, T. (2023). MafBrestricted local monocyte proliferation precedes lung interstitial macrophage differentiation. Nature Immunology, 24 (5), 827 - 840.

Radermecker, C.* , Sabatel, C.* , Vanwinge, C., **Ruscitti, C.**, Marechal, P., Perin, F., Schyns, J., Rocks, N., Toussaint, M., Cataldo, D., Johnston, S. L., Bureau, F.* , & Marichal, T.*. (2019). Locally instructed CXCR4(hi) neutrophils trigger environment-driven allergic asthma through the release of neutrophil extracellular traps. Nature Immunology. * These authors have contributed equally to this work.

Schyns, J., Bai, Q., **Ruscitti, C**., Radermecker, C., De Schepper, S., Chakarov, S., Farnir, F., Pirottin, D., Ginhoux, F., Boeckxstaens, G., Bureau, F., & Marichal, T. (2019). Non-classical tissue monocytes and two functionally distinct populations of interstitial macrophages populate the mouse lung. Nature Communications, 10 (1), 3964.

APPENDIX

Available online at www.sciencedirect.com

ScienceDirect

Current Opinion in Virology

Review

Journey of monocytes and macrophages upon influenza A virus infection☆

Cecilia Ruscitti[1,2,*], Coraline Radermecker[1,2,*] and Thomas Marichal[1,2,3,*]

Influenza A virus (IAV) infections pose a global health challenge that necessitates a comprehensive understanding of the host immune response to devise effective therapeutic interventions. As monocytes and macrophages play crucial roles in host defence, inflammation, and repair, this review explores the intricate journey of these cells during and after IAV infection. First, we highlight the dynamics and functions of lung-resident macrophage populations post-IAV. Second, we review the current knowledge of recruited monocytes and monocyte-derived cells, emphasising their roles in viral clearance, inflammation, immunomodulation, and tissue repair. Third, we shed light on the consequences of IAV-induced macrophage alterations on long-term lung immunity. We conclude by underscoring current knowledge gaps and exciting prospects for future research in unravelling the complexities of macrophage responses to respiratory viral infections.

Addresses
[1] Laboratory of Immunophysiology, GIGA Institute, Liège University, Avenue de l'Hôpital 11, 4000 Liège, Belgium
[2] Faculty of Veterinary Medicine, Liège University, Avenue de Cureghem 5D, 4000 Liège, Belgium
[3] Walloon Excellence in Life Sciences and Biotechnology (WELBIO) Department, WEL Research Institute, 1300 Wavre, Belgium

Corresponding author: Marichal, Thomas (t.marichal@uliege.be)
* All authors contributed equally.

Current Opinion in Virology 2024, **66**:101409

This review comes from a themed issue on **Mucosal Immunology**

Edited by **Zhou Xing** and **Jean-Michel Sallenave**

Available online xxxx

https://doi.org/10.1016/j.coviro.2024.101409

Introduction

Influenza viruses are enveloped, single-stranded, negative-sense RNA viruses belonging to the *Orthomyxoviridae* family. Infections with influenza A viruses (IAV), classified based on hemagglutinin (HA) and neuraminidase glycoproteins, represent a significant global health issue with an annual estimate of 1 billion cases and 250–500 000 deaths worldwide [1].

IAV infections pose a formidable challenge to the host, which needs to mount effective defence and repair responses while avoiding excessive lung inflammation and damage associated with severe hypoxemia and acute respiratory distress syndrome (ARDS) [2–5]. Indeed, in order to allow efficient gas diffusion and support life, the airways must be permeable, and the air–blood barrier must remain very thin. Hence, the lung immune system has evolved as a sophisticated surveillance and defence system to sustain physiological functions and host protection. Dedicated to these tasks, distinct populations of monocytes and resident tissue macrophages (ResMacs) populate the steady-state lung (Box 1). Upon IAV infection, additional monocytes and monocyte-derived Macs (Mo-Macs) are recruited and undergo a dynamic response postinfection, which unfolds with remarkable complexity [6,7]. In this article, we aim to review the journey of monocytes and macrophages during and after IAV infection, thus unravelling the intricacies of their roles in viral clearance, inflammation, tissue repair, immunomodulation, and tissue imprinting (Figure 1).

Influenza A virus–triggered perturbations and functions of resident homeostatic alveolar macrophages

Alveolar macrophages (AMs) are strategically located in the alveolar lumen to be the first responders to IAV (Box 1), and investigations about resident AMs in IAV infections consistently pointed towards beneficial, protective roles, as reviewed in detail elsewhere [8,9]. Human and mouse AMs are permissive to IAV, and AMs can uptake viruses by direct infection or by phagocytosis of infected apoptotic cells [10]. Viral replication in AMs is limited by their production of type I interferons (IFNs) [11,12], which can also orchestrate recruitment of other immune cells [13] (Figure 1a, b).

Of note, AM infection rate is highly variable, with higher infectivity by highly pathogenic strains and rather unproductive infections by moderate viral strains, which is

☆ 2024 Mucosal Immunology issue, Current Opinion in Virology

Box 1 The homeostatic landscape of monocytes and macrophages in the lung.

In mice, CCR2^{-}CX3CR1^{hi}Ly6C^{-} 'patrolling' monocytes depend on the transcription factor Nr4a1 and constantly clear the luminal side of capillary endothelial cells from cell debris [88,89]. A small proportion of Ly6C^{-} monocytes also resides in the lung parenchyma and may act as precursor of Mo-DCs or IMs [36,90]. In addition, small numbers of CCR2^{hi}CX3CR1^{lo}Ly6C^{+} classical monocytes are found in the parenchyma at steady state, have the ability to sample and transport antigens to the lymph nodes [91,92] and may also act as precursors of IMs [37,44]. Similar monocyte subsets are found in humans [90].

AMs are self-maintaining ResMacs that reside in the lumen of the alveoli. Their strategic positioning 'outside' the host arguably place them as early responders to lung insults. AMs are characterised by elevated expression of CD11c and Siglec-F in mice. Their development and maintenance require type 2 alveolar epithelial cell–derived GM-CSF and AM-intrinsic transforming growth factor-β, both instructive signals triggering sustained expression of peroxisome proliferator-activated receptor gamma (PPAR-γ) and imprinting a functional specification that allows efficient recycling of excess surfactant and cell debris [7,93–96]. While AMs arise almost completely from embryonically derived fetal monocytes in young adult mice [96], they are progressively replaced by bone marrow–derived cells as mice age [24,32].

Lung IMs populate the parenchyma and are less represented and less accessible than AMs. In adult mice, CD11b^{+}CD64^{+}CD88^{+}Siglec-F^{-} IMs are slowly replenished by classical monocytes [36,37,43,44], require MafB for their development [44] and encompass distinct subsets based on their origin, phenotype and localisation [35,36,43,97–99]. On the one hand, CD11c^{lo}Lyve1^{hi}CD206^{+} IMs represent a major source of the immunoregulatory cytokine IL-10 and preferentially associate with blood vessels and the bronchi, consistent with blood vessel–supportive and immunosuppressive functions [36,37,43,97]. On the other hand, CD11c$^{int/hi}$Lyve1^{lo}CD206^{-} IMs express high levels of MHC-II, can present soluble antigens to T cells and are located in the vicinity of nerve bundles [36,43,97,98,100]. Based on phenotypic similarities, CD206^{-} IMs might partially overlap with CD169^{+} NAM [35] and antigen-presenting CD11c^{+}Cx3cr1^{hi}MHC-II^{hi} bronchus-associated Macs [98].

thought to contribute to limit viral spread [14–17]. Human AMs are less permissive and responsive to IAVs than Mo-Macs [14], which also produce larger amounts of tumour necrosis factor α [14,15], C-C motif chemokine ligand 5 (CCL5) and C-X-C motif chemokine ligand 10 (CXCL10) compared with AMs [15]. A recent report suggests that the inhibitory effects of AMs on viral replication could also be mediated by extracellular vesicles acting on epithelial cells [18].

Seminal reports showed that wild-type mice injected with supraphysiological doses of granulocyte–monocyte colony–stimulating factor (GM-CSF) [19] or mutant mice overexpressing GM-CSF in the lung [20] were protected from IAV infection. This protective effect was associated with improved lung functions, decreased protein exudates in the bronchoalveolar lavage (BAL), a better clinical recovery and a repolarisation of AMs from a M1-like to a M2-like phenotype [19–21]. Furthermore, the protective effects of GM-CSF were abrogated by airway administration of clodronate liposomes [20], suggesting a role for AMs in GM-CSF-mediated protection against IAV. Further supporting their beneficial roles, Schneider et al. showed that neonatal adoptive transfers of AM progenitors in *Csf2rb*$^{-/-}$ mice, lacking GM-CSF receptor, prevented severe disease post-IAV, while depletion of AM by clodronate liposomes in wild type mice before IAV infection exacerbated morbidity and mortality [11]. Recently, a study showed that an appropriate imprinting of AMs by their niche could contribute to host protection against IAV pathology. Indeed, the authors showed that *Alox15*$^{-/-}$ AMs, deficient in 12- and 15-lipoxygenase, were not properly instructed during the neonatal period by neutrophil-derived eicosanoids (Figure 1b) and were thus no longer able to control IAV replication later in life, which was associated with increased levels of C-C motif chemokine ligand 2 (CCL2), accumulation of monocytes and increased mortality of IAV-infected mice [22].

Mouse AMs have been reported to be depleted post-IAV [23,24]. The mechanisms driving AM depletion have been shown to be dependent on IFN-γ in BALB/c mice [23] and may involve AM apoptosis subsequent to a robust antiviral response [25], inhibition of AM self-renewal capacity by IAV-induced Wnt ligands [26] or modifications of the AM niche triggered by IAV infection of epithelial cells [5]. The extent of AM depletion is thought to be dependent on the host genetic background [23,24]. Indeed, employing a sublethal infection model with the H1N1 PR8 strain, Califano et al. reported a massive loss of AMs 7 and 9 days post-IAV in BALB/c mice, but not C57BL/6NCrl mice [23], while Li et al. recently showed that such infection also induced a rapid loss of resident AMs in C57BL/6J mice [24]. We also consistently observe AM depletion in PR8-infected C57BL/6J mice raised in our animal facilities (unpublished observations). The reasons for these discrepancies remain currently unclear and likely evolve a combination of genetic and environmental factors. In their study, Li et al. further showed that the AM pool was quickly replenished by Siglec-F^{hi} 'survivor' AMs (5–10% of original AMs) between day 4 and 15 post-IAV in mice [24]. After viral clearance, AMs were gradually replaced by proinflammatory monocyte-derived Siglec-F^{lo} Mo-Macs that would eventually outcompete embryonically derived AMs on a long-term basis [24,27]. Eventually, the alveolar niche can return to a homeostatic, noninflammatory state, and repopulated AMs can become similar to the native ones [7,28,29] (Figure 1d).

Ageing can affect AM microenvironment, ontogeny and functions, which might account for the enhanced mortality and morbidity post-IAV in the elderly [24,30–32]. The ageing microenvironment can confer resistance of AMs to GM-CSF responsiveness [33], which correlates with decreased AM numbers and proliferative abilities

Figure 1

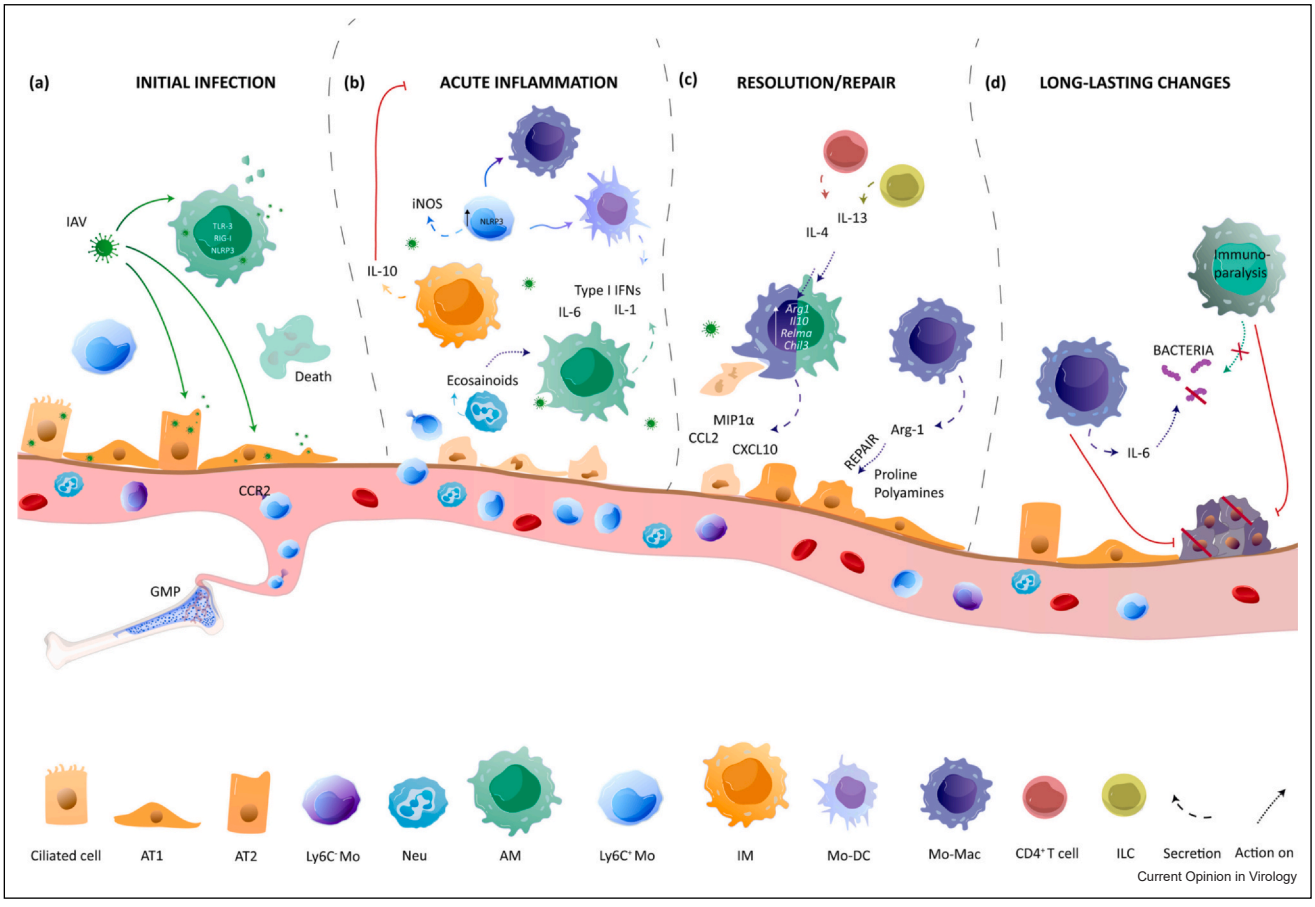

Monocytes and macrophages after IAV infection. **(a)** IAV-derived HA proteins can bind to sialylated glycan receptors on lung epithelial cells from the airways and the alveoli. AMs are equipped with the viral RNA sensing machinery and are permissive to IAV, which results in an unproductive infection and a self-limiting disease and can lead to AM death. **(b)** IAV infection can trigger AM activation and production of cytokines, chemokines and type I IFNs, thereby controlling viral spread and coordinating the recruitment of additional immune cells. A proper AM imprinting by neutrophil-derived eicosanoids is essential for AM protective functions post-IAV. The role of IMs in the antiviral response is less clear, with IM-derived IL-10 playing a beneficial role in the downregulation of inflammation. Lung-recruited Ly6C$^+$ Mos can activate the NLRP3 pathway and produce elevated amount of iNOS, which can contribute to the acute inflammatory response and, sometimes, to undesirable tissue damage. Ly6C$^+$ Mos can differentiate into type I IFN–producing Mo-DCs or into proinflammatory Mo-Macs participating to efficient viral clearance. **(c)** Infected cells can release 'find me' signals and cytokines attracting Mo-Macs and inducing their engulfment. Efferocytosis limits viral spread and induces a reprogramming in efferocytic Mo-Macs toward a proresolving phenotype associated with upregulation of anti-inflammatory genes, such as *Arg1, Il10, Relma and Chil3*. Furthermore, during the resolution phase, T cells and ILC2s can produce type 2 cytokines (IL-4 and IL-13) triggering the production of Arginase-1 by Mo-Macs. Arg-1 metabolism results in production of polyamines et proline enhancing cell growth and collagen production and thereby contributing to tissue repair. **(d)** IAV infection leads to long-term consequences for lung immunity. Niche signals produced post-IAV infection induce an immunoparalysis in resident AMs, which exhibit impaired bacterial phagocytosis, thus enhancing the susceptibility to secondary bacterial infection. Mo-Macs replenishing the alveolar niche post-IAV maintain a proinflammatory phenotype conferring efficient IL-6-dependent protection against bacterial infection but leading to exacerbated lethal response in recurrent viral infection. IAV-instructed Macs can also contribute to protection against tumours by maintaining their phagocytic and cytotoxic potential despite tumour-induced immunosuppression. AT1/2, type 1/2 alveolar epithelial cell; Mo, monocyte; Neu, neutrophil.

[30]. Aged AMs have also been shown to be impaired in their ability to phagocyte neutrophils compared to young AMs, and high neutrophil counts might account for excessive tissue damage [30]. Finally, embryonically derived AMs are gradually replaced by bone marrow–derived AMs in aged mice, which can intrinsically contribute to disease severity post-IAV [24].

Enigmatic fate and function of resident interstitial macrophages post-influenza A virus

Lung interstitial macrophages (IMs) have been less studies than AMs (Box 1). To date, most of the studies aiming at addressing the contributions of IMs to disease physiopathology, including IAV-triggered pathology, have faced

two main challenges [34]. First, Mo-Macs recruited when homeostasis is broken often exhibit a phenotype that can largely overlap the one of IMs. Hence, while it is repeatedly reported that IMs 'expand' upon exposure to insults or pathogen-associated molecular patterns [35–42], the IM compartment arguably contains a mix of resident IMs and Mo-Macs, and the respective contributions of IMs versus Mo-Macs to disease physiopathology remain often unclear. Second, transgenic tools allowing a specific and efficient tracking or depletion of resident IMs while sparing AMs and Mo-Macs are difficult to obtain. To date, at least three models of diphtheria toxin (DT)–induced bolus IM depletion exist, namely, *Lyve1*$^{Cre/GFP}$ *Slco2b1*$^{LSL\text{-}DTR}$ [43], *Cd169*^{Cre} *Cx3cr1*$^{LSL\text{-}DTR}$ (NAM-DTR) [35] and *Tmem119*^{Cre} *Cx3cr1*$^{LSL\text{-}DTR}$ (IM^{DTR}) [44] mice. However, IM depletion is transient and rapidly followed by the recruitment of monocytes that refill the empty niche, and it remains to be determined whether DT treatment also targets Mo-Macs when such transgenic mice are subjected to disease models.

In the context of IAV infection, Ural et al. depleted nerve-associated IMs (NAMs) before IAV infection with the H1N1 PR8 strain in C57BL/6 NAM-DTR mice and found that depleted mice displayed increased morbidity at day 12 post-IAV compared with controls, even though the viral loads were unchanged [35]. As NAMs were the main producers of interleukin (IL)-10, the authors proposed that NAMs can downregulate IAV-triggered inflammatory responses. These data highlight potential beneficial, immunoregulatory functions of IMs after IAV, as shown in other contexts [37,43,45,46] (Figure 1b). Future investigations comparing different viral strains (e.g. H1N1, H3N2) and mouse strains (e.g. BALB/c, C57BL/6) and employing complementary models of IM-specific targeting along with additional cellular and molecular read-outs of inflammatory and repair responses will help deciphering their roles post-IAV. Along the same line, a model in which resident IMs could be tracked and discriminated from Mo-Macs post-IAV would open many opportunities for more comprehensive molecular, spatial and functional investigations.

Monocytes and monocyte-derived Macs trajectories and functions post-influenza A virus

Monocytes are, along with neutrophils, the first innate cells recruited to the infected lung. Type I IFNs produced early post-IAV can trigger an emergency monopoiesis in the bone marrow, associated with the proliferation of granulocyte—monocyte progenitors, their upregulation of the M-CSF receptor and the egress of Ly6C$^+$ monocytes exhibiting increased expression of stem cell antigen-1 at the expense of dendritic cell differentiation [47–49]. Type I IFN signalling also promotes the differentiation and lung recruitment of CCL2-producing Ly6C$^+$ monocytes, which further facilitates the influx of CCR2$^+$Ly6C$^+$ monocytes into the lung [24,50,51] (Figure 1b). Type II IFNs have also been shown to regulate inflammatory monocyte recruitment post-IAV [52]. Along with AMs, recruited monocytes orchestrate the acute inflammatory response in part via the activation of nucleotide oligomerization domain (NOD)-like receptor family pyrin domain–containing 3 (NLRP3) inflammasome [53]. In lethal models of IAV infection, early NLRP3 inflammasome activity is thought to be protective [54], while an excess of activation may worsen lung damage and increase mortality [55]. Several reports support that the global outcome of CCR2$^+$ monocyte accumulation is detrimental and associated with increased morbidity and mortality [4,24,56,57]. Deleterious effects of CCR2$^+$ monocytes may be related to an elevated production of induced nitric oxide synthase (iNOS), which, unlike for other pathogens, does not display antiviral activity against IAV but rather inhibits an effective adaptive immune response [58].

Upon recruitment, a portion of monocytes can differentiate into monocyte-derived dendritic cells (Mo-DCs), peaking in the lung at days 7–10 post-IAV [57]. Type I IFN–producing Mo-DCs have been shown to contribute to the antiviral response [59] (Figure 1b) and ensure appropriate virus-specific CD8$^+$ T cell memory responses [60]. Recruited monocytes can also develop into Mo-Macs that are either short lived or can establish in particular niches with functional consequences for lung immunity [7,8,27,28,61]. While Mo-Macs have long been considered as detrimental and pathogenic cells after IAV infection [24,57], their functional specification is arguably much more complex than previously thought.

During the acute inflammatory phase, IFN-γ-induced Mo-Macs with a proinflammatory profile are thought to contribute to efficient viral clearance. They are progressively replaced by proresolving Mo-Macs, thereby facilitating tissue healing [25,62,63] (Figure 1c). The phagocytosis of dying cells, called efferocytosis, is an integral part of the resolution of inflammation [64]. Before cell death, infected cells can release 'find me' signals and cytokines such as macrophage inflammatory protein-1α, CCL2, CXCL10, able to direct Mo-Macs towards apoptotic cells for engulfment [25,63]. This process contributes to limit the progression of IAV infection in mice by clearing infected cells and promoting a proresolving phenotype in efferocytic Mo-Macs [65–67]. Degradation of engulfed cells induces a substantial metabolic shift from proinflammatory glycolytic pathways towards oxidative phosphorylation pathways associated with anti-inflammatory functions [64,68,69] (Figure 1c). After H1N1 infection in mice, genes related to anti-inflammatory functions, such as *Arg1*, *Il10*, *Relma* and *Chil3*, are upregulated in macrophages as soon as 7 days post-IAV [70]. Of note, the resolution phase post-IAV is characterised by a local type 2 profile, including elevated levels of IL-13$^+$ type 2 helper T cells, innate lymphoid type 2 (ILC2s) cells, IL-4 and IL-13 [70,71], which participate to macrophage reprogramming towards a wound-healing phenotype [72,73]. The receptor for IL-4 and IL-13 (IL4R) starts to be expressed on

Figure 2

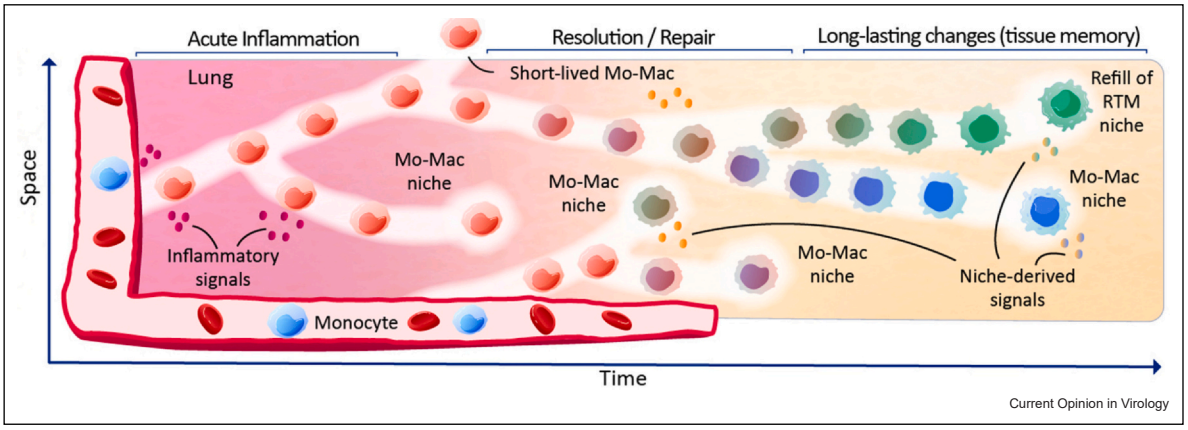

Updated view on the determinants of Mo-Mac identities and functions after lung injury. Upon IAV infection or exposure to other pathogens or insults, the diversity of lung macrophages increases as monocytes are recruited and differentiate into Mo-Macs that join the pool of macrophages. As opposed to ResMacs, Mo-Macs are highly plastic and exhibit a higher potential for imprinting by inflammation and by tissue cues. Hence, they can adopt distinct identities that are regulated spatiotemporally and can also refill homeostatic ResMac niches if space is available and homeostatic cues are present. The origin, the differentiation trajectories, the stress-derived and microanatomical niche-derived cues they encounter, the time spent in the tissue and their localisation are increasingly thought to be essential determinants of Mo-Mac identities and functions.

proinflammatory Mo-Macs [74] and its activation triggers expression of Arginase-1, an enzyme competing with IFN-γ-induced iNos for the common substrate L-Arginine [75]. The Arg-1 product L-ornithine can be further converted into polyamines and proline that can contribute to tissue repair via enhancement of efferocytosis, regulation of cell growth and collagen production [76–78]. GM-CSF, overexpressed by infected alveolar epithelial cells, is also involved in macrophage reprogramming from a proinflammatory to a proresolving state [19,79] and has been shown to confer protection against lethal IAV infection in mice [20,21]. Whether GM-CSF acts on homeostatic AMs, Mo-Macs, or both, would require further investigations.

Consequences of influenza A virus–shaped macrophages for lung immunity

The shaping of the alveolar niche by respiratory infections and the long-term consequences for lung immunity have been reviewed recently [8]. We will focus here on studies supporting the idea that IAV-induced changes in macrophages are associated with short- and long-term modifications in the ability of the host to respond to subsequent insults and stimuli (Figure 1d). IAV-triggered AM depletion can increase susceptibility to secondary bacterial pneumonia [80]. Moreover, IFN-γ produced by T cells after IAV infection can impair AM antibacterial properties and increase the risk of secondary bacterial infections [81,82]. Such impaired capacity of resident AMs to capture bacteria has been shown to last for months and to rely on signal regulatory protein alpha (SIRPα)-dependent immunosuppressive signals released in the local environment, leading to immunoparalysis after IAV infection [83]. Influenza-trained AMs have recently been proposed to confer antitumour immunity [84]. Indeed, in a model of B16 melanoma, IAV-trained AM could maintain their phagocytic and cytotoxic potential despite tumour-induced immunosuppression, thereby enabling enhanced antitumour function [84]. However, concerns have been raised as to whether these effects might rather be mediated by recruited Mo-Macs resembling AMs [85]. Mo-Macs replenishing the alveolar spaces post-IAV have been shown to exhibit a more proinflammatory phenotype associated with higher glycolytic activity [24] and IL-6 production [27] compared with AMs, which can confer protection against secondary bacterial infection 1 month post-IAV [27] but can also be responsible for increased mortality in recurrent viral infection [24].

Conclusions and future directions

Substantial progress has been made to understand the roles of monocytes and macrophages during and after IAV infection. Yet, recruitment of monocytes and Mo-Macs induces a highly dynamic and complex response in the lung, and such cells can no longer be considered as a single entity based on their origin. Indeed, they are thought to be highly plastic, and as they navigate through the infected lung and interact with other immune cells, structural cells and extracellular matrix components, they undergo a spectrum of activation states and phenotypic changes and can adopt distinct functional identities that depend on their differentiation trajectory, the diseased tissue microenvironment and the extent and phase of inflammation [6,7,28,29] (Figure 2). Therefore, we believe that resolving IAV-triggered macrophage adaptations and the complexity of the macrophage compartment after IAV, including the

investigation of the stress-related and tissue-instructive signals integrated by Mo-Macs and of the intrinsic molecular programmes that mediate distinct spatiotemporal trajectories and functions, is still in its infancy and represents an exciting challenge for future research. Single-cell and spatial transcriptomic analyses arguably represent the first important step in such investigations [86,87], which will be critical to fully understand myeloid cell contributions to IAV-triggered immunopathology, to understand why they become dysregulated in the elderly or in severe and chronic diseases, and to ultimately be able to manipulate their fate and functions for medically relevant conditions such as severe respiratory viral infections and ARDS. To succeed, it will be important to undertake a systems biology approach in order to connect single-cell gene expression and regulation within structural and immune cells to cell identity, functions, cell–cell interactions, and ultimately disease physiopathology.

Accordingly, efforts should be made to employ clinically relevant human samples and preclinical models that better reflect the human disease, along with top-notch multi-omic and spatial technologies that are currently revolutionising research in life sciences.

Data Availability

No data were used for the research described in the article.

Declaration of Competing Interest

The authors declare that they have no known competing financial interests or personal relationships that could have appeared to influence the work reported in this paper.

Acknowledgements

The authors thank all members of the Immunophysiology laboratory (GIGA Institute, Liège, Belgium) for discussions; Adeline Deward (Illumine) for helping with the design of the figures; Raja Fares, Ilham Sbai and Axelle Lio for their excellent administrative support. This work was supported by a Welbio Advanced Grant (WELBIO-CR-2022A-10), an European Research Council Starting Grant (IM-ID: 801823), the Baillet Latour Biomedical Fund and a Research Project of the F.R.S.-FNRS (Fonds National de la Recherche Scientifique), Belgium (T015021F) to Thomas Marichal.

References and recommended reading

Papers of particular interest, published within the period of review, have been highlighted as:

- • of special interest
- •• of outstanding interest

1. Iuliano AD, Roguski KM, Chang HH, Muscatello DJ, Palekar R, Tempia S, Cohen C, Gran JM, Schanzer D, Cowling BJ, *et al.*: **Estimates of global seasonal influenza-associated respiratory mortality: a modelling study**. *Lancet* 2018, **391**:1285-1300.

2. Kalil AC, Thomas PG: **Influenza virus-related critical illness: pathophysiology and epidemiology**. *Crit Care* 2019, **23**:258.

3. Herold S, Becker C, Ridge KM, Budinger GRS: **Influenza virus-induced lung injury: pathogenesis and implications for treatment**. *Eur Respir J* 2015, **45**:1463-1478.

4. • Wei X, Narasimhan H, Zhu B, Sun J: **Host recovery from respiratory viral infection**. *Annu Rev Immunol* 2023, **41**:277-300, https://doi.org/10.1146/annurev-immunol-101921-040450.
This review summarises the immune mechanisms involved in host recovery from respiratory viruses, mainly from SARS-CoV-2 and influenza viruses, from initial antiviral responses towards tissue repair. It emphasises the fragile equilibrium between beneficial and pathological immune responses in this context.

5. • Planer JD, Morrisey EE: **After the storm: regeneration, repair, and reestablishment of homeostasis between the alveolar epithelium and innate immune system following viral lung injury**. *Annu Rev Pathol* 2023, **18**:337-359.
This review highlights the major mechanisms implicated in epithelial regeneration or repair following epithelial damage triggered by respiratory viruses.

6. Bain CC, MacDonald AS: **The impact of the lung environment on macrophage development, activation and function: diversity in the face of adversity**. *Mucosal Immunol* 2022, **15**:223-234.

7. Aegerter H, Lambrecht BN, Jakubzick CV: **Biology of lung macrophages in health and disease**. *Immunity* 2022, **55**:1564-1580.

8. • Rodriguez-Rodriguez L, Gillet L, Machiels B: **Shaping of the alveolar landscape by respiratory infections and long-term consequences for lung immunity**. *Front Immunol* 2023, **14**:1149015.
In this review, the authors focus on the concept of innate imprinting of the alveolar niche by respiratory viruses and how viral-triggered alterations of macrophages can affect subsequent responses to other stimuli on the long term.

9. Li H, Wang A, Zhang Y, Wei F: **Diverse roles of lung macrophages in the immune response to influenza A virus**. *Front Microbiol* 2023, **14**:1260543.

10. Hashimoto Y, Moki T, Takizawa T, Shiratsuchi A, Nakanishi Y: **Evidence for phagocytosis of influenza virus-infected, apoptotic cells by neutrophils and macrophages in mice**. *J Immunol* 2007, **178**:2448-2457.

11. •• Schneider C, Nobs SP, Heer AK, Kurrer M, Klinke G, van Rooijen N, Vogel J, Kopf M: **Alveolar macrophages are essential for protection from respiratory failure and associated morbidity following influenza virus infection**. *PLoS Pathog* 2014, **10**:e1004053.
The authors used multiple approaches *in vivo* to demonstrate the beneficial roles of GM-CSF-dependent AMs in host protection from morbidity and mortality post-IAV. In particular, they elegantly employed a neonatal intranasal adoptive transfer of CD45+ lung cells from E18.5 wild-type fetuses into AM-deficient Csf2rb$^{-/-}$ mice to restore AM development and, thereby, prevent severe disease post-IAV.

12. Kumagai Y, Takeuchi O, Kato H, Kumar H, Matsui K, Morii E, Aozasa K, Kawai T, Akira S: **Alveolar macrophages are the primary interferon-α producer in pulmonary infection with RNA viruses**. *Immunity* 2007, **27**:240-252.

13. Essers MAG, Offner S, Blanco-Bose WE, Waibler Z, Kalinke U, Duchosal MA, Trumpp A: **IFNα activates dormant haematopoietic stem cells in vivo**. *Nature* 2009, **458**:904-908.

14. Riel D, van Leijten LME, Eerden M, van der Hoogsteden HC, Boven LA, Lambrecht BN, Osterhaus ADME, Kuiken T: **Highly pathogenic avian influenza virus H5N1 infects alveolar macrophages without virus production or excessive TNF-alpha induction**. *PLoS Pathog* 2011, **7**:e1002099.

15. Yu WCL, Chan RWY, Wang J, Travanty EA, Nicholls JM, Peiris JSM, Mason RJ, Chan MCW: **Viral replication and innate host responses in primary human alveolar epithelial cells and alveolar macrophages infected with influenza H5N1 and H1N1 viruses**. *J Virol* 2011, **85**:6844-6855.

16. Londrigan SL, Short KR, Ma J, Gillespie L, Rockman SP, Brooks AG, Reading PC: **Infection of mouse macrophages by seasonal influenza viruses can be restricted at the level of virus entry and at a late stage in the virus life cycle**. *J Virol* 2015, **89**:12319-12329.

17. Tumpey TM, García-Sastre A, Taubenberger JK, Palese P, Swayne DE, Pantin-Jackwood MJ, Schultz-Cherry S, Solórzano A, Van Rooijen N, Katz JM, *et al.*: **Pathogenicity of influenza viruses with genes from the 1918 pandemic virus: functional roles of alveolar macrophages and neutrophils in limiting virus replication and mortality in mice**. *J Virol* 2005, **79**:14933-14944.

18. Schneider DJ, Smith KA, Latuszek CE, Wilke CA, Lyons DM, Penke LR, Speth JM, Marthi M, Swanson JA, Moore BB, *et al.*: **Alveolar macrophage-derived extracellular vesicles inhibit endosomal fusion of influenza virus**. *EMBO J* 2020, **39**:e105057.

19. Halstead ES, Umstead TM, Davies ML, Kawasawa YI, Silveyra P, Howyrlak J, Yang L, Guo W, Hu S, Hewage EK, *et al.*: **GM-CSF overexpression after influenza a virus infection prevents mortality and moderates M1-like airway monocyte/macrophage polarization**. *Respir Res* 2018, **19**:3.

20. Huang F-F, Barnes PF, Feng Y, Donis R, Chroneos ZC, Idell S, Allen T, Perez DR, Whitsett JA, Dunussi-Joannopoulos K, *et al.*: **GM-CSF in the lung protects against lethal influenza infection**. *Am J Respir Crit Care Med* 2011, **184**:259-268.

21. Sever-Chroneos Z, Murthy A, Davis J, Florence JM, Kurdowska A, Krupa A, Tichelaar JW, White MR, Hartshorn KL, Kobzik L, *et al.*: **GM-CSF modulates pulmonary resistance to influenza A infection**. *Antivir Res* 2011, **92**:319-328.

22. Pernet E, Sun S, Sarden N, Gona S, Nguyen A, Khan N, Mawhinney M, Tran KA, Chronopoulos J, Amberkar D, *et al.*: **Neonatal imprinting of alveolar macrophages via neutrophil-derived 12-HETE**. *Nature* 2023, **614**:530-538.

23. Califano D, Furuya Y, Metzger DW: **Effects of influenza on alveolar macrophage viability are dependent on mouse genetic strain**. *J Immunol* 2018, **201**:134-144.

24. •• Li F, Piattini F, Pohlmeier L, Feng Q, Rehrauer H, Kopf M: **Monocyte-derived alveolar macrophages autonomously determine severe outcome of respiratory viral infection**. *Sci Immunol* 2022, **7**:eabj5761.

This study provides a comprehensive profiling of AM niche depletion and repletion post-IAV in mice. The authors provide evidence, in their experimental setting tracking embryonically derived versus bone marrow–derived AMs, that bone marrow–derived AMs exhibit a more proinflammatory profile and trigger a more severe outcome post-IAV compared with embryonically derived AMs. The study thus supports the idea that the origin of AMs, rather than the training of AMs, determines the outcome of respiratory viral infection. It also suggests that Siglec-F expression levels could be used, if confirmed by fate-mapping, to track the origin of macrophages populating the alveoli for extended periods of time.

25. Hofmann P, Sprenger H, Kaufmann A, Bender A, Hasse C, Nain M, Gemsa D: **Susceptibility of mononuclear phagocytes to influenza A virus infection and possible role in the antiviral response**. *J Leukoc Biol* 1997, **61**:408-414.

26. Zhu B, Wu Y, Huang S, Zhang R, Son YM, Li C, Cheon IS, Gao X, Wang M, Chen Y, *et al.*: **Uncoupling of macrophage inflammation from self-renewal modulates host recovery from respiratory viral infection**. *Immunity* 2021, **54**:1200-1218.e9.

27. •• Aegerter H, Kulikauskaite J, Crotta S, Patel H, Kelly G, Hessel EM, Mack M, Beinke S, Wack A: **Influenza-induced monocyte-derived alveolar macrophages confer prolonged antibacterial protection**. *Nat Immunol* 2020, **21**:145-157.

This study investigates the mechanisms of enhanced protection against bacterial infection following infection with IAV. The authors show that, 1 month after IAV infection, monocyte-derived AMs are more responsive than resident AMs and produce more IL-6, which confer prolonged antibacterial protection. Of note, monocyte-derived AMs exhibit an epigenetic landscape suggestive of a dual imprinting both by the inflammation and the AM niche.

28. Guilliams M, Svedberg FR: **Does tissue imprinting restrict macrophage plasticity?** *Nat Immunol* 2021, **22**:118-127.

29. Park MD, Silvin A, Ginhoux F, Merad M: **Macrophages in health and disease**. *Cell* 2022, **185**:4259-4279.

30. Wong CK, Smith CA, Sakamoto K, Kaminski N, Koff JL, Goldstein DR: **Aging impairs alveolar macrophage phagocytosis and increases influenza-induced mortality in mice**. *J Immunol* 2017, **199**:1060-1068.

31. • McQuattie-Pimentel AC, Ren Z, Joshi N, Watanabe S, Stoeger T, Chi M, Lu Z, Sichizya L, Aillon RP, Chen C-I, *et al.*: **The lung microenvironment shapes a dysfunctional response of alveolar macrophages in aging**. *J Clin Invest* 2021, **131**:140299.

The investigation of age-related changes in the AM compartment supports that the ageing microenvironment is triggering a resistance of AM to proliferation via a hypo-responsiveness to GM-CSF, which could account for increased pneumonia severity in older patients.

32. Liu Z, Gu Y, Chakarov S, Bleriot C, Kwok I, Chen X, Shin A, Huang W, Dress RJ, Dutertre C-A, *et al.*: **Fate mapping via Ms4a3-expression history traces monocyte-derived cells**. *Cell* 2019, **178**:1509-1525.e19.

33. McQuattie-Pimentel AC, Ren Z, Joshi N, Watanabe S, Stoeger T, Chi M, Lu Z, Sichizya L, Aillon RP, Chen C-I, *et al.*: **The lung microenvironment shapes a dysfunctional response of alveolar macrophages in aging**. *J Clin Invest* 2021, **131**:e140299.

34. Schyns J, Bureau F, Marichal T: **Lung interstitial macrophages: past, present, and future**. *J Immunol Res* 2018, **2018**:5160794.

35. • Ural BB, Yeung ST, Damani-Yokota P, Devlin JC, de Vries M, Vera-Licona P, Samji T, Sawai CM, Jang G, Perez OA, *et al.*: **Identification of a nerve-associated, lung-resident interstitial macrophage subset with distinct localization and immunoregulatory properties**. *Sci Immunol* 2020, **5**:eaax8756.

This study characterises the phenotype, origin and transcriptional profile, function of a nerve-associated CD169+ macrophage (NAMs) subset localised to the bronchovascular tree. DT infection in Cd169Cre Cx3cr1LSL-DTR mice allowed a bolus depletion of NAMs, which supported the immunoregulatory roles of NAMs in the context of IAV infection.

36. Schyns J, Bai Q, Ruscitti C, Radermecker C, De Schepper S, Chakarov S, Farnir F, Pirottin D, Ginhoux F, Boeckxstaens G, *et al.*: **Non-classical tissue monocytes and two functionally distinct populations of interstitial macrophages populate the mouse lung**. *Nat Commun* 2019, **10**:3964.

37. Sabatel C, Radermecker C, Fievez L, Paulissen G, Chakarov S, Fernandes C, Olivier S, Toussaint M, Pirottin D, Xiao X, *et al.*: **Exposure to bacterial CpG DNA protects from airway allergic inflammation by expanding regulatory lung interstitial macrophages**. *Immunity* 2017, **46**:457-473.

38. Corry J, Kettenburg G, Upadhyay AA, Wallace M, Marti MM, Wonderlich ER, Bissel SJ, Goss K, Sturgeon TJ, Watkins SC, *et al.*: **Infiltration of inflammatory macrophages and neutrophils and widespread pyroptosis in lung drive influenza lethality in nonhuman primates**. *PLoS Pathog* 2022, **18**:e1010395.

39. Zhou B, Magana L, Hong Z, Huang LS, Chakraborty S, Tsukasaki Y, Huang C, Wang L, Di A, Ganesh B, *et al.*: **The angiocrine Rspondin3 instructs interstitial macrophage transition via metabolic-epigenetic reprogramming and resolves inflammatory injury**. *Nat Immunol* 2020, **21**:1430-1443.

40. Ogawa T, Shichino S, Ueha S, Bando K, Matsushima K: **Profibrotic properties of C1q+ interstitial macrophages in silica-induced pulmonary fibrosis in mice**. *Biochem Biophys Res Commun* 2022, **599**:113-119.

41. Aran D, Looney AP, Liu L, Wu E, Fong V, Hsu A, Chak S, Naikawadi RP, Wolters PJ, Abate AR, *et al.*: **Reference-based analysis of lung single-cell sequencing reveals a transitional profibrotic macrophage**. *Nat Immunol* 2019, **20**:163-172.

42. Misharin AV, Morales-Nebreda L, Reyfman PA, Cuda CM, Walter JM, McQuattie-Pimentel AC, Chen C-I, Anekalla KR, Joshi N, Williams KJN, *et al.*: **Monocyte-derived alveolar macrophages**

drive lung fibrosis and persist in the lung over the life span. *J Exp Med* 2017, **214**:2387-2404.

43. Chakarov S, Lim HY, Tan L, Lim SY, See P, Lum J, Zhang X-M, Foo S, Nakamizo S, Duan K, *et al*.: **Two distinct interstitial macrophage populations coexist across tissues in specific subtissular niches**. *Science* 2019, **363**:eaau0964.

44. • Vanneste D, Bai Q, Hasan S, Peng W, Pirottin D, Schyns J, Maréchal P, Ruscitti C, Meunier M, Liu Z, *et al*.: **MafB-restricted local monocyte proliferation precedes lung interstitial macrophage differentiation**. *Nat Immunol* 2023, **24**:827-840.

This study provides a real-time analysis of the trajectory of monocyte-to-IM development at steady-state thanks to a DT-inducible model of IM niche depletion and refilling using Tmem119Cre Cx3cr1LSL-DTR mice. A similar approach could be used to investigate monocyte-to-macrophage development in the context of IAV infection.

45. Bedoret D, Wallemacq H, Marichal T, Desmet C, Quesada Calvo F, Henry E, Closset R, Dewals B, Thielen C, Gustin P, *et al*.: **Lung interstitial macrophages alter dendritic cell functions to prevent airway allergy in mice**. *J Clin Invest* 2009, **119**:3723-3738.

46. Kawano H, Kayama H, Nakama T, Hashimoto T, Umemoto E, Takeda K: **IL-10-producing lung interstitial macrophages prevent neutrophilic asthma**. *Int Immunol* 2016, **28**:489-501.

47. Essers MAG, Offner S, Blanco-Bose WE, Waibler Z, Kalinke U, Duchosal MA, Trumpp A: **IFNalpha activates dormant haematopoietic stem cells in vivo**. *Nature* 2009, **458**:904-908.

48. Lin S-J, Lin K-M, Chen S-YJ, Ku C-C, Huang C-W, Huang C-H, Gale M, Tsai C-H: **Type I interferon orchestrates demand-adapted monopoiesis during influenza A virus infection via STAT1-mediated upregulation of macrophage colony-stimulating factor receptor expression**. *J Virol* 2023, **97**:e00102-23.

49. Beshara R, Sencio V, Soulard D, Barthélémy A, Fontaine J, Pinteau T, Deruyter L, Ismail MB, Paget C, Sirard J-C, *et al*.: **Alteration of Flt3-ligand-dependent de novo generation of conventional dendritic cells during influenza infection contributes to respiratory bacterial superinfection**. *PLoS Pathog* 2018, **14**:e1007360.

50. Seo S-U, Kwon H-J, Ko H-J, Byun Y-H, Seong BL, Uematsu S, Akira S, Kweon M-N: **Type I interferon signaling regulates Ly6C(hi) monocytes and neutrophils during acute viral pneumonia in mice**. *PLoS Pathog* 2011, **7**:e1001304.

51. Herold S, von Wulffen W, Steinmueller M, Pleschka S, Kuziel WA, Mack M, Srivastava M, Seeger W, Maus UA, Lohmeyer J: **Alveolar epithelial cells direct monocyte transepithelial migration upon influenza virus infection: impact of chemokines and adhesion molecules**. *J Immunol* 2006, **177**:1817-1824.

52. Schmit T, Guo K, Tripathi JK, Wang Z, McGregor B, Klomp M, Ambigapathy G, Mathur R, Hur J, Pichichero M, *et al*.: **Interferon-γ promotes monocyte-mediated lung injury during influenza infection**. *Cell Rep* 2022, **38**:110456.

53. •• Allen IC, Scull MA, Moore CB, Holl EK, McElvania-TeKippe E, Taxman DJ, Guthrie EH, Pickles RJ, Ting JP-Y: **The NLRP3 inflammasome mediates in vivo innate immunity to influenza A virus through recognition of viral RNA**. *Immunity* 2009, **30**:556-565.

These back-to-back papers describe a critical role for viral RNA-mediated NLRP3 inflammasome activation in the protection against IAV infection via a sensing in epithelial cells or macrophages leading to IL-1β release.

54. •• Thomas PG, Dash P, Aldridge JR, Ellebedy AH, Reynolds C, Funk AJ, Martin WJ, Lamkanfi M, Webby RJ, Boyd KL, *et al*.: **The intracellular sensor NLRP3 mediates key innate and healing responses to influenza A virus via the regulation of caspase-1**. *Immunity* 2009, **30**:566-575.

These back-to-back papers describe a critical role for viral RNA-mediated NLRP3 inflammasome activation in the protection against IAV infection via a sensing in epithelial cells or macrophages leading to IL-1β release.

55. Coates BM, Staricha KL, Ravindran N, Koch CM, Cheng Y, Davis JM, Shumaker DK, Ridge KM: **Inhibition of the NOD-Like receptor protein 3 inflammasome is protective in juvenile influenza A virus infection**. *Front Immunol* 2017, **8**:782.

56. Dawson TC, Beck MA, Kuziel WA, Henderson F, Maeda N: **Contrasting effects of CCR5 and CCR2 deficiency in the pulmonary inflammatory response to influenza A virus**. *Am J Pathol* 2000, **156**:1951-1959.

57. Lin KL, Suzuki Y, Nakano H, Ramsburg E, Gunn MD: **CCR2+ monocyte-derived dendritic cells and exudate macrophages produce influenza-induced pulmonary immune pathology and mortality**. *J Immunol* 2008, **180**:2562-2572.

58. Karupiah G, Chen JH, Mahalingam S, Nathan CF, MacMicking JD: **Rapid interferon gamma-dependent clearance of influenza A virus and protection from consolidating pneumonitis in nitric oxide synthase 2-deficient mice**. *J Exp Med* 1998, **188**:1541-1546.

59. Cao W, Taylor AK, Biber RE, Davis WG, Kim JH, Reber AJ, Chirkova T, De La, Cruz JA, Pandey A, Ranjan P, *et al*.: **Rapid differentiation of monocytes into type I IFN-producing myeloid dendritic cells as an antiviral strategy against influenza virus infection**. *J Immunol* 2012, **189**:2257-2265.

60. Cruz JLG, Pérez-Girón JV, Lüdtke A, Gómez-Medina S, Ruibal P, Idoyaga J, Muñoz-Fontela C: **Monocyte-derived dendritic cells enhance protection against secondary influenza challenge by controlling the switch in CD8+ T-cell immunodominance**. *Eur J Immunol* 2017, **47**:345-352.

61. Machiels B, Dourcy M, Xiao X, Javaux J, Mesnil C, Sabatel C, Desmecht D, Lallemand F, Martinive P, Hammad H, *et al*.: **A gammaherpesvirus provides protection against allergic asthma by inducing the replacement of resident alveolar macrophages with regulatory monocytes**. *Nat Immunol* 2017, **18**:1310-1320.

62. Stout RD, Jiang C, Matta B, Tietzel I, Watkins SK, Suttles J: **Macrophages sequentially change their functional phenotype in response to changes in microenvironmental influences**. *J Immunol* 2005, **175**:342-349.

63. Mosser DM, Edwards JP: **Exploring the full spectrum of macrophage activation**. *Nat Rev Immunol* 2008, **8**:958-969.

64. • Schilperoort M, Ngai D, Sukka SR, Avrampou K, Shi H, Tabas I: **The role of efferocytosis-fueled macrophage metabolism in the resolution of inflammation**. *Immunol Rev* 2023, https://doi.org/10.1111/imr.13214.

This review underlies the central role of efferocytosis in the regulation of inflammation and in the reprogramming of macrophage metabolism towards a proresolving phenotype.

65. Watanabe Y, Hashimoto Y, Shiratsuchi A, Takizawa T, Nakanishi Y: **Augmentation of fatality of influenza in mice by inhibition of phagocytosis**. *Biochem Biophys Res Commun* 2005, **337**:881-886.

66. Fujimoto I, Pan J, Takizawa T, Nakanishi Y: **Virus clearance through apoptosis-dependent phagocytosis of influenza A virus-infected cells by macrophages**. *J Virol* 2000, **74**:3399-3403.

67. Kourtzelis I, Hajishengallis G, Chavakis T: **Phagocytosis of apoptotic cells in resolution of inflammation**. *Front Immunol* 2020, **11**:553.

68. Diskin C, Pålsson-McDermott EM: **Metabolic modulation in macrophage effector function**. *Front Immunol* 2018, **9**:270.

69. Zhang S, Weinberg S, DeBerge M, Gainullina A, Schipma M, Kinchen JM, Ben-Sahra I, Gius DR, Yvan-Charvet L, Chandel NS, *et al*.: **Efferocytosis fuels requirements of fatty acid oxidation and the electron transport chain to polarize macrophages for tissue repair**. *Cell Metab* 2019, **29**:443-456.e5.

70. Chen WH, Toapanta FR, Shirey KA, Zhang L, Giannelou A, Page C, Frieman MB, Vogel S, Cross AS: **Potential role for alternatively activated macrophages in the secondary bacterial infection during recovery from influenza**. *Immunol Lett* 2012, **141**:227-234.

71. Li BWS, de Bruijn MJW, Lukkes M, van Nimwegen M, Bergen IM, KleinJan A, GeurtsvanKessel CH, Andeweg A, Rimmelzwaan GF, Hendriks RW: **T cells and ILC2s are major effector cells in**

influenza-induced exacerbation of allergic airway inflammation in mice. *Eur J Immunol* 2019, **49**:144-156.

72. Wynn TA, Vannella KM: **Macrophages in tissue repair, regeneration, and fibrosis**. *Immunity* 2016, **44**:450-462.

73. Gieseck RL, Wilson MS, Wynn TA: **Type 2 immunity in tissue repair and fibrosis**. *Nat Rev Immunol* 2018, **18**:62-76.

74. O'Brien EM, Spiller KL: **Pro-inflammatory polarization primes macrophages to transition into a distinct M2-like phenotype in response to IL-4**. *J Leukoc Biol* 2022, **111**:989-1000.

75. Modolell M, Corraliza IM, Link F, Soler G, Eichmann K: **Reciprocal regulation of the nitric oxide synthase/arginase balance in mouse bone marrow-derived macrophages by TH 1 and TH 2 cytokines**. *Eur J Immunol* 1995, **25**:1101-1104.

76. Yurdagul A, Subramanian M, Wang X, Crown SB, Ilkayeva OR, Darville L, Kolluru GK, Rymond CC, Gerlach BD, Zheng Z, *et al*.: **Macrophage metabolism of apoptotic cell-derived arginine promotes continual efferocytosis and resolution of injury**. *Cell Metab* 2020, **31**:518-533.e10.

77. Baek AR, Hong J, Song KS, Jang AS, Kim DJ, Chin SS, Park SW: **Spermidine attenuates bleomycin-induced lung fibrosis by inducing autophagy and inhibiting endoplasmic reticulum stress (ERS)-induced cell death in mice**. *Exp Mol Med* 2020, **52**:2034-2045.

78. Karna E, Szoka L, Huynh TYL, Palka JA: **Proline-dependent regulation of collagen metabolism**. *Cell Mol Life Sci* 2020, **77**:1911-1918.

79. Ito Y, Correll K, Zemans RL, Leslie CC, Murphy RC, Mason RJ: **Influenza induces IL-8 and GM-CSF secretion by human alveolar epithelial cells through HGF/c-Met and TGF-α/EGFR signaling**. *Am J Physiol Lung Cell Mol Physiol* 2015, **308**:L1178-L1188.

80. Ghoneim HE, Thomas PG, McCullers JA: **Depletion of alveolar macrophages during influenza infection facilitates bacterial superinfections**. *J Immunol* 2013, **191**:1250-1259.

81. Sun K, Metzger DW: **Inhibition of pulmonary antibacterial defense by interferon-gamma during recovery from influenza infection**. *Nat Med* 2008, **14**:558-564.

82. Verma AK, McKelvey M, Uddin MB, Palani S, Niu M, Bauer C, Shao S, Sun K: **IFN-γ transforms the transcriptomic landscape and triggers myeloid cell hyperresponsiveness to cause lethal lung injury**. *Front Immunol* 2022, **13**:1011132.

83. •• Roquilly A, Jacqueline C, Davieau M, Mollé A, Sadek A, Fourgeux C, Rooze P, Broquet A, Misme-Aucouturier B, Chaumette T, *et al*.: **Alveolar macrophages are epigenetically altered after inflammation, leading to long-term lung immunoparalysis**. *Nat Immunol* 2020, **21**:636-648.

This study shows that resident AMs undergo a tolerogenic epigenetic reprogramming after inflammation, which relies on SIRPα-dependent micro-environmental signals and leads to AM immunoparalysis, poor phagocytic capacity and enhanced risks of secondary bacterial infections.

84. Wang T, Zhang J, Wang Y, Li Y, Wang L, Yu Y, Yao Y: **Influenza-trained mucosal-resident alveolar macrophages confer long-term antitumor immunity in the lungs**. *Nat Immunol* 2023, **24**:423-438.

85. Iliakis CS, Kulikauskaite J, Aegerter H, Li F, Piattini F, Jakubzick CV, Guilliams M, Kopf M, Wack A: **The role of recruitment versus training in influenza-induced lasting changes to alveolar macrophage function**. *Nat Immunol* 2023, **24**:1639-1641.

86. Steuerman Y, Cohen M, Peshes-Yaloz N, Valadarsky L, Cohn O, David E, Frishberg A, Mayo L, Bacharach E, Amit I, *et al*.: **Dissection of influenza infection in vivo by single-cell RNA sequencing**. *Cell Syst* 2018, **6**:679-691.e4.

87. Kasmani MY, Topchyan P, Brown AK, Brown RJ, Wu X, Chen Y, Khatun A, Alson D, Wu Y, Burns R, *et al*.: **A spatial sequencing atlas of age-induced changes in the lung during influenza infection**. *Nat Commun* 2023, **14**:6597.

88. Carlin LM, Stamatiades EG, Auffray C, Hanna RN, Glover L, Vizcay-Barrena G, Hedrick CC, Cook HT, Diebold S, Geissmann F: **Nr4a1-dependent Ly6C(low) monocytes monitor endothelial cells and orchestrate their disposal**. *Cell* 2013, **153**:362-375.

89. Hanna RN, Carlin LM, Hubbeling HG, Nackiewicz D, Green AM, Punt JA, Geissmann F, Hedrick CC: **The transcription factor NR4A1 (Nur77) controls bone marrow differentiation and the survival of Ly6C- monocytes**. *Nat Immunol* 2011, **12**:778-785.

90. Geissmann F, Jung S, Littman DR: **Blood monocytes consist of two principal subsets with distinct migratory properties**. *Immunity* 2003, **19**:71-82.

91. Jakubzick C, Gautier EL, Gibbings SL, Sojka DK, Schlitzer A, Johnson TE, Ivanov S, Duan Q, Bala S, Condon T, *et al*.: **Minimal differentiation of classical monocytes as they survey steady-state tissues and transport antigen to lymph nodes**. *Immunity* 2013, **39**:599-610.

92. Rawat K, Tewari A, Li X, Mara AB, King WT, Gibbings SL, Nnam CF, Kolling FW, Lambrecht BN, Jakubzick CV: **CCL5-producing migratory dendritic cells guide CCR5+ monocytes into the draining lymph nodes**. *J Exp Med* 2023, **220**:e20222129.

93. Schneider C, Nobs SP, Kurrer M, Rehrauer H, Thiele C, Kopf M: **Induction of the nuclear receptor PPAR-gamma by the cytokine GM-CSF is critical for the differentiation of fetal monocytes into alveolar macrophages**. *Nat Immunol* 2014, **15**:1026-1037.

94. Gschwend J, Sherman SPM, Ridder F, Feng X, Liang H-E, Locksley RM, Becher B, Schneider C: **Alveolar macrophages rely on GM-CSF from alveolar epithelial type 2 cells before and after birth**. *J Exp Med* 2021, **218**:e20210745.

95. Yu X, Buttgereit A, Lelios I, Utz SG, Cansever D, Becher B, Greter M: **The cytokine TGF-β promotes the development and homeostasis of alveolar macrophages**. *Immunity* 2017, **47**:903-912.e4.

96. Guilliams M, De Kleer I, Henri S, Post S, Vanhoutte L, De Prijck S, Deswarte K, Malissen B, Hammad H, Lambrecht BN: **Alveolar macrophages develop from fetal monocytes that differentiate into long-lived cells in the first week of life via GM-CSF**. *J Exp Med* 2013, **210**:1977-1992.

97. Gibbings SL, Thomas SM, Atif SM, McCubbrey AL, Desch AN, Danhorn T, Leach SM, Bratton DL, Henson PM, Janssen WJ, *et al*.: **Three unique interstitial macrophages in the murine lung at steady state**. *Am J Respir Cell Mol Biol* 2017, **57**:66-76.

98. Tang X-Z, Kreuk LSM, Cho C, Metzger RJ, Allen CDC: **Bronchus-associated macrophages efficiently capture and present soluble inhaled antigens and are capable of local Th2 cell activation**. *eLife* 2022, **11**:e63296.

99. Dick SA, Wong A, Hamidzada H, Nejat S, Nechanitzky R, Vohra S, Mueller B, Zaman R, Kantores C, Aronoff L, *et al*.: **Three tissue resident macrophage subsets coexist across organs with conserved origins and life cycles**. *Sci Immunol* 2022, **7**:eabf7777.

100. Legrand C, Vanneste D, Hego A, Sabatel C, Mollers K, Schyns J, Maréchal P, Abinet J, Tytgat A, Liégeois M, *et al*.: **Lung interstitial macrophages can present soluble antigens and induce Foxp3+ regulatory T cells**. *Am J Respir Cell Mol Biol* 2024, https://doi.org/10.1165/rcmb.2023-0254OC

MACROPHAGES

Recruited atypical Ly6G$^+$ macrophages license alveolar regeneration after lung injury

Cecilia Ruscitti[1,2], Joan Abinet[1,2], Pauline Maréchal[1,2], Margot Meunier[1,2], Constance de Meeûs[2,3], Domien Vanneste[1,2], Pierre Janssen[1,2], Mickael Dourcy[2,4], Marc Thiry[5], Fabrice Bureau[2,6], Christoph Schneider[7], Benedicte Machiels[2,4], Andres Hidalgo[8,9], Florent Ginhoux[10,11,12,13], Benjamin G. Dewals[2,4], Julien Guiot[14,15], Florence Schleich[14,15], Mutien-Marie Garigliany[2,3], Akeila Bellahcène[16], Coraline Radermecker[1,2]*†, Thomas Marichal[1,2,17]*†

The lung is constantly exposed to airborne pathogens and particles that can cause alveolar damage. Hence, appropriate repair responses are essential for gas exchange and life. Here, we deciphered the spatiotemporal trajectory and function of an atypical population of macrophages after lung injury. Post–influenza A virus (IAV) infection, short-lived monocyte-derived Ly6G-expressing macrophages (Ly6G$^+$ Macs) were recruited to the alveoli of lung perilesional areas. Ly6G$^+$ Macs engulfed immune cells, exhibited a high metabolic potential, and clustered with alveolar type 2 epithelial cells (AT2s) in zones of active epithelial regeneration. Ly6G$^+$ Macs were partially dependent on granulocyte-macrophage colony-stimulating factor and interleukin-4 receptor signaling and were essential for AT2-dependent alveolar regeneration. Similar macrophages were recruited in other models of injury and in the airspaces of lungs from patients with suspected pneumonia. This study identifies perilesional alveolar Ly6G$^+$ Macs as a spatially restricted, short-lived macrophage subset promoting epithelial regeneration postinjury, thus representing an attractive therapeutic target for treating lung damage.

INTRODUCTION

Severe respiratory viral infections represent a global health issue and a major threat for health care systems given that they often require hospitalization, as seen during annual influenza A virus (IAV) outbreaks or the COVID-19 pandemic. Acute lung infectious episodes are typically associated with excessive lung inflammation, damage, and abnormal tissue repair that can lead to acute respiratory distress syndrome (ARDS), pneumonia, and death (*1*–*5*). Deciphering the mechanisms eliciting appropriate lung regeneration and host recovery after viral-triggered lung injury is urgently needed to improve clinical management and broaden therapeutic opportunities.

Blood monocytes are heavily recruited to the lungs during the acute inflammatory phase postinfection, thereby contributing to host innate defense mechanisms. When not appropriately regulated, they are also thought to contribute to uncontrolled inflammation via the aberrant release of cytokines, which, in its extreme form, is known as a "cytokine storm," which has been well described in patients with severe COVID-19 (*3*, *6*–*9*). Recruited monocytes can also differentiate into monocyte-derived macrophages (Mo-Macs) that are short lived or can establish long-term residency in particular niches and can have functional consequences for lung immunity (*10*–*15*). The idea that recruited Mo-Macs are considered pathogenic after influenza infection (*15*, *16*) or COVID-19 (*6*, *17*) whereas lung-resident alveolar macrophages (AMs) and interstitial macrophages (IMs) exert beneficial roles (*13*, *18*–*24*) is likely oversimplistic. Recruited Mo-Macs are increasingly recognized as heterogeneous and can adopt distinct functional identities that depend on their differentiation trajectory, the diseased tissue microenvironment, the extent and phase of inflammation, and their activation state (*9*, *13*, *14*, *18*, *25*). In this regard, the fate and functions of short-lived Mo-Macs after lung injury remain incompletely described.

Here, we used an in vivo model of IAV-triggered injury to investigate the spatiotemporal trajectory and function of an atypical population of Mo-Macs expressing Ly6G, a marker considered to be restricted to granulocytes. We found that Ly6G$^+$ Macs emerged transiently from Ccr2-dependent monocytes during the early recovery phase post-IAV, populated the alveolar lumen of lung perilesional areas, and could promote progenitor AT2 differentiation and alveolar reepithelization. Our study thus unravels the fate and function of a previously undescribed Ly6G$^+$ Mac population that engages in cross-talk with epithelial cells to promote epithelial regeneration after viral-triggered lung injury.

RESULTS

Lung Ly6G$^+$ Macs emerge in the early recovery phase post-IAV infection

To investigate the dynamic of myeloid cell responses after lung injury, we performed time-course flow cytometry studies in a clinically

[1]Laboratory of Immunophysiology, GIGA Institute, University of Liège, Liège, Belgium. [2]Faculty of Veterinary Medicine, University of Liège, Liège, Belgium. [3]Department of Pathology, FARAH Institute, University of Liège, Liège, Belgium. [4]Laboratory of Immunology-Vaccinology, FARAH Institute, University of Liège, Liège, Belgium. [5]Laboratory of Cellular and Tissular Biology, GIGA Institute, University of Liège, Liège, Belgium. [6]Laboratory of Cellular and Molecular Immunology, GIGA Institute, University of Liège, Liège, Belgium. [7]Institute of Physiology, University of Zurich, Zurich, Switzerland. [8]Area of Cell & Developmental Biology, Centro Nacional de Investigaciones Cardiovasculares Carlos III, Madrid, Spain. [9]Vascular Biology and Therapeutics Program and Department of Immunobiology, Yale University School of Medicine, New Haven, CT, USA. [10]Shanghai Institute of Immunology, Shanghai JiaoTong University School of Medicine, Shanghai, China. [11]Inserm U1015, Gustave Roussy, Bâtiment de Médecine Moléculaire, Villejuif, France. [12]Singapore Immunology Network (SIgN), Agency for Science, Technology and Research (A*STAR), Singapore, Singapore. [13]Translational Immunology Institute, SingHealth Duke-NUS Academic Medical Centre, Singapore, Singapore. [14]Laboratory of Pneumology, GIGA Institute, University of Liège, Liège, Belgium. [15]Department of Respiratory Medicine, CHU University Hospital, Liège, Belgium. [16]Metastasis Research Laboratory, GIGA Institute, University of Liège, Liège, Belgium. [17]Walloon Excellence in Life Sciences and Biotechnology (WELBIO) Department, WEL Research Institute, Wavre, Belgium.
*Corresponding author. Email: c.radermecker@uliege.be (C.R.); t.marichal@uliege.be (T.M.)
†These authors contributed equally to this work.

relevant mouse model of lung infectious injury after IAV infection (*2*). Eight- to 12-week-old C57BL/6 wild-type (WT) mice were infected intranasally with 5 plaque-forming units (PFUs) of IAV H1N1 strain PR8/34, which triggered self-limiting disease with a peak in viral RNA at day 5 after IAV and viral clearance at day 10 after IAV (fig. S1, A and B). In this model, Ly6G$^+$CD11b$^+$CD64$^-$ neutrophils (Neus) increased at day 5 after IAV and returned to baseline by day 15 (Fig. 1, A and B). A partial loss of Ly6G$^-$CD64$^+$SiglecF$^+$CD11c$^+$ AMs was observed between day 5 and day 10 after IAV, which was restored at day 15 after IAV, as previously described (*15*) (Fig. 1, A and B). The numbers of CD64$^-$Ly6C$^-$ monocytes (Ly6C$^-$ Mos) remained stable over the course of infection, unlike those of classical CD64$^-$Ly6C$^+$ Mos (Ly6C$^+$ Mos) and inflammatory CD64$^+$Ly6C$^+$ monocytes (iMos) that peaked around day 5 after IAV (Fig. 1, A and B). Macs resembling IMs (IM-like), defined as F4/80$^+$CD11b$^+$Ly6G$^-$ SiglecF$^-$Ly6C$^-$CD64$^+$ cells and likely encompassing resident IMs and recruited Mo-Macs, increased over time (Fig. 1, A and B). We also observed emergence, from day 5 onward, of a distinct population of IAV-triggered Ly6G$^+$CD11b$^+$CD64$^+$ Macs that fell in the classical Ly6G$^+$CD11b$^+$ Neu gate but were distinct from Neus on the basis of their elevated CD64 expression (Fig. 1, C and D), which we call Ly6G$^+$ Macs hereafter. Ly6G$^+$ Macs were absent in the blood (Fig. 1E), peaked at day 10 after IAV in the lung, and could still be detected at days 15 and 20 after IAV (Fig. 1D). Morphologically, Ly6G$^+$ Macs analyzed at day 10 after IAV exhibited a kidney-shaped nucleus, like iMos, and had numerous cytoplasmic vacuolated structures and a cell membrane rich in protrusions (Fig. 1F and fig. S1C). Phenotypically, Ly6G$^+$ Macs were F4/80^{hi}SiglecF^{lo}CD11c^{lo} (fig. S1, D and E) and expressed high levels of the chemokine receptor CXCR4, type II major histocompatibility complex (MHC-II), CD101, and CD319, a regulator of Mac functions (Fig. 1, G and H) (*26*, *27*). However, Ly6G$^+$ Macs exhibited low expression of the Neu activation marker CD177 (Fig. 1, G and H).

Next, we performed single-cell RNA sequencing (scRNA-seq) analyses of lung myeloid cells at day 10 after IAV. Lung CD45$^+$F4/80$^+$ and/or CD11b$^+$ cells were sorted from five mock-infected and five IAV-infected mice and were subjected to single-cell droplet encapsulation (*28*), scRNA-seq, and quality control filtering. The curated data were integrated with a published dataset of steady-state lung monocytes and IMs (*29*) and projected in global and condition-specific uniform manifold approximation and projection (UMAP) plots (Fig. 2A). Myeloid cells from mock-infected mice mainly comprised clusters annotated as AMs (*Chil3*, *Ear1*, and *Fapb1*; C6), Ly6C$^-$ Mos (*Ace*, *Nr4a1*, and *Fcgr4*; C3), Ly6C$^+$ Mos (*Ccr2* and *Ly6c2*; C4), and dendritic cells (DCs; *H2-Ab1*, *Cd209a*, and *Flt3;* C9) (Fig. 2, A to C, and fig. S2A). Few cycling Macs (*Birc5*, *Top2a*, and *Mki67*; C11) were also detected in mock-infected mice, along with few CD206$^-$ IMs (*C1qa*, *C1qc*, *H2-Ab1*, *Cd74*, and *Tmem119;* C1) and CD206$^+$ IMs (*C1qa*, *C1qc*, *Mrc1*, and *Maf*; C8) (Fig. 2, A to C, and fig. S2A) (*29*). Ten days after IAV, AMs (C6) disappeared; a small cluster of IAV-associated AMs was present instead (*Chil3*, *Ear1*, and *Ear2*; C12), Neus were recruited (*S100a8*, *S100a9*, and *Mmp9*; C7), and IMs (C1 and C8) and iMos (*Ccr2*, *Ly6c2*, and *Irf7*; C5) expanded (Fig. 2, A to C, and fig. S2A). Of note, clusters C2 and C10 were specifically triggered by IAV. C10 had an elevated content in mitochondrial genes and low numbers of detected genes (fig. S2B) and was therefore annotated as dying Macs. C2 expressed significantly higher levels of cathepsins (*Ctsb* and *Ctsz*), galectins (*Lgals1* and *Lgals3*), arginase-1 (*Arg1*), and osteopontin (*Spp1*) as compared with the other clusters (Fig. 2D). Intracellular flow cytometry staining for arginase-1 and osteopontin showed that the combined expression of these two proteins was restricted to Ly6G$^+$ Macs at day 10 after IAV (Fig. 2, E and F), supporting that C2 corresponded to Ly6G$^+$ Macs identified by flow cytometry. Of note, Ly6G$^+$ Macs expressed high levels of *Csf1r* and *Slamf7* (coding for CD319) but did not express any of the Neu-related transcripts *Csf3r*, *S100a8*, *S100a9*, *Mmp8*, *Mmp9*, *Mpo*, *Slpi*, or *Cd177* (fig. S2, A and C). *Ly6g* transcripts were not detectable in Neus or Ly6G$^+$ Macs (fig. S2, A and C). Ly6G$^+$ Macs (C2) displayed both "M1-like" or "M2-like" signature scores and genes and could not be categorized as such on the basis of their expression profile (fig. S2, D and E). Together, our data show that a phenotypically and transcriptionally distinct subset of Ly6G$^+$ Macs emerges during a specific time window corresponding to early weight recovery post-IAV.

Ly6G$^+$ Macs arise from recruited monocytes and are partially dependent on GM-CSF receptor signaling

We next investigated the origin of Ly6G$^+$ Macs and asked whether they could expand via local proliferation. We observed that the percentage of cells positive for the proliferation Ki67 was very low in Ly6G$^+$ Macs (fig. S3A). Next, we treated mice at day 10 after IAV intraperitoneally with 5-ethynyl-2′-deoxyuridine (EdU) 4 hours before analysis. Although the percentage of EdU$^+$ cells was higher in AMs compared with all other lung myeloid cells, indicative of active proliferation, nearly, no EdU$^+$ cells were detected in Ly6G$^+$ Macs, ruling out their active proliferation (fig. S3, B and C). Third, we assessed whether Ly6G$^+$ Macs arose from the bone marrow (BM) or from local progenitor monocytes (*30*). We generated chimeric mice in which lethally irradiated, thorax-protected CD45.2 WT mice were reconstituted with BM cells from *Ms4a3*^{Cre}*R26*^{LSLtdTomato} mice (subsequently referred to as *Ms4a3*^{tdTom}), in which the progeny of granulocyte–monocyte progenitors (GMPs) are constitutively labeled (*31*). At week 4 after transfer, the percentage of tdTomato$^+$ blood Ly6C$^+$ Mos was around 50%, whereas the percentages of tdTomato$^+$ lung AMs and IMs were very low, confirming efficient reconstitution and thorax protection (fig. S3, D to G). At day 10 after IAV, we found that the percentage of tdTomato$^+$ Ly6G$^+$ Macs was similar to that of Ly6C$^+$ Mos (fig. S3, H and I), consistent with a major contribution of BM-derived GMPs, but not local progenitors, to Ly6G$^+$ Macs.

The kinetics of Ly6G$^+$ Mac emergence post-IAV was comparable to but delayed compared with that of Ly6C$^+$ Mos and iMos, consistent with the idea that recruited Ly6C$^+$ Mos could give rise to Ly6G$^+$ Macs. Supporting this, Slingshot trajectory analyses of the scRNA-seq data identified two main trajectories starting from Ly6C$^+$ Mos, transiting through iMos to give rise to either IM-like cells or Ly6G$^+$ Macs (Fig. 3A) (*32*). Genes that exhibited the same pattern of down-regulation along pseudotime in each trajectory encompassed the classical monocyte-associated genes *Ccr2* and *Ly6c2* (Fig. 3B). We also found, in both trajectories, a time-restricted up-regulation of interferon-stimulated genes (*Ifi209*, *Ifitm3*, *Ifi47*, and *Isg15*) that likely corresponded to transitioning iMos (Fig. 3B). Last, trajectory-specific genes were gradually and specifically up-regulated along pseudotime in the IM-like (e.g., *C1qa*, *C1qc*, *C1qb*, *Mrc1*, *Cd74*, *H2-Ab1*, and *H2-Eb1*) or the Ly6G$^+$ Mac (e.g., *Arg1*, *Spp1*, *Ccl2*, *Ccl7*, and *Ctsb*) trajectories (Fig. 3B).

Next, we infected the monocyte fate-mapper mice *Ms4a3*^{tdTom} (*31*) and *Cx3cr1*^{GFP} (*33*) with IAV and found that, at day 10 after IAV, Ly6G$^+$ Macs were Tomato$^+$ and GFP^{hi}, respectively, consistent with their

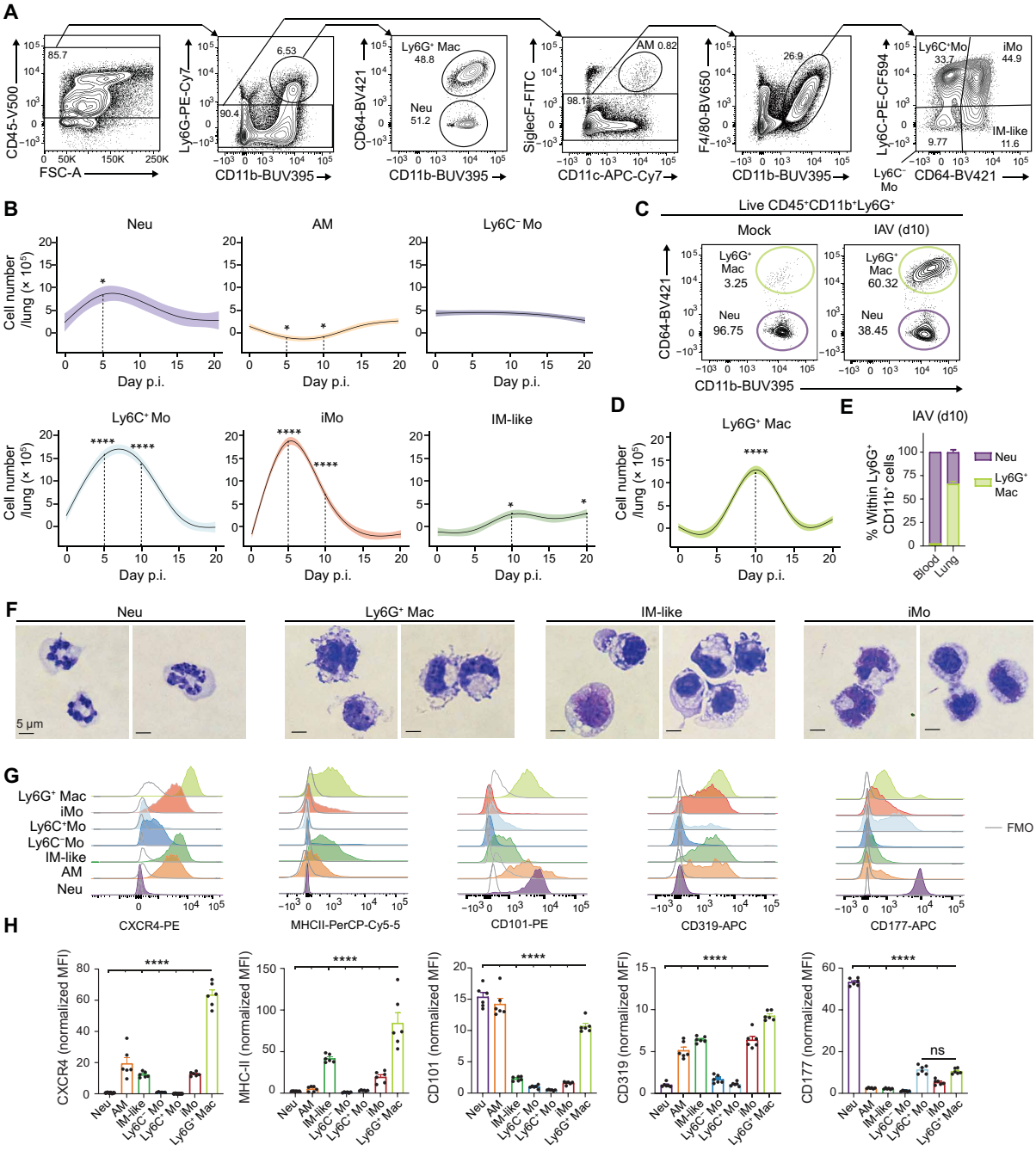

Fig. 1. Ly6G$^+$ Macs culminate during the early recovery phase post-IAV infection. (**A**) Representative flow cytometry gating strategy showing live CD45$^+$CD11b$^+$Ly6G$^+$CD64$^-$ Neus, CD45$^+$CD11b$^+$Ly6G$^+$CD64$^+$ macrophages (Ly6G$^+$ Macs), CD45$^+$Ly6G$^-$CD11c$^+$SiglecF$^+$ AMs, CD45$^+$Ly6G$^-$SiglecF$^-$F4/80$^+$CD11b$^+$Ly6C$^+$CD64$^-$ monocytes (Ly6C$^+$ Mos), CD45$^+$Ly6G$^-$SiglecF$^-$F4/80$^+$CD11b$^+$Ly6C$^-$CD64$^-$ monocytes (Ly6C$^-$ Mos), CD45$^+$Ly6G$^-$SiglecF$^-$F4/80$^+$CD11b$^+$Ly6C$^+$CD64$^+$ iMos, and CD45$^+$Ly6G$^-$SiglecF$^-$F4/80$^+$CD11b$^+$Ly6C$^-$CD64$^+$ IM-like cells in lungs of C57BL/6 WT mice at day 10 after IAV. (**B**) Time course of absolute numbers of Neus, AMs, Ly6C$^-$ Mos, Ly6C$^+$ Mos, iMos, and IM-like cells quantified by flow cytometry at days 0, 5, 10, 15, and 20 after IAV in WT mice. (**C**) Representative contour plots of CD64 and CD11b expression within lung CD45$^+$CD11b$^+$Ly6G$^+$ cells at day 10 after infection in mock-infected or IAV-infected WT mice. (**D**) Time course of absolute numbers of Ly6G$^+$ Macs quantified by flow cytometry, as in (B). (**E**) Percentage of Neu and Ly6G$^+$ Macs within Ly6G$^+$CD11b$^+$ cells quantified by flow cytometry in the blood and lungs of WT mice at day 10 after IAV. (**F**) Photographs of Neus, Ly6G$^+$ Macs, IM-like cells, and iMos sorted by FACS from IAV-infected WT mice at day 10 after infection. Pictures are representative of one of three independent sorting experiments, each giving similar results. (**G**) Representative histograms of CXCR4, MHC-II, CD101, CD319, and CD177 expression in the indicated myeloid cell populations, quantified by flow cytometry at day 10 after IAV in WT mice. (**H**) Quantification of the expression of the indicated markers, as in (G). MFI, mean fluorescence intensity. [(B) and (D)] Data show means (centerline) ± SEM (colored area) and are pooled from two or three independent experiments ($n = 6$ mice per time point); [(E) and (H)] Data show means + SEM and are pooled from two independent experiments ($n = 5$ or 6 mice). [(B), (D), and (H)] P values were calculated using one-way analysis of variance (ANOVA) with Dunnett's post hoc tests. *$P < 0.05$; ****$P < 0.0001$. FMO, fluorescence minus one; ns, not significant; p.i., postinfection. (F) Scale bars, 5 µm.

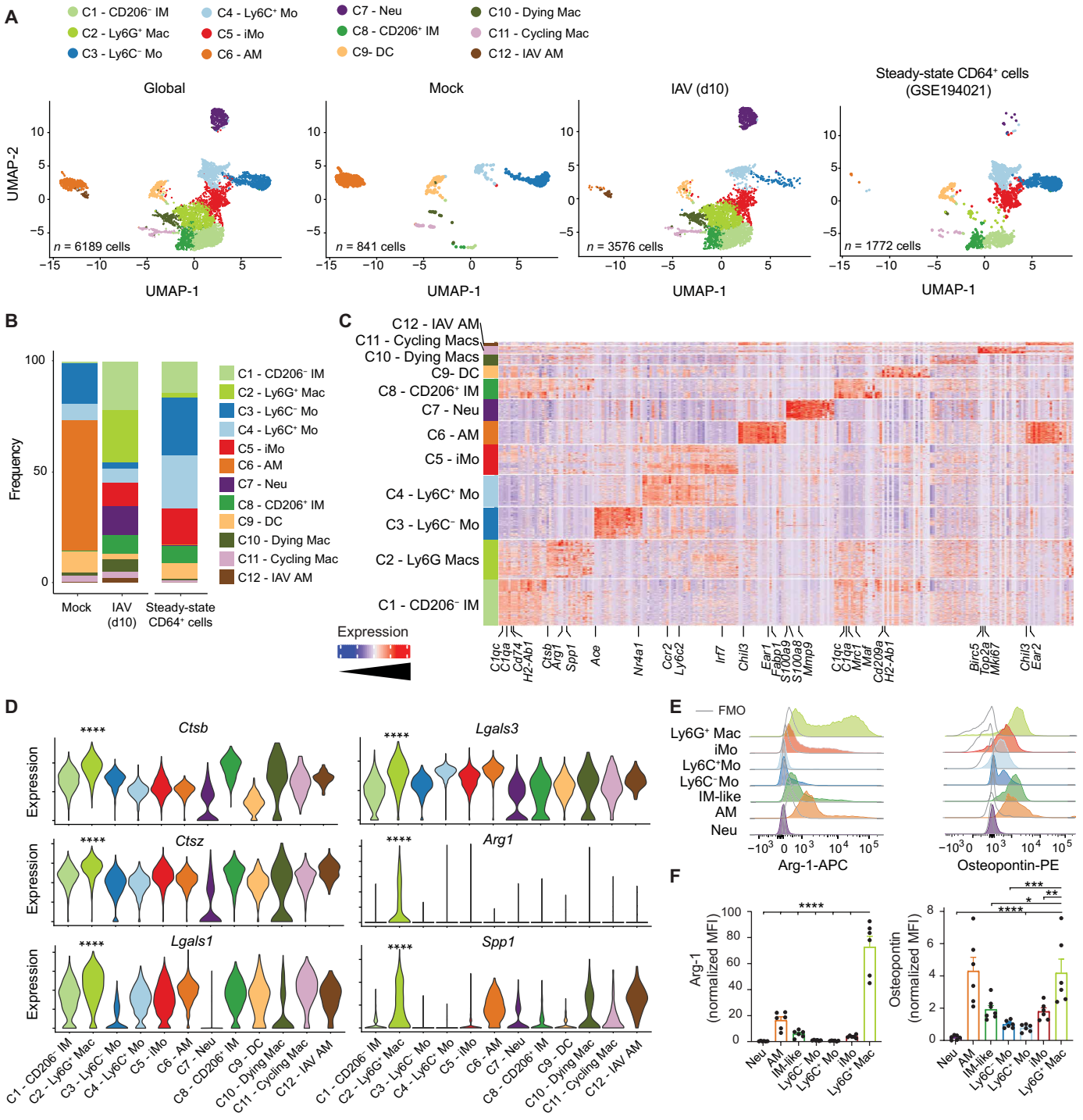

Fig. 2. Ly6G$^+$ Macs are transcriptionally distinct from other lung myeloid cells at day 10 after IAV. (**A**) UMAP plots of scRNA-seq data depicting the transcriptional identity of FACS-sorted lung live CD45$^+$F4/80$^+$ and/or CD11b$^+$ cells from mock-infected or IAV-infected WT mice 10 days after infection (pooled from five mice per condition), merged with a published dataset of steady-state lung monocytes and IMs (*29*). (**B**) Frequency of each cluster for each experimental condition, as in (A). (**C**) Heatmap depicting the single-cell expression of the most up-regulated genes within each cluster. (**D**) Expression of the indicated genes within each cluster, as depicted by violin plots (height: expression; width: abundance of cells). (**E**) Representative histograms of intracellular Arg-1 and osteopontin expression in the indicated lung myeloid cell populations, quantified by flow cytometry at day 10 after IAV in WT mice. (**F**) Quantification of Arg-1 and osteopontin expression, as in (E). (F) Data show means + SEM and are pooled from two independent experiments ($n = 6$ mice). *P* values were calculated using (D) Wilcoxon rank sum test and comparing C2 versus all other clusters or (F) one-way ANOVA with Dunnett's post hoc tests. *$P < 0.05$; **$P < 0.01$; ***$P < 0.001$; ****$P < 0.0001$.

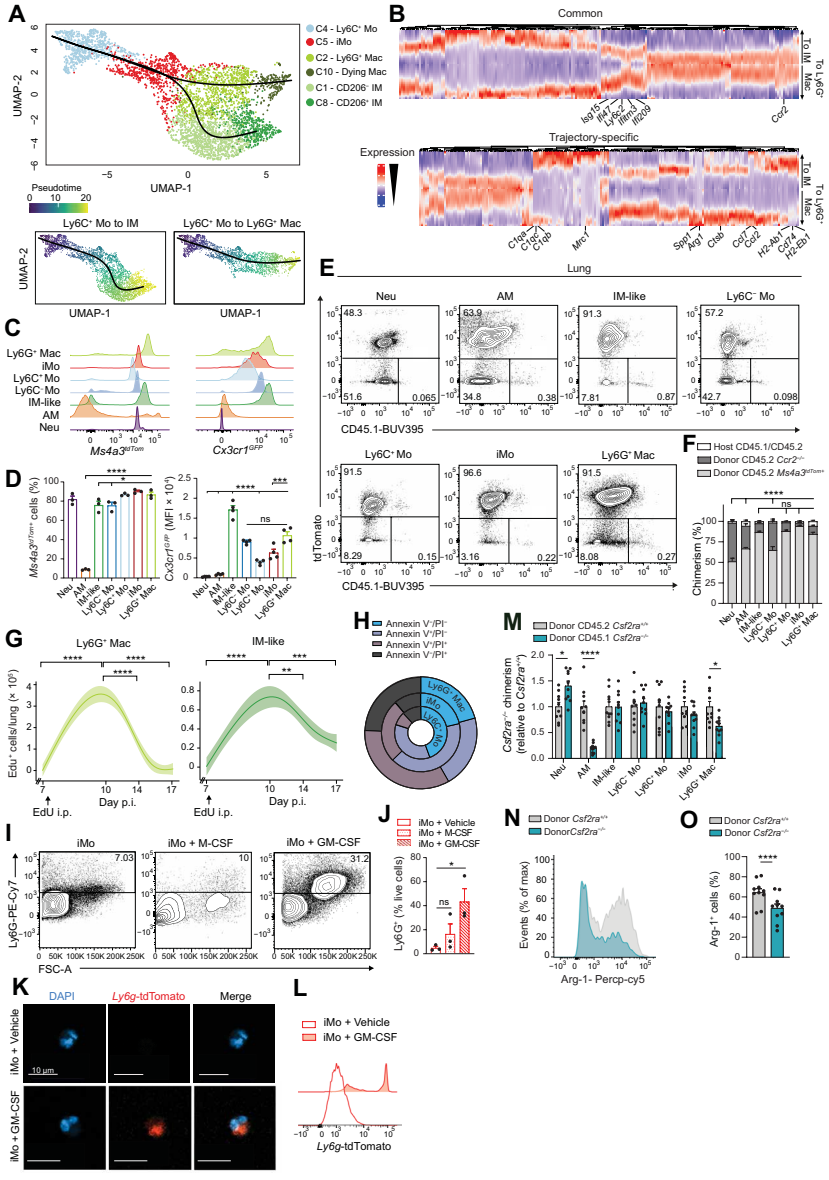

Fig. 3. IAV-triggered Ly6G$^+$ Macs are recruited from classical monocytes and are short lived. (**A**) UMAP plot depicting the transcriptional identity and cell trajectories (top) and pseudotime trajectory values (bottom) of lung Ly6C$^+$ Mos, iMos, Ly6G$^+$ Macs, dying Macs, CD206$^-$ IMs, and CD206$^+$ IMs, as in Fig. 2A, evaluated by Slingshot trajectory analyses. (**B**) Heatmap plot depicting the differentially expressed genes along pseudotime evaluated by tradeSeq in the trajectory starting from Ly6C$^+$ Mos and ending either in IMs or in Ly6G$^+$ Macs. (**C**) Representative histograms of tdTomato (left) and GFP (right) expression in the indicated myeloid cell populations, quantified by flow cytometry at day 10 after IAV in *Ms4a3*^{tdTom} and *Cx3Cr1*^{GFP} mice, respectively. (**D**) Quantification of tdTomato$^+$ cells (left) and GFP expression (right), as in (C). (**E**) Representative tdTomato and CD45.1 contour plots and (**F**) bar graph showing % of host, donor *Ccr2*$^{-/-}$, and donor *Ms4a3*$^{tdTom+}$ chimerism in the indicated cell populations from lethally irradiated CD45.1/CD45.2 mice reconstituted with a 1:1 mix of CD45.2 *Ccr2*$^{-/-}$ and *Ms4a3*$^{tdTom+}$ BM cells, infected with IAV 4 weeks later, and evaluated at day 10 after IAV. (**G**) Time course of absolute numbers of EdU$^+$ Ly6G$^+$ Macs and EdU$^+$ IM-like cells quantified by flow cytometry at days 7, 10, 14, and 17 after IAV in EdU-pulsed WT mice at day 7 after IAV. (**H**) Pie chart representation of the mean frequency of annexin V– and PI-negative and/or positive fractions within lung Ly6C$^+$ Mos, iMos, and Ly6G$^+$ Macs, quantified at day 10 after IAV in WT mice. (**I**) Representative Ly6G and FSC contour plots and (**J**) bar graph showing % of Ly6G$^+$ cells within lung iMos sorted from WT mice at day 10 after IAV and cultured 18 hours ex vivo with vehicle, M-CSF, or GM-CSF. (**K**) Representative confocal microscopy pictures and (**L**) representative flow cytometry histograms of tdTomato expression within lung iMos sorted from *Ly6g*^{tdTom} mice at day 10 after IAV and treated ex vivo with tamoxifen and GM-CSF or vehicle for 18 hours. (**M**) Bar graph showing donor *Csf2ra*$^{-/-}$ chimerism relative to donor *Csf2ra*$^{+/+}$ chimerism in the indicated cell populations from thorax-protected, lethally irradiated CD45.1/CD45.2 mice reconstituted with a 1:1 mix of CD45.1 *Csf2ra*$^{-/-}$ and CD45.2 *Csf2ra*$^{+/+}$ BM cells, infected with IAV 4 weeks later, and evaluated at day 10 after IAV. (**N**) Representative histograms and (**O**) quantification of Arg-1$^+$ cells (%) in Ly6G$^+$ Macs from donor *Csf2ra*$^{+/+}$ and *Csf2ra*$^{-/-}$ BM cells, as in (M). Data show [(D), (F), (J), (M), and (O)] means + SEM and [(D) and (F)] are representative of one of three independent experiments ($n = 3$ or 4 mice); (J) are pooled from three independent sorting experiments, with each dot representing one biological replicate; and [(M) and (O)] are pooled from two independent experiments ($n = 10$ mice). Data show (G) means (centerline) ± SEM (colored area) and are pooled from two independent experiments ($n = 6$ mice per time point). *P* values compare CD45.2 donor *Ccr2*$^{-/-}$ chimerism in (F). *P* values were calculated using (D) one-way ANOVA with Dunnett's post hoc tests, (F) two-way ANOVA with Tukey's post hoc tests, [(G) and (J)] one-way ANOVA with Tukey's post hoc tests, (M) two-way ANOVA with Šídák's post hoc tests, or (O) two-tailed Student's *t* test. *$P < 0.05$; **$P < 0.01$; ***$P < 0.001$; ****$P < 0.0001$. (K) Scale bars, 10 μm.

GMP-derived monocytic origin (Fig. 3, C and D). To address the dependency of Ly6G$^+$ Macs on Ccr2-dependent BM-derived Ly6C$^+$ Mos (*34*), we generated BM competitive chimeras in which lethally irradiated CD45.1/CD45.2 WT mice were engrafted with a 1:1 mix of CD45.2 *Ccr2*$^{-/-}$ and CD45.2 *Ms4a3*^{tdTom} BM cells. At week 4 after reconstitution, most blood Ly6C$^+$ Mos were of donor Tomato$^+$ origin, as expected (fig. S3, J and K) (*34*). At day 10 after IAV, most Ly6G$^+$ Macs were also of donor *Ms4a3*^{tdTom} origin, indicating their dependency on Ccr2 (Fig. 3, E and F).

We next sought to assess the fate and life span of Ly6G$^+$ Macs. The abundance of Ly6G$^+$ Macs during a limited time window post-IAV suggested that they might be short lived. In line with this, trajectory analyses in Fig. 3A suggested that Ly6G$^+$ Macs (C2) gave rise to Macs with low RNA content (C10) (fig. S2B). We performed EdU pulse experiments at day 7 after IAV and found that Ly6G$^+$ Macs staining positive for EdU at day 10 after IAV were completely cleared from the lung at day 17 (Fig. 3G). Annexin V/propidium iodide (PI) staining at day 10 after IAV further supported that Ly6C$^+$ Mos transitioning to iMos and differentiating into Ly6G$^+$ Macs became progressively more sensitive to death, with a substantial portion of Ly6G$^+$ Macs being either early or late apoptotic (annexin V$^+$/PI$^{+/-}$) or necrotic (annexin V$^-$/PI$^+$) (Fig. 3H and fig. S3L). Hence, our data show that Ly6G$^+$ Macs represent a short-lived Mac subset arising from Ccr2-dependent Ly6C$^+$ Mos.

The Ly6G signal on Ly6G$^+$ Macs, considered to be Neuspecific, was unexpected and required careful validation. First, we verified that the Ly6G fluorescence intensity was nearly absent in unstained or isotype antibody (Ab)–stained CD11b$^+$ cells from IAV-infected WT mice (fig. S4A). Second, we evaluated whether Ly6G$^+$ Mac precursors, namely, iMos, could intrinsically up-regulate Ly6G on their surface when isolated from the lungs of IAV-infected mice at day 10 after IAV. We found that iMos from IAV-infected mice and stimulated ex vivo with granulocyte-macrophage colony-stimulating factor (GM-CSF), and to a lesser extent with macrophage colony-stimulating factor (M-CSF), had up-regulated Ly6G protein on their surface (Fig. 3, I and J). We also found that lung iMos isolated from IAV-infected *Ly6g*^{CreERT2}*R26*$^{LSL\text{tdTomato}}$ mice (*Ly6g*^{tdTom}) treated with tamoxifen and stimulated with GM-CSF ex vivo became tdTomato$^+$, indicative of active *Ly6g* gene transcription in monocytic cells (Fig. 3, K and L). These data demonstrate that Ly6G can be actively expressed by Mo-Macs.

Given the ability of GM-CSF to trigger Ly6G expression on lung iMos isolated from IAV-infected mice, we assessed the dependency of Ly6G$^+$ Macs on GM-CSF receptor signaling in vivo. We generated BM competitive chimeras in which thorax-protected, lethally irradiated CD45.1/CD45.2 WT mice were engrafted with a 1:1 mix of CD45.1 *Csf2ra*$^{-/-}$ and CD45.2 *Csf2ra*$^{+/+}$ BM donor cells. At week 4 after reconstitution, blood Neus and Mos of donor origin arose equally from CD45.1 *Csf2ra*$^{-/-}$ and CD45.2 *Csf2ra*$^{+/+}$ BM cells (fig. S4, B and C). At day 10 after IAV, we found that CD45.2 *Csf2ra*$^{+/+}$ BM cells had a competitive advantage over CD45.1 *Csf2ra*$^{-/-}$ BM cells to become Ly6G$^+$ Macs, which was not observed among most other lung myeloid cells (Fig. 3M and fig. S4, C to E), and the percentage of Arg-1$^+$ cells was lower in *Csf2ra*$^{-/-}$ Ly6G$^+$ Macs as compared with *Csf2ra*$^{-/-}$ Ly6G$^+$ Macs (Fig. 3, N and O), indicating their partial dependency on GM-CSF receptor signaling.

Ly6G$^+$ Macs exhibit distinct ultrastructural features associated with elevated metabolic and phagocytic abilities

Gene set enrichment analysis (GSEA) of the transcriptomic profile of Ly6G$^+$ Macs (C2) compared with all other clusters identified a response to interferon-γ (IFN-γ) and cytokines, chemotactic and viral processes, an active metabolic state, a highly developed endomembrane system, and elevated phagocytic abilities in Ly6G$^+$ Macs (Fig. 4A). We analyzed fluorescence-activated cell sorting (FACS)–sorted Ly6G$^+$ Macs by transmission electron microscopy (TEM) at day 10 after IAV and found that they exhibited a kidney-shaped nucleus, a microvilli-rich membrane, secretory granules, and a cytoplasm rich in rough endoplasmic reticulum (RER), Golgi apparatus, lysosomes, and autophagy vacuoles, distinguishing them from Neus, Ly6C$^+$ Mos, and IM-like cells (Fig. 4B). The morphology of Ly6G$^+$ Macs was reminiscent to that of an atypical population of monocytes, called SatM monocytes, which arise from particular GMPs during the fibrotic phase in lungs post–bleomycin administration, contribute to fibrosis, and are regulated by CCAAT/enhancer binding protein β (C/EBPβ) (*35*). We conducted a single-cell regulatory network inference and clustering (SCENIC) analysis (*36*) and found that C/EBPβ activity was lower in Ly6G$^+$ Macs compared with Ly6C$^-$ Mos, Ly6C$^+$ Mos, iMos, and Neus (fig. S5A). Moreover, we generated a SatM signature score based on the genes unregulated in SatM monocytes (*35*), mapped this score to our scRNA-seq data, and found that Ly6G$^+$ Macs displayed a lower SatM score compared with IMs, Ly6C$^+$ Mos, Ly6C$^-$ Mos, or iMos (fig. S5, B and C), supporting that Ly6G$^+$ Macs are not dependent on C/EBPβ and are transcriptionally distinct from SatM monocytes (*35*).

Next, we characterized the metabolic profile of Ly6G$^+$ Macs using a metabolic flux assay and found that the extracellular acidification rate (ECAR) was higher in Ly6G$^+$ Macs compared with IM-like cells, both at baseline and under stress, supporting that the glycolytic pathway was highly active in Ly6G$^+$ Macs (Fig. 4C). Moreover, whereas the basal mitochondrial oxygen consumption rate (OCR) was similar between Ly6G$^+$ Macs and IM-like cells, the OCR under stress conditions was higher in Ly6G$^+$ Macs compared with IM-like cells (Fig. 4D), supporting that they had a high metabolic potential (Fig. 4E).

We administered infected mice fluorescently labeled *Escherichia coli* particles intratracheally at day 10 after IAV and confirmed that Ly6G$^+$ Macs were highly phagocytic compared with Neus, Ly6C$^+$ Mos, IM-like cells, and AMs (Fig. 4, F and G). Hence, we asked whether Ly6G$^+$ Macs could perform efferocytosis in vivo. To this end, we infected BM competitive chimeras in which lethally irradiated CD45.2 WT mice were engrafted with a 1:1 mix of *Cx3cr1*$^{GFP/+}$ and *Ms4a3*^{tdTom} BM cells. Of note, at day 10 after IAV, 60% of *Cx3cr1*$^{GFP/+}$ Ly6G$^+$ Macs were also tdTomato$^+$ (Fig. 4, H and I, and fig. S6, A to C), demonstrating that they were highly potent in engulfing myeloid cells in vivo. To assess whether Ly6G molecules could be transferred from Neus to Ly6G$^+$ Macs during efferocytosis, we infected BM competitive chimeras in which lethally irradiated CD45.1/CD45.2 WT mice were engrafted with a 1:1 mix of *Cx3cr1*$^{GFP/+}$ BM cells and *Ly6g*$^{-/-}$ (i.e., homozygous *Ly6g*^{CreERT2} mice) (*37*) or *Ly6g*$^{+/+}$ BM cells. At day 10 after IAV, we found that the levels of Ly6G on *Cx3cr1*$^{GFP+}$ Ly6G$^+$ Macs from *Cx3cr1*$^{GFP+}$: *Ly6g*$^{-/-}$ BM chimeric mice, in which half of the Neus were *Ly6g*$^{-/-}$, were similar to those from *Cx3cr1*$^{GFP+}$: *Ly6g*$^{+/+}$ BM chimeric mice, supporting no evidence for a Ly6G transfer from Neus to Ly6G$^+$ Macs (fig. S6, D and E). Together, these data show that IAV-triggered Ly6G$^+$ Macs are characterized by metabolic, morphological, and efferocytic properties distinct from other lung myeloid cells.

Ly6G$^+$ Macs populate the alveolar lumen of perilesional regenerating areas

Next, we investigated the localization and the spatial organization of Ly6G$^+$ Macs. First, we performed confocal microscopy staining of

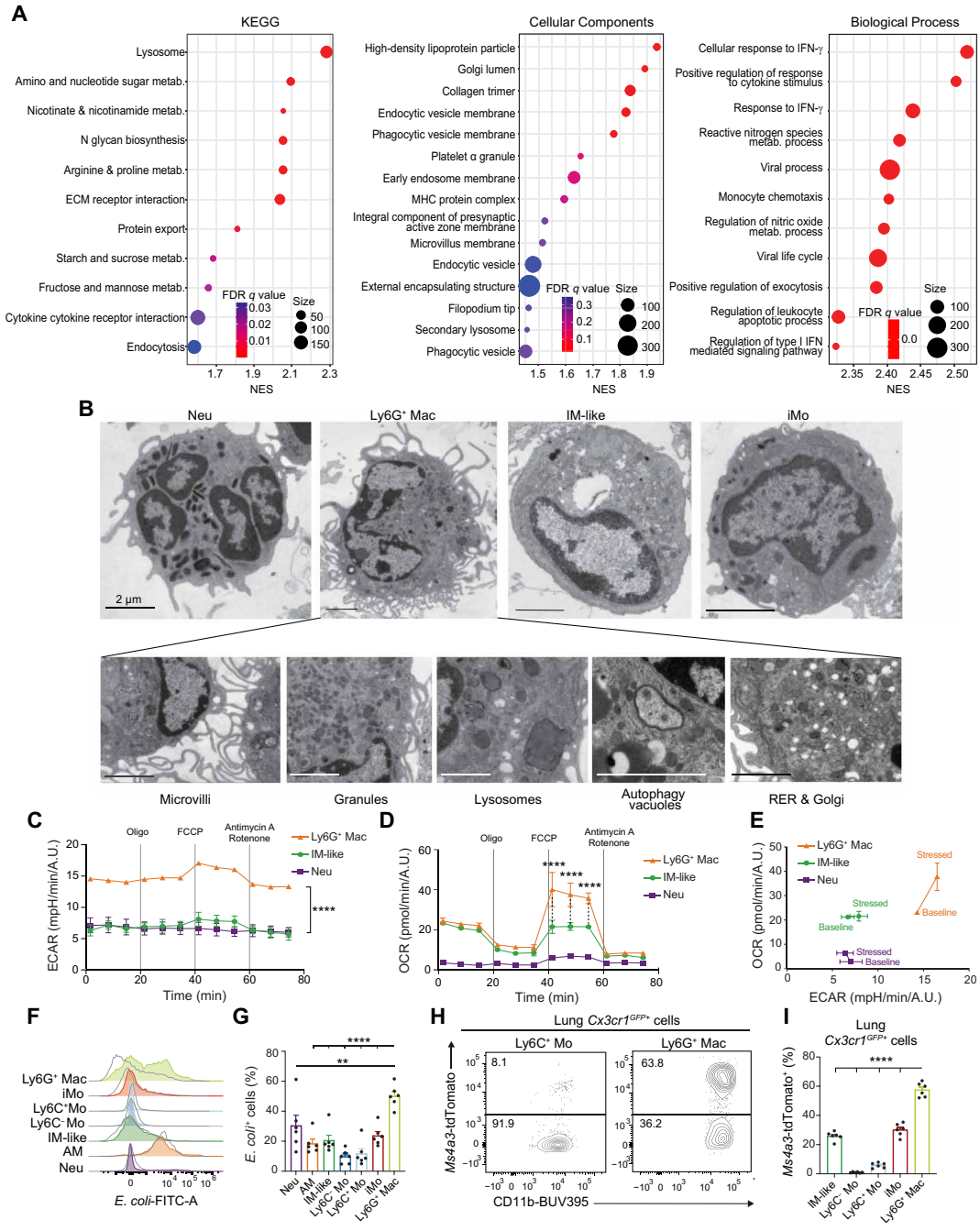

Fig. 4. Ly6G$^+$ Macs exhibit an atypical morphology and have distinct metabolic, phagocytic, and efferocytic capabilities. (**A**) GSEA of the Ly6G$^+$ Mac (C2) profile compared with other clusters using the Kyoto Encyclopedia of Genes and Genomes (KEGG), cellular components, and biological process gene sets. The normalized enrichment score (NES), false discovery rate (FDR), and size of the gene set are shown for each process. ECM, extracellular matrix. (**B**) Representative TEM pictures of Neus, Ly6G$^+$ Macs, IM-like cells, and iMos FACS-sorted from lungs of WT mice at day 10 after IAV. (**C**) ECAR of FACS-sorted Ly6G$^+$ Macs, Neus, and IM-like cells, as in (B), quantified at baseline and under stress over time using a Seahorse assay. A.U., arbitrary units; FCCP, carbonyl cyanide p-trifluoromethoxyphenylhydrazone. (**D**) OCR of Ly6G$^+$ Macs, Neus, and IM-like cells, as in (C). (**E**) ECAR and OCR of Ly6G$^+$ Macs, Neus, and IM-like cells, as in [(C) and (D)]. (**F**) Representative histograms of the *E. coli*–fluorescein isothiocyanate (FITC) signal in the indicated myeloid cell populations, quantified by flow cytometry at day 10 after IAV and 3 hours after intratracheal injection of *E. coli*–FITC particles. Noninjected mice were used as controls (gray line). (**G**) Quantification of *E. coli*–FITC$^+$ cells, as in (F). (**H**) Representative tdTomato and CD11b contour plots and (**I**) bar graph showing % of tdTomato$^+$ cells in the indicated *Cx3cr1*$^{GFP+}$ donor cell populations from lethally irradiated CD45.2 WT mice reconstituted with a 1:1 mix of CD45.2 *Cx3cr1*$^{GFP+}$ and *Ms4a3*$^{tdTom+}$ BM cells, infected with IAV 4 weeks later and evaluated at day 10 after IAV. Data show [(C) and (D)] means ± SEM and are representative of one of three independent experiments, each giving similar results; data show [(G) and (I)] means + SEM and are pooled from two independent experiments ($n = 6$ mice). *P* values [(C) and (D)] compare Ly6G$^+$ Macs versus IM-like cells or Neus and were calculated using two-way ANOVA with Bonferroni's post hoc tests; *P* values [(G) and (I)] were calculated using one-way ANOVA with Dunnett's post hoc tests. $^{**}P < 0.01$; $^{****}P < 0.0001$. (B) Scale bars, 2 µm.

lung sections of infected *Cx3cr1*^{GFP} mice at day 10 after IAV. By defining Ly6G$^+$ Macs as cells double positive for Ly6G and green fluorescent protein (GFP), we found that they were located in the alveolar lumen (Fig. 5A), which was also confirmed by in situ electron microscopy (Fig. 5B).

To further investigate the spatial distribution of Ly6G$^+$ Macs and the molecular signatures of Ly6G$^+$ Mac–rich areas, we performed spatial transcriptomic analyses using the GeoMx Digital Spatial Profiler (DSP), which allows whole-genome transcript analyses within regions of interest (ROIs). Lung sections from two mock-infected and four IAV-infected mice were collected at day 10 after IAV and stained with anti-CD68 and anti-Ly6G antibodies, and ROIs were selected in control lungs (4 ROIs), extralesional zones (4 ROIs), intralesional zones (5 ROIs), and zones rich in Ly6G$^+$CD68$^+$ cells that were mostly located in the periphery of consolidated areas (perilesional; 11 ROIs) (Fig. 5C and fig. S7A). Unsupervised principal components (PCs) analysis showed that perilesional ROIs were separated from the other regions (Fig. 5D). Volcano plot representation of the differentially expressed genes between conditions and the heatmap of the 522 significantly up-regulated genes in perilesional areas compared with the other areas supported that perilesional areas were transcriptionally very active (fig. S7, B and C). General cellular deconvolution indicated that perilesional zones were also enriched in tissue Macs as compared with the other regions (fig. S7D). We next mapped cell signature scores of lung myeloid cell populations analyzed by scRNA-seq to the ROIs and confirmed that perilesional zones were enriched in Ly6G$^+$ Macs compared with the other zones (Fig. 5E and fig. S7E). GSEA indicated that perilesional areas were enriched in biological responses related to cytoskeleton activity, epithelial cell migration, and elevated metabolic activity compared with intralesional areas, consistent with intense remodeling activities (Fig. 5F).

Next, we took advantage of a publicly available scRNA-seq dataset of alveolar epithelial cell states present during alveolar regeneration after bleomycin-induced lung injury (*38*) and containing type 1 and type 2 alveolar epithelial cells (AT1s and AT2s, respectively) as well as transitional states appearing during AT2-to-AT1 differentiation, called primed AT2s and damage-associated transient progenitors (DATPs) (*38*). By mapping the signature scores of such transitional epithelial cell states to the ROIs, we found that Ly6G$^+$ Mac–rich perilesional zones were enriched in primed AT2s and DATPs compared with control and intralesional zones (fig. S7, F and G). Accordingly, the Ly6G$^+$ Mac score correlated positively with those of primed AT2s and DATPs (Fig. 5G). We also confirmed by confocal microscopy that Ly6G$^+$ Macs were particularly abundant in the periphery of consolidated areas and clustered with AT2s, whereas intralesional consolidated areas, which exhibited low levels of staining for AT1s and AT2s, contained few Ly6G$^+$ Macs (Fig. 5H and fig. S8). Together, these data are consistent with perilesional areas serving as the site of active epithelial regeneration post-IAV and indicate that Ly6G$^+$ Macs, which cluster in such areas, contribute to this process.

Ly6G$^+$ Macs promote alveolar epithelial regeneration through IL-4R signaling

To formally assess the function of Ly6G$^+$ Macs in vivo, we aimed to generate a transgenic mouse strain in which Ly6G$^+$ Mac differentiation was impaired. Thus, we applied the SCENIC algorithm to our scRNA-seq data to map gene regulatory networks and predict

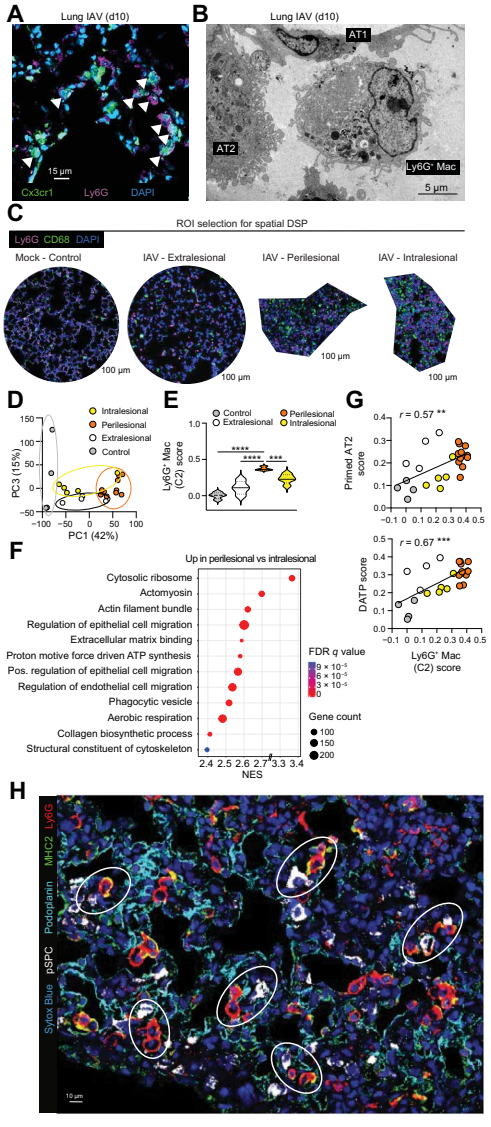

Fig. 5. Ly6G$^+$ Macs populate the alveoli of perilesional regenerating areas. (**A**) Representative confocal microscopy picture of lung sections from *Cx3cr1*^{GFP} mice at day 10 after IAV, with Ly6G$^+$ Macs identified as Ly6G$^+$*Cx3cr1*$^{GFP+}$ cells. (**B**) Representative in situ electron microscopy picture of Ly6G$^+$ Macs in the vicinity of AT2s and AT1s, identified on lung sections from WT mice at day 10 after IAV. (**C**) Representative examples of ROIs selected on lung sections from mock-infected or IAV-infected WT mice at day 10 after IAV stained with anti-Ly6G and anti-CD68 antibodies. (**D**) Unsupervised PCs analysis of the ROIs analyzed by the DSP. Percentages indicate the variability explained by each component. (**E**) Ly6G$^+$ Mac signature score within control, extralesional, perilesional, and intralesional ROIs, as depicted by violin plots (height: scores; width: abundance of cells). (**F**) GSEA of perilesional ROIs compared with intralesional ROIs using the cellular components, molecular function, and biological process gene sets. The NES, FDR, and size of the gene set are shown for each process. ATP, adenosine triphosphate. (**G**) Correlation of the Ly6G$^+$ Mac score with the primed AT2 (top) and DATP (bottom) scores of the ROIs. (**H**) Representative picture of perilesional Ly6G$^+$ Macs (i.e., Ly6G$^+$MHC-II$^+$ cells), prosurfactant protein C (pSPC)$^+$ AT2s, and podoplanin (Pdpn)$^+$ AT1s identified by confocal microscopy on lung sections from WT mice at day 10 after IAV. [(A), (B), and (H)] Pictures are representative of one of six mice, each giving similar results. (E) *P* values were calculated using one-way ANOVA with Tukey's post hoc tests. (G) The correlation analysis used was the parametric Pearson correlation coefficient. $^{**}P < 0.01$; $^{***}P < 0.001$; $^{****}P < 0.0001$. Scale bars, (A) 15 µm, (B) 5 µm, (C) 100 µm, and (H) 10 µm.

transcription factor activities in Ly6G$^+$ Macs (*36*). Of note, c-Maf and MafB exhibited a high regulon activity in Ly6G$^+$ Macs and IM-like cells, as previously described (*29*), but not in other lung myeloid cells (Fig. 6A and fig. S9). Elevated c-Maf and MafB protein levels were also detected in Ly6G$^+$ Macs at day 10 after IAV by flow cytometry (Fig. 6, B and C), and *Maf* and *Mafb* transcript levels were elevated in lung Ly6G$^+$ Mac–rich perilesional areas of IAV-infected mice (Fig. 6D). We generated mice with myeloid-restricted *Maf* and *Mafb* deficiency by crossing *Maf* and *Mafb* floxed mice (*Maf/Mafb*$^{fl/fl}$) with mice constitutively expressing Cre recombinase under the control of the lysozyme M promoter (*Lyz2*^{Cre}), called *Maf/Mafb*^{MyeloKO} mice hereafter. At day 10 after IAV, *Maf/Mafb*^{MyeloKO} mice showed a near absence of Ly6G$^+$ Macs, whereas numbers of Neus, AMs, IM-like cells, Ly6C$^+$ Mos, and iMos were similar and numbers of Ly6C$^-$ Mos were higher compared with control mice (Fig. 6E). Hence, we used this model to address the consequences of Ly6G$^+$ Mac deficiency on viral control, morbidity, and alveolar epithelial repair after IAV infection.

We assessed the levels of lung mRNA coding for the nonstructural influenza protein NS1 post-IAV and found that they were not significantly different between *Maf/Mafb*^{MyeloKO} and controls and returned to baseline at day 10 after IAV (Fig. 6F), supporting that Ly6G$^+$ Macs did not substantially influence host viral control. However, *Maf/Mafb*^{MyeloKO} mice lost more weight post-IAV compared with controls (Fig. 6G), suggestive of a more severe IAV-induced pathology. Histopathological analyses of lung sections at day 20 after IAV indicated broader lesional areas in *Maf/Mafb*^{MyeloKO} mice compared with controls as well as more pronounced dysplastic repair and bronchiolization of the alveoli on the basis of quantification of the mucus area in lung lesional areas (Fig. 6, H to J). These results suggested that, in the absence of Ly6G$^+$ Macs, the classical pathway of alveolar epithelial regeneration involving progenitor AT2 expansion and differentiation toward AT1s (*39*, *40*) was defective and compensated by dysplastic repair. Next, we evaluated the numbers of AT1s, AT2s, and regAT2s at day 20 after IAV in *Maf/Mafb*^{MyeloKO} and control mice by flow cytometry and observed a significant decrease in the numbers of AT2s and regAT2s in *Maf/Mafb*^{MyeloKO} mice compared with controls (Fig. 6, K and L), confirming that AT2s were less able to expand and differentiate into AT1s in the absence of Ly6G$^+$ Macs. Of note, intratracheal transfer of Ly6G$^+$ Macs isolated from lungs of WT mice at day 10 after IAV into IAV-infected *Maf/Mafb*^{MyeloKO} mice partially improved weight recovery and restored numbers of AT2s to the levels observed in IAV-infected control mice (Fig. 6, M and N). These results suggest that Ly6G$^+$ Macs are key players of euplastic epithelial regeneration after IAV-induced lung injury.

To determine whether Ly6G$^+$ Mac–rich perilesional areas were imprinted by a type 2 reparative environment (*19*, *41*, *42*), we mapped a type 2 signature score based on genes involved in interleukin-4 (IL-4) receptor (IL-4R) downstream signaling pathways to the DSP spatial transcriptomic data and found that perilesional areas exhibited the highest type 2 score as compared with the other ROIs (Fig. 7A). Hence, we asked whether IL-4R signaling, whose activation is known to induce a repair phenotype in Macs (*19*, *41*, *42*), was involved in Ly6G$^+$ Mac identity and function. First, we found that Ly6G$^+$ Macs expressed high levels of the IL-4R α chain (IL-4Rα) (Fig. 7, B and C). Next, we generated BM competitive chimeras in which lethally irradiated CD45.1/CD45.2 WT mice were engrafted with a 1:1 mix of CD45.2 *Il4ra*$^{-/-}$ and CD45.2 *Ms4a3*^{tdTom} BM cells. At week 4 after reconstitution, efficient BM reconstitution was confirmed in the blood (fig. S10, A and B). At day 10 after IAV, we found that Ly6G$^+$ Macs of donor *Ms4a3*^{tdTom} origin exhibited a competitive advantage over those of donor *Il4ra*$^{-/-}$ origin, which was not observed among other lung myeloid cells (Fig. 7D and fig. S10, C and D), and the remaining *Il4ra*$^{-/-}$ Ly6G$^+$ Macs were impaired in their ability to express Arg-1 (Fig. 7, E and F). Last, WT chimeric mice fully reconstituted with *Il4ra*$^{-/-}$ or WT BM cells were generated (*Il4ra*$^{-/-}$ BM → WT or WT BM → WT, respectively) and infected with IAV. We found that, like in *Maf/Mafb*^{MyeloKO} mice, *Il4ra*$^{-/-}$ BM → WT mice had an impaired recovery post-IAV compared with WT BM → WT mice (Fig. 7G). These data suggest that Ly6G$^+$ Macs exert their function via IL-4R–dependent pathways, at least in part.

Last, we asked whether Ly6G$^+$ Macs could directly influence AT2 fate and whether cell-cell contact was needed. To this end, we performed a scratch assay in vitro using the murine lung epithelial 12 (MLE-12) mouse AT2 cell line and evaluated the confluence of AT2s 12 hours after scratch in the presence or absence of Ly6G$^+$ Macs isolated from infected lungs at day 10 after IAV. Coculture with Ly6G$^+$ Macs but not with Neus, IM-like cells, or iMos was associated with an increase in cell confluence (Fig. 7H), indicating that Ly6G$^+$ Macs can directly and specifically promote wound healing in vitro. A similar scratch assay was also performed using the conditioned medium (CM) from FACS-sorted Ly6G$^+$ Macs that were cultured overnight with or without the type 2 cytokines IL-4 and IL-13. In this setting, the CM from IL-4/IL-13–pulsed Ly6G$^+$ Macs could promote wound healing compared with the control medium (containing only IL-4 and IL-13) or the CM from unpulsed Ly6G$^+$ Macs (Fig. 7, I and J). We performed proteome profiling on such CM and found that Ly6G$^+$ Macs were highly potent in secreting soluble factors, among which were chemokines (CCL5, CXCL16, CCL12, and CXCL10), cytokines [tumor necrosis factor–α (TNF-α), IL-10, and IL-1α] and osteopontin, some of which were increased upon IL-4R activation (Fig. 7K). Some of the molecules detected in the CM of Ly6G$^+$ Macs had significantly up-regulated transcript levels in Ly6G$^+$ Macs (C2) as compared with other clusters (fig. S11). Together, our data demonstrate that Ly6G$^+$ Macs can release soluble factors upon IL-4R triggering that act directly on AT2s to promote epithelial regeneration (fig. S12).

Ly6G$^+$ Macs belong to a conserved host response to injury across organs, triggers, and species

We evaluated whether Ly6G$^+$ Macs were specifically recruited in the IAV model or were also triggered in other models of injury. First, we used a model of noninfectious lung injury based on bleomycin instillation and performed time-course flow cytometry analyses. Ly6G$^+$ Macs expressing high levels of Arg-1 and CXCR4 were mostly present between day 7 and day 14 after bleomycin administration, which correlated with signs of epithelial damage, as reflected by the decrease in numbers of AT1s and AT2s (Fig. 8, A to E). We also found similar Ly6G$^+$ Macs peaking at days 1 and 2 after treatment in an acute model of acetaminophen-induced liver injury, which correlated with the release of alanine aminotransaminase (ALT) in plasma (Fig. 8, F to I). Our data thus suggested that Ly6G$^+$ Macs are a component of a conserved response to tissue damage, regardless of the organ or trigger.

Last, we asked whether Macs sharing a similar transcriptomic signature were also present in the bronchoalveolar lavage fluid

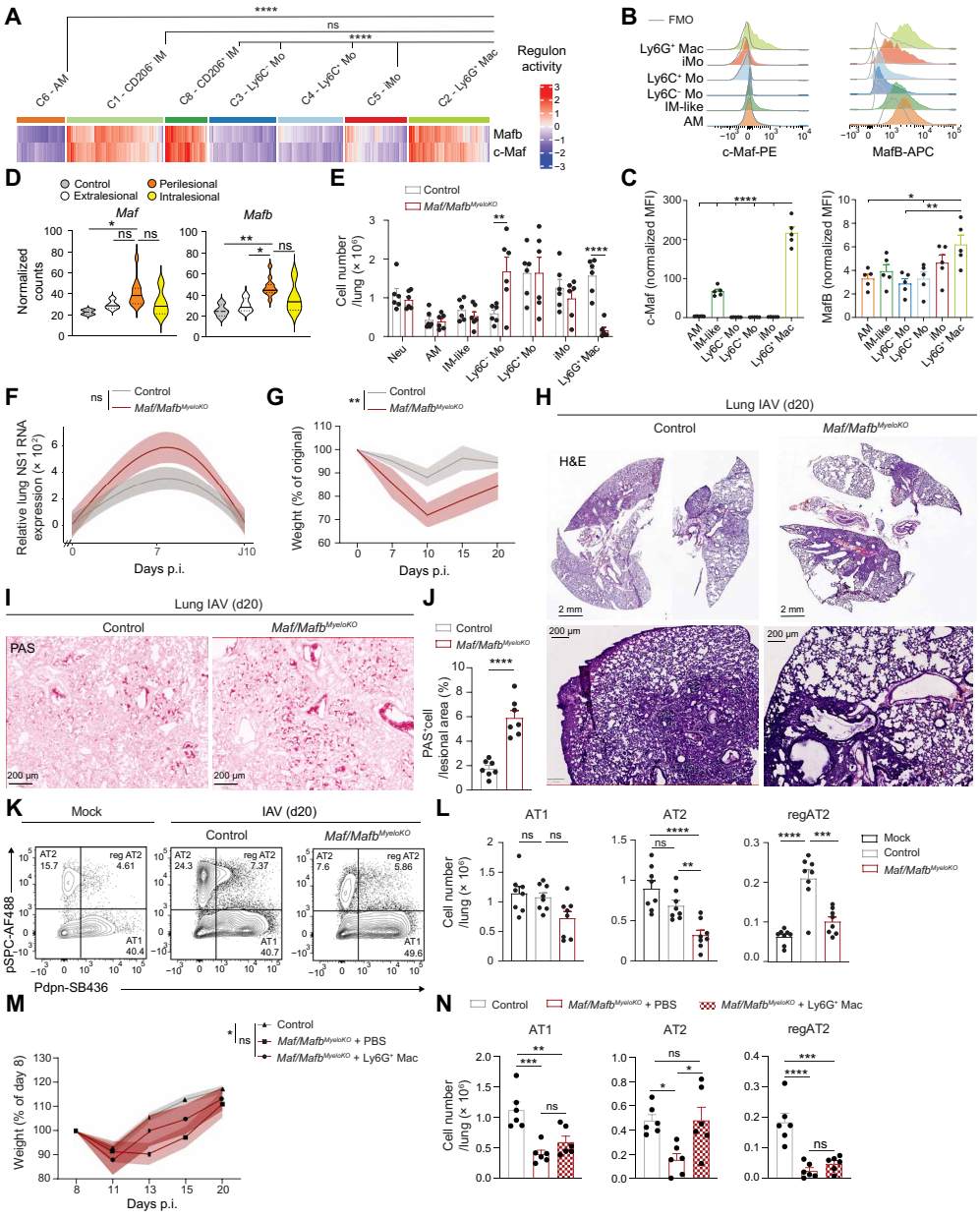

Fig. 6. c-Maf/MafB-dependent Ly6G$^+$ Macs promote euplastic alveolar epithelial regeneration. (**A**) Heatmap depicting predicted activities of c-Maf and MafB across lung myeloid cells post-IAV, evaluated by SCENIC analysis of the scRNA-seq data, as in Fig. 2A. (**B**) Representative histograms of intracellular c-Maf and MafB expression in the indicated lung myeloid cell populations, quantified at day 10 after IAV. (**C**) Quantification of expression of intracellular c-Maf and MafB, as in (B). (**D**) Expression of *Maf* and *Mafb* within control, extralesional, perilesional, and intralesional ROIs, as depicted by violin plots (height: normalized counts; width: abundance of cells). (**E**) Absolute numbers of the indicated lung myeloid cell populations, quantified at day 10 after IAV in control and *Maf/Mafb*^{MyeloKO} mice. (**F**) Time course of relative lung NS1 RNA expression, assessed by real-time quantitative polymerase chain reaction at days 0, 7, and 10 after IAV in control and *Maf/Mafb*^{MyeloKO} mice. (**G**) Time course of weight, expressed as the % of the original weight at day 0 and assessed at days 0, 7, 10, 15, and 20 after IAV in control and *Maf/Mafb*^{MyeloKO} mice. (**H** and **I**) Representative (H) H&E (top) and (I) periodic acid–Schiff (PAS; bottom) pictures of lung sections of control and *Maf/Mafb*^{MyeloKO} mice at day 20 after IAV. Pictures are representative of one of seven mice analyzed. (**J**) Percentage of PAS$^+$ cells in lung lesional areas of control and *Maf/Mafb*^{MyeloKO} mice at day 20 after IAV. (**K**) Representative pSPC and Pdpn contour plots of CD45$^-$CD31$^-$EpCam$^+$ cells in mock-infected or IAV-infected mice at day 20 after IAV. (**L**) Absolute numbers of pSPC$^+$Pdpn$^-$ AT2s, pSPC$^-$Pdpn$^+$ AT1s, and pSPC$^+$Pdpn$^+$ regenerating AT2s (regAT2s), quantified as in (K). (**M**) Time course of weight, expressed as the % of the original weight at day 8 and assessed at days 8, 11, 13, 15, and 20 after IAV in control mice and *Maf/Mafb*^{MyeloKO} mice instilled intratracheally at days 8, 11, 13, and 15 after IAV with PBS or Ly6G$^+$ Macs (3×10^5) isolated from WT mice at day 10 after IAV. (**N**) Absolute numbers of pSPC$^+$Pdpn$^-$ AT2s, pSPC$^-$Pdpn$^+$ AT1s, and pSPC$^+$Pdpn$^+$ regAT2s, quantified at day 20 after IAV, as in (M). [(C), (E), (J), (L), and (N)] Data show means + SEM and are pooled from two independent experiments [(C) $n = 5$ mice per group; (E) and (N) $n = 6$ mice per group; (J) $n = 7$ mice per group; (L) $n = 8$ mice per group]. [(F), (G), and (M)] Data show means (centerline) ± SEM (colored area) and are pooled from two or three independent experiments [(F) $n = 10$ mice per group; (G) $n = 7$ mice per group; (M) $n = 6$ mice per group]. *P* values were calculated using (A) Wilcoxon rank sum test, (C) one-way ANOVA with Dunnett's post hoc tests, [(D) and (L)] one-way ANOVA with Tukey's post hoc tests, [(E), (F), (G), and (M)] two-way ANOVA with Šídák's post hoc tests, and (J) two-tailed Student's *t* test, $^*P < 0.05$; $^{**}P < 0.01$; $^{***}P < 0.001$; $^{****}P < 0.0001$. Scale bars: [(H), top] 2 mm and [(H), bottom, and (I)] 200 µm.

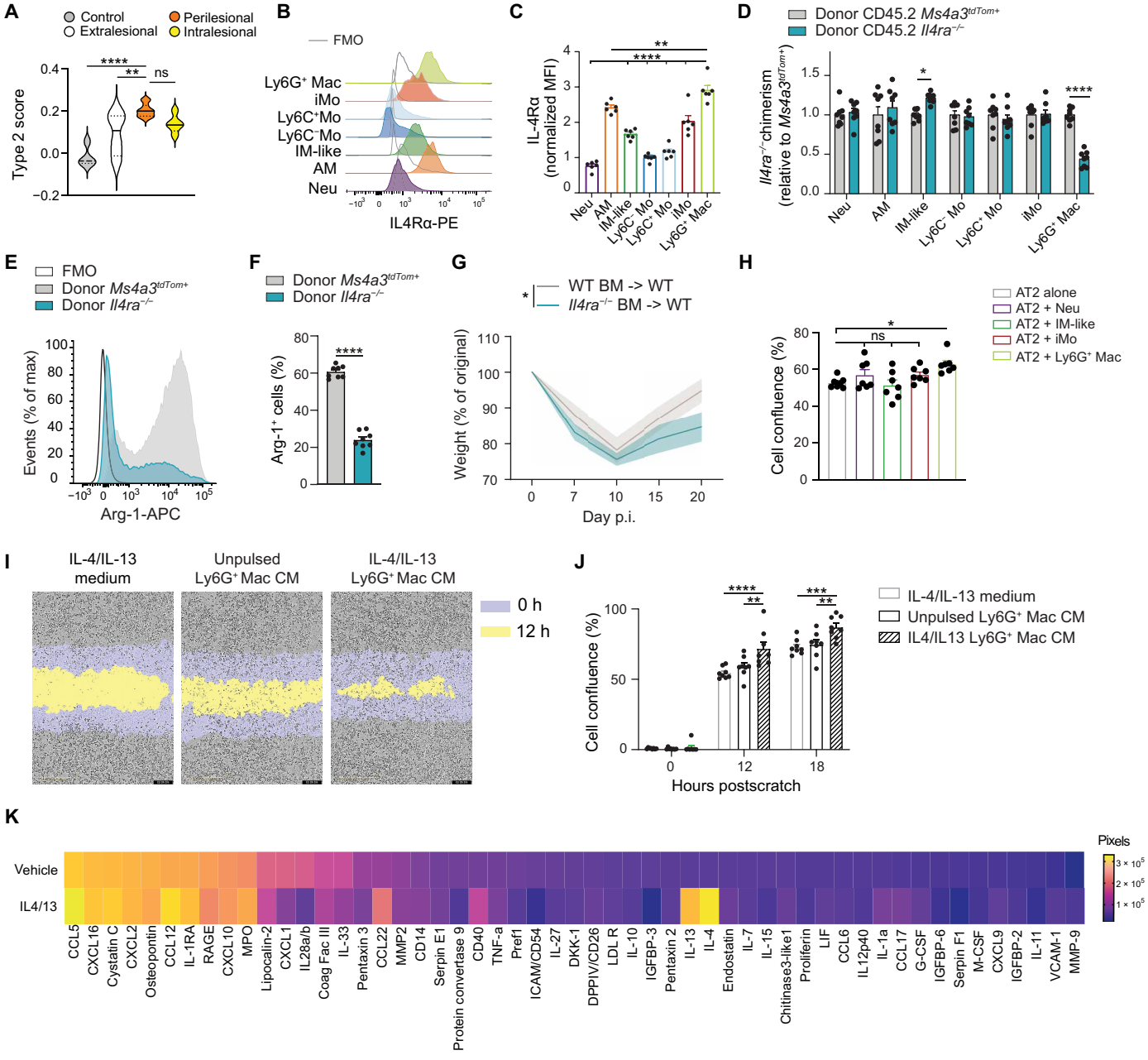

Fig. 7. IL-4R–dependent Ly6G$^+$ Macs release soluble factors that improve alveolar regeneration from AT2s. (**A**) Type 2 signature score within control, extralesional, perilesional, and intralesional ROIs, as depicted by violin plots (height: scores; width: abundance of cells). (**B**) Representative histograms of IL-4R expression in the indicated lung myeloid cell populations, quantified at day 10 after IAV. (**C**) Quantification of IL-4R expression, as in (B). (**D**) Bar graph showing donor *Il4ra*$^{-/-}$ chimerism relative to donor *Ms4a3*$^{tdTom+}$ chimerism in the indicated cell populations from lethally irradiated CD45.1 mice reconstituted with a 1:1 mix of CD45.2 *Il4ra*$^{-/-}$ and *Ms4a3*$^{tdTom+}$ BM cells, infected with IAV 4 weeks later and evaluated at day 10 after IAV. (**E**) Representative histograms and (**F**) quantification of Arg-1$^+$ cells (%) in Ly6G$^+$ Macs from donor *Il4ra*$^{-/-}$ or *Ms4a3*$^{tdTom+}$ BM cells, as in (D). (**G**) Time course of weight, expressed as the % of the original weight at day 0 and assessed at days 0, 7, 10, 15, and 20 after IAV in lethally irradiated CD45.1/CD45.2 WT mice reconstituted with CD45.2 *Il4ra*$^{-/-}$ BM cells (*Il4ra*$^{-/-}$ BM → WT) or CD45.2 WT BM cells (WT BM → WT) and infected with IAV 4 weeks later. (**H**) Cell confluence of AT2s (MLE-12) quantified 12 hours after a standardized scratch by live cell analysis when AT2s were cocultured in the presence of Neus, IM-like cells, iMos, or Ly6G$^+$ Macs isolated from the lungs of WT mice at day 10 after IAV. (**I**) Representative pictures of cell confluence of AT2s at 0 and 12 hours after scratch when AT2s were cultured with IL-4/IL-13 or with the CM of unpulsed or IL-4/IL-13–pulsed Ly6G$^+$ Macs isolated from the lungs of WT mice at day 10 after IAV. (**J**) Bar graph of cell confluence of AT2s quantified 0, 12, and 18 hours after scratch, as in (I). (**K**) Heatmap showing the proteome profiling of the CM of vehicle and IL-4/IL-13–treated Ly6G$^+$ Macs isolated from the lungs of WT mice at day 10 after IAV. [(C), (D), (F), (H), and (J)] Data show means + SEM and [(C), (D), and (F)] are pooled from two independent experiments [(C) $n = 6$ mice; (D) and (F) $n = 8$ mice] or [(H) and (J)] are pooled from three independent sorting experiments. (G) Data show means (centerline) ± SEM (colored area) and are pooled from two independent experiments ($n = 6$ mice per group). *P* values were calculated using (C) one-way ANOVA with Dunnett's post hoc tests, [(D) and (G)] two-way ANOVA with Šídák's post hoc tests, (F) two-tailed Student's *t* test, and (H) one-way or (J) two-way ANOVA with Tukey's post hoc tests. $*P < 0.05$; $**P < 0.01$; $***P < 0.001$; $****P < 0.0001$.

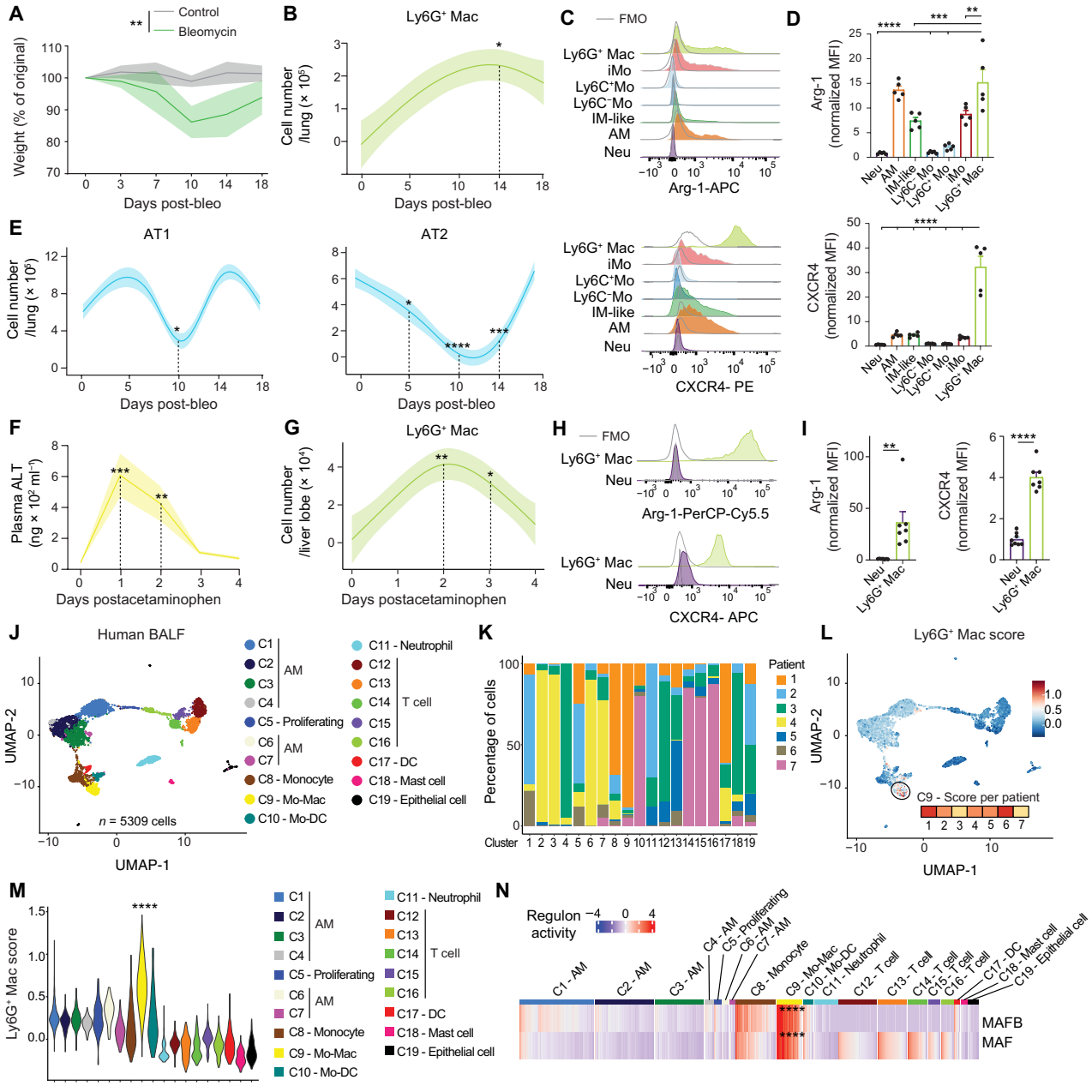

Fig. 8. Ly6G$^+$ Macs are triggered by other insults and have a human counterpart. (**A**) Time course of weight, expressed as the % of the original weight at day 0 and assessed at days 0, 3, 7, 10, 14, and 18 after injection in C57BL/6 WT mice instilled intratracheally with bleomycin (bleo). (**B**) Time course of absolute numbers of lung Ly6G$^+$ Macs quantified at days 0, 5, 10, 14, and 18 after bleomycin (post–bleo) administration in WT mice. (**C**) Representative histograms of intracellular Arg-1 and CXCR4 expression in the indicated lung myeloid cell populations, quantified at day 14 after bleomycin administration. (**D**) Quantification of intracellular Arg-1 and CXCR4 expression, as in (C). (**E**) Time course of absolute numbers of pSPC$^-$Pdpn$^+$ AT1s and pSPC$^+$Pdpn$^-$ AT2s, quantified at days 0, 7, 10, 14, and 18 after bleomycin administration. (**F**) Amount of ALT in the plasma of WT mice injected intraperitoneally with acetaminophen at days 0, 1, 2, 3, and 4 after injection. (**G**) Time course of absolute numbers of liver Ly6G$^+$ Macs quantified at days 0, 1, 2, 3, and 4 after acetaminophen administration. (**H**) Representative histograms of intracellular Arg-1 and CXCR4 expression in liver Neus and Ly6G$^+$ Macs, quantified at day 1 after acetaminophen administration. (**I**) Quantification of intracellular Arg-1 and CXCR4 expression, as in (H). (**J**) UMAP plot depicting the transcriptional identity of human BALF cells collected from seven patients with suspected pneumonia and analyzed by scRNA-seq. Annotations of cell clusters are shown. (**K**) Representation of each patient within each cluster, shown as frequency. (**L**) UMAP feature plot, as in (J), according to the Ly6G$^+$ Mac signature score. The score level in cluster C9 is shown for each patient. (**M**) Ly6G$^+$ Mac signature score of single cells within each cluster, as depicted by violin plots (height: score; width: abundance of cells). (**N**) Heatmap depicting predicted activities of MAFB and MAF across BALF cell populations, evaluated by SCENIC analysis of the scRNA-seq data shown in (J). [(A), (B), (E), (F), and (G)] Data show means (centerline) ± SEM (colored area) and are pooled from two independent experiments ($n = 5$ or 6 mice). [(D) and (I)] Data show means + SEM and are pooled from two independent experiments ($n = 5$ to 7 mice). *P* values were calculated using (A) two-way ANOVA, [(B), (D), (E), (F), and (G)] one-way ANOVA with Dunnett's post hoc tests, (I) two-tailed Student's *t* test, or [(M) and (N)] Wilcoxon rank sum test. (M) *P* values compare C9 versus all other clusters. *$P < 0.05$; **$P < 0.01$; ***$P < 0.001$; ****$P < 0.0001$.

(BALF) of diseased humans. We performed scRNA-seq analyses of BALF cells from seven patients with a suspicion of pneumonia and manually annotated the cell clusters on the basis of the most up-regulated genes (Fig. 8, J and K, and fig. S13). Next, we mapped a Ly6G$^+$ Mac score on the basis of orthologous genes in humans to the BALF cells and found that cells exhibiting the highest Ly6G$^+$ Mac score belonged to the same cluster C9 identified as Mo-Macs on the basis of their high expression of monocyte genes and their low expression of AM-associated genes (Fig. 8, L and M). SCENIC analyses (*36*) predicted higher MAF and MAFB activities in the Mo-Mac cluster compared with other clusters (Fig. 8N), further supporting that the airspace of human pneumonia lungs contains Mo-Macs that are transcriptionally similar to mouse Ly6G$^+$ Macs.

DISCUSSION

Restoration of gas exchange after lung injury is critical for life and relies on appropriate regulation of inflammation and regeneration of the damaged alveoli. Even though recent progress has been made in understanding the epithelial-intrinsic mechanisms underlying alveolar regeneration postinjury (*3*, *38*, *40*, *43*–*46*), an important gap resides in our understanding of the innate immune-epithelial cross-talk taking place to promote epithelial repair and host recovery. Although recruited Mo-Macs are often seen as culprits and drivers of disease progression in different contexts, such as in COVID-19, interstitial fibrosis, or lung cancer (*13*, *17*, *18*, *47*), advances in single-cell and spatial technologies have enabled new opportunities to investigate the spatiotemporal regulation of Mo-Mac responses in depth. Here, using such approaches combined with lineage tracing, BM chimeras, gene targeting, multiparameter flow cytometry, and imaging, our work identifies a previously undescribed atypical population of short-lived recruited Ly6G$^+$ Macs that critically contributes to alveolar epithelial regeneration postinjury in mice.

To our knowledge, there is no report of such Ly6G$^+$ Macs in the literature. Of note, Ly6G is largely considered a Neu-specific marker (*48*), and, in many studies using cytometry, anti-Ly6G antibodies are included to gate out Neus before gating on Macs. Hence, Ly6G$^+$ Macs might have been previously overlooked and considered part of the Neu compartment. Here, we provide evidence that the Ly6G signal is specific and that lung iMos, the precursors of Ly6G$^+$ Macs, can actively express the *Ly6g* gene and Ly6G protein upon GM-CSF stimulation ex vivo. Of note, GM-CSF is mainly produced by AT2s (*40*, *49*), which are located in the vicinity of Ly6G$^+$ Macs, and Ly6G$^+$ Macs were dependent on GM-CSF receptor signaling for their generation and Arg-1 expression post-IAV infection in vivo. Further supporting an intrinsic up-regulation of Ly6G, we found no evidence of Ly6G protein transfer from Neus to Ly6G$^+$ Macs. In addition to Ly6G expression, Ly6G$^+$ Macs were phenotypically and transcriptionally distinct from Neus and exhibited key developmental, phenotypic, and transcriptomic macrophage features, including their dependency on Ccr2, elevated Cx3cr1 expression, and their dependency on the transcription factors c-Maf and MafB. However, *Ly6g* does not appear as a target gene of c-Maf and MafB in the ChIP-Atlas, suggesting alternative gene regulatory mechanisms.

We found that Ly6G$^+$ Macs were transiently recruited to the alveolar spaces of particular lung areas and remained phenotypically and transcriptionally distinct from tissue-resident AMs. Our data thus suggest that the local microenvironment of Ly6G$^+$ Macs, which can shape Mac identity (*13*, *50*–*52*), is dynamically regulated and distinct from that of AMs. First, we found that Ly6G$^+$ Macs originate from BM-derived monocytes recruited to the lung in a Ccr2-dependent manner. Second, we showed that such inflammatory monocytes differentiating into Ly6G$^+$ Macs could phagocytose GMP-derived myeloid cells, such as Neus, in vivo. Such a process has been shown to trigger a metabolic rewiring that is associated with Arg-1 activity and aerobic respiration and is important for the resolution of inflammation and tissue repair (*53*, *54*). Third, we provided evidence that GM-CSF and type 2 cytokine signaling through the IL-4R are involved in the generation of Ly6G$^+$ Macs and their function. Although the cellular source of type 2 cytokines remains unknown, a peak of T helper type 2 (T_H2) and type 2 innate lymphoid cells (ILC2s) has been reported in lungs of IAV-infected mice around day 10 after infection (*55*), a time point that coincides with the peak of Ly6G$^+$ Macs. Moreover, Ly6G$^+$ Macs can release the T_H2-attracting and ILC2-activating signals CCL22 and IL-33, respectively, consistent with the idea that Ly6G$^+$ Macs can contribute to the type 2 milieu that promotes their repair phenotype (*56*–*58*). Fourth, we found that Ly6G$^+$ Macs were spatially restricted to perilesional areas, zones that were enriched in transitional epithelial cell states involved in AT2-mediated alveolar regeneration (*38*). Perilesional areas were also sites of intense cytoskeleton activity, aerobic respiration, extracellular matrix deposition, and cell migration, all of which are involved in active alveolar epithelial regeneration (*3*, *9*, *40*). Our findings are in line with a previous report that identified damaged zones of IAV-infected lungs that were in the periphery of consolidated areas and were sites of active tissue regeneration and AT2 proliferation and differentiation (*46*).

By disrupting myeloid-specific c-Maf– and MafB-dependent pathways, we obtained *Maf/Mafb*^{MyeloKO} mice in which Ly6G$^+$ Macs were no longer able to differentiate post-IAV, thus representing a valuable tool to address their functions. We identified Ly6G$^+$ Macs as essential actors to license optimal alveolar epithelial regeneration requiring the differentiation of progenitor AT2s toward AT1s (*40*). In the absence of Ly6G$^+$ Macs, AT2-to-AT1 transitioning cells were nearly absent, and a more pronounced dysplastic alveolar repair associated with a bronchiolization of the alveoli was observed. Such an epithelial phenotype was associated with exacerbated morbidity and is reminiscent of what is observed in severe forms of respiratory viral infections (*3*, *40*). In addition, local adoptive transfer of Ly6G$^+$ Macs in IAV-infected *Maf/Mafb*^{MyeloKO} mice improved weight recovery and restored AT2 numbers to levels seen in IAV-infected control mice, suggesting that Ly6G$^+$ Macs could support AT2 expansion postinjury. We further dissected the underlying mechanisms ex vivo and found that Ly6G$^+$ Macs could directly promote wound healing of murine AT2s through IL-4R–mediated release of soluble factors. Among these factors, osteopontin is expressed by Ly6G$^+$ Macs and is a ligand for the receptor CD44 (*59*). Of note, CD44^{hi} AT2s represent a subset of AT2s with stem cell properties (*60*), consistent with the hypothesis that the osteopontin-CD44 axis might trigger alveolar regeneration, although osteopontin release was not potentiated by type 2 cytokine stimulation of Ly6G$^+$ Macs under the experimental conditions tested. The elevated Arg-1 expression by Ly6G$^+$ Macs could also influence AT2s, either via the local deprivation of L-arginine or the generation of ornithine and polyamines (*61*, *62*). Last, Ly6G$^+$ Macs can also secrete proinflammatory cytokines, such as IL-1 and TNF-α, which have been shown to support alveolar regeneration (*38*, *63*).

In the last part of the work, we provided evidence that Macs similar to Ly6G$^+$ Macs are part of a host response to injury that is independent of the organ or the initial trigger and that is conserved across species. We found that Ly6G$^+$ Macs were also recruited in a bleomycin-induced model of noninfectious lung injury and in a model of acute acetaminophen-induced liver injury in mice. Although Ly6G$^+$ Mac numbers were lower in these models compared with the IAV model, the peak of Ly6G$^+$ Macs correlated with the presence of damage, as attested by the drop in AT1s and AT2s in the lungs or the release of the hepatic enzyme ALT in the liver. These data are consistent with the idea that they may contribute to tissue repair in these models as well, although it remains to be addressed experimentally. We also reported the presence of transcriptionally similar Macs in the BALF of patients with pneumonia by performing scRNA-seq analyses of BALF cells. Of note, cells exhibiting an elevated Ly6G$^+$ Mac score belonged to a cluster identified as Mo-Macs, and SCENIC analyses suggested that such Mo-Macs displayed high MAF and MAFB activities, reminiscent of Ly6G$^+$ Macs in mice. Speculating that such Mo-Macs also depend on GM-CSF and exhibit similar reparative functions in human lungs, our findings provide a rationale to investigate the benefits of inhaled GM-CSF, beyond the restoration of the AM niche (*64*), to improve epithelial regeneration after severe viral-induced disorders. One could speculate that the fate or functions of Ly6G$^+$ Macs are modified and become dysregulated in uncontrolled forms of respiratory viral infections or in chronic fibrotic diseases. Of note, *SPP1*, which encodes osteopontin, has been linked to fibrosis and is often used as a proxy for "profibrotic," pathogenic Macs (*47*, *65*–*67*). Our data support that Spp1$^+$ Mo-Macs, like Ly6G$^+$ Macs, can also exert beneficial roles, whereas other Spp1$^+$ Mo-Macs can become dysregulated, persistent, and pathogenic, like in chronic COVID-19 or idiopathic pulmonary fibrosis. Understanding what drives beneficial or pathological responses of *SPP1*$^+$ Macs represents an avenue for future research.

No therapeutic options exist to promote lung regeneration thus far. By characterizing in depth a short-lived atypical Mac population that licenses alveolar regeneration postinjury, our findings could serve as a basis to devise myeloid-centered regenerative strategies for medically relevant conditions such as severe or chronic respiratory viral infections or ARDS.

MATERIALS AND METHODS

Study design

In this study, we investigated the spatiotemporal distribution, transcriptional regulation, fate, identity, and function of Ly6G$^+$ Macs in an infectious model of lung injury. To this end, we used flow cytometry, microscopy, single-cell and spatial transcriptomic approaches, BM chimeras, monocyte fate mapping, and gene targeting. In most of the mouse experiments, 4 to 10 mice per group per time point were used to identify differences between groups with at least 80% power and 5% significance level. In some experiments, no statistical methods were used to predetermine sample sizes, but our sample sizes were similar to those reported in previous publications (*29*, *68*–*70*). No statistical methods to predetermine the sample size were used for the analyses of human BALF cells from patients with pneumonia. Data from independent experiments were pooled for analysis in each data panel, unless otherwise indicated. No data were excluded from the analyses, and all attempts at replication were successful and gave similar results. Histopathological examination of lung sections was blinded. Allocation of animals into experimental groups was done randomly at the start of the experiments. The specific numbers of mice, the number of experimental replicates, and the statistical tests performed are all included in the respective figure legends.

Mice

All experiments, unless otherwise specified, were performed on age-matched 8- to 12-week-old male and female mice on the C57BL/6 background. Details about the transgenic strains can be found in the Supplementary Materials. Mice were housed under specific pathogen–free conditions and maintained in a 12-hour–12-hour light-dark cycle with food and water ad libitum. All animal experiments described in this study were carried out in an animal biosafety level 3 containment unit. Experiments were reviewed and approved by the Institutional Animal Care and Use Committee of the University of Liège (ethical approval no. 2276). The Guide for the Care and Use of Laboratory Animals, prepared by the Institute of Laboratory Animal Resources, National Research Council, and published by the National Academy Press, as well as European and local legislations, was followed carefully. Accordingly, the temperature and relative humidity were 21°C and 45 to 60%, respectively.

In vivo models of injury

The mouse-adapted influenza strain A/Puerto Rico/8/34 (H1N1; PR8) was kindly provided by F. Trottein (Institut Pasteur, France). The viral stock suspension (10^8 PFU ml^{-1}) was diluted, and 5 PFUs were administered intranasally to isoflurane-anesthetized mice in 50 µl of phosphate-buffered saline (PBS) (Thermo Fisher Scientific). Control groups received an equal volume of PBS intranasally for mock infection.

For bleomycin-induced lung injury, isoflurane-anesthetized mice were treated intratracheally with a single instillation of 0.06 IU bleomycin (Bio-Connect) in a volume of 50 µl of PBS. Control animals received 50 µl of PBS alone.

For acetaminophen-induced liver injury, mice were fasted during 15 hours with free access to water and were injected intraperitoneally with acetaminophen (300 mg kg^{-1}; Sigma-Aldrich) in saline solution (0.9% NaCl). Free access to food was allowed after treatment.

Reagents and antibodies

A complete list of the reagents and antibodies used in this manuscript can be found in tables S2 and S3, respectively.

Flow cytometry

Staining reactions were performed in the dark at 4°C for 30 min with 2% v/v Fc block (BD Biosciences) to avoid nonspecific binding. For intracellular staining, extracellular-stained cells were fixed and permeabilized with the Foxp3/Transcription Factor Staining Buffer Set (Thermo Fisher Scientific). For EdU staining, extracellular-stained cells were permeabilized and stained using the Click-iT EdU Alexa Fluor 488 Flow Cytometry Assay Kit (Thermo Fisher Scientific), according to the manufacturer's instructions.

Cell viability was assessed using 7-AAD (BD Biosciences) or Fixable Viability Dye eFluor 780 (Thermo Fisher Scientific). Cell suspensions were analyzed with a FACSCANTO II or an LSRFortessa (BD Biosciences). Results were analyzed using FlowJo software

(Tree Star). For scRNA-seq, TEM, cytological examination, and ex vivo experiments, lung myeloid cells were sorted using a FACSAria III (BD Biosciences) or a Sony MA900.

In vivo treatments

For EdU incorporation experiments shown in fig. S3 (B and C), mice were injected intraperitoneally at day 10 after IAV with 1 mg of EdU (Santa Cruz Biotechnology) in 200 µl of PBS 4 hours before sacrifice. For experiments addressing the life span of Ly6G$^+$ Macs (Fig. 3G), 1 mg of EdU in 200 µl of PBS was injected intraperitoneally twice 5 hours apart at day 7 after IAV, and EdU incorporation was evaluated in blood leucocytes at day 8 after IAV. The incorporation of EdU in lung myeloid cells was evaluated at days 10, 14, and 17 after IAV. Assessment of phagocytic activity was performed as previously described (*68*). Briefly, isoflurane-anesthetized mice were instilled intratracheally with pHrodo Green *E. coli* BioParticles (2×10^8; Thermo Fisher Scientific) in 100 µl of PBS. Lungs were harvested 3 hours later for flow cytometry analyses.

Generation of BM (competitive) chimeras

CD45.2, CD45.1, or CD45.1/CD45.2 WT mice were anesthetized by intraperitoneal injection of 200 µl of PBS containing ketamine (75 mg kg^{-1}; Nimatek, Dechra) and xylazine (10 mg kg^{-1}; Rompun, Bayer). When mentioned, the thoracic cavity was protected with a 0.6-cm–thick lead cover. Mice were irradiated with two consecutive doses of 6 grays 15 min apart. Once recovered from the anesthesia, mice were reconstituted by intravenous administration of BM cells (2×10^6) from *Ms4a3*^{tdtom} or *Il4ra*$^{-/-}$ mice for full chimeras. For mixed BM chimeras, mice were reconstituted intravenously with BM cells (2×10^6) consisting of a 1:1 mix of BM cells obtained from the following mice: CD45.1 WT, *Ms4a3*^{tdtom}, *Ccr2*$^{-/-}$, CD45.1 *Csf2ra*$^{-/-}$, CD45.2 *Csf2ra*$^{+/+}$, *Cx3cr1*$^{GFP+}$, *Il4ra*$^{-/-}$, or homozygous *Ly6g*^{CreERT2} mice (also called *Ly6g*$^{-/-}$ mice). From the day of irradiation, mice were treated for 4 weeks with enrofloxacin (0.05 mg ml^{-1}; Baytril, Bayer) in drinking water. Chimerism was assessed by flow cytometry in the blood 4 weeks after irradiation.

scRNA-seq and analyses

For mouse experiments, lung myeloid cells were FACS-sorted as living singlet CD45$^+$, F4/80$^+$, and/or CD11b$^+$ cells from lung single-cell suspensions pooled from five mock-infected and IAV-infected C57BL/6 male WT mice at day 10 after IAV. For each sample, an aliquot of trypan blue–treated cells was examined under the microscope for counting, viability, and aggregate assessment after FACS. Viability was above 90% for all samples, and no aggregates were observed. Cell preparations were centrifuged, and pellets were resuspended in calcium-free and magnesium-free PBS containing UltraPure bovine serum albumin (0.4 mg ml^{-1}; Thermo Fisher Scientific). The 10x Genomics platform (Single Cell 3′ Solution) was used. For library preparation, ~2000 (mock group) and 6000 (IAV group) cells were loaded into the Chromium Controller, in which they were partitioned, and their polyadenylate RNAs were captured and barcoded using the Chromium Single Cell 3′ GEM (gel bead in emulsion), Library & Gel Bead Kit v3 (10x Genomics). The cDNAs were amplified, and libraries compatible with Illumina sequencers were generated using the Chromium Single Cell 3′ GEM, Library & Gel Bead Kit v3 (10x Genomics).

For human BALF cell analyses, Chromium Fixed RNA Profiling for multiplexed samples (10x Genomics) was used for scRNA-seq analysis of human BALF cells, allowing the storage of fixed cells and enabling analysis of multiple samples in one single GEM reaction. Fresh samples were directly fixed in a 4% formaldehyde solution after collection for storage at −80°C. For GEM creation, the Multiplex-compatible Chromium Next GEM Single Cell Fixed RNA Human Transcriptome Probe Kit including a probe barcode that permits sample multiplexing and subsequent demultiplexing was used. Details about scRNA-seq analyses can be found in the Supplementary Materials.

Transmission electron microscopy

FACS-sorted myeloid cell populations or lung tissues from IAV-infected mice at day 10 after IAV were fixed in 2.5% glutaraldehyde [diluted in Sorensen's buffer: 0.1 M Na_2HPO_4/NaH_2PO_4 buffer (pH 7.4)] for 1 hour at 4°C and postfixed for 30 min in 2% OsO_4 (diluted in 0.1 M Sorensen's buffer). After dehydration in graded ethanol, samples were embedded in Epon resin. Ultrathin sections obtained with a Reichert Ultracut S ultramicrotome (Reichert Technologies) were contrasted with 2% uranyl acetate and 4% lead citrate. For ultrastructural analyses, random fields of cells were examined under a Jeol TEM JEM-1400 transmission electron microscope at 80 kV and photographed using an 11-megapixel camera system (Quemesa, Olympus).

Extracellular flux analysis

OCR was measured using the Seahorse XF Cell Mito Stress Test (Agilent) according to the manufacturer's recommendations and as previously described (*71*, *72*). Briefly, Neus, IM-like cells, and Ly6G$^+$ Macs were FACS-sorted at day 10 after IAV and seeded (10×10^4, 7×10^4, and 8×10^4 cells per well, respectively) in XFp mini-plates (Agilent) precoated with CellTak. Cells were kept in unbuffered serum-free Dulbecco's modified Eagle's medium (DMEM) supplemented with pyruvate (1 mM), glutamine (2 mM), and glucose (10 mM) at pH 7.4, 37°C, and ambient CO_2 for 1 hour before the assay. Analysis was performed using the XFp analyzer (Seahorse Bioscience) as per the manufacturer's instructions. Additional details can be found in the Supplementary Materials.

Spatial transcriptomic analyses using the DSP

Formalin-fixed, paraffin-embedded sections (5 µm in thickness) were prepared using the protocol from NanoString Technologies. Briefly, two tissue slides, each containing one mock and two IAV samples harvested 10 days after IAV, were analyzed. Slides were first stained with antibodies against CD68 and Ly6G (clone 1A8), and DNA was visualized with 500 nM Syto83. Mouse Whole Transcriptome Atlas probes targeting more than 19,000 targets were hybridized, and slides were loaded on the GeoMx DSP. Briefly, entire slides were imaged at ×20 magnification, and ROIs were chosen on the basis of serial hematoxylin and eosin (H&E) sections and morphological markers to select lesional, perilesional, and extralesional areas. ROIs were exposed to ultraviolet light, releasing the indexing oligos and collecting them in a 96-well plate for subsequent processing and sequencing, as previously described (*73*). Raw count and third quartile–normalized count data of target genes from ROIs were provided by the vendor, which were used as inputs to downstream analyses. Additional details can be found in the Supplementary Materials.

Immunofluorescence

Immunofluorescence staining of mouse lungs was performed as previously described (*29*). Briefly, lungs from WT or *Cx3cr1*$^{GFP+}$ mice

were perfused with 5 ml of PBS through the right ventricle and then with 5 ml of 4% paraformaldehyde (PFA) (Thermo Fisher Scientific) in PBS, and lungs were collected. Lungs were fixed for 4 hours in 4% PFA at 4°C and then cryoprotected overnight in 30% sucrose (VWR) in PBS at 4°C, followed by embedding in optimal cutting temperature compound (VWR) and stored at −80°C. Sections (7 μm in thickness) were cut and left in a 100% methanol (Merck) bath at −20°C for 20 min before staining. Additional details can be found in the Supplementary Materials. All images were acquired on an LSM 980 with Airyscan 2 inverted confocal microscope (Zeiss) using an LD C-Apochromat ×40/1.1 W objective and Zen Black software. Additional details can be found in the Supplementary Materials.

Ex vivo experiments

For ex vivo stimulation and coculture experiments, single-cell suspensions isolated from IAV-infected lungs of WT or *Ly6g*^{tdTom} mice at day 10 after IAV were enriched in CD11b$^+$ cells by magnetic-activated cell sorting (MACS) using CD11b microbeads (Miltenyi). Cells were then stained and FACS-sorted using the gating strategy shown in Fig. 1A. After sorting, cells were counted, spun down, and either directly added to the coculture with MLE-12 cells or seeded in 96 wells at a concentration of 5×10^4 cells per well in complete RPMI (Thermo Fisher Scientific), containing 1 mM sodium pyruvate, 1% v/v minimum essential medium nonessential amino acids, penicillin-streptomycin (50 U ml^{-1}), and 10% v/v fetal bovine serum. For stimulation experiments, recombinant mouse GM-CSF (20 ng ml^{-1}; PeproTech), mouse M-CSF (20 ng ml^{-1}; PeproTech), mouse IL-4 (20 ng ml^{-1}; PeproTech), or mouse IL-13 (20 ng ml^{-1}; PeproTech) were added. When required, Cre-ERT2 activation was achieved by adding 4-hydroxytamoxifen (0.02 mg ml^{-1}; Sigma-Aldrich). After 18 hours of culture, cell supernatants were collected (CM), and cells were harvested for flow cytometry phenotyping.

MLE-12 cells (American Type Culture Collection, CVCL_3751) were used. The scratch wound assay was performed using IncuCyte S3 (Sartorius). MLE-12 cells were seeded in a 96-well plate (Sartorius) at a density of 4×10^4 cells per well and incubated for 24 hours in a DMEM/F12 medium. An open wound area was created in the cell monolayer using the IncuCyte Wound Maker tool and subsequently cocultured with FACS-sorted cells or incubated with the CM from unpulsed or IL-4/IL-13–pulsed Ly6G$^+$ Macs. Additional details can be found in the Supplementary Materials.

Adoptive transfer of Ly6G$^+$ Macs in vivo

Ly6G$^+$ Macs were isolated from the lungs of CD45.2 WT mice at day 10 after IAV. Lung single-cell suspensions were first enriched in CD11b$^+$ cells by MACS using CD11b microbeads (Miltenyi Biotec) and were FACS-sorted using Sony MA900. Ly6G$^+$ Macs (4×10^5) were resuspended in 50 μl of sterile PBS and were instilled intratracheally in lightly isoflurane-anesthetized *Maf/Mafb*^{MyeloKO} mice at days 8, 11, 13, and 15 after IAV. Control *Maf/Mafb*^{MyeloKO} mice and WT mice received 50 μl of PBS as a vehicle.

Human BALF cells

The use of human BALF cells was approved in 2022 by the Ethics Reviewing Board of the University Hospital of Liege, Belgium (ref. 2022/159). The characteristics of the patients are summarized in table S1. Human BALF cells were fixed directly after collection for storage and scRNA-seq analyses.

Statistical analysis

Graphs were prepared with GraphPad Prism 9 (GraphPad Software) or R Bioconductor (3.5.1) (*74*). Data distribution was assumed to be normal when parametric tests were performed. Data from independent experiments were pooled for analysis in each data panel, unless otherwise indicated. No data were excluded from the analyses. Statistical analyses were performed with Prism 9 (GraphPad Software) and with R Bioconductor (3.5.1) (*74*) and Seurat (*75*) for scRNA-seq data. The statistical analyses performed for each experiment are indicated in the respective figure legends. We considered a P value lower than 0.05 to be significant ($^*P < 0.05$; $^{**}P < 0.01$; $^{***}P < 0.001$; $^{****}P < 0.0001$; ns, not significant). Additional sections and details about Materials and Methods can be found in the Supplementary Materials.

Supplementary Materials

This PDF file includes:
Materials and Methods
Figs. S1 to S13
Tables S1 to S3
References (*76–88*)

Other Supplementary Material for this manuscript includes the following:
Data file S1
MDAR Reproducibility Checklist

REFERENCES AND NOTES

1. A. C. Kalil, P. G. Thomas, Influenza virus-related critical illness: Pathophysiology and epidemiology. *Crit. Care* **23**, 258 (2019).
2. S. Herold, C. Becker, K. M. Ridge, G. R. S. Budinger, Influenza virus-induced lung injury: Pathogenesis and implications for treatment. *Eur. Respir. J.* **45**, 1463–1478 (2015).
3. X. Wei, H. Narasimhan, B. Zhu, J. Sun, Host recovery from respiratory viral infection. *Annu. Rev. Immunol.* **41**, 277–300 (2023).
4. World Health Organization, Burden of disease–Global influenza programme; https://who.int/teams/global-influenza-programme/surveillance-and-monitoring/burden-of-disease.
5. A. D. Iuliano, K. M. Roguski, H. H. Chang, D. J. Muscatello, R. Palekar, S. Tempia, C. Cohen, J. M. Gran, D. Schanzer, B. J. Cowling, P. Wu, J. Kyncl, L. W. Ang, M. Park, M. Redlberger-Fritz, H. Yu, L. Espenhain, A. Krishnan, G. Emukule, L. van Asten, S. Pereira da Silva, S. Aungkulanon, U. Buchholz, M.-A. Widdowson, J. S. Bresee, Global Seasonal Influenza-associated Mortality Collaborator Network, Estimates of global seasonal influenza-associated respiratory mortality: A modelling study. *Lancet* **391**, 1285–1300 (2018).
6. P. Bost, A. Giladi, Y. Liu, Y. Bendjelal, G. Xu, E. David, R. Blecher-Gonen, M. Cohen, C. Medaglia, H. Li, A. Deczkowska, S. Zhang, B. Schwikowski, Z. Zhang, I. Amit, Host-viral infection maps reveal signatures of severe COVID-19 patients. *Cell* **181**, 1475–1488.e12 (2020).
7. M. Merad, J. C. Martin, Pathological inflammation in patients with COVID-19: A key role for monocytes and macrophages. *Nat. Rev. Immunol.* **20**, 355–362 (2020).
8. M. Guilliams, A. Mildner, S. Yona, Developmental and functional heterogeneity of monocytes. *Immunity* **49**, 595–613 (2018).
9. C. Ruscitti, C. Radermecker, T. Marichal, Journey of monocytes and macrophages upon influenza A virus infection. *Curr. Opin. Virol.* **66**, 101409 (2024).
10. L. Rodriguez-Rodriguez, L. Gillet, B. Machiels, Shaping of the alveolar landscape by respiratory infections and long-term consequences for lung immunity. *Front. Immunol.* **14**, 1149015 (2023).
11. B. Machiels, M. Dourcy, X. Xiao, J. Javaux, C. Mesnil, C. Sabatel, D. Desmecht, F. Lallemand, P. Martinive, H. Hammad, M. Guilliams, B. Dewals, A. Vanderplasschen, B. N. Lambrecht, F. Bureau, L. Gillet, A gammaherpesvirus provides protection against allergic asthma by inducing the replacement of resident alveolar macrophages with regulatory monocytes. *Nat. Immunol.* **18**, 1310–1320 (2017).
12. H. Aegerter, J. Kulikauskaite, S. Crotta, H. Patel, G. Kelly, E. M. Hessel, M. Mack, S. Beinke, A. Wack, Influenza-induced monocyte-derived alveolar macrophages confer prolonged antibacterial protection. *Nat. Immunol.* **21**, 145–157 (2020).
13. H. Aegerter, B. N. Lambrecht, C. V. Jakubzick, Biology of lung macrophages in health and disease. *Immunity* **55**, 1564–1580 (2022).
14. M. Guilliams, F. R. Svedberg, Does tissue imprinting restrict macrophage plasticity? *Nat. Immunol.* **22**, 118–127 (2021).

15. F. Li, F. Piattini, L. Pohlmeier, Q. Feng, H. Rehrauer, M. Kopf, Monocyte-derived alveolar macrophages autonomously determine severe outcome of respiratory viral infection. *Sci. Immunol.* **7**, eabj5761 (2022).
16. K. L. Lin, Y. Suzuki, H. Nakano, E. Ramsburg, M. D. Gunn, $CCR2^+$ monocyte-derived dendritic cells and exudate macrophages produce influenza-induced pulmonary immune pathology and mortality. *J. Immunol.* **180**, 2562–2572 (2008).
17. S. T. Chen, M. D. Park, D. M. Del Valle, M. Buckup, A. Tabachnikova, R. C. Thompson, N. W. Simons, K. Mouskas, B. Lee, D. Geanon, D. D'Souza, T. Dawson, R. Marvin, K. Nie, Z. Zhao, J. LeBerichel, C. Chang, H. Jamal, G. Akturk, U. Chaddha, K. Mathews, S. Acquah, S.-A. Brown, M. Reiss, T. Harkin, M. Feldmann, C. A. Powell, J. L. Hook, S. Kim-Schulze, A. H. Rahman, B. D. Brown, Mount Sinai COVID-19 Biobank Team, N. D. Beckmann, S. Gnjatic, E. Kenigsberg, A. W. Charney, M. Merad, A shift in lung macrophage composition is associated with COVID-19 severity and recovery. *Sci. Transl. Med.* **14**, eabn5168 (2022).
18. M. D. Park, A. Silvin, F. Ginhoux, M. Merad, Macrophages in health and disease. *Cell* **185**, 4259–4279 (2022).
19. T. A. Wynn, K. M. Vannella, Macrophages in tissue repair, regeneration, and fibrosis. *Immunity* **44**, 450–462 (2016).
20. S. P. Nobs, M. Kopf, Tissue-resident macrophages: Guardians of organ homeostasis. *Trends Immunol.* **42**, 495–507 (2021).
21. F. Ginhoux, M. Guilliams, Tissue-resident macrophage ontogeny and homeostasis. *Immunity* **44**, 439–449 (2016).
22. F.-F. Huang, P. F. Barnes, Y. Feng, R. Donis, Z. C. Chroneos, S. Idell, T. Allen, D. R. Perez, J. A. Whitsett, K. Dunussi-Joannopoulos, H. Shams, GM-CSF in the lung protects against lethal influenza infection. *Am. J. Respir. Crit. Care Med.* **184**, 259–268 (2011).
23. C. Schneider, S. P. Nobs, A. K. Heer, M. Kurrer, G. Klinke, N. van Rooijen, J. Vogel, M. Kopf, Alveolar macrophages are essential for protection from respiratory failure and associated morbidity following influenza virus infection. *PLOS Pathog.* **10**, e1004053 (2014).
24. B. B. Ural, S. T. Yeung, P. Damani-Yokota, J. C. Devlin, M. de Vries, P. Vera-Licona, T. Samji, C. M. Sawai, G. Jang, O. A. Perez, Q. Pham, L. Maher, P. Loke, M. Dittmann, B. Reizis, K. M. Khanna, Identification of a nerve-associated, lung-resident interstitial macrophage subset with distinct localization and immunoregulatory properties. *Sci. Immunol.* **5**, eaax8756 (2020).
25. C. C. Bain, A. S. MacDonald, The impact of the lung environment on macrophage development, activation and function: Diversity in the face of adversity. *Mucosal Immunol.* **15**, 223–234 (2022).
26. J. Chen, M.-C. Zhong, H. Guo, D. Davidson, S. Mishel, Y. Lu, I. Rhee, L.-A. Pérez-Quintero, S. Zhang, M.-E. Cruz-Munoz, N. Wu, D. C. Vinh, M. Sinha, V. Calderon, C. A. Lowell, J. S. Danska, A. Veillette, SLAMF7 is critical for phagocytosis of haematopoietic tumour cells via Mac-1 integrin. *Nature* **544**, 493–497 (2017).
27. Y. Wu, Q. Wang, M. Li, J. Lao, H. Tang, S. Ming, M. Wu, S. Gong, L. Li, L. Liu, X. Huang, SLAMF7 regulates the inflammatory response in macrophages during polymicrobial sepsis. *J. Clin. Invest.* **133**, e150224 (2023).
28. G. X. Zheng, J. M. Terry, P. Belgrader, P. Ryvkin, Z. W. Bent, R. Wilson, S. B. Ziraldo, T. D. Wheeler, G. P. McDermott, J. Zhu, M. T. Gregory, J. Shuga, L. Montesclaros, J. G. Underwood, D. A. Masquelier, S. Y. Nishimura, M. Schnall-Levin, P. W. Wyatt, C. M. Hindson, R. Bharadwaj, A. Wong, K. D. Ness, L. W. Beppu, H. J. Deeg, C. McFarland, K. R. Loeb, W. J. Valente, N. G. Ericson, E. A. Stevens, J. P. Radich, T. S. Mikkelsen, B. J. Hindson, J. H. Bielas, Massively parallel digital transcriptional profiling of single cells. *Nat. Commun.* **8**, 14049 (2017).
29. D. Vanneste, Q. Bai, S. Hasan, W. Peng, D. Pirottin, J. Schyns, P. Maréchal, C. Ruscitti, M. Meunier, Z. Liu, C. Legrand, L. Fievez, F. Ginhoux, C. Radermecker, F. Bureau, T. Marichal, MafB-restricted local monocyte proliferation precedes lung interstitial macrophage differentiation. *Nat. Immunol.* **24**, 827–840 (2023).
30. C. Sabatel, C. Radermecker, L. Fievez, G. Paulissen, S. Chakarov, C. Fernandes, S. Olivier, M. Toussaint, D. Pirottin, X. Xiao, P. Quatresooz, J. C. Sirard, D. Cataldo, L. Gillet, H. Bouabe, C. J. Desmet, F. Ginhoux, T. Marichal, F. Bureau, Exposure to bacterial CpG DNA protects from airway allergic inflammation by expanding regulatory lung interstitial macrophages. *Immunity* **46**, 457–473 (2017).
31. Z. Liu, Y. Gu, S. Chakarov, C. Bleriot, I. Kwok, X. Chen, A. Shin, W. Huang, R. J. Dress, C.-A. Dutertre, A. Schlitzer, J. Chen, L. G. Ng, H. Wang, Z. Liu, B. Su, F. Ginhoux, Fate mapping via Ms4a3-expression history traces monocyte-derived cells. *Cell* **178**, 1509–1525.e19 (2019).
32. K. Street, D. Risso, R. B. Fletcher, D. Das, J. Ngai, N. Yosef, E. Purdom, S. Dudoit, Slingshot: Cell lineage and pseudotime inference for single-cell transcriptomics. *BMC Genomics* **19**, 477 (2018).
33. S. Yona, K. W. Kim, Y. Wolf, A. Mildner, D. Varol, M. Breker, D. Strauss-Ayali, S. Viukov, M. Guilliams, A. Misharin, D. A. Hume, H. Perlman, B. Malissen, E. Zelzer, S. Jung, Fate mapping reveals origins and dynamics of monocytes and tissue macrophages under homeostasis. *Immunity* **38**, 79–91 (2013).
34. N. V. Serbina, E. G. Pamer, Monocyte emigration from bone marrow during bacterial infection requires signals mediated by chemokine receptor CCR2. *Nat. Immunol.* **7**, 311–317 (2006).
35. T. Satoh, K. Nakagawa, F. Sugihara, R. Kuwahara, M. Ashihara, F. Yamane, Y. Minowa, K. Fukushima, I. Ebina, Y. Yoshioka, A. Kumanogoh, S. Akira, Identification of an atypical monocyte and committed progenitor involved in fibrosis. *Nature* **541**, 96–101 (2017).
36. S. Aibar, C. B. González-Blas, T. Moerman, V. A. Huynh-Thu, H. Imrichova, G. Hulselmans, F. Rambow, J.-C. Marine, P. Geurts, J. Aerts, J. van den Oord, Z. K. Atak, J. Wouters, S. Aerts, SCENIC: Single-cell regulatory network inference and clustering. *Nat. Methods* **14**, 1083–1086 (2017).
37. I. Ballesteros, A. Rubio-Ponce, M. Genua, E. Lusito, I. Kwok, G. Fernández-Calvo, T. E. Khoyratty, E. van Grinsven, S. González-Hernández, J. Á. Nicolás-Ávila, T. Vicanolo, A. Maccataio, A. Benguría, J. L. Li, J. M. Adrover, A. Aroca-Crevillen, J. A. Quintana, S. Martín-Salamanca, F. Mayo, S. Ascher, G. Barbiera, O. Soehnlein, M. Gunzer, F. Ginhoux, F. Sánchez-Cabo, E. Nistal-Villán, C. Schulz, A. Dopazo, C. Reinhardt, I. A. Udalova, L. G. Ng, R. Ostuni, A. Hidalgo, Co-option of neutrophil fates by tissue environments. *Cell* **183**, 1282–1297.e18 (2020).
38. J. Choi, J.-E. Park, G. Tsagkogeorga, M. Yanagita, B.-K. Koo, N. Han, J.-H. Lee, Inflammatory signals induce AT2 cell-derived damage-associated transient progenitors that mediate alveolar regeneration. *Cell Stem Cell* **27**, 366–382.e7 (2020).
39. I. Y. Adamson, D. H. Bowden, The type 2 cell as progenitor of alveolar epithelial regeneration. A cytodynamic study in mice after exposure to oxygen. *Lab. Invest.* **30**, 35–42 (1974).
40. J. D. Planer, E. E. Morrisey, After the storm: Regeneration, repair, and reestablishment of homeostasis between the alveolar epithelium and innate immune system following viral lung injury. *Annu. Rev. Pathol.* **18**, 337–359 (2023).
41. C. M. Minutti, L. H. Jackson-Jones, B. García-Fojeda, J. A. Knipper, T. E. Sutherland, N. Logan, E. Ringqvist, R. Guillamat-Prats, D. A. Ferenbach, A. Artigas, C. Stamme, Z. C. Chroneos, D. M. Zaiss, C. Casals, J. E. Allen, Local amplifiers of IL-4Rα-mediated macrophage activation promote repair in lung and liver. *Science* **356**, 1076–1080 (2017).
42. L. Bosurgi, Y. G. Cao, M. Cabeza-Cabrerizo, A. Tucci, L. D. Hughes, Y. Kong, J. S. Weinstein, P. Licona-Limon, E. T. Schmid, F. Pelorosso, N. Gagliani, J. E. Craft, R. A. Flavell, S. Ghosh, C. V. Rothlin, Macrophage function in tissue repair and remodeling requires IL-4 or IL-13 with apoptotic cells. *Science* **356**, 1072–1076 (2017).
43. M. C. Basil, J. Katzen, A. E. Engler, M. Guo, M. J. Herriges, J. J. Kathiriya, R. Windmueller, A. B. Ysasi, W. J. Zacharias, H. A. Chapman, D. N. Kotton, J. R. Rock, H.-W. Snoeck, G. Vunjak-Novakovic, J. A. Whitsett, E. E. Morrisey, The cellular and physiological basis for lung repair and regeneration: Past, present, and future. *Cell Stem Cell* **26**, 482–502 (2020).
44. W. J. Zacharias, D. B. Frank, J. A. Zepp, M. P. Morley, F. A. Alkhaleel, J. Kong, S. Zhou, E. Cantu, E. E. Morrisey, Regeneration of the lung alveolus by an evolutionarily conserved epithelial progenitor. *Nature* **555**, 251–255 (2018).
45. A. N. Nabhan, D. G. Brownfield, P. B. Harbury, M. A. Krasnow, T. J. Desai, Single-cell Wnt signaling niches maintain stemness of alveolar type 2 cells. *Science* **359**, 1118–1123 (2018).
46. D. C. Liberti, M. M. Kremp, W. A. Liberti, I. J. Penkala, S. Li, S. Zhou, E. E. Morrisey, Alveolar epithelial cell fate is maintained in a spatially restricted manner to promote lung regeneration after acute injury. *Cell Rep.* **35**, 109092 (2021).
47. A. V. Misharin, L. Morales-Nebreda, P. A. Reyfman, C. M. Cuda, J. M. Walter, A. C. McQuattie-Pimentel, C.-I. Chen, K. R. Anekalla, N. Joshi, K. J. N. Williams, H. Abdala-Valencia, T. J. Yacoub, M. Chi, S. Chiu, F. J. Gonzalez-Gonzalez, K. Gates, A. P. Lam, T. T. Nicholson, P. J. Homan, S. Soberanes, S. Dominguez, V. K. Morgan, R. Saber, A. Shaffer, M. Hinchcliff, S. A. Marshall, A. Bharat, S. Berdnikovs, S. M. Bhorade, E. T. Bartom, R. I. Morimoto, W. E. Balch, J. I. Sznajder, N. S. Chandel, G. M. Mutlu, M. Jain, C. J. Gottardi, B. D. Singer, K. M. Ridge, N. Bagheri, A. Shilatifard, G. R. S. Budinger, H. Perlman, Monocyte-derived alveolar macrophages drive lung fibrosis and persist in the lung over the life span. *J. Exp. Med.* **214**, 2387–2404 (2017).
48. P. Y. Lee, J.-X. Wang, E. Parisini, C. C. Dascher, P. A. Nigrovic, Ly6 family proteins in neutrophil biology. *J. Leukoc. Biol.* **94**, 585–594 (2013).
49. L. Cakarova, L. M. Marsh, J. Wilhelm, K. Mayer, F. Grimminger, W. Seeger, J. Lohmeyer, S. Herold, Macrophage tumor necrosis factor-alpha induces epithelial expression of granulocyte-macrophage colony-stimulating factor: Impact on alveolar epithelial repair. *Am. J. Respir. Crit. Care Med.* **180**, 521–532 (2009).
50. Y. Lavin, D. Winter, R. Blecher-Gonen, E. David, H. Keren-Shaul, M. Merad, S. Jung, I. Amit, Tissue-resident macrophage enhancer landscapes are shaped by the local microenvironment. *Cell* **159**, 1312–1326 (2014).
51. L. van de Laar, W. Saelens, S. De Prijck, L. Martens, C. L. Scott, G. Van Isterdael, E. Hoffmann, R. Beyaert, Y. Saeys, B. N. Lambrecht, M. Guilliams, Yolk sac macrophages, fetal liver, and adult monocytes can colonize an empty niche and develop into functional tissue-resident macrophages. *Immunity* **44**, 755–768 (2016).
52. P. Loos, J. Baiwir, C. Maquet, J. Javaux, R. Sandor, F. Lallemand, T. Marichal, B. Machiels, L. Gillet, Dampening type 2 properties of group 2 innate lymphoid cells by a

gammaherpesvirus infection reprograms alveolar macrophages. *Sci. Immunol.* **8**, eabl9041 (2023).
53. M. Schilperoort, D. Ngai, S. R. Sukka, K. Avrampou, H. Shi, I. Tabas, The role of efferocytosis-fueled macrophage metabolism in the resolution of inflammation. *Immunol. Rev.* **319**, 65–80 (2023).
54. S. Zhang, S. Weinberg, M. DeBerge, A. Gainullina, M. Schipma, J. M. Kinchen, I. Ben-Sahra, D. R. Gius, L. Yvan-Charvet, N. S. Chandel, P. T. Schumacker, E. B. Thorp, Efferocytosis fuels requirements of fatty acid oxidation and the electron transport chain to polarize macrophages for tissue repair. *Cell Metab.* **29**, 443–456.e5 (2019).
55. B. W. S. Li, M. J. W. de Bruijn, M. Lukkes, M. van Nimwegen, I. M. Bergen, A. KleinJan, C. H. GeurtsvanKessel, A. Andeweg, G. F. Rimmelzwaan, R. W. Hendriks, T cells and ILC2s are major effector cells in influenza-induced exacerbation of allergic airway inflammation in mice. *Eur. J. Immunol.* **49**, 144–156 (2019).
56. L. A. Monticelli, G. F. Sonnenberg, M. C. Abt, T. Alenghat, C. G. K. Ziegler, T. A. Doering, J. M. Angelosanto, B. J. Laidlaw, C. Y. Yang, T. Sathaliyawala, M. Kubota, D. Turner, J. M. Diamond, A. W. Goldrath, D. L. Farber, R. G. Collman, E. J. Wherry, D. Artis, Innate lymphoid cells promote lung-tissue homeostasis after infection with influenza virus. *Nat. Immunol.* **12**, 1045–1054 (2011).
57. R. L. Gieseck, M. S. Wilson, T. A. Wynn, Type 2 immunity in tissue repair and fibrosis. *Nat. Rev. Immunol.* **18**, 62–76 (2018).
58. A. J. Lechner, I. H. Driver, J. Lee, C. M. Conroy, A. Nagle, R. M. Locksley, J. R. Rock, Recruited monocytes and type 2 immunity promote lung regeneration following pneumonectomy. *Cell Stem Cell* **21**, 120–134.e7 (2017).
59. G. F. Weber, S. Ashkar, M. J. Glimcher, H. Cantor, Receptor-ligand interaction between CD44 and osteopontin (Eta-1). *Science* **271**, 509–512 (1996).
60. Q. Chen, V. S. Kumar, J. Finn, D. Jiang, J. Liang, Y-Y. Zhao, Y. Liu, $CD44^{high}$ alveolar type II cells show stem cell properties during steady-state alveolar homeostasis. *Am. J. Physiol. Lung Cell. Mol. Physiol.* **313**, L41–L51 (2017).
61. K. S. Burrack, T. E. Morrison, The role of myeloid cell activation and arginine metabolism in the pathogenesis of virus-induced diseases. *Front. Immunol.* **5**, 428 (2014).
62. R. A. Crompton, H. Williams, L. Campbell, L. Hui Kheng, C. Saville, D. M. Ansell, A. Reid, J. Wong, L. A. Vardy, M. J. Hardman, S. M. Cruickshank, An epidermal-specific role for arginase1 during cutaneous wound repair. *J. Invest. Dermatol.* **142**, 1206–1216.e8 (2022).
63. H. Katsura, Y. Kobayashi, P. R. Tata, B. L. M. Hogan, IL-1 and TNFα contribute to the inflammatory niche to enhance alveolar regeneration. *Stem Cell Rep.* **12**, 657–666 (2019).
64. C. Bosteels, K. F. A. Van Damme, E. De Leeuw, J. Declercq, B. Maes, V. Bosteels, L. Hoste, L. Naesens, N. Debeuf, J. Deckers, B. Cole, M. Pardons, D. Weiskopf, A. Sette, Y. V. Weygaerde, T. Malfait, S. J. Vandecasteele, I. K. Demedts, H. Slabbynck, S. Allard, P. Depuydt, E. Van Braeckel, J. De Clercq, L. Martens, S. Dupont, R. Seurinck, N. Vandamme, F. Haerynck, D. F. Roychowdhury, L. Vandekerckhove, M. Guilliams, S. J. Tavernier, B. N. Lambrecht, Loss of GM-CSF-dependent instruction of alveolar macrophages in COVID-19 provides a rationale for inhaled GM-CSF treatment. *Cell Rep. Med.* **3**, 100833 (2022).
65. P. A. Reyfman, J. M. Walter, N. Joshi, K. R. Anekalla, A. C. McQuattie-Pimentel, S. Chiu, R. Fernandez, M. Akbarpour, C.-I. Chen, Z. Ren, R. Verma, H. Abdala-Valencia, K. Nam, M. Chi, S. Han, F. J. Gonzalez-Gonzalez, S. Soberanes, S. Watanabe, K. J. N. Williams, A. S. Flozak, T. T. Nicholson, V. K. Morgan, D. R. Winter, M. Hinchcliff, C. L. Hrusch, R. D. Guzy, C. A. Bonham, A. I. Sperling, R. Bag, R. B. Hamanaka, G. M. Mutlu, A. V. Yeldandi, S. A. Marshall, A. Shilatifard, L. A. N. Amaral, H. Perlman, J. I. Sznajder, A. C. Argento, C. T. Gillespie, J. Dematte, M. Jain, B. D. Singer, K. M. Ridge, A. P. Lam, A. Bharat, S. M. Bhorade, C. J. Gottardi, G. R. S. Budinger, A. V. Misharin, Single-cell transcriptomic analysis of human lung provides insights into the pathobiology of pulmonary fibrosis. *Am. J. Respir. Crit. Care Med.* **199**, 1517–1536 (2019).
66. C. Morse, T. Tabib, J. Sembrat, K. L. Buschur, H. T. Bittar, E. Valenzi, Y. Jiang, D. J. Kass, K. Gibson, W. Chen, A. Mora, P. V. Benos, M. Rojas, R. Lafyatis, Proliferating SPP1/MERTK-expressing macrophages in idiopathic pulmonary fibrosis. *Eur. Respir. J.* **54**, 1802441 (2019).
67. T. S. Adams, J. C. Schupp, S. Poli, E. A. Ayaub, N. Neumark, F. Ahangari, S. G. Chu, B. A. Raby, G. Deluliis, M. Januszyk, Q. Duan, H. A. Arnett, A. Siddiqui, G. R. Washko, R. Homer, X. Yan, I. O. Rosas, N. Kaminski, Single-cell RNA-seq reveals ectopic and aberrant lung-resident cell populations in idiopathic pulmonary fibrosis. *Sci. Adv.* **6**, eaba1983 (2020).
68. J. Schyns, Q. Bai, C. Ruscitti, C. Radermecker, S. De Schepper, S. Chakarov, F. Farnir, D. Pirottin, F. Ginhoux, G. Boeckxstaens, F. Bureau, T. Marichal, Non-classical tissue monocytes and two functionally distinct populations of interstitial macrophages populate the mouse lung. *Nat. Commun.* **10**, 3964 (2019).
69. C. Radermecker, C. Sabatel, C. Vanwinge, C. Ruscitti, P. Maréchal, F. Perin, J. Schyns, N. Rocks, M. Toussaint, D. Cataldo, S. L. Johnston, F. Bureau, T. Marichal, Locally instructed $CXCR4^{hi}$ neutrophils trigger environment-driven allergic asthma through the release of neutrophil extracellular traps. *Nat. Immunol.* **20**, 1444–1455 (2019).
70. C. L. Scott, F. Zheng, P. De Baetselier, L. Martens, Y. Saeys, S. De Prijck, S. Lippens, C. Abels, S. Schoonooghe, G. Raes, N. Devoogdt, B. N. Lambrecht, A. Beschin, M. Guilliams, Bone marrow-derived monocytes give rise to self-renewing and fully differentiated Kupffer cells. *Nat. Commun.* **7**, 10321 (2016).
71. M.-J. Nokin, F. Durieux, J. Bellier, O. Peulen, K. Uchida, D. A. Spiegel, J. R. Cochrane, C. A. Hutton, V. Castronovo, A. Bellahcène, Hormetic potential of methylglyoxal, a side-product of glycolysis, in switching tumours from growth to death. *Sci. Rep.* **7**, 11722 (2017).
72. G. Rademaker, V. Hennequière, L. Brohée, M.-J. Nokin, P. Lovinfosse, F. Durieux, S. Gofflot, J. Bellier, B. Costanza, M. Herfs, R. Peiffer, L. Bettendorff, C. Deroanne, M. Thiry, P. Delvenne, R. Hustinx, A. Bellahcène, V. Castronovo, O. Peulen, Myoferlin controls mitochondrial structure and activity in pancreatic ductal adenocarcinoma, and affects tumor aggressiveness. *Oncogene* **37**, 4398–4412 (2018).
73. K. H. Dinnon, S. R. Leist, K. Okuda, H. Dang, E. J. Fritch, K. L. Gully, G. De la Cruz, M. D. Evangelista, T. Asakura, R. C. Gilmore, P. Hawkins, S. Nakano, A. West, A. Schäfer, L. E. Gralinski, J. L. Everman, S. P. Sajuthi, M. R. Zweigart, S. Dong, J. McBride, M. R. Cooley, J. B. Hines, M. K. Love, S. D. Groshong, A. VanSchoiack, S. J. Phelan, Y. Liang, T. Hether, M. Leon, R. E. Zumwalt, L. M. Barton, E. J. Duval, S. Mukhopadhyay, E. Stroberg, A. Borczuk, L. B. Thorne, M. K. Sakthivel, Y. Z. Lee, J. S. Hagood, J. R. Mock, M. A. Seibold, W. K. O'Neal, S. A. Montgomery, R. C. Boucher, R. S. Baric, SARS-CoV-2 infection produces chronic pulmonary epithelial and immune cell dysfunction with fibrosis in mice. *Sci. Transl. Med.* **14**, eabo5070 (2022).
74. W. Huber, V. J. Carey, R. Gentleman, S. Anders, M. Carlson, B. S. Carvalho, H. C. Bravo, S. Davis, L. Gatto, T. Girke, R. Gottardo, F. Hahne, K. D. Hansen, R. A. Irizarry, M. Lawrence, M. I. Love, J. MacDonald, V. Obenchain, A. K. Oles, H. Pages, A. Reyes, P. Shannon, G. K. Smyth, D. Tenenbaum, L. Waldron, M. Morgan, Orchestrating high-throughput genomic analysis with Bioconductor. *Nat. Methods* **12**, 115–121 (2015).
75. T. Stuart, A. Butler, P. Hoffman, C. Hafemeister, E. Papalexi, W. M. Mauck, Y. Hao, M. Stoeckius, P. Smibert, R. Satija, Comprehensive integration of single-cell data. *Cell* **177**, 1888–1902.e21 (2019).
76. S. Jung, J. Aliberti, P. Graemmel, M. J. Sunshine, G. W. Kreutzberg, A. Sher, D. R. Littman, Analysis of fractalkine receptor CX(3)CR1 function by targeted deletion and green fluorescent protein reporter gene insertion. *Mol. Cell. Biol.* **20**, 4106–4114 (2000).
77. L. Boring, J. Gosling, S. W. Chensue, S. L. Kunkel, R. V. Farese, H. E. Broxmeyer, I. F. Charo, Impaired monocyte migration and reduced type 1 (Th1) cytokine responses in C-C chemokine receptor 2 knockout mice. *J. Clin. Invest.* **100**, 2552–2561 (1997).
78. L. Madisen, T. A. Zwingman, S. M. Sunkin, S. W. Oh, H. A. Zariwala, H. Gu, L. L. Ng, R. D. Palmiter, M. J. Hawrylycz, A. R. Jones, E. S. Lein, H. Zeng, A robust and high-throughput Cre reporting and characterization system for the whole mouse brain. *Nat. Neurosci.* **13**, 133–140 (2010).
79. H. Wende, S. G. Lechner, C. Cheret, S. Bourane, M. E. Kolanczyk, A. Pattyn, K. Reuter, F. L. Munier, P. Carroll, G. R. Lewin, C. Birchmeier, The transcription factor c-Maf controls touch receptor development and function. *Science* **335**, 1373–1376 (2012).
80. B. E. Clausen, C. Burkhardt, W. Reith, R. Renkawitz, I. Forster, Conditional gene targeting in macrophages and granulocytes using LysMcre mice. *Transgenic Res.* **8**, 265–277 (1999).
81. C. Schneider, S. P. Nobs, A. K. Heer, E. Hirsch, J. Penninger, O. M. Siggs, M. Kopf, Frontline science: Coincidental null mutation of Csf2rα in a colony of $PI3K\gamma^{-/-}$ mice causes alveolar macrophage deficiency and fatal respiratory viral infection. *J. Leukoc. Biol.* **101**, 367–376 (2017).
82. F. Andreata, C. Blériot, P. Di Lucia, G. De Simone, V. Fumagalli, X. Ficht, C. G. Beccaria, M. Kuka, F. Ginhoux, M. Iannacone, Isolation of mouse Kupffer cells for phenotypic and functional studies. *STAR Protoc.* **2**, 100831 (2021).
83. A. M. Rieger, K. L. Nelson, J. D. Konowalchuk, D. R. Barreda, Modified annexin V/propidium iodide apoptosis assay for accurate assessment of cell death. *J. Vis. Exp.* **50**, 2597 (2011).
84. K. Van den Berge, H. Roux de Bézieux, K. Street, W. Saelens, R. Cannoodt, Y. Saeys, S. Dudoit, L. Clement, Trajectory-based differential expression analysis for single-cell sequencing data. *Nat. Commun.* **11**, 1201 (2020).
85. Z. Gu, R. Eils, M. Schlesner, Complex heatmaps reveal patterns and correlations in multidimensional genomic data. *Bioinformatics* **32**, 2847–2849 (2016).
86. A. Subramanian, P. Tamayo, V. K. Mootha, S. Mukherjee, B. L. Ebert, M. A. Gillette, A. Paulovich, S. L. Pomeroy, T. R. Golub, E. S. Lander, J. P. Mesirov, Gene set enrichment analysis: A knowledge-based approach for interpreting genome-wide expression profiles. *Proc. Natl. Acad. Sci. U.S.A.* **102**, 15545–15550 (2005).
87. P. Danaher, Y. Kim, B. Nelson, M. Griswold, Z. Yang, E. Piazza, J. M. Beechem, Advances in mixed cell deconvolution enable quantification of cell types in spatial transcriptomic data. *Nat. Commun.* **13**, 385 (2022).
88. M. Foroutan, D. D. Bhuva, R. Lyu, K. Horan, J. Cursons, M. J. Davis, Single sample scoring of molecular phenotypes. *BMC Bioinformatics* **19**, 404 (2018).

Acknowledgments: We thank all members of the Immunophysiology Laboratory (GIGA Institute, Liège, Belgium) for discussions; N. Maloujahmoum (Metastasis Research Laboratory, GIGA Institute) for expert technical assistance; S. Ormenese, R. Stefan, A. Hego, G. Lefevre, and C. Vanwinge from the GIGA In Vitro Imaging Platform; P. Drion, G. Lambert, L. B. Remy, and all staff members from the GIGA Mouse Facility and Transgenics Platform; W. Coppieters, L. Karim, M. Deckers, A. Mayer, A. Lavergne, and members from the GIGA Genomics Platform; and

R. Fares, I. Sbai, and A. Lio for excellent administrative support. **Funding:** This work was supported by the FRFS-Welbio Advanced Grant WELBIO-CR-2022A-10 (T.M.), ERC Starting Grant ERC StG 2018 IM-ID: 801823 (T.M.), Baillet Latour Biomedical Fund (T.M.), Research Project of the F.R.S.-FNRS T015021F (T.M.), and Research Concerted Action of the Fédération Wallonie-Bruxelles (T.M.). **Author contributions:** T.M. and C. Radermecker conceived, supervised, and secured funding for the project. C. Ruscitti, C. Radermecker, and T.M. designed the experiments. C. Ruscitti did most of the experiments, compiled the data, and prepared the figures. J.A. performed all of the bioinformatic analyses. P.M., M.M., D.V., and C. Radermecker helped with in vivo–related experiments. C.d.M. and M.-M.G. were implicated in experiments related to the histopathological analyses of myeloid-restricted *Maf* and *Mafb*-deficient mice. P.J., J.G., and F.S. were involved in human BALF collection and processing. M.D. and B.M. performed viral titrations and helped with viral RNA quantifications. M.T. performed electron microscopy experiments and analyses. F.B., C.S., A.H., F.G., and B.G.D. were implicated in experiments involving BM chimeric mice. A.B. performed extracellular flux analyses. C. Ruscitti, C. Radermecker, and T.M. wrote the manuscript. All authors provided feedback on the original and revised manuscript. **Competing interests:** The authors declare that they have no competing interests. **Data and materials availability:** All data needed to evaluate the conclusions in the paper are present in the paper or the Supplementary Materials. *Ms4a3*^{Cre} mice are used under the terms of a material transfer agreement (MTA) signed between Singapore Immunology Network (SIgN), A*STAR Research Entities (Singapore), and the University of Liege (Belgium). *Ly6g*^{CreERT2} mice are used under the terms of an MTA signed between Centro Nacional de Investigaciones Cardiovasculares Carlos III (CNIC, Madrid, Spain) and the University of Liege (Belgium). Mouse and human scRNA-seq data have been deposited in the GEO and are available under GEO accession number GSE244765. All original codes have been deposited at Zenodo and are available via this link: https://zenodo.org/records/11354523. Requests for *Mab*$^{fl/fl}$ mice should be addressed to T.M. and will be shared via an MTA.

Submitted 17 January 2024
Accepted 31 May 2024
Published 2 August 2024
10.1126/sciimmunol.ado1227

Science Immunology
AAAS

Supplementary Materials for

Recruited atypical Ly6G$^+$ macrophages license alveolar regeneration after lung injury

Cecilia Ruscitti *et al.*

Corresponding author: Coraline Radermecker, c.radermecker@uliege.be; Thomas Marichal, t.marichal@uliege.be

Sci. Immunol. **9**, eado1227 (2024)
DOI: 10.1126/sciimmunol.ado1227

The PDF file includes:

Other Supplementary Material for this manuscript includes the following:

Materials and Methods

Mice

All experiments, unless otherwise specified, were performed on age-matched 8–12-wk-old male and female mice on the C57BL/6 background. The following strains of mice were used: CD45.2 wild-type (WT) C57BL/6J (The Jackson Laboratory, #000664); CD45.1 WT (The Jackson Laboratory, #002014); *Cx3cr1*$^{GFP/+}$ (*77*) (The Jackson Laboratory, #005582); *Ccr2*$^{-/-}$ (*78*) (The Jackson Laboratory, #004999); *Ms4a3*^{Cre} (*31*); *Ly6g*^{CreERT2} (*37*); *R26*$^{LSL\text{tdTomato}}$ (*79*) (The Jackson Laboratory, #007909); *Maf*$^{fl/fl}$ (*80*), *Mafb*$^{fl/fl}$ (*39*); *Lyz2*^{Cre} (*81*) (The Jackson Laboratory, #004781); *Il4ra*$^{-/-}$*;* CD45.1 *Csf2ra*$^{-/-}$ (*82*). *Il4ra*$^{-/-}$ mice were kindly provided by Bernhard Ryffel (CNRS Orléans, France). CD45.1/CD45.2 WT C57BL/6J mice were obtained from CD45.1 WT crossed with CD45.2 WT mice. Myeloid-restriced c-Maf and Mafb depletion was achieved by crossing *Maf*$^{fl/fl}$ and *Mafb*$^{fl/fl}$ mice with Lyz2^{Cre} mice. *Ms4a3*^{tdTom} and *Ly6g*^{tdTom} mice were obtained by crossing *R26*$^{LSL\text{tdTomato}}$ with *Ms4a3*^{Cre} and *Ly6g*^{CreERT2} mice, respectively.

Mice were housed under specific pathogen-free conditions and maintained in a 12-h light–dark cycle with food and water ad libitum. All animal experiments described in this study were carried out in an animal biosafety level 3 containment unit. Experiments were reviewed and approved by the Institutional Animal Care and Use Committee of the University of Liège (ethical approval #2276). The 'Guide for the Care and Use of Laboratory Animals,' prepared by the Institute of Laboratory Animal Resources, National Research Council, and published by the National Academy Press, as well as European and local legislations, was followed carefully. Accordingly, the temperature and relative humidity were 21°C and 45-60%, respectively

In vivo models of injury

The mouse-adapted influenza strain A/Puerto Rico/8/34 (H1N1; PR8) was kindly provided by F. Trottein (Institut Pasteur, France). The viral stock suspension (10^8 Plaque Forming Units [PFU] ml^{-1}) was diluted and 5 PFU were administered intranasally (i.n.) to isoflurane-anesthetized mice in 50 µl of PBS (Thermo Fisher). Control groups received an equal volume of PBS i.n. for mock infection.

For bleomycin-induced lung injury, isoflurane-anesthetized mice were treated intratracheally (i.t.) with a single instillation of 0.06 IU of bleomycin (Bio-Connect) in a volume of 50µl PBS. Control animals received 50µl PBS alone.

For acetaminophen-induced liver injury, mice were fasted during 15 hours with free access to water and were injected intraperitoneally (i.p.) with 300mg kg^{-1} of acetaminophen (Sigma) in saline solution (NaCl 0.9%). Free access to food was allowed after treatment.

Assessment of viral NS1 mRNA levels

Whole lungs were excised and total mRNA was isolated from homogenized tissues according to the Immgen protocol (www.immgen.org). cDNA was obtained with RevertAid First Strand cDNA Synthesis Kit (Thermo Fisher), and qPCR was performed in duplicate with iTaq Universal SYBR green supermix (BioRad). Primer sequences were as follows: 5′-TTCACCATTGCCTTCTCTTC-3′ and 5′-CCCATTCTCATTACTGCTTC-3′ for viral NS1, 5′-CATGGCTCGCTCGGTGACC-3′ and 5′-AATGTGAGGCGGGTGGAACTG-3′ for housekeeping gene B2m. Expression levels of NS1 were normalized relative B2M control gene.

Reagents and antibodies

A complete list of the reagents and antibodies used in this manuscript can be found in Tables S2 and S3, respectively.

Bone marrow, blood and tissue cell isolation

Cell isolation was achieved as previously described (*39*, *74*). Briefly, for BM cells, femurs were dissected and cleaned of soft adhering tissue. Distal and proximal ends were opened, and BM cells were flushed out. After centrifugation, cell pellets were re-suspended in ice-cold PBS containing 10 mM EDTA and cell suspensions were filtered using a cell strainer (70 µM, Corning) to obtain a single cell suspension. Blood was collected from the tail vein in a 100 mM EDTA (Merck Millipore)-containing tube, and red blood cells were lysed with RBC lysis buffer (ThermoFischer). For the isolation of lung leucocytes and structural cells, lung vessels were perfused with 5 ml PBS through the right ventricle and 1 ml HBSS (Lonza) containing 0.5 UI dispase II (Sigma-Aldrich), 0.1mg ml^{-1} elastase (MedChemExpress), 0.075 mg ml^{-1} DNAse (Roche) was injected i.t. before dissecting the lung and digesting it for 30 minutes at 37°C in the same digestion medium. After 30 minutes of digestion, lungs were cut into small pieces with razor blades and further digested for 30 minutes at 37°C in HBSS containing 5% vol/vol FBS (Thermo Fisher), 0.5 UI dispase II, 0.05 mg ml^{-1} DNAse, 1 mg ml^{-1} collagenase A (Roche). After 30 minutes, the cell suspension was flushed using a 18-gauge needle to dissociate aggregates. Ice-cold PBS containing 10 mM EDTA was added to stop the digestion process and cell suspensions were filtered using a 70 µm cell strainer. Residual red blood cells were lysed with RBC lysis buffer. Leucocytes isolation from the liver was obtained as previously described (*83*). Briefly, after sacrifice, mice were perfused with 10 ml PBS through right ventricle, the liver middle lobe was dissected and the gallbladder removed. The liver was cut into small pieces with razor blades and digested for 45 minutes at 37°C in 10 ml HBSS containing 0.2mg ml^{-1} collagenase IV (ThermoFisher), 5U ml^{-1} DNase I and 10% vol/vol FBS (Thermo Fischer). After incubation, the homogenized liver suspension was filtered using a 70 µm cell strainer, washed with 10 ml ice-cold PBS containing 10mM EDTA and centrifuged at 50 rcf for 3 minutes. The aqueous phase was recovered, filtered in a new tube and centrifuged at 400 rfc for 5 minutes. The cell pellet was suspended in RBC lysis buffer for 2 minutes, then washed with 10 ml ice-cold PBS containing 10mM EDTA. In all experiments, the number of cells was counted using an automatic cell counter (iPrasense Norma XS).

Flow cytometry

Staining reactions were performed in the dark at 4°C for 30 minutes with 2% v/v of Fc block (BD Biosciences) to avoid nonspecific binding. For intracellular stainings, extracellular-stained cells were fixed and permeabilized with the Foxp3/Transcription factor Staining Buffer Set (Thermo Fisher). For EdU stainings, extracellular-stained cells were permeabilized and stained using Click-iT EdU Alexa Fluor 488 Flow Cytometry Assay Kit (Thermo Fisher), according to the manufacturer's instructions.

Cell viability was assessed using 7-AAD (BD Bioscience) or Fixable Viability Dye eFluor™ 780 (Thermo Fisher). Cell suspensions was analysed with a FACSCANTO II or a LSRFortessa (BD Biosciences). Results were analyzed using FlowJo software (Tree Star). For scRNA-seq, transmission electron microscopy, cytological examination and *ex vivo* experiments, lung myeloid cells were sorted using a FACSAria III (BD Biosciences) or a Sony MA900.

Cytologic examination

Cytologic examination of FACS-sorted neutrophils, iMo, IM-like cells, iMo and Ly6G$^+$ Macs at 10 days post-IAV was performed on cytospin preparations stained with Hemacolor (Merck KgaA). Sections were examined with an Echo Revolve microscope.

Annexin V/Propidium iodide assay

Annexin V/Propidium iodide (PI) apoptosis assay was performed as described (*84*). Briefly, after lung cell isolation, cells were resuspended in Annexin V binding buffer (ThermoFisher) and 2.10^6 cells were stained with Annexin V-APC and incubated in the dark for 15 minutes at room temperature. Cells were washed with 100 µl of Annexin V binding buffer and 2 µg ml^{-1} PI (ThermoFisher) were added to each sample and incubated in the dark for 15 minutes at room temperature. After washing with 500µl of Annexin V buffer, cells were centrifuged, cell pellet was resuspended in fixative solution of 1% vol/vol formaldehyde in PBS and incubated for 10 minutes on ice. Cells were washed with PBS, centrifuged, resuspended in PBS supplemented with 50 µg ml^{-1} RNase A (Merck Millipore) and incubated for 15 minutes at 37°C. Cell suspension was washed with PBS, centrifuged and resuspended for flow cytometry stainings.

In vivo treatments

For EdU incorporation experiments shown in fig. S3, B and C, mice were injected i.p. at day 10 post-IAV with 1 mg EdU (Santa Cruz Biotechnology) in 200 µl PBS 4 hours before sacrifice. For experiments addressing the lifespan of Ly6G$^+$ Macs (Fig. 3G), 1mg EdU in 200 µL PBS was injected i.p. twice 5 hours apart at day 7 post-IAV, and EdU incorporation was evaluated in blood leucocytes at day 8 post-IAV. The incorporation of EdU in lung myeloid cells was evaluated at days 10, 14 and 17 post-IAV. Assessment of phagocytic activity was performed as previously described (*69*). Briefly, isoflurane-anesthetized mice were instilled i.t. with 2.10^8 pHrodo™ Green E. coli BioParticules (Thermo Fisher) in 100 µl PBS. Lungs were harvested 3 hours later for flow cytometry analyses.

Generation of BM (competitive) chimeras

CD45.2, CD45.1 or CD45.1/CD45.2 WT mice were anesthetized by i.p. injection of 200 µl PBS containing ketamine (Nimatek, Dechra, 75 mg kg^{-1}) and xylazine (Rompun, Bayer, 10 mg kg^{-1}). When mentioned, the thoracic cavity was protected with a 0.6-cm-thick lead cover. Mice were irradiated with two consecutive doses of 6 Gy 15 minutes apart. Once recovered from the anaesthesia, mice were reconstituted by intravenous (i.v.) administration of 2.10^6 BM cells from *Ms4a3*^{tdtom} or *Il4ra*$^{-/-}$ mice, for full chimeras. For mixed BM chimeras, mice were reconstituted i.v. with 2.10^6 BM cells consisting of a 1:1 mix of BM cells obtained from the following mice: CD45.1 WT, *Ms4a3*^{tdtom}, *Ccr2*$^{-/-}$, CD45.1 *Csf2ra*$^{-/-}$, CD45.2 *Csf2ra*$^{+/+}$, *Cx3cr1*$^{GFP+}$, *Il4ra*$^{-/-}$, or homozygous *Ly6g*^{CreERT2} mice *(*also called *Ly6g*$^{-/-}$ mice). From the day of irradiation, mice were treated for 4 weeks with 0.05 mg ml^{-1} of enrofloxacin (Baytril, Bayer) in drinking water. Chimerism was assessed by flow cytometry in the blood 4 weeks after irradiation.

scRNA-sequencing and analyses

Mouse scRNA-seq analyses

Lung myeloid cells were FACS-sorted as living singlet CD45$^+$, F4/80$^+$ and/or CD11b$^+$ cells from lung single-cell suspensions pooled from 5 mock-infected and IAV-infected C57BL/6 male WT

mice at day 10 post-IAV. For each sample, an aliquot of Trypan blue-treated cells was examined under the microscope for counting, viability and aggregate assessment following FACS sorting. Viability was above 90% for all samples and no aggregates were observed. Cell preparations were centrifuged and pellets were resuspended in calcium- and magnesium-free PBS containing 0.4 mg ml^{-1} UltraPure BSA (Thermo Fisher Scientific).

The 10X Genomics platform (Single Cell 3' Solution) was used. For library preparation, approximately 2,000 (Mock group) and 6,000 (IAV group) cells were loaded into the Chromium Controller, in which they were partitioned, their polyA RNAs captured and barcoded using Chromium Single Cell 3' GEM, Library & Gel Bead Kit v3 (10X Genomics). The cDNAs were amplified and libraries compatible with Illumina sequencers were generated using Chromium Single Cell 3' GEM, Library & Gel Bead Kit v3 (10X Genomics). The libraries were sequenced on an Illumina NovaSeq sequencer on an SP100 cell flow (Read1: 28 cy, read2: 76 cy, index1: 10cy, index2: 10cy) at a depth of 50,000 reads per cell.

The Cell Ranger (v6.1.2) application (10x Genomics) was used to demultiplex the BCL files into FASTQ files (cellranger mkfastq), to perform alignment (to Cell Ranger mouse genome references 6.1.2 GRCm38/release 102), filtering and unique molecular identifier counting and to produce gene-barcode matrices.

Filtered matrix files were used for further scRNA-seq analyses with R Bioconductor (3.17) and Seurat (4.3.0) (31178118). Briefly, filtered matrices containing cell IDs and feature names in each sample were used to build a Seurat object. We performed quality control by filtering out the cells with less than 200 detected genes, the genes detected in less than three cells and the cells exhibiting more than 10% of mitochondrial genes. Gene counts in each sample were normalized separately by default method 'LogNormalize' with a scale factor of 10,000 and log transformation. Two thousand highly variable features were identified with the 'vst' method. After merging cells from all samples, cell contaminants were removed based on the expression of cell-specific genes, and 12 clusters were identified in the remaining cells using the FindClusters function (15 Principal Components [PC] included and a resolution of 0.7 was selected) and the differentially expressed genes (DEGs) were calculated using the FindAllMarkers function (Seurat package). ScRNA_seq datasets containing steady-state $CD64^+$ lung cells (GSE194021) were integrated with the lung myeloid cells of this study using FindIntegrationAnchors function (Seurat) with anchor.features = 2000.

Single-cell regulatory network inference and clustering analysis

To predict the potential active transcription factors, lung myeloid cells analyzed by scRNA-seq were subjected to SCENIC analysis (*36*). The normalized counts, nFeature_RNA and nCount_RNA in the merged Seurat object were used for the initial SCENIC analysis. The genes expressed with a value of 3 in 0.1% of the cells and detected in 1% of the cells were kept, and coexpression network analysis was made with GENIE3 in the SCENIC package. To represent the SCENIC results, the results of the '3.4_regulonAUC' output were added to the metadata of Seurat object so that regulon AUC scores could be plotted as a heatmap.

Slingshot and tradeSeq pseudotime trajectory analyses

To evaluate trajectory-based differential expression analysis, $CD206^-$ IMs, $Ly6G^+$ Macs, $Ly6C^+$ Mos, iMos, $CD206^+$ IMs and dying Macs were subjected to Slingshot analysis (*32*). The trajectories along pseudotime were built using umap embedding from the Seurat object. To

compare the expression patterns of DEGs across pseudotime, the counts matrix, pseudotime and cell weights calculated above were then used as input in fitGAM function (tradeSeq package) (*85*). The association of average expression of each gene with pseudotime was tested using associationTest and the DEGs between IMs and Ly6G$^+$ Mac trajectories were calculated with the patternTest function. The value of the estimated smoother on a grid of pseudotimes was estimated for each DEG using predictSmooth. The 200 DEGs with the biggest FcMedian and waldStat > 200 were annotated as 'changed genes', meaning that their expression patterns were different in IMs and Ly6G$^+$ Mac trajectories, while the 200 genes whose average expression was associated with pseudotime in both lineages were selected based on their Fold change and labeled as 'unchanged genes'. Genes whose expression patterns appeared to be influenced by a small number of cells behaving as outliers were manually removed. Finally, the scaled estimated smoothers calculated by predictSmooth were used to build heat maps with the ComplexHeatmap package (*86*).

Gene Set Enrichment Analyses (GSEA)

In order to analyse enrichment of published signatures in the scRNA-seq data, the normalized counts were used as expression datasets in GSEA. GSEA was carried out using the GSEA software (version 4.1.0) (*87*). We used the hallmark gene sets from the Molecular Signatures Database (MSigDB) to test for enrichment. The analyses involved a gene set permutation method with 1,000 permutations to calculate the enrichment scores.

scRNA-seq of human BALF cells

Chromium Fixed RNA Profiling for multiplexed samples (10X Genomics) was used for scRNA-seq analysis of human BALF cells, allowing the storage of fixed cells and enabling analysis of multiple samples in one single GEM reaction. Fresh samples were directly fixed in a 4% formaldehyde solution after collection for storage at -80°C. For GEM creation, the Multiplex-compatible Chromium Next GEM Single Cell Fixed RNA Human Transcriptome Probe Kit including a Probe Barcode that permits sample multiplexing and subsequent demultiplexing was used. The Cell Ranger (v7.1.0) application (10x Genomics) was used to demultiplex the BCL files into FASTQ files (cellranger mkfastq), to perform alignment (to Cell Ranger human genome reference GRCh38-2020-A), filtering and unique molecular identifier counting and to produce gene-barcode matrices. Filtered matrix files were used for further scRNA-seq analyses. Samples from two different multiplexed batches were integrated with FindIntegrationAnchorsfunction (using canonical correlation analysis). A total of 19 clusters were identified, with 16 PCs were included and a resolution of 0.9.

Orthologous genes of the Ly6G$^+$ Mac signature in humans were manually identified using the gene database of NCBI. The signature was then used to calculate the score for each cell using AddModuleScore function (Seurat). The scores were stored in the seurat object and plotted using FeaturePlot function.

Single-cell regulatory network inference and clustering analysis was performed on scRNA-seq data from human BALF cells, as explained above.

Transmission electron microscopy

FACS-sorted myeloid cell populations or lung tissues from IAV-infected mice at day 10 post-IAV were fixed in 2.5% glutaraldehyde (diluted in Sorensen's buffer: 0.1 M Na2HPO4/NaH2PO4 buffer, pH 7.4) for 1h at 4 °C and postfixed for 30 min in 2% OsO4 (diluted in 0.1 M Sorensen's

Buffer). After dehydration in graded ethanol, samples were embedded in Epon resin. Ultrathin sections obtained with a Reichert Ultracut S ultramicrotome (Reichert Technologies) were contrasted with 2% uranyl acetate and 4% lead citrate.

For ultrastructural analyses, random fields of cells were examined under a Jeol TEM JEM-1400 Transmission Electron Microscope at 80 kV, and photographed using an 11-megapixel camera system (Quemesa, Olympus).

Extracellular flux analysis

Oxygen consumption rate (OCR) was measured using Seahorse XF Cell Mito Stress Test (Agilent) according to manufacturer's recommendations and as described previously (*70*, *71*). Briefly, Neu, IM-like cells and Ly6G$^+$ Macs were FACS-sorted at day 10 post-IAV and seeded (10.10^4, 7.10^4 and 8.10^4 cells/well, respectively) in XFp mini-plates (Agilent) pre-coated with CellTak. Cells were kept in unbuffered serum-free DMEM supplemented with pyruvate (1mM), glutamine (2mM), glucose (10mM), at pH 7.4, 37 °C and ambient CO_2 for 1h before the assay. Analysis was performed using the XFp analyser (Seahorse Bioscience) as per manufacturer's instructions. Cells were sequentially challenged with 1 µM oligomycin, 1 µM carbonyl cyanide p-(trifluoromethoxy) phenylhydrazone (FCCP), and rotenone/antimycin mix (0.5 µM each). All results were normalized according to the cell number evaluated by Hoechst (2 mg ml^{-1}) incorporation after cold methanol/acetone fixation.

Spatial transcriptomic analyses using Digital Spatial Profiling (DSP)

Five-µm-thick formalin-fixed, paraffin-embedded (FFPE) sections were prepared using the protocol from NanoString Technologies. Briefly, 2 tissue slides, each containing 1 mock and 2 IAV samples harvested 10 days post-IAV, were analyzed. Slides were first stained with antibodies against CD68, Ly6G (clone 1A8), and DNA was visualized with 500 nM Syto83. Mouse Whole Transcriptome Atlas probes targeting more than 19,000 targets were hybridized, and slides were loaded on the GeoMx DSP. Briefly, entire slides were imaged at x20 magnification, and Regions of Interest (ROIs) were chosen based on serial Hematoxylin & Eosin sections and on morphological markers to select lesional, perilesional and extralesional areas. ROIs were exposed to ultraviolet light, releasing the indexing oligos and collecting them in a 96-well plate for subsequent processing and sequencing, as described (*72*). Raw count, third quartile (Q3)–normalized count data of target genes from ROIs were provided by the vendor, which were used as input to downstream analyses. Pairwise differential expression analysis between perilesional, lesional, extralesional and control ROIs were performed using the GeoMx Digital Spatial Profiler Data Analysis Suite (DSPDA version 3.0.0.111). The R script SpatialDecon (*88*) was loaded into the DSPDA and run using the Mouse Adult Lung profile matrix. For cell signature scoring, the gene signatures were obtained from scRNA-seq data using the 20 most specific markers obtained using the FindAllMarkers function (Seurat package), genes were then ordered according to their average log_2FC. Lung myeloid cell signature scores were obtained from our own scRNA-seq datasets, while the AT2, primed AT2, DATPs and AT1 signature score were calculated from previously published data (*38*) using the same procedure. The geneset from the activation pathway of IL4 (BIOCARTA_IL4_PATHWAY) was download from MSigDB and was used to generate the type 2 signature score shown in Fig. 7A. The signatures were then used to calculate the score for each ROI using the simpleScore function (singscore package) (*89*) on the ranked gene expression matrix.

Immunofluorescence

Immunofluorescence stainings of mouse lungs were performed as previously described (*39*). Briefly, lungs from WT or *Cx3cr1*$^{GFP+}$ mice were perfused with 5 ml PBS through the right ventricle then with 5 ml paraformaldehyde (PFA) 4% (Thermo Fisher) in PBS, and lungs were collected. Lungs were fixed for 4 h in 4% PAF at 4 °C, then cryoprotected overnight in 30% sucrose (VWR) in PBS at 4 °C, followed by embedding in optimal cutting temperature compound (OCT) (VWR) and stored at −80 °C.

For staining of lungs from *Cx3cr1*$^{GFP+}$ mice (Fig. 5A), 7-µm-thick sections were cut and left in a methanol 100% (Merck) bath at −20 °C for 20 minutes prior to be stained for 2h at room temperature with a rabbit anti-GFP antibody (ThermoFischer) and a rat anti-mouse Ly6G (BDBioscience). After washing samples with PBS, a secondary anti-rat AF594 (Invitrogen) was added in blocking buffer and incubated for 2 hours in the dark at room temperature.

For stainings of WT lungs (Fig. 5H and fig. S8), 7-µm-thick sections were cut and left in a methanol 100% (Merck) bath at −20 °C for 20 minutes prior to be stained overnight at 4°C in blocking buffer (PBS with 0.3% Triton X-100 [Merck], 2% donkey serum [Merck]) with the following antibodies: rabbit anti-mouse pSPC (Abcam); rat anti-mouse Ly6G (BDBioscience). After washing samples with PBS, secondary antibodies (anti-rabbit AF532; anti-rat AF594 [Invitrogen]) were added in blocking buffer and incubated for 2 hours in the dark at room temperature. Samples were washed with PBS and incubated with directly-coupled antibodies (eFluor570-Ki67 [Invitrogen]; anti-mouse AF700-MHC-II [ThermoFischer]; anti-mouse Superbright432-Pdpn [ThermoFischer]) in blocking buffer for 6 hours at 4 °C.

Finally, all samples were washed one last time with PBS and were mounted with 10 µl ProLong Antifade reagent (Invitrogen) containing 0.1% Sytox blue nucleic acid stain (Invitrogen) on glass slides and stored at room temperature in the dark overnight.

Images shown in Fig. 3K and 5A were acquired on an LSM 980 inverted confocal microscope using Plan-Apochromat 20x/0.8 or LD C-Apochromat 40x/1.1 W objectives. Fluorophores were excited simultaneously at 405/561 nm (Fig. 3K) or 405/488/561 nm (Fig. 5A) with detection wavelength at 300-735/499-594/573-627 with GaAsP-PMT in Zeiss FastAiryScanSheppardSum SR-4y:3.7 mode and bidirectional acquisition. Analysis was performed with Zeiss Blue software.

Images shown in Fig. 5H and fig. S8 were acquired on a Leica Stellaris 8 Inverted Confocal microsocope with a White Light Laser (WLL) using 20x APO CS2 or 40x 1.30 NA Oil objectives and 512x512, 400 Hz, unidirectional acquisition. The acquisition was finalized by 3 sequential settings, all with WLL at 85% and a pinhole at 1 AU (65,3). We used, for the first sequence, the combination of diode laser 405 (dsetector HyD S 415-443 nm) and WLL with a laser line of 556 nm (Detector HyD S 570-620nm); for the second sequence, the WWL with a laser line of 528 nm (Detector HyD S 541-564 nm) and 445 nm (Detector HyD S 450-515nm); for the third sequence, the WLL with a laser line of 499nm (Detector HyD S 504-539 nm) and 696nm (Detector HyD X 706-752 nm). The images were then analyzed with LAS X software version 4.7.0.28176.

Histology

Seven-µm-thick sections from frozen lung tissues obtained from mock- and IAV-infected mice at day 20 post-IAV were mounted onto glass slides and stained with Hematoxylin & Eosin (H&E) or periodic-acid Schiff (PAS). The slides were scanned with an Axioscan 7 scanner (Zeiss,

Germany). Whole slide images were analysed with an open-source automated software analysis program for digital pathology (QuPath version 0.4.3). Briefly, lesional areas were determined manually and automated tissue detection was performed in the lesional area to correct for alveolar blank spaces. Thereafter, built-in algorithms for pixel classification of QuPath and machine learning were used on PAS sections and a threshold was determined to quantify % of mucus$^+$ cells within the lesional area.

Ex vivo experiments

For *ex vivo* stimulation and co-culture experiments, single cell suspensions isolated from IAV-infected lungs of WT or *Ly6g*^{tdTom} mice at day 10 post-IAV were enriched in CD11b$^+$ cells by a magnetic-activated cell sorting (MACS) using CD11b MicroBeads (Myltenyi). Cells were then stained and FACS-sorted using the gating strategy shown in Fig. 1A. After sorting, cells were counted, spinned down, and either directly added to the co-culture with MLE-12 cells, or seeded in 96 wells at a concentration 5.10^4 cells/well in complete RPMI (ThermoFischer), containing 1mM sodium pyruvate, 1% vol/vol MEM non-essential amino acids, 50 U ml^{-1} Penicillin-Streptomycin and 10% vol/vol FBS. For stimulation experiments, recombinant mouse GM-CSF (20 ng ml^{-1}, Peprotech), mouse M-CSF (20 ng ml^{-1}, Peprotech), mouse IL-4 (20 ng ml^{-1}, Peprotech) or mouse IL-13 (20 ng ml^{-1}, Peprotech) were added. When required, Cre-ERT2 activation was achieved by adding 0.02 mg ml^{-1} of 4-hydroxytamoxifen (Sigma-Aldrich). After 18 hours of culture, cell supernatants were collected (conditioned medium, CM) and cells were harvested for flow cytometry phenotyping. For the visualisation of tdTomato induction in tamoxifen-treated iMos from *Ly6g*^{tdTom} mice by confocal microscopy, iMos were seeded and cultured in 8-chambers slides (Nunc Lab-Tek II Chamber Slide system, Sigma) precoated with poly-D-lysin hydrobromide (Sigma). Cells were incubated in complete RPMI containing 0.02 mg ml^{-1} 4-hydroxytamoxifen and 20ng ml^{-1} GM-CSF or vehicle. Supernatants were removed and chambers were rinsed with PBS. Slides were then fixed with paraformaldehyde 10% for 10 minutes, rinsed twice with PBS and mounted with ProLong Antifade reagent with DAPI (ThermoFisher). Images were acquired as above.

Proteome profiler (R&D) was performed on CM from Ly6G$^+$Macs cultured for 18h in complete RPMI with or without 20ng ml^{-1} IL-4 and 20ng ml^{-1} IL-13 treatment. The assay was performed following the manufacturer's instructions and was analysed using the Protein Array Analyzer plug-in for ImageJ.

Murine lung epithelial (MLE)-12 cells (ATCC, CVCL_3751) were cultured in DMEM/F12 (ThermoFisher) complemented with 1% Insulin-Transferrin-Selenium (ITS-G) (ThermoFisher), L-glutamine 2mM (ThermoFisher), FBS 2% and HEPES 10mM (ThermoFisher). Cells were incubated at 37 °C in a humidified atmosphere containing 5% CO2. Cells were passaged at 80–90% confluence using 0.05% Trypsin-EDTA (ThermoFisher). Experiments were performed with passage numbers ranging from 4 to 6. Scratch Wound Assay were performed using IncucyteS3 (Sartorius). MLE-12 cells were seeded in 96-well (Sartorius) at density of 4.10^4 cells/well and incubated 24 hours in DMEM/F12 medium. An open wound area was created in the cell monolayer using the IncuCyte ® Wound Maker tool, washed with PBS and subsequently co-cultured with 5.10^4 Neu, IM-like cells, iMos or Ly6G$^+$ Macs, or incubated with CM from unpulsed or IL-4/IL-13-pulsed Ly6G$^+$ Macs. Complete DMEM medium containing 20 ng ml^{-1} IL-4 and 20 ng ml^{-1} IL-13 was used as control. Cells were imaged after wounding every 3 hours at 10 x magnification using the Sartorius Incucyte S3 Inverted brighfield microscope with motorized XYZ in a chamber

for 37°C temperature, 5% CO2 and 90-95% humidity. Images were acquired by Basler Ace 1920-155um, acA1920-155umEBS camera with 10 x 0.3 NA, Dry, 16mm WD objective. For each time point, relative wound closure was calculated using the Scratch Wound analyses pipeline of the IncuCyte 2023A Rev1 software.

Adoptive transfer of Ly6G$^+$ Macs *in vivo*

Ly6G$^+$ Macs were isolated from the lungs of CD45.2 WT mice at day 10 poist-IAV. Lung single cell suspensions were first enriched in CD11b$^+$ cells by MACS using CD11b MicroBeads (Miltenyi Biotec) and were FACS-sorted using a Sony MA900. Four hundred thousands (4 x 10^5) Ly6G$^+$ Macs were resuspended in 50 µl sterile PBS and were instilled i.t. in lightly isoflurane-anesthetized *Maf/Mafb*^{MyeloKO} mice at days 8, 11, 13, 15 post-IAV. Control *Maf/Mafb*^{MyeloKO} mice and WT mice received 50 µl PBS as vehicle.

Quantification of alanine aminotransferase (ALT)

Blood was collected in a a 100 mM EDTA (Merck Millipore)-containing tube and centrifuged at 4000 rpm for 4 minutes. Plasma was collected and levels of ALT were determined usinf a mouse ALT ELISA Kit (Abcam) following manufacturer's instructions.

Human BALFs

The use of human BALF cells was approved in 2022 by the Ethics Reviewing Board of the University Hospital of Liege, Belgium (ref. 2022/159). The characteristics of the patients are summarized in Table S1. Human BALFs were fixed directly after collection for storage and scRNA-seq analyses.

Statistical analysis

Graphs were prepared with GraphPad Prism 9 (GraphPad software) or R Bioconductor (3.5.1) (*73*). Data distribution was assumed to be normal when parametric tests were performed. Data from independent experiments were pooled for analysis in each data panel, unless otherwise indicated. No data were excluded from the analyses. Statistical analyses were performed with Prism 9 (GraphPad software), and with R Bioconductor (3.5.1) (*73*) and Seurat (*76*) for scRNA-seq data, respectively. The statistical analyses performed for each experiment are indicated in the respective figure legends. We considered a P value lower than 0.05 to be significant (*, $P < 0.05$; **, $P < 0.01$; ***, $P < 0.001$; ****, $P < 0.0001$; ns, not significant).

Additional sections and details about Materials and Methods can be found in the Supplemental Materials.

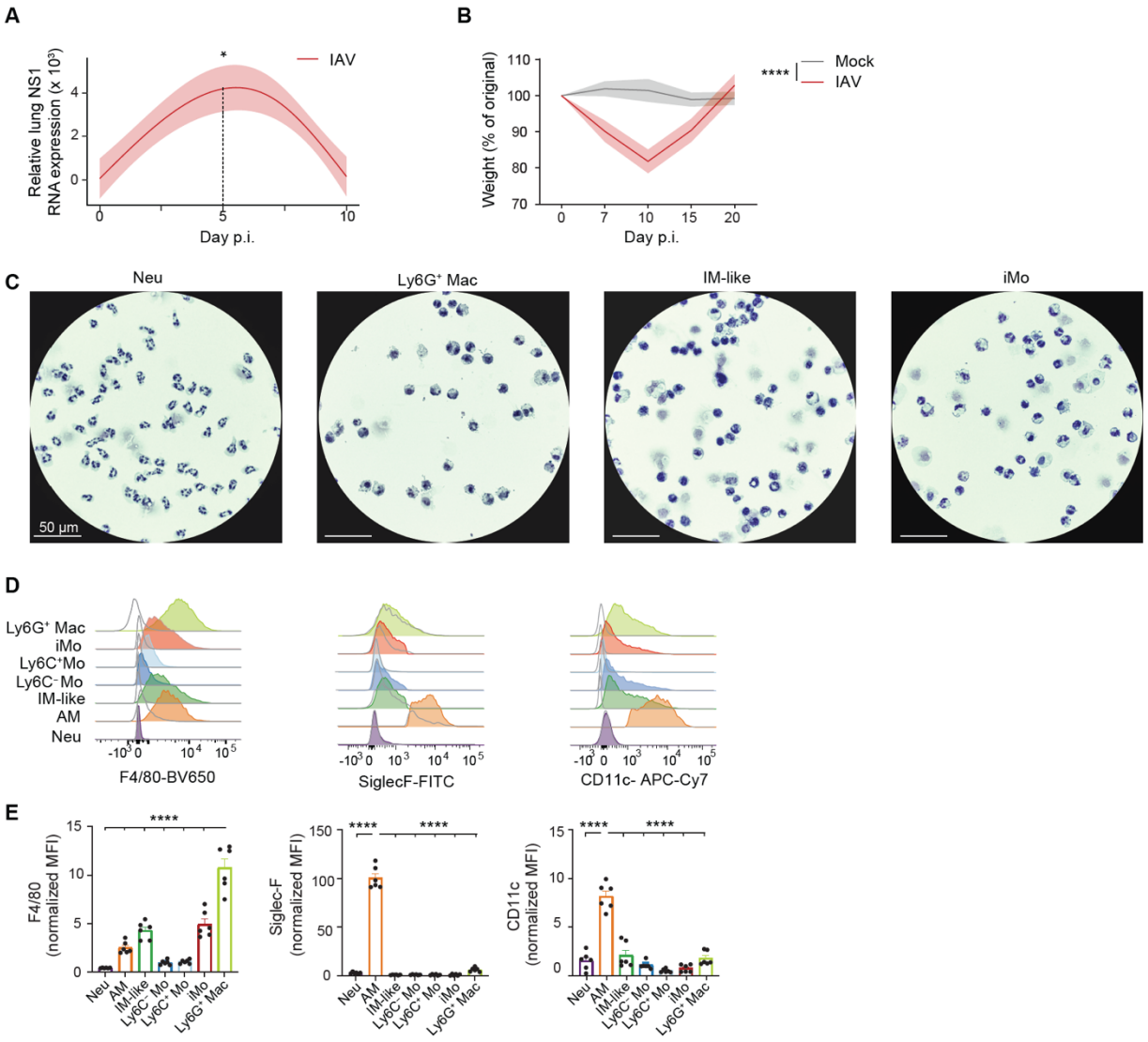

Fig. S1. Morphology and phenotype of lung myeloid cells at day 10 post-IAV. (**A**) Time course of relative lung NS1 RNA expression, assessed by RT-qPCR at days 0, 5 and 10 post-IAV in WT mice. (**B**) Time course of weight, expressed as the % of the original weight at day 0 and assessed at days 0, 7, 10, 15 and 20 post-IAV in WT mice. (**C**) Photographs of Neu, Ly6G$^+$ Macs, IM-like cells and iMo sorted by FACS from IAV-infected WT mice at day 10 p.i.. Pictures are representative of 1 of 3 independent sorting experiments, each giving similar results. (**D**) Representative histograms of F4/80, SiglecF and CD11c expression in the indicated myeloid cell populations, quantified by flow cytometry at day 10 post-IAV in WT mice. (**E**) Quantification of expression of the indicated markers, as in (D). (A,B) Data show mean (centerline) ± SEM (colored area) and are pooled from 2 independent experiments (*n*=6-7 mice per time point). (E) Data show mean + SEM and are pooled from 2 independent experiments (*n*= 6 mice). *P* values compare day 5 vs. day 0 in (A) and were calculated using (A,D) a one-way ANOVA with Dunnett's post hoc tests or (B) a two-way ANOVA. *, $P<0.05$; ****, $P<0.0001$. p.i., post-infection. (C) Scale bar: 50 µm.

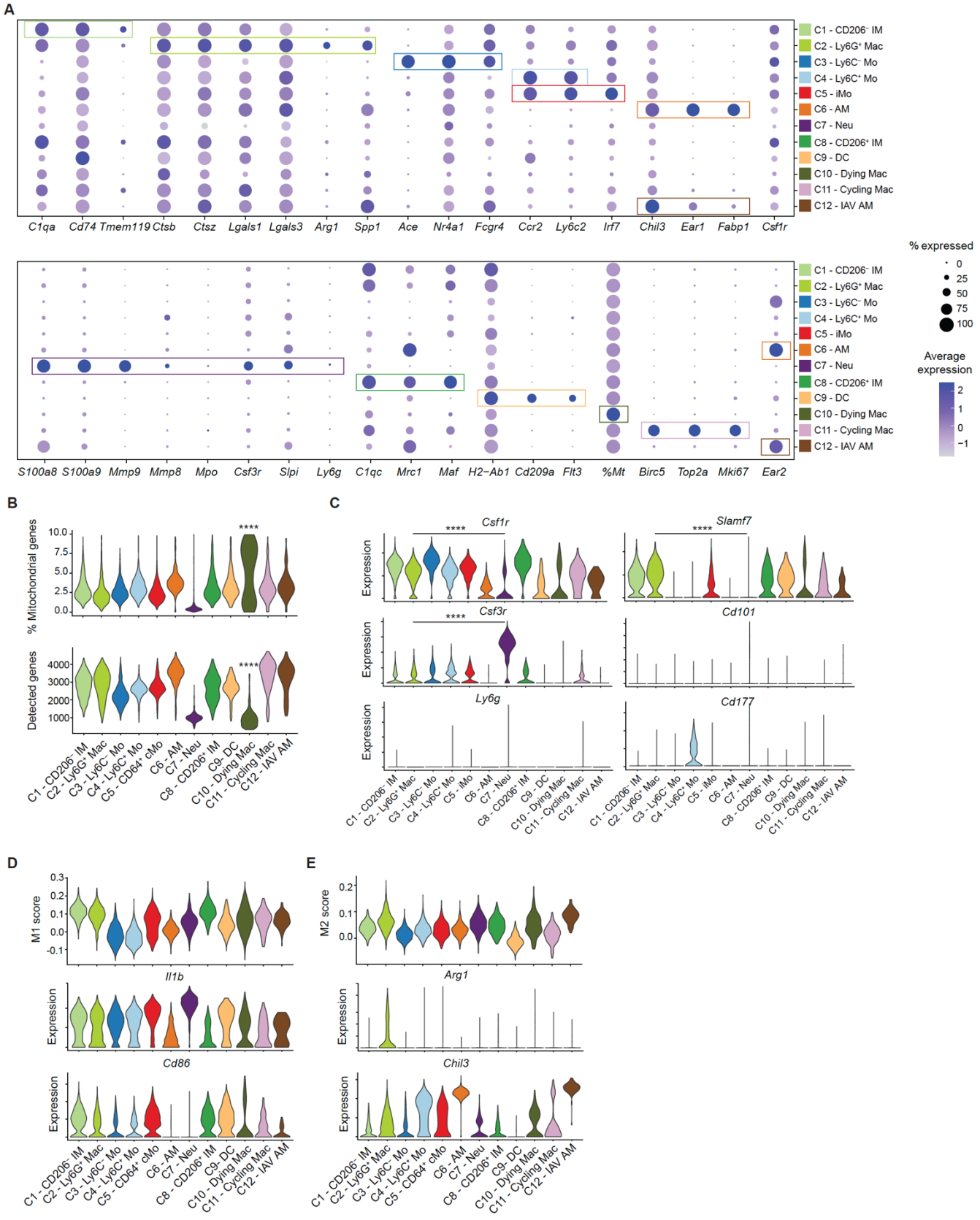
A
C1 - CD206⁻ IM
C2 - Ly6G⁺ Mac
C3 - Ly6C⁻ Mo
C4 - Ly6C⁺ Mo
C5 - iMo
C6 - AM
C7 - Neu
C8 - CD206⁺ IM
C9 - DC
C10 - Dying Mac
C11 - Cycling Mac
C12 - IAV AM
C1qa Cd74 Tmem119 Ctsb Ctsz Lgals1 Lgals3 Arg1 Spp1 Ace Nr4a1 Fcgr4 Ccr2 Ly6c2 Irf7 Chil3 Ear1 Fabp1 Csf1r
S100a8 S100a9 Mmp9 Mmp8 Mpo Csf3r Slpi Ly6g C1qc Mrc1 Maf H2−Ab1 Cd209a Flt3 %Mt Birc5 Top2a Mki67 Ear2
% expressed
0
25
50
75
100
Average expression
2
1
0
−1
B
% Mitochondrial genes
Detected genes
****
C
Csf1r
Slamf7
Csf3r
Cd101
Ly6g
Cd177
Expression
D
M1 score
Il1b
Cd86
E
M2 score
Arg1
Chil3

Fig. S2. Gene expression in and features of myeloid cell clusters identified by scRNA-seq at day 10 post-IAV. (**A**) Dot plots showing average expression of the indicated genes and % of cells expressing the genes within each cluster, related to Fig. 2A. (**B**) Percentage of mitochondrial genes (top) and number of detected genes (bottom) within each cluster, as depicted by violin plots (width: abundance of cells). (**C**) Expression of the indicated genes within each cluster, as depicted by violin plots (height: gene expression; width: abundance of cells). (**D**) M1 signature score (top) and expression of M1-related genes within each cluster, as depicted by violin plots (height: M1 score or gene expression; width: abundance of cells). (**E**) M2 signature score (top) and expression of M2-related genes within each cluster, as depicted by violin plots (height: M2 score or gene expression; width: abundance of cells). *P* values compare (B) C10 – dyings Macs *vs.* all other clusters or (C) C2 – $Ly6G^+$ Macs *vs.* C7 – Neutrophils and were calculated using a Wilcoxon rank sum test. ****, $P<0.0001$.

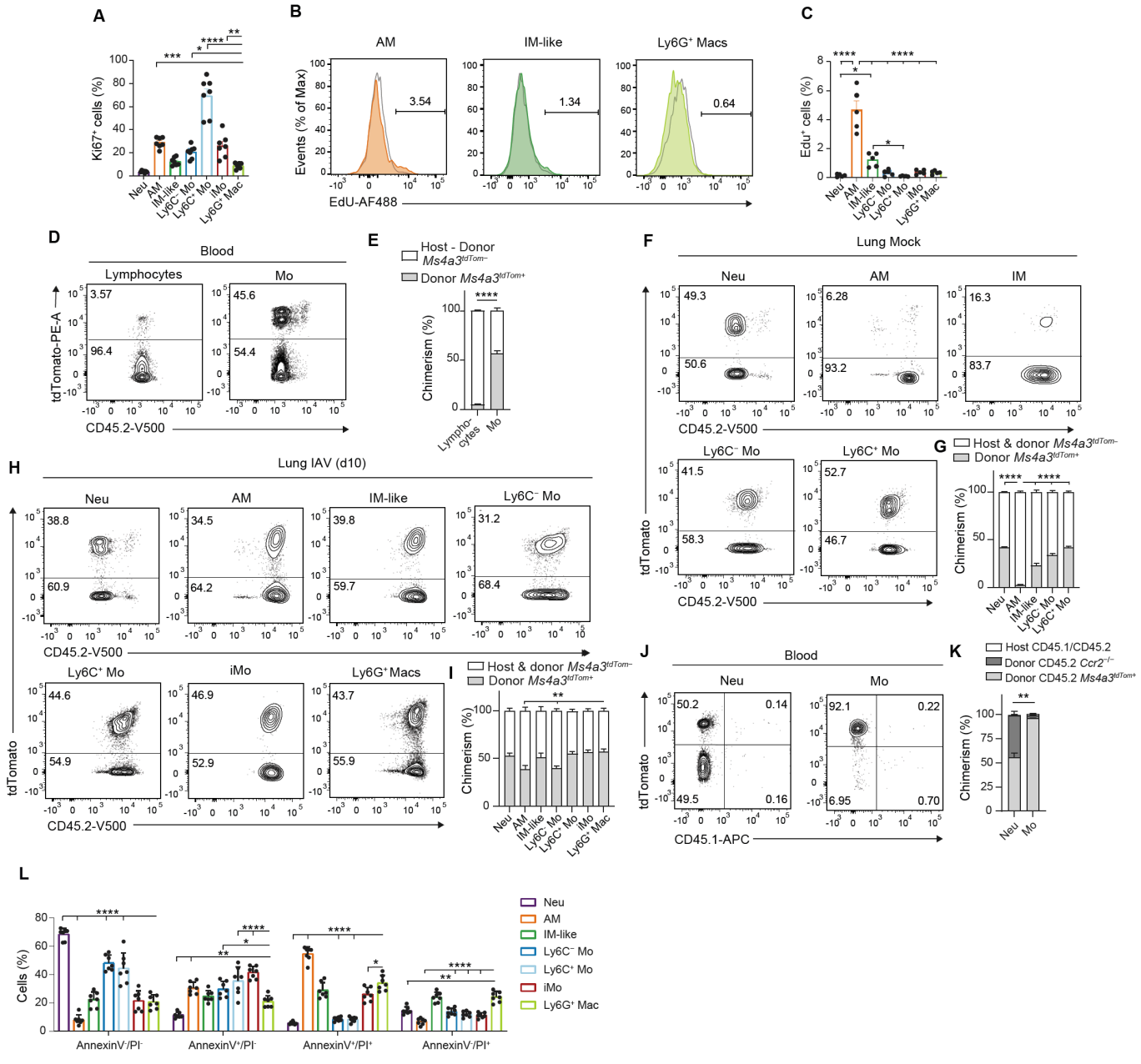
A
Ki67⁺ cells (%)
Neu
AM
IM-like
Ly6C⁻ Mo
Ly6C⁺ Mo
iMo
Ly6G⁺ Mac
B
AM
IM-like
Ly6G⁺ Macs
Events (% of Max)
3.54
1.34
0.64
EdU-AF488
C
Edu⁺ cells (%)
D
Blood
Lymphocytes
Mo
tdTomato-PE-A
3.57
96.4
45.6
54.4
CD45.2-V500
E
Host - Donor
Ms4a3tdTom−
Donor Ms4a3tdTom+
Chimerism (%)
Lympho-cytes
Mo
F
Lung Mock
Neu
AM
IM
49.3
50.6
6.28
93.2
16.3
83.7
CD45.2-V500
Ly6C⁻ Mo
Ly6C⁺ Mo
41.5
58.3
52.7
46.7
tdTomato
G
Host & donor Ms4a3tdTom−
Donor Ms4a3tdTom+
Chimerism (%)
H
Lung IAV (d10)
Neu
AM
IM-like
Ly6C⁻ Mo
38.8
60.9
34.5
64.2
39.8
59.7
31.2
68.4
CD45.2-V500
Ly6C⁺ Mo
iMo
Ly6G⁺ Macs
44.6
54.9
46.9
52.9
43.7
55.9
tdTomato
I
Host & donor Ms4a3tdTom−
Donor Ms4a3tdTom+
Chimerism (%)
J
Blood
Neu
Mo
50.2
0.14
49.5
0.16
92.1
0.22
6.95
0.70
tdTomato
CD45.1-APC
K
Host CD45.1/CD45.2
Donor CD45.2 Ccr2−/−
Donor CD45.2 Ms4a3tdTom+
Chimerism (%)
Neu
Mo
L
Cells (%)
AnnexinV⁻/PI⁻
AnnexinV⁺/PI⁻
AnnexinV⁺/PI⁺
AnnexinV⁻/PI⁺
Neu
AM
IM-like
Ly6C⁻ Mo
Ly6C⁺ Mo
iMo
Ly6G⁺ Mac

Fig. S3. Ly6G$^+$ Macs do not proliferate, are short-lived and arise from recruited BM-derived monocytes post-IAV. (**A**) Bar graphs showing the % of Ki67$^+$ cells in the indicated lung myeloid cell populations, as quantified by flow cytometry in lungs of WT mice at day 10 post-IAV. (**B**) Representative histograms of EdU levels in AMs, IM-like cells and Ly6G$^+$ Macs from EdU-pulsed WT mice at day 10 post-IAV. Unpulsed mice were used as controls (grey line). (**C**) Bar graphs showing the % of EdU$^+$ cells in the indicated lung myeloid cell populations, as in (B). (**D**) Representative tdTomato and CD45.2 contour plots and (**E**) bar graph showing % of host and donor *Ms4a3*$^{tdTom-}$ chimerism and donor *Ms4a3*$^{tdTom+}$ chimerism of blood lymphocytes and monocytes (Mo) from lethally-irradiated thorax-protected WT mice reconstituted with *Ms4a3*$^{tdTom+}$ BM donor cells, evaluated by flow cytometry 4 weeks after reconstitution. (**F**) Representative tdTomato and CD45.2 contour plots and (**G**) bar graph showing % of host and donor *Ms4a3*$^{tdTom-}$ chimerism and donor *Ms4a3*$^{tdTom+}$ chimerism of the indicated lung myeloid cell populations, as in (D-E), evaluated by flow cytometry 4 weeks after reconstitution and 10 days after mock infection. (**H**) Representative tdTomato and CD45.2 contour plots and (**I**) bar graphs showing % of host + donor *Ms4a3*$^{tdTom-}$ chimerism and donor *Ms4a3*$^{tdTom+}$ chimerism of the indicated lung myeloid cell populations, as in (F-G), evaluated by flow cytometry 4 weeks after reconstitution and 10 days after IAV infection. (**J**) Representative tdTomato and CD45.1 contour plots and (**K**) bar graph showing % of host CD45.1/CD45.2, CD45.2 donor *Ccr2*$^{-/-}$ and *Ms4a3*$^{tdTom+}$ chimerism of blood neutrophils (Neu) and Mo from lethally-irradiated CD45.1/CD45.2 mice reconstituted with a 1:1 mix of CD45.2 *Ccr2*$^{-/-}$ and *Ms4a3*$^{tdTom+}$ BM cells, evaluated by flow cytometry 4 weeks after reconstitution. (**L**) Bar graph showing the frequency of Annexin V and PI negative and/or positive fractions within the indicated lung myeloid cell populations, quantified by flow cytometry at day 10 post-IAV in WT mice. (A,C,E,G,I,K,L) Data show mean + SEM and are pooled from 2 independent experiments (n=4-10 mice). *P* values compare donor *Ms4a3*$^{tdTom+}$ chimerism in (D,F,H,J) and were calculated using (A,C) a one-way ANOVA with Dunnett's post hoc tests, (E,K) a two-way ANOVA with Sidak's post hoc tests or (G,I,L) a two-way ANOVA with Tukey's post hoc tests. *, $P<0.05$; **, $P<0.01$; ****, $P<0.0001$.

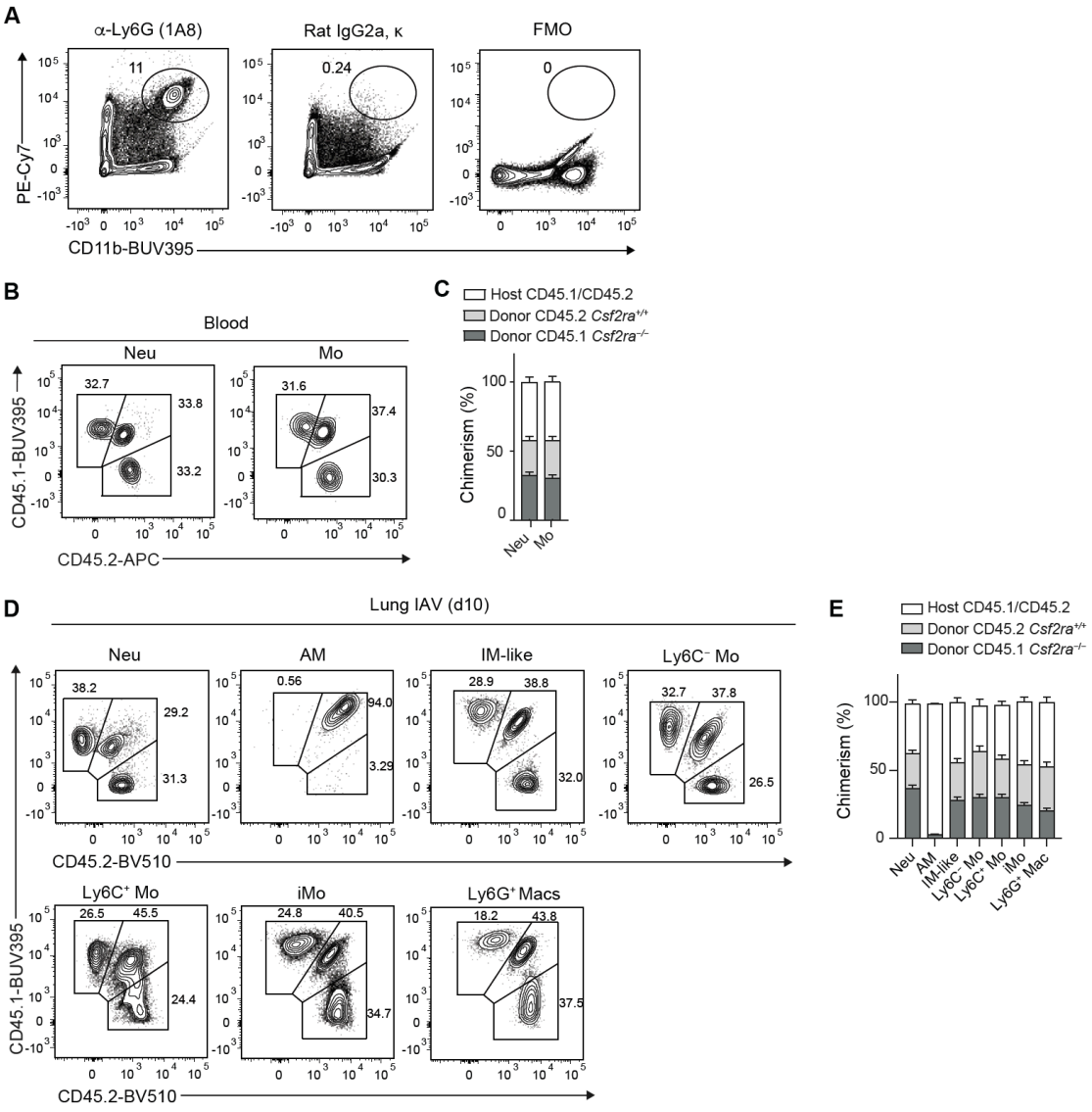

Fig. S4. Specificity of the anti-Ly6G staining and analysis of IAV-infected *Csf2ra*$^{-/-}$: *Csf2ra*$^{+/+}$ mixed BM chimeras. (**A**) Representative contour plots of PE-Cy7 and CD11b expression within lung live CD45^{+} cells in IAV-infected WT mice at day 10 post-IAV. Plots are representative of 1 of 6 mice analyzed, each giving similar results. (**B**) Representative CD45.1 and CD45.2 contour plots and (**C**) bar graph showing % of host CD45.1/CD45.2, CD45.2 donor *Csf2ra*$^{-/-}$ and CD45.1 *Csf2ra*$^{+/+}$ chimerism of blood neutrophils (Neu) and monocytes (Mo) from thorax-protected, lethally-irradiated CD45.1/CD45.2 mice reconstituted with a 1:1 mix of CD45.2 *Csf2ra*$^{-/-}$ and CD45.1 *Csf2ra*$^{+/+}$ BM cells, evaluated by flow cytometry 4 weeks after reconstitution. (**D**) Representative CD45.1 and CD45.2 contour plots and (**E**) bar graph showing % of host CD45.1/CD45.2, donor CD45.1 *Csf2ra*$^{-/-}$ and donor CD45.2 *Csf2ra*$^{+/+}$ chimerism of the indicated lung myeloid cell populations, as in (B-C), infected with IAV 4 weeks later and evaluated at day 10 post-IAV. (C,E) Data show mean + SEM and are pooled from 2 independent experiments (n=10 mice).

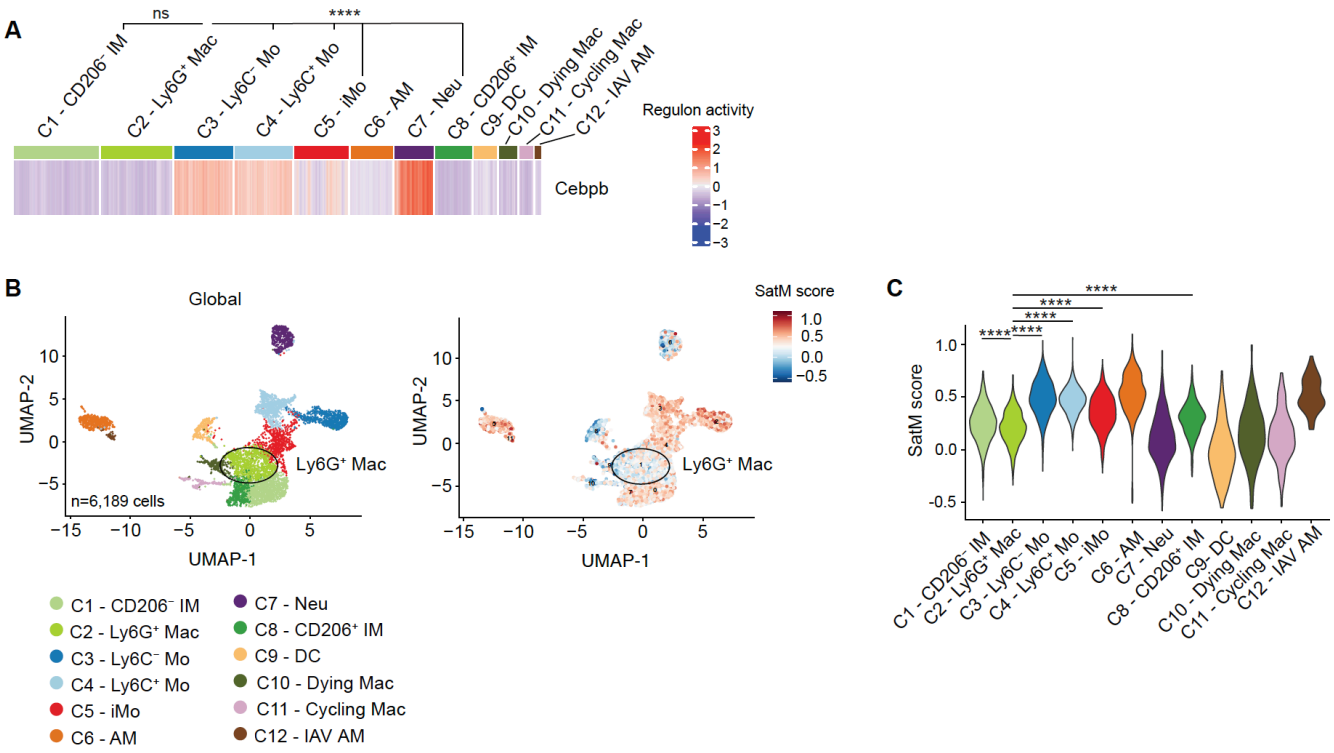

Fig. S5. Transcriptomic comparison of Ly6G$^+$ Macs and SatM monocytes. (**A**) Heatmap depicting predicted activities of Cebpb across lung myeloid cells post-IAV, evaluated by SCENIC analysis of the scRNA-seq data shown in Fig. 2A. (**B**) UMAP plots of scRNA-seq data depicting (left) the transcriptional identity of sorted lung live CD45$^+$F4/80$^+$ and/or CD11b$^+$ cells from mock- or IAV-infected WT mice 10 days post-infection (5 mice per time points), merged with a published dataset of steady-state lung monocytes and IMs (*69*), and (right) a SatM monocyte signature score (*35*). (C) SatM monocyte signature score within each scRNA-seq cluster, as depicted by violin plots (height: score; width: abundance of cells). (A,C) *P* values were calculated using a Wilcoxon rank sum test. ****, $P<0.0001$. ns, not significant.

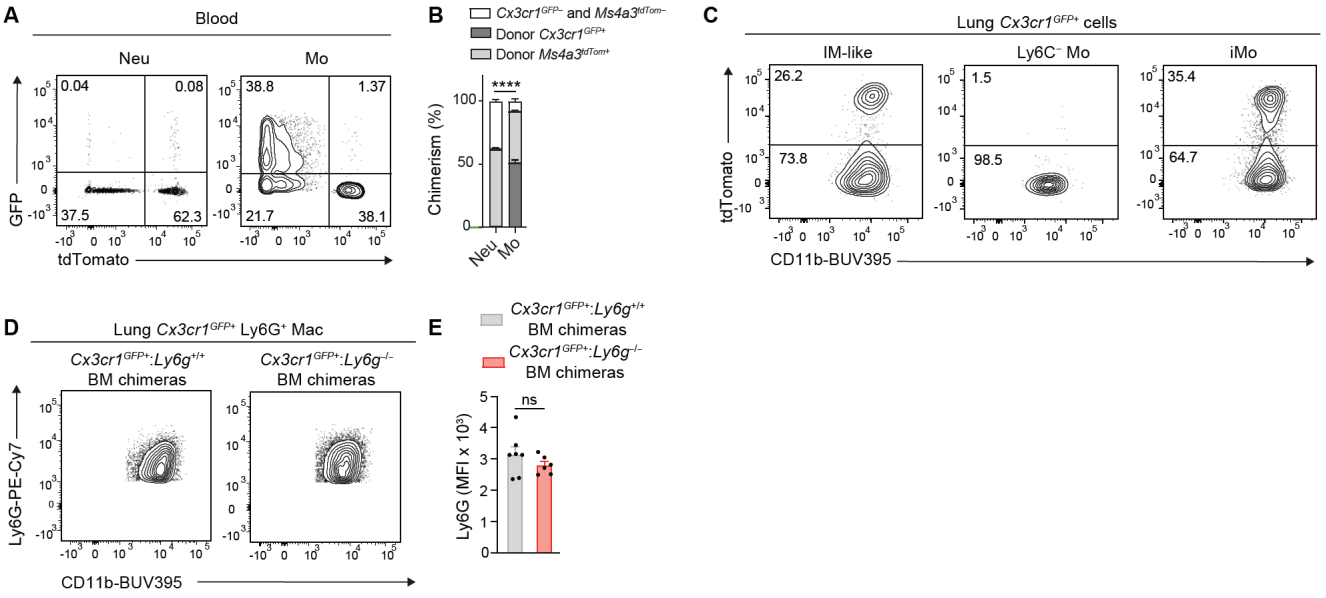

Fig. S6. Efferocytic abilities of lung myeloid cells post-IAV. (**A**) Representative GFP and tdTomato contour plots and (**B**) bar graph showing chimerism of *Cx3cr1*$^{GFP-}$*Ms4a3*$^{tdTom-}$, donor *Cx3cr1*$^{GFP+}$ and donor *Ms4a3*$^{tdTom+}$ cells in blood neutrophils (Neu) and monocytes (Mo) from lethally-irradiated CD45.2 WT mice reconstituted with a 1:1 mix of CD45.2 *Cx3cr1*$^{GFP+}$ and *Ms4a3*$^{tdTom+}$ BM cells, evaluated by flow cytometry 4 weeks after reconstitution. (**C**) Representative tdTomato and CD11b contour plots of the indicated lung *Cx3cr1*$^{GFP+}$ donor cell populations from lethally-irradiated CD45.2 WT mice reconstituted with a 1:1 mix of CD45.2 *Cx3cr1*$^{GFP+}$ and *Ms4a3*$^{tdTom+}$ BM cells, infected with IAV 4 weeks later and evaluated at day 10 post-IAV. (**D**) Representative Ly6G and CD11b contour plots of lung *Cx3cr1*$^{GFP+}$ Ly6G^{+} Macs from lethally-irradiated CD45.1/CD45.2 mice reconstituted with a 1:1 mix of CD45.2 *Cx3cr1*$^{GFP+}$ and *Ly6g*$^{+/+}$ (left) or *Ly6g*$^{-/-}$ (right) BM cells, infected with IAV 4 weeks later and evaluated at day 10 post-IAV. (**E**) Bar graph showing Ly6G expression levels in lung *Cx3cr1*$^{GFP+}$ Ly6G^{+} Macs, as in (D). (B,E) Data show mean + SEM and are pooled from 2 independent experiments (B: *n*=14 mice; E: *n*=6 mice). (B) *P* values compare donor *Cx3cr1*^{GFP} chimerism and were calculated using a two-way ANOVA with Sidak's post hoc tests. (E) *P* values were calculated using a two-tailed Student's *t* test. ns, not significant.

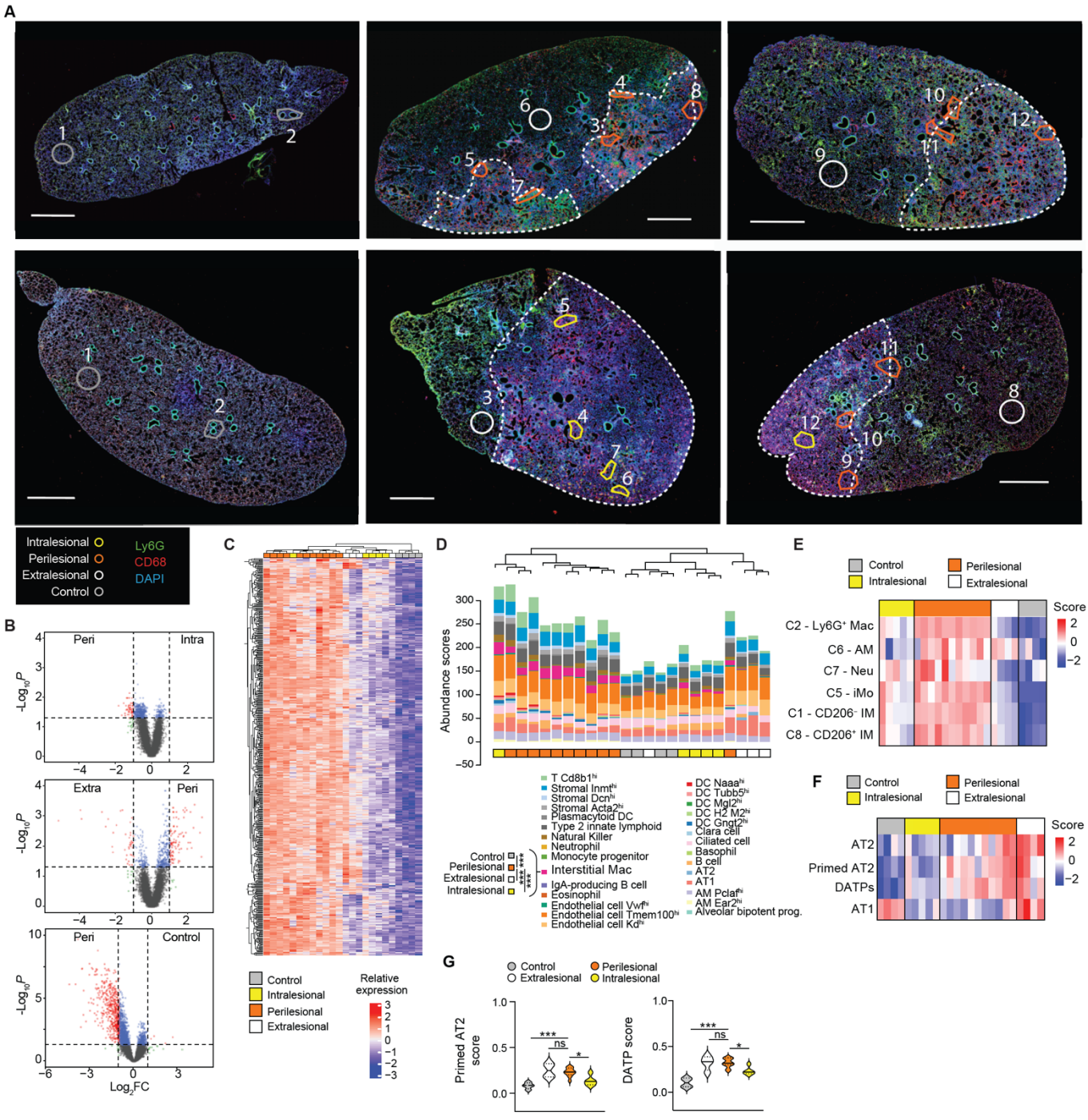
A
Intralesional
Perilesional
Extralesional
Control
Ly6G
CD68
DAPI
B
Peri
Intra
Extra
Peri
Peri
Control
-Log10P
Log2FC
C
Control
Intralesional
Perilesional
Extralesional
Relative expression
D
Abundance scores
T Cd8b1hi
Stromal Inmthi
Stromal Dcnhi
Stromal Acta2hi
Plasmacytoid DC
Type 2 innate lymphoid
Natural Killer
Neutrophil
Monocyte progenitor
Interstitial Mac
IgA-producing B cell
Eosinophil
Endothelial cell Vwfhi
Endothelial cell Tmem100hi
Endothelial cell Kdhi
DC Naaahi
DC Tubb5hi
DC Mgl2hi
DC H2 M2hi
DC Gngt2hi
Clara cell
Ciliated cell
Basophil
B cell
AT2
AT1
AM Pclafhi
AM Ear2hi
Alveolar bipotent prog.
E
Score
C2 - Ly6G+ Mac
C6 - AM
C7 - Neu
C5 - iMo
C1 - CD206- IM
C8 - CD206+ IM
F
Score
AT2
Primed AT2
DATPs
AT1
G
Primed AT2 score
DATP score
ns
***
*

Fig. S7. Identification of Ly6G$^+$ Macs-AT2 clusters by confocal microscopy in lung perilesional areas post-IAV. (**A**) Selection of regions of interest (ROIs) on lung sections from mock- or IAV-infected WT mice at day 10 post-IAV, stained with anti-Ly6G and anti-CD68 antibodies. (**B**) Volcano Plot depicting the differentially expressed genes (DEGs) between perilesional (Peri) and intralesional (Intra) areas (top), extralesional (Extra) and Peri areas (middle), and Peri and control areas (bottom). (**C**) Heatmap depicting the significantly upregulated genes in Peri areas as compared to Intra areas. (**D**) Cell deconvolution of the ROIs and abundance score of cell populations in individual ROIs using SpatialDecon algorithm. (**E**) Heatmap showing the signature score of the indicated myeloid cell populations within individual ROIs, inferred from the scRNA-seq data presented in Fig. 2A. (**F**) Heatmap showing the signature score of transitional epithelial cell states during AT2-mediated regeneration after bleomycin-induced lung injury, inferred from previously published scRNA-seq data **(*38*)**. (**G**) Primed AT2 (left) and DATPs (right) signature scores within control, extralesional, perilesional and intralesional ROIs, as in (F), as depicted by violin plots (height: scores; width: abundance of cells). *P* values were calculated using (D) a two-way ANOVA with Tukey's post-hoc tests or (G) a one-way ANOVA with Tukey's post-hoc tests. *, $P<0.05$; ***, $P<0.001$. ns, not significant.

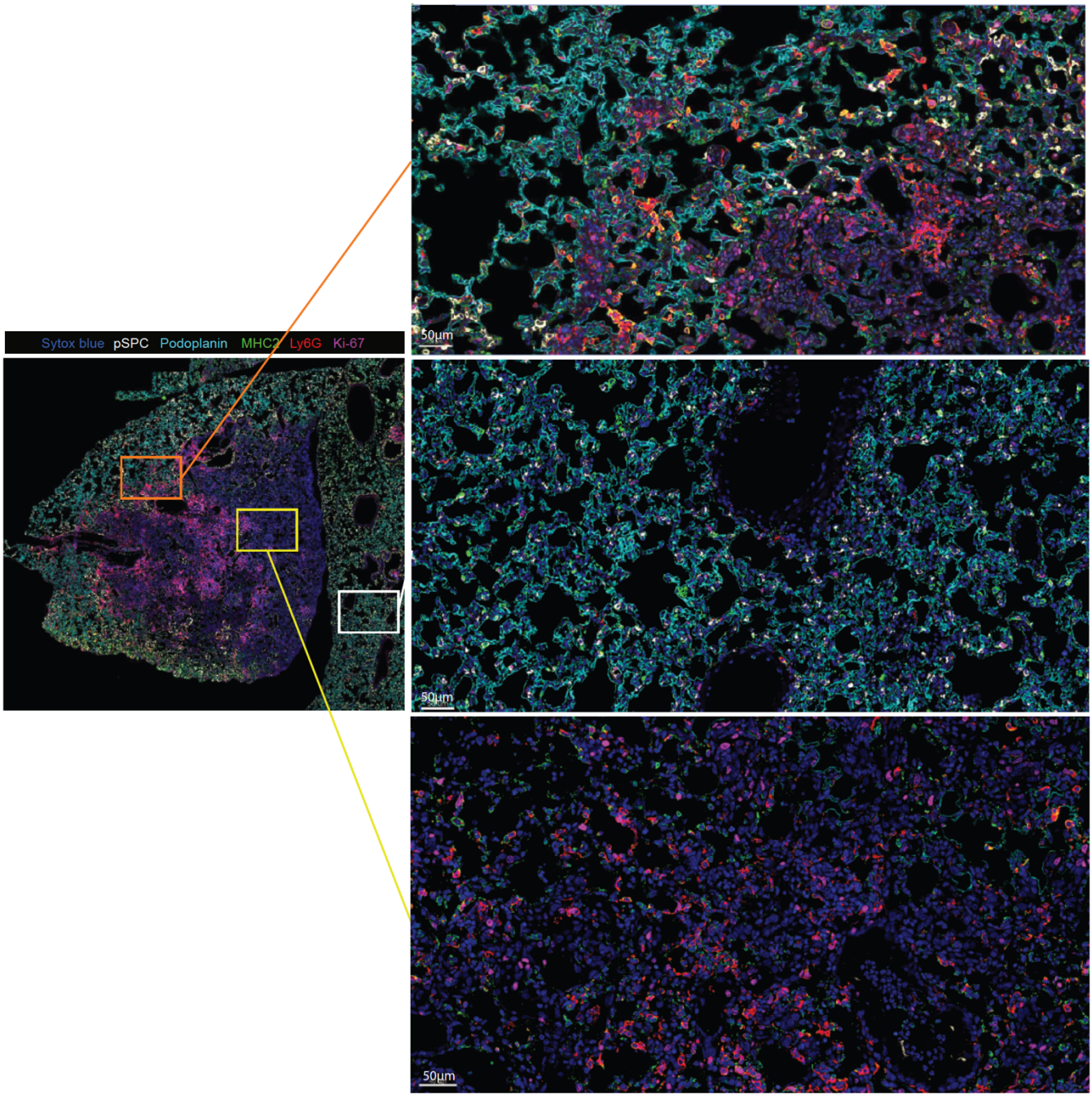
Sytox blue pSPC Podoplanin MHC2 Ly6G Ki-67
50µm
50µm
50µm

Fig. S8. Ly6G$^+$ Macs cluster with AT2 cells in perilesional areas. Representative high-resolution confocal laser scanning microscopy picture of a lung section from an IAV-infected WT mouse at day 10 post-IAV. Zooms of perilesional (orange) and intralesional (yellow) areas are shown. Pictures are representative of 1 of 6 mice analyzed, each of them giving similar results. Scale bar: 50 μm.

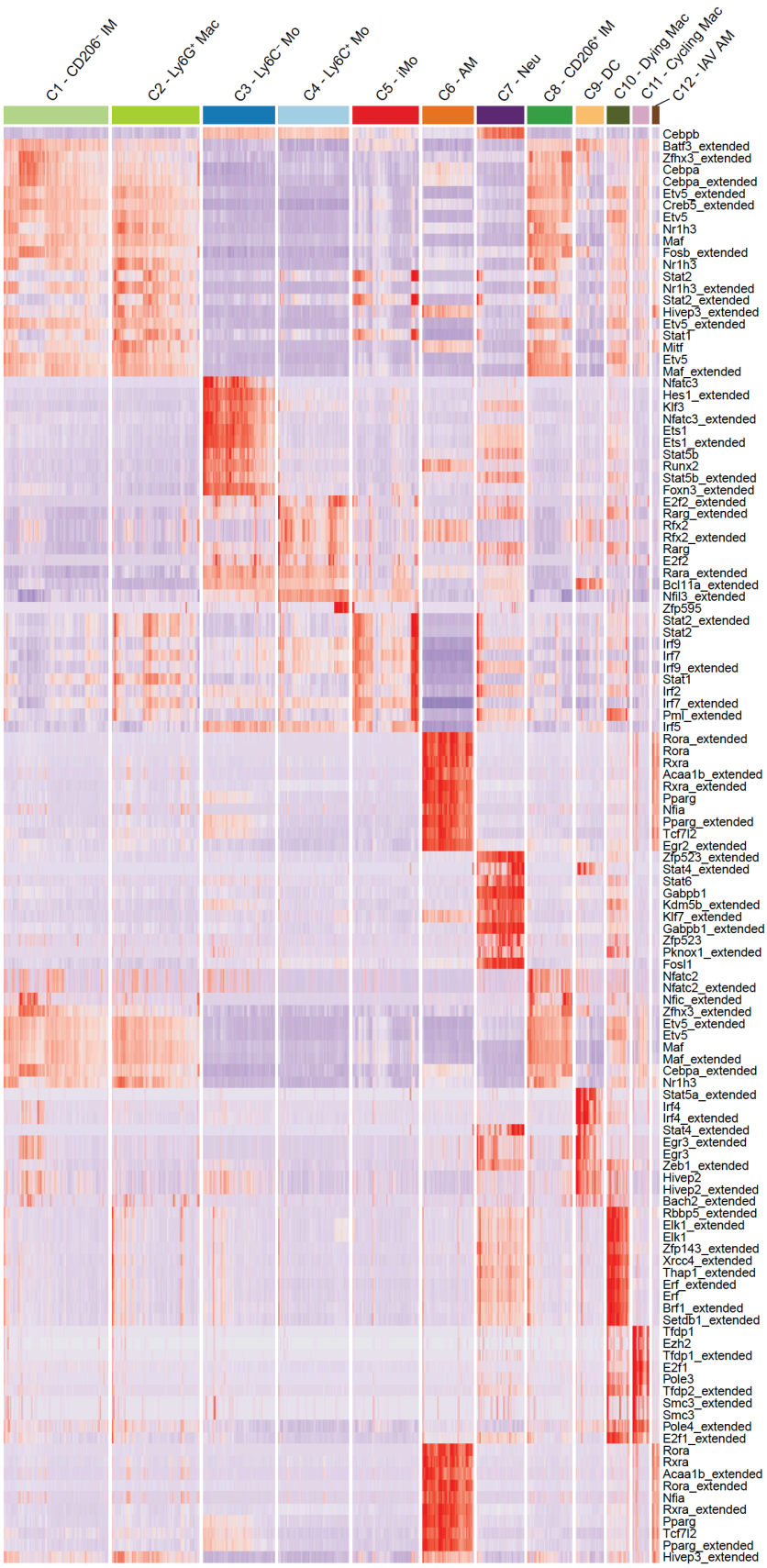
C1 - CD206- IM
C2 - Ly6G+ Mac
C3 - Ly6C- Mo
C4 - Ly6C+ Mo
C5 - iMo
C6 - AM
C7 - Neu
C8 - CD206+ IM
C9- DC
C10 - Dying Mac
C11 - Cycling Mac
C12 - IAV AM
Cebpb
Batf3_extended
Zfhx3_extended
Cebpa
Cebpa_extended
Etv5_extended
Creb5_extended
Etv5
Nr1h3
Maf
Fosb_extended
Nr1h3
Stat2
Nr1h3_extended
Stat2_extended
Hivep3_extended
Etv5_extended
Stat1
Mitf
Etv5
Maf_extended
Nfatc3
Hes1_extended
Klf3
Nfatc3_extended
Ets1
Ets1_extended
Stat5b
Runx2
Stat5b_extended
Foxn3_extended
E2f2_extended
Rarg_extended
Rfx2
Rfx2_extended
Rarg
E2f2
Rara_extended
Bcl11a_extended
Nfil3_extended
Zfp595
Stat2_extended
Stat2
Irf9
Irf7
Irf9_extended
Stat1
Irf2
Irf7_extended
Pml_extended
Irf5
Rora_extended
Rora
Rxra
Acaa1b_extended
Rxra_extended
Pparg
Nfia
Pparg_extended
Tcf7l2
Egr2_extended
Zfp523_extended
Stat4_extended
Stat6
Gabpb1
Kdm5b_extended
Klf7_extended
Gabpb1_extended
Zfp523
Pknox1_extended
Fosl1
Nfatc2
Nfatc2_extended
Nfic_extended
Zfhx3_extended
Etv5_extended
Etv5
Maf
Maf_extended
Cebpa_extended
Nr1h3
Stat5a_extended
Irf4
Irf4_extended
Stat4_extended
Egr3_extended
Egr3
Zeb1_extended
Hivep2
Hivep2_extended
Bach2_extended
Rbbp5_extended
Elk1_extended
Elk1
Zfp143_extended
Xrcc4_extended
Thap1_extended
Erf_extended
Erf
Brf1_extended
Setdb1_extended
Tfdp1
Ezh2
Tfdp1_extended
E2f1
Pole3
Tfdp2_extended
Smc3_extended
Smc3
Pole4_extended
E2f1_extended
Rora
Rxra
Acaa1b_extended
Rora_extended
Nfia
Rxra_extended
Pparg
Tcf7l2
Pparg_extended
Hivep3_extended

Fig. S9. SCENIC analysis of lung myeloid cells at day 10 post-IAV. Heat map depicting predicted transcription factor (TF) activities across lung myeloid cells at day 10 post-IAV, as assessed by SCENIC analysis of the scRNA-seq data shown in Fig. 2A.

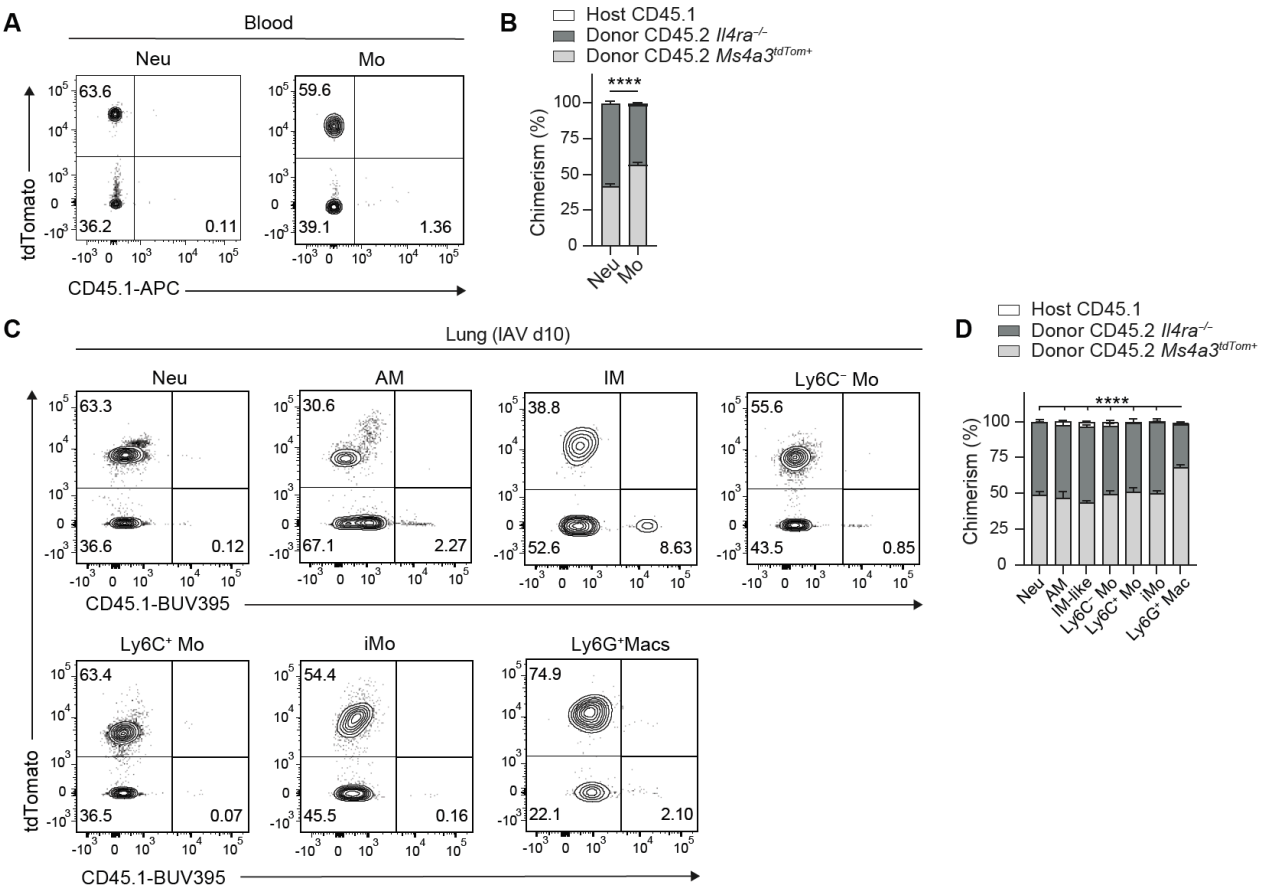

Fig. S10. Analysis of IAV-infected *Il4ra*$^{-/-}$:*Il4ra*$^{+/+}$ mixed BM chimeras. (**A**) Representative tdTomato and CD45.1 contour plots and (**B**) bar graph showing % of host CD45.1, donor CD45.2 *Il4ra*$^{-/-}$ and donor CD45.2 *Ms4a3*$^{tdTom+}$ chimerism of blood neutrophils (Neu) and monocytes (Mo) from lethally-irradiated CD45.1 mice reconstituted with a 1:1 mix of CD45.2 *Il4ra*$^{-/-}$ and *Ms4a3*$^{tdTom+}$ BM cells, evaluated 4 weeks after transplantation by flow cytometry. (**C**) Representative tdTomato and CD45.1 contour plots and (**D**) bar graph showing % of host CD45.1, donor CD45.2 *Il4ra*$^{-/-}$ and *Ms4a3*$^{tdTom+}$ chimerism of the indicated lung myeloid cell populations from lethally-irradiated CD45.1 mice reconstituted with a 1:1 mix of CD45.2 *Il4ra*$^{-/-}$ and *Ms4a3*$^{tdTom+}$ BM cells, infected with IAV 4 weeks later and evaluated at day 10 post-IAV. (B,D) Data show mean + SEM and are pooled from 2 independent experiments (B: n=4 mice; D: n=8 mice). (B,D) P values compare donor CD45.2 *Il4ra*$^{-/-}$ chimerism and were calculated using (B) a two-way ANOVA with Sidak's post hoc tests or (D) a two-way ANOVA with Tukey's post hoc tests. ***, P<0.001; ****, P<0.0001.

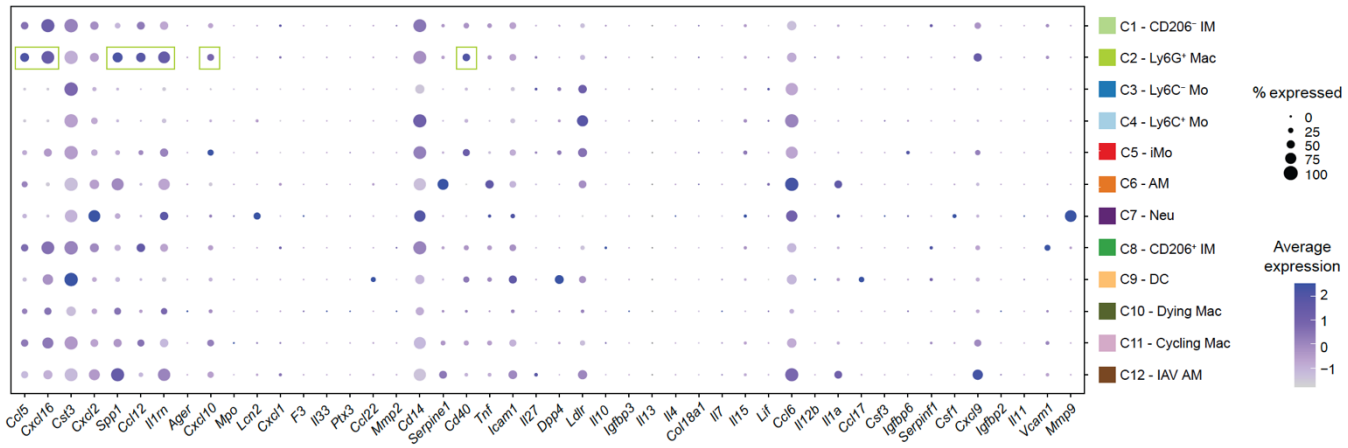

Fig. S11. Gene expression in myeloid cell clusters identified by scRNA-seq at day 10 post-IAV. Dot plots showing average expression of the indicated genes and % of cells expressing the genes within each cluster, related to Fig. 7K and 2A. Dot plots framed in green indicated gene that are significantly (P<0.0001) upregulated in C2 - Ly6G^{+} Macs as compared to other clusters. P values were calculated using a Wilcoxon rank sum test.

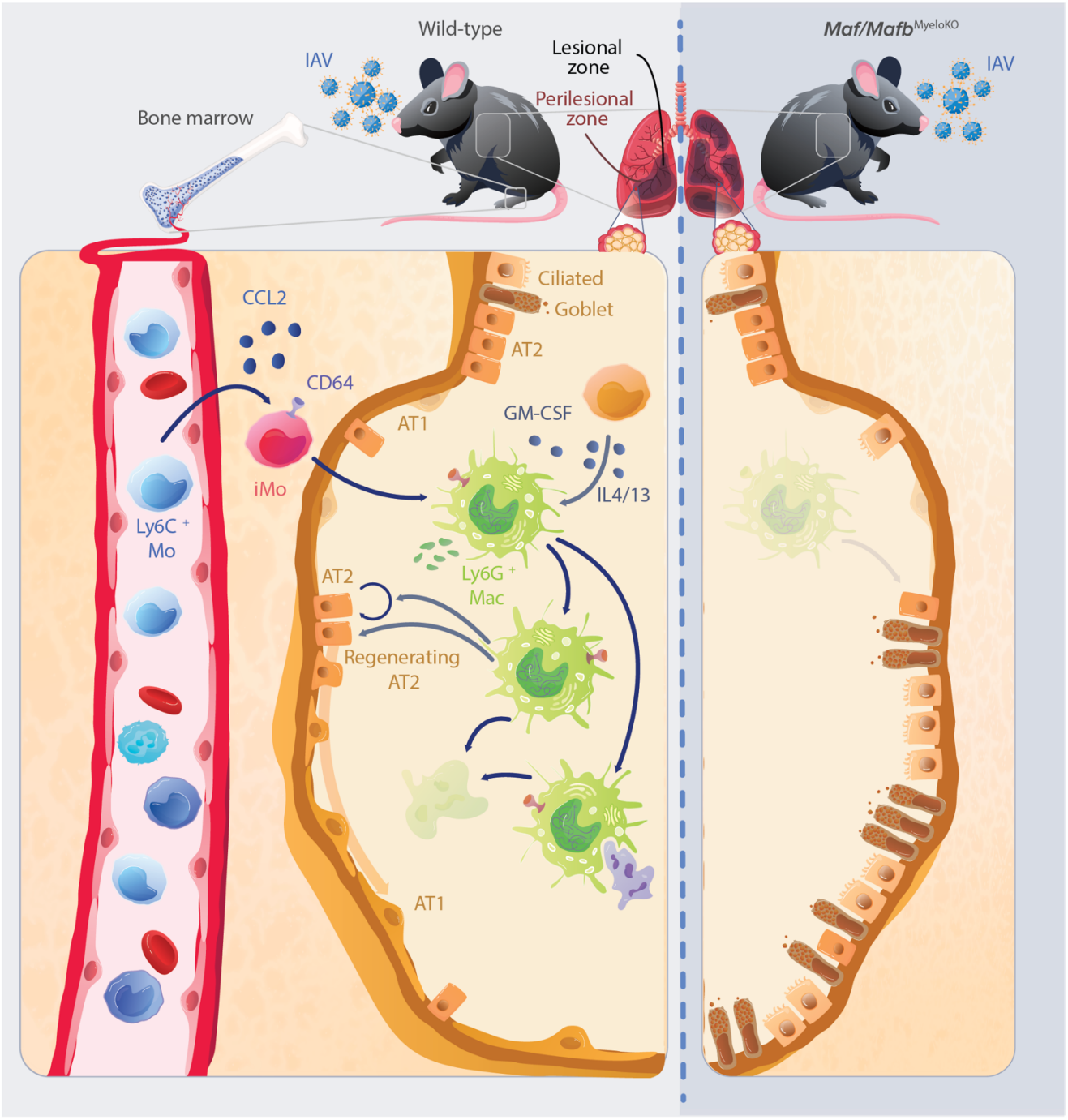
Wild-type
Maf/Mafb MyeloKO
IAV
IAV
Lesional zone
Perilesional zone
Bone marrow
CCL2
CD64
iMo
Ly6C + Mo
Ciliated
Goblet
AT2
AT1
GM-CSF
IL4/13
Ly6G + Mac
AT2
Regenerating AT2
AT1

Fig. S12. Proposed model of Ly6G$^+$ Mac-mediated alveolar epithelial regeneration after IAV-triggered injury. In mice, an atypical population of Ly6G$^+$ Macs is recruited from BM-derived Ccr2-dependent monocytes during the early recovery phase of IAV infection. Ly6G$^+$ Macs exhibit atypical ultrastructural features, are metabolically very active and short-lived, and are endowed with powerful phagocytic and efferocytic capabilities. They inhabit the alveolar spaces of lung perilesional areas, where they promote euplastic alveolar regeneration and AT2-to-AT1 differentiation via IL-4R-dependent mechanisms and soluble factors. In the absence of Ly6G$^+$ Macs, *Maf/MafB*^{MyeloKO} mice exhibit exacerbated morbidity, pathology and dysplastic bronchiolization of the alveoli.

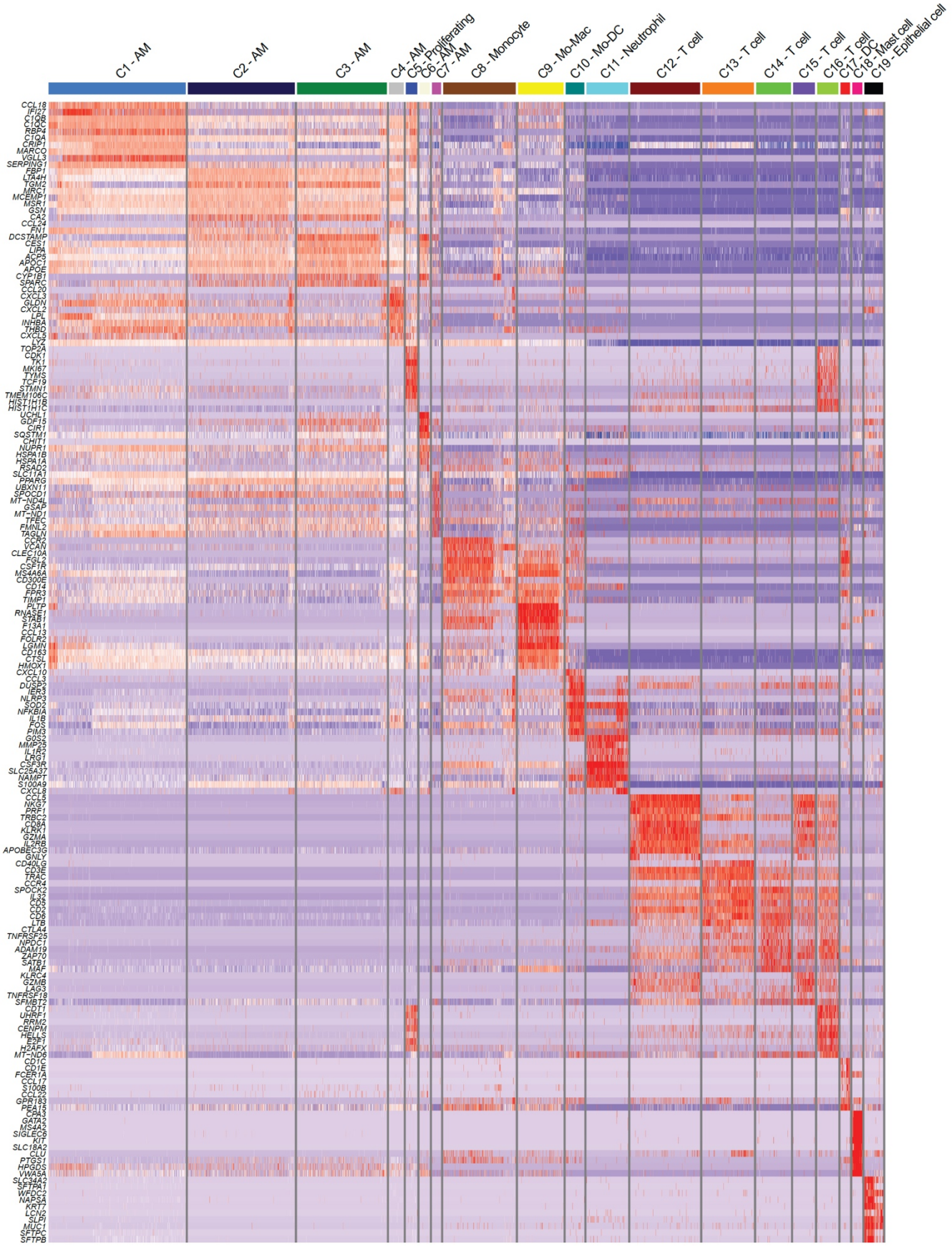
C1 - AM
C2 - AM
C3 - AM
C4 - AM
C5 - Proliferating
C6 - AM
C7 - AM
C8 - Monocyte
C9 - Mo-Mac
C10 - Mo-DC
C11 - Neutrophil
C12 - T cell
C13 - T cell
C14 - T cell
C15 - T cell
C16 - T cell
C17 - DC
C18 - Mast cell
C19 - Epithelial cell
CCL18
IFI27
C1QB
C1QC
RBP4
C1QA
CRIP1
MARCO
VSIG4
SERPINA1
FBP1
LTA4H
TGM2
MRC1
MCEMP1
MSR1
GSN
CA2
CCL24
FN1
DCSTAMP
CES1
LIPA
ACP5
APOC1
APOE
CYP1B1
SPARC
CCL20
CXCL3
GLDN
CXCL2
LPL
INHBA
THBS1
THBD
CXCL5
LYZ
TOP2A
CDK1
UK1
MKI67
TYMS
TCP19
STMN1
TMEM106C
HIST1H1B
HIST1H1C
UCHL1
GDF15
CIR1
SQSTM1
CHIT1
NUPR1
HSPA1B
HSPA1A
PSAT2
SLC17A1
PPARG
UBXN11
SPOCD1
MT-ND4L
GSAP
MT-ND1
TFEC
FMNL3
TAGLN
CCR2
VCAN
CLEC10A
FGL2
CSF1R
MS4A6A
CD300E
CD14
FPR3
TIMP1
PLTP
RNASE1
STAB1
F13A1
CCL13
FOLR2
LGMN
CD163
CTSL
HMOX1
CXCL10
CCL3
DUSP2
IER3
NLRP3
SOD2
NFKBIA
IL1B
FOS
PIM3
G0S2
MMP25
IL1R2
LRG1
CSF3R
SLC25A37
NAMPT
S100A9
CXCL8
CCL5
NKG7
PRF1
TRBC2
CD8A
KLRK1
GZMA
IL2RB
APOBEC3G
GNLY
CD40LG
CD3E
TRAC
CCR4
SPOCK2
IL32
CD5
CD2
CD6
LTB
CTLA4
TNFRSF25
NPDC1
ADAM19
ZAP70
SATB1
MAF
KLRC4
GZMB
LAG3
TNFRSF18
SFMBT2
CDT1
UHRF1
RRM2
CENPM
HELLS
E2F1
H2AFX
MT-ND6
CD1C
CD1E
FCER1A
CCL17
S100B
CCL22
GPR183
PEA15
CPA3
GATA2
MS4A2
SIGLEC6
KIT
SLC18A2
CLU
PTGS1
HPGDS
VWA5A
SLC34A2
SFTPA1
WFDC2
NAPSA
KRT7
LCN2
SLPI
MUC1
SFTPC
SFTPB

Fig. S13. Transcriptomic identities of human BALF single cells analyzed by scRNA-seq. Heatmap depicting the single cell expression of the 20 most upregulated genes within each cluster of human BALF cells analyzed by scRNA-seq, as shown in Fig. 8J.

Patient	Gender	Age	Disease status	Number of BALF cells analyzed
1	**M**	50	Bacterial pneumonia	858
2	**F**	63	Immunosuppressed, bacterial pneumonia	1,032
3	**M**	58	Interstitial pneumonia, metapneumovirus and cytomegalovirus infections	811
4	**M**	60	Pneumonia	1,445
5	**M**	71	Lung fibrosis and bacterial bronchopneumonia	311
6	**F**	62	Pneumonia	289
7	**M**	71	Immunosuppressed, bronchopneumonia	563

Table S1. Characteristics of patients from whom originate the BALF cells analyzed by scRNA-seq.

Reagents	Source	Cat. number
5-Ethynyl-2′-deoxyuridine	Santa Cruz Biotechnology	sc-284628
(Z)-4-Hydroxytamoxifen	Sigma-Aldrich	H7904
10X RBC Lysis Buffer (Multi-species)	Thermo Fisher Scientific	15270658
2-Mercaptoethanol	Thermo Fisher Scientific	21985023
Acetaminophen	Sigma-Aldrich	A7085
ALT ELISA Kit (Mouse)	Abcam	Ab2828-82
Agilent Seahorse XF Base Medium	Agilent	102353-100
Binding Buffer for Annexin V	Thermo Fisher Scientific	BMS500BB
Bleomycin sulfate - 10 mg	BIO-CONNECT	HY-17565
CD11b MicroBeads, human and mouse	Miltenyi Biotec	130-097-142
Cell-Tak™ Cell and Tissue Adhesive, 1 mg	Corning	354240
Click-iT™ Plus EdU Alexa Fluor™ 488 Flow Cytometry Assay Kit	Thermo Fisher Scientific	C10632
Collagenase IV	Thermo Fisher Scientific	17104019
Collagenase A	Roche	10103578001
Dispase® II protease	Sigma-Aldrich	D4693-1G
DMEM/F-12, no phenol red	Thermo Fisher Scientific	21041025
DNase I	Roche	11284932001
Donkey serum	Sigma-Aldrich	D9663
DPBS	Thermo Fisher Scientific	14190094
eBioscience™ Foxp3 / Transcription Factor Staining Buffer Set	Thermo Fisher Scientific	00-5523-00
Elastase from porcine pancreas	MedChemExpress	HY-P2974
Epoxy Embedding Medium kit	Sigma-Aldrich	45359
Fetal Bovine Serum	Thermo Fisher Scientific	A3160801
Formaldehyde, Extra Pure, Solution 37-41%, SLR, Fisher Chemical™	Thermo Fisher Scientific	F/1501/PB15
Hanks Balanced Salt Solution (HBSS)	Lonza	10-508F
Hemacolor	Sigma-Aldrich	111674
HEPES (1 M)	Thermo Fisher Scientific	15630080
Incucyte® Imagelock 96-well Plate	Sartorius	BA-04856
Insulin-Transferrin-Selenium (ITS -G) (100X)	Thermo Fisher Scientific	41400045
iTaq Universal SYBR Green Supermix	BioRad	1725120
L-Glutamine (200 mM)	Thermo Fisher Scientific	25030081
MEM Non-Essential Amino Acids Solution (100X)	Thermo Fisher Scientific	11140050
Méthanol	MerkMillipore	67-56-1
Milieu RPMI 1640	Thermo Fisher Scientific	21875091
Nimatek	Dechra	804132
Nunc® Lab-Tek® Chamber Slide™ system	Sigma-Aldrich	C7182
Penicillin-Streptomycin (10,000 U/mL)	Thermo Fisher Scientific	15140122
pHrodo™ Green E. coli BioParticles™ Conjugate for Phagocytosis	Thermo Fisher Scientific	P35366

Poly-D-lysine hydrobromide	Sigma-Aldrich	P6407
ProLong™ Diamond Antifade Mountant	Thermo Fisher Scientific	P36961
ProLong™ Gold Antifade Mountant with DNA Stain DAPI	Thermo Fisher Scientific	P36931
Propidium iodide	Thermo Fisher Scientific	P1304MP
Proteome Profiler Mouse XL Cytokine Array	R&D	ARY028
Recombinant Murine GM-CSF	Preprotech	315-03
Recombinant Murine IL-13	Preprotech	210-13
Recombinant Murine IL-4	Preprotech	214-14
Recombinant Murine M-CSF	Preprotech	315-02
RevertAid First Strand cDNA Synthesis Kit	Thermo Fisher Scientific	K1621
RNase A	Merck Millipore	70856
Rompun Sol Inj 2%	Bayer	76901
Sucrose	VWR	57-50-1
SYTOX™ Blue Nucleic Acid Stain	Thermo Fisher Scientific	S11348
Tissue-Tek® O.C.T. Compound	VWR	4583
Titriplex® III	Merck Millipore,	1084181000
TRITON® X-100 Detergent	MerkMillipore	648466
Trypsin-EDTA (0.05%), phenol red	Thermo Fisher Scientific	25300062
Tween 20	Acros Organics	AC233360010
UltraPure™ BSA (50 mg/mL)	Thermo Fisher Scientific	AM2616
Zytomed Systems HIER Citrate Buffer pH 6,0 (10 X)	Zytomed	ZUC028-500

Table S2. List of reagents used in this study.

Antibody	Source	Cat. number	RRID	Dilution (1.10^6 cells in 100 µL)
Annexin V APC Conjugate	Thermo Fisher	A35110		
Arginase 1 (A1exF5), APC	Thermo Fisher	17-3697-82	AB_2734835	1/100
Arginase 1 (A1exF5), PerCP-eFluor™ 710	Thermo Fisher	46-3697-82	AB_2734843	1/100
CD101 (Moushi101), PE	Thermo Fisher	12-1011-80	AB_1210729	1/100
CD115 (c-fms) (AFS98), APC	Thermo Fisher	17-1152-82	AB_1210789	1/100
CD11b (M1/70), BUV395	BD Bioscience	563553	AB_2738276	1/200
CD11b (M1/70), APC	Thermo Fisher	17-0112-83	AB_469344	1/100
CD11c (HL3), APC-Cy™7	BD Bioscience	561241	AB_10611727	1/200
CD124/IL4Ra (mILAR-M1), PE	BD Bioscience	561695	AB_10894018	1/100
CD170/Siglec F) (E50-2440), PE	BD Bioscience	552126	AB_394341	1/200
CD170/Siglec F (S17007L)FITC	Biolegend	155503	AB_2750232	1/200
CD177 Alexa Fluor™ 647	BD Bioscience	566599	AB_2869790	1/100
CD184/CXCR4 (2B11), APC	Thermo Fisher	17-9991-82	AB_10670878	1/60
CD31/PECAM-1 (390), APC	Thermo Fisher	17-0311-82	AB_657735	1/100
CD319 (4G2), APC	Biolegend	152003	AB_2632674	1/100
CD326/Epcam (G8.8), BV510	BD Bioscience	747748	AB_2738075	1/100
CD45.1(A20), APC	BD Bioscience	558701	AB_1645214	1/100
CD45.2 (104)V500	BD Bioscience	562129	AB_10897142	1/100
CD45.2 (104), BUV395	BD Bioscience	564616	AB_2738867	1/100
CD45.2 (104), FITC	BD Bioscience	561874	AB_10894189	1/100
CD64 (FcγRI) (X54-5/7.1), Brilliant Violet 421	Biolegend	139309	AB_2562694	1/100
c-MAF (sym0F1), PE	Thermo Fisher	12-9855-42	AB_2572747	1/100
CXCR4 (UMB2), Purified	AbCam	ab124824	AB_2564589	1/100
F4/80 (BM8), Brilliant Violet 650™	Biolegend	123149	AB_11220285	1/100
Ki-67 (SolA15), eFluor™ 570	Thermo Fisher	41-5698-82	AB_11040981	1/600
Ki-67 (SolA15), PerCP-eFluor™ 710	Thermo Fisher	46-5698-82	AB_11040981	0.3
Ly-6C (AL-21), PE-CF594	BD Bioscience	562728	AB_2737749	1/200
Ly-6G (1A8), PE-Cy™7	BD Bioscience	560601	AB_1727562	1/200
Ly-6G (1A8), Purified	BD Bioscience	551459	AB_394206	1/50
MafB (BRL046F), Purified	Bethyl Laboratories Inc.	A700-046		1/100

MHC Class II (I-A/I-E) (M5/114.15.2), Alexa Fluor™ 700	Thermo Fisher	56-5321-82	AB_494009	1/200
MHC II (IA/IE) (M5/114.15.2), PerCP/Cy5.5	Sony	1138130		1/600
Osteopontin (OPN), PE	R&D	IC808P	AB_10643832	1/100
Podoplanin (eBio8.1.1(8.1.1)), Super Bright™ 436	Thermo Fisher	62-5381-82	AB_2744800	1/200
Prosurfactant Protein C (EPR19839), Purified	AbCam	ab211326	AB_2927746	1/200
Secondary antibodies				
Goat anti-Rabbit IgG (H+L) Cross-Adsorbed Secondary Antibody, Alexa Fluor™ 532	Invitrogen	A11009	AB_2534076	1/1000
Goat anti-Rabbit IgG (H+L) Highly Cross-Adsorbed Secondary Antibody, Alexa Fluor™ 488	Invitrogen	A21209	AB_2535795	1/1000
GFP Polyclonal Antibody, Alexa Fluor™ 488	Invitrogen	A21311	AB_221477	1/200

Table S3. List of antibodies used in this study.